CORE LOSS CHARACTERIZATION AND DESIGN OPTIMIZATION OF HIGH-FREQUENCY POWER FERRITE DEVICES IN POWER ELECTRONICS APPLICATIONS

by

Pawel Miroslaw Gradzki

Dissertation submitted to the Faculty of the

Virginia Polytechnic Institute and State University

in partial fulfillment of the requirements for the degree of

Doctor of Philosophy

in

Electrical Engineering

APPROVED

Fred C. Lee, Chairman

Frederick W. Stephenson

Dan Y. Chen

Bo H. Cho

Robert W. Hendricks

March 30, 1992

Blacksburg, Virginia

CORE LOSS CHARACTERIZATION AND DESIGN OPTIMIZATION OF HIGH-FREQUENCY POWER FERRITE DEVICES IN POWER ELECTRONICS APPLICATIONS

by

Pawel Miroslaw Gradzki

Fred C. Lee, Chairman

Electrical Engineering

(ABSTRACT)

An impedance-based core loss measurement technique for power ferrites, the modeling and analysis of mechanisms of high-frequency losses, and design methodology for optimization for high-frequency magnetics are presented.

The high-frequency losses of ferrite materials are characterized employing a large-signal impedance measurement technique. The impedance analyzer, controlled through an IEEE-488 interface, measures the impedance of the inductor under test under large signal excitation via a power amplifier. The core loss is a form of a parallel resistance is derived from measured impedance characteristics. A wideband impedance probe, enables core loss characterization up to 100 MHz.

A comprehensive analysis of all major loss mechanisms in ferrites is presented. A new form of residual losses due to a magnetoelectric effect is postulated to account for losses at high frequencies. Two models of losses in ferrites are proposed, one with emphasis on analysis of loss mechanisms, and the other with an emphasis on the design of high-frequency magnetic components. Both models include the important effect of static bias field, which is the case in many power electronics applications. Magnetic losses due to magnetostriction are measured. Dependence of magnetoelastic resonances on the magnetic bias, core material, core shape and size is studied. The influence of diffusion after-effect on core loss under time-varying bias field is investigated.

Thermal stability of high-frequency magnetics is studied. A verification of one- and two-dimensional models of winding losses for solid and litz wire is performed. The optimum design method for high-frequency power transformers and inductors is proposed.

To my wife, Malgorzata,

and my son Adam

Acknowledgements

I would like to express my gratitude and appreciation to my advisor, Prof. Fred C. Lee, for his constant support, valuable expertise, and encouragement through the course of this work. His diverse interests and commitment to research made this work possible.

I thank Profs. Frederick W. Stephenson, Robert W. Hendricks, Dan Y. Chen, and Bo. H. Cho, for their excellent teaching in microelectronics, material science, and power electronics, for their contributions as members of my doctoral committee, and for their suggestions regarding this work.

I am thankful to Profs. Marian Kazimierczuk and Jan Ebert for their advise and help to initiate my doctoral studies at Virginia Polytechnic Institute and State University.

My study and research at the Virginia Power Electronics Center was an enjoyable and valuable experience mainly due to the excellent VPEC faculty, staff, and students. In particular I would like to thank Prof. Milan M. Jovanovic, Mr. Ashraf Lotfi, and Mr. Richard Farrington for scholastic discussions and cooperation in research. I also thank Mr. Grant G. Carpenter, Mr. Richard Gean, and Mr. William H. Cockey, Jr., for their help by providing laboratory equipment and parts for my experimental work.

I greatly thank my late father Apolinary Gradzki and my mother Barbara Gradzka for their sacrifices in bringing me up, for their guidance, and for introducing me to science and engineering.

Most importantly, I wish to thank my dear wife Malgorzata for her love, understanding, and continuous encouragement.

Finally, I thank Zytec Corporation of Eden Prairie, Minnesota, for awarding me the fellowship which enabled much of this work. This work was also supported by Virginia Center for Innovative Technology. I also thank Philips Components, Materials Group of Saugerties, New York, and Eindhoven, Netherlands, and Magnetics of Butler, Pennsylvania for providing ferrite samples.

Table of Contents

Table of Figures

Table of Tables

Chapter 1

Introduction

1.1 Survey of Previous Research

The development of solid-state electronics led to miniaturization of electronic equipment. The size of magnetic components in power supplies was also reduced due to improved materials and higher operating frequencies. Ferrites became the materials of choice because of their low losses at high frequencies where ultra-thin alloy laminations are prohibitively expensive.

Recent studies have shown that it is difficult to achieve miniaturization of magnetic components for high-frequency power conversion, while maintaining relatively high efficiency [1, 2, 3, 4, 5, 6, 7]. This problem is one of the major obstacles that hinders the development of high-frequency, high-density power converters.

The recent introduction of high-frequency quasi-resonant and multi-resonant converter topologies [8, 9, 10] has prompted research efforts for developing design tools for power transformers and inductors operating above 100 kHz. Since the size of high-frequency power transformers and inductors is limited by temperature rise due to core and winding losses, the design objective is to minimize total power dissipation. To accomplish this, it is necessary to accurately determine core and winding losses in magnetic components.

1.1.1 Measurement of High-Frequency Ferrites

In 1887 Lord Rayleigh [11] made the first measurements of magnetic properties of iron wire and determined the shape of the hysteresis loop using a magnetometer. Later, Weiss [12] introduced a ballistic method, Wien [13] an ac bridge, and Kelsall [14] an impedance transforming permeameter for use with the ac bridge. When ferrite magnetic materials with attractive properties at high frequencies became available, Lindenhovius and Breggen [15] introduced the resonant coaxial cavity method for frequencies above 30 MHz. For low-frequency measurements, the Kelsall's permeameter was improved to operate up to 50 MHz [16, 17, 18, 19], and a low-impedance ac bridge was developed [20]. For high-frequency power measurements up to 4 MHz, Christensen introduced an improved B-H tracer [21]. Early measurements of high-frequency power losses were performed to characterize ferrite materials for broad band power transformers in radio transmitters [22] and particle accelerators [23]. Recently new instrumentation improved the accuracy of permeability and loss measurements [24, 25, 26]. These methods are based on the measurement of the impedance that the magnetic core introduces into the transmission line. The characterization of magnetic materials for the application in power electronics requires a large number of data points because of the wide range of frequency, flux density, and temperature at which magnetic materials are used. This poses a particular problem at high frequencies where calibration at each frequency is essential for the accuracy of the measurement. Most of the instruments for impedance measurements provide signals with amplitudes too small for a large flux density excitation of magnetic cores at high frequencies. Therefore, in order to measure large-signal permeability and core loss, the most commonly used measurement method uses the digitizing oscilloscope or digitizer measuring voltage and current in the test transformer driven by a signal generator with power amplifier [27, 28, 29, 30, 31, 32, 33].

1.1.2 Characterization and Analysis of Losses in Ferrites

Traditionally, magnetic properties are characterized by hysteresis loop, permeability, and energy loss per cycle, as separated by Jordan [34] into three parts: hysteresis, eddy current, and residual loss. Permeability and loss in magnetic materials can be also represented by real and imaginary parts of the complex permeability [35]. Other common representations for magnetic losses are: relative tangent of magnetic loss divided by permeability, $\tan\delta/\mu$, core loss per unit volume, P_m, and core loss per unit weight. Parallel resistance and complex parallel permeability are also used [36].

Hysteresis losses at low fields are introduced by an irreversible displacement, nucleation, and extinction of the domain walls [37]. At high fields most of the domain walls are extinct, and the main contribution to hysteresis is due to irreversible rotation of magnetization [38, 39]. Eddy current losses occur due to the current induced in the conducting magnetic material by changes in the flux density [40, 41, 42, 43, 44]. Residual losses result from damping of the reversible domain wall motion [45, 46, 47, 48, 49, 50, 51, 52, 53], and the reversible domain rotation [54, 55, 56, 57].

Magnetomechanical coupling can also contribute to the permeability and loss [58, 59, 60, 61, 62, 63, 64, 65], particularly at resonance. Magnetoelastic resonances have been reported in ferromagnetic metals and alloys [66], nickel-zinc ferrites [67], ferrites for memory cores [68], and metallic glasses [69, 70, 71, 72, 73, 74].

In power electronics applications, the stability of core loss characteristics is very important because of the adverse effects of an elevated temperature on the windings, and the possibility of thermal runaway. Therefore, special attention must be paid to change of losses in time due to a diffusion after-effect [75].

1.1.3 Optimization of Power Transformer and Inductor Design

There is an increasing demand for size and weight reduction of magnetic components in power electronics applications. Design optimization of inductors and transformers is particularly critical in airborne and space applications [76, 77, 78] since 1950s. Often attempts [79, 80, 81, 82, 83] failed to yield an optimum design because of arbitrary constraints imposed on the design process. Constrained optimal design for low frequency power transformers was shown by Judd and Kressler [84]. The design of high-frequency power transformers and inductors is more difficult because of frequency-dependent winding and core losses. The expressions for output power of high-frequency transformers were derived by Snelling [85], but the design optimization effort was directed only at a winding structure [86]. The design procedure proposed by Coonrod [87] involves an elaborate algorithm but the proximity losses are not accounted for accurately.

For an optimum design procedure, the winding and core losses have to be modeled accurately. Eddy current losses in the windings have been analyzed quite extensively using one-dimensional model [88, 89, 90, 91]. However, little data on the experimental verification of the accuracy of that theory is available [92, 93, 94], particularly in litz wire, which is used at high frequencies to limit eddy current losses.

1.2 Formulation of Research Goals

The purpose of this work is to improve core loss measurement technique for high-frequency power ferrites, to analyze and quantify their losses, and to develop a methodology of the design optimization for high-frequency magnetics. Three particular research goals are set.

1. Develop the method for high-frequency core loss measurement technique for ferrite magnetic materials under large signal excitations for power electronics applications.

2. Characterize ferrite materials, by identifying their permeability and loss mechanisms, including the effects of static and dynamic bias magnetic fields, and losses due to magnetostriction. An analytical model of the core loss, encompassing all core loss mechanisms, is proposed.

3. Develop an optimum design procedure for high-frequency power inductors and transformers.

1.3 Outline of the Work

Chapter 2 describes the measurement technique used for high-frequency characterization of ferrite materials. Recent advances in measurement technology have enabled fast and accurate measurements of the impedance in a wide frequency and amplitude range [95]. The new instruments, used with power amplifiers and controlled through an IEEE-488 interface, are capable of producing high-frequency magnetic material characteristics at a range of flux densities in a reasonable time [96, 97].

An impedance analyzer is used to measure the impedance of the inductor under large signal excitation. The core loss is derived from measured impedance characteristics. A wideband impedance probe, together with a high-frequency power amplifier, enable core loss characterization up to 100 MHz at different temperatures. Three programs were written in Pascal for the measurement of permeability and the loss of ferrites under the following conditions:

- constant flux density and variable frequency,
- constant frequency and variable flux density,
- constant core loss per unit volume and variable frequency.

Chapter 3 contains a brief description of major loss mechanisms in ferrites. A new theory of residual losses due to a magnetoelectric effect is proposed. The models of losses in ferrites is examined with emphasis on analysis of loss mechanisms. The model includes the effect of a

static bias field. Permeability and loss characteristics of various grades of ferrites are measured and compared to proposed models, with an emphasis on the influence of a static bias field. Magnetic losses due to magnetostriction are measured and dependence of magnetoelastic resonances on the shape, size, material, and bias of the core is studied. The influence of diffusion after-effect on core loss is investigated.

In Chapter 4 verifications of the one- and two-dimensional analyses of winding losses for solid and litz wire are performed. A second model of magnetic losses in ferrites is proposed, with an emphasis on the design of high-frequency magnetic components. The optimum design method for high-frequency power transformers and inductors is proposed based on the analytical model developed previously.

All formulas in this work, except where noted, follow the International System of Units (SI).

Chapter 2

Measurement of Permeability and Losses in Ferrites

2.1 Measurement Methods and Sources of Errors

The design of high-frequency power inductors and transformers requires data on core loss and permeability of the magnetic material. Most manufacturers do not provide this data at high flux density levels, under bias, elevated temperatures, and at high frequencies. There are two method categories for measuring permeability and loss of magnetic material: direct methods and indirect methods [98]. Indirect methods, such as calorimetry, include not only losses in the core but also losses of the rest of the circuit, such as copper loss and dielectric loss of the resonant capacitor. The direct method derives permeability and core loss based on measurement of the voltage and current in the inductor or transformer. Following are the methods suitable for characterization of ferrites for power electronics applications. All except the last one are direct methods.

2.1.1 Dynamic B-H Tracer

The method initially proposed by Tamsky [99] for low-frequency power measurements was later improved by Christensen [100] for frequencies up to 4 MHz. The block diagram of the method is shown in Fig. 2.1. The loss and permeability can be determined from the area and

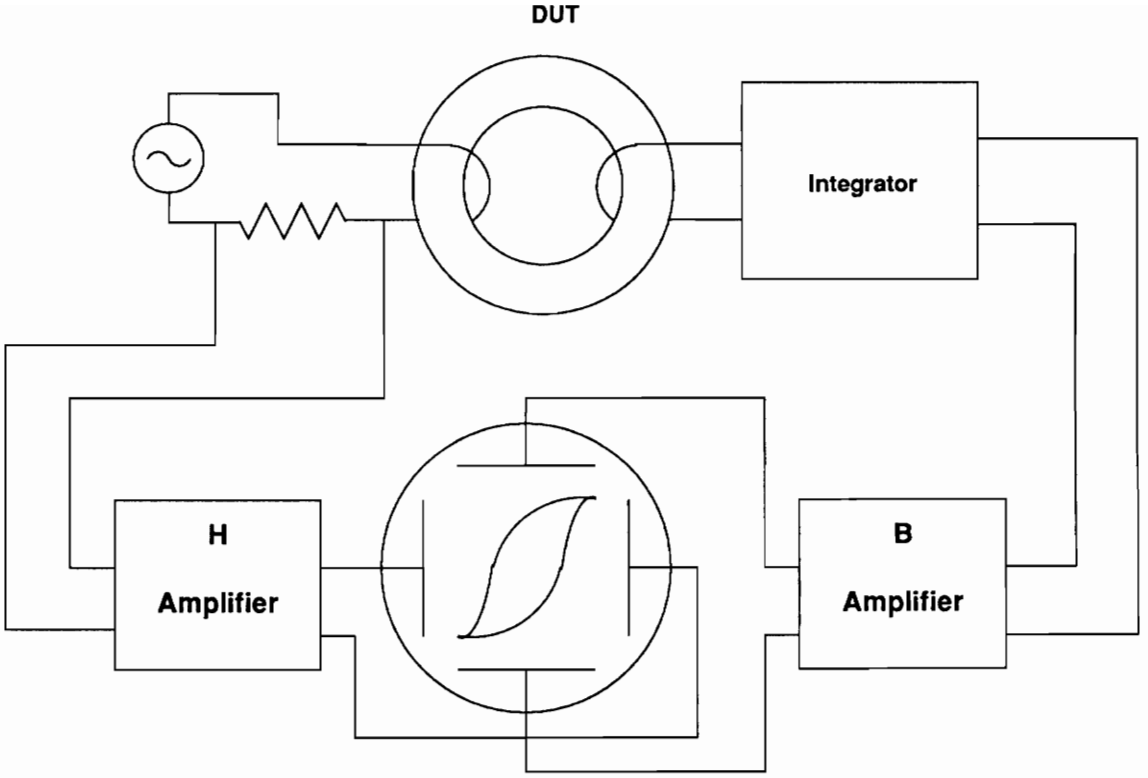

Fig. 2.1. *Block diagram of B-H tracer. Instantaneous voltage and current are plotted on the screen of the CRT (cathode ray tube). Even small phase errors result in a severe distortion of the B-H loop.*

slope of the B-H loop. Recently a digitizer [101, 102, 103] and a digitizing oscilloscope [104] were used to automate the data acquisition and calculations.

There are five major sources of error in this method:

- phase error in the amplifiers,
- phase error in the digitizer,
- amplitude error in the amplifiers,
- amplitude error in the digitizer, and
- stray inductance and capacitance of the test transformer.

Lord [105] pointed out that this method is very sensitive to phase errors and, even under sinusoidal flux density, the magnetizing current may contain 20 harmonics for square loop materials. In order to keep the phase error below 0.25 degrees, he recommended the lower and upper 3-dB roll-off frequencies of the B amplifier be at least two orders of magnitude below and above the measurement frequency, respectively. For the H amplifier, the upper frequency should be about 250 times the measurement frequency. Therefore a B-H tracer with maximum operating frequency of 10 MHz requires amplifiers and digitizer with an upper frequency of 2.5 GHz. The design of amplifiers, digitizers, and a current shunt or current probe with such a bandwidth poses great difficulties. Therefore the method is more suitable for low-frequency measurements.

2.1.2 Impedance Methods

Today there are six commonly used impedance measurement methods [106]:

- bridge method,
- resonant method,
- I-V method,

- network analysis method,
- time domain network analysis method, and
- auto balancing bridge method.

The bridge method for magnetic material measurements was introduced by Wien [107]. The circuit diagram of his setup is shown in Fig. 2.2. A telephone speaker was used as a null detector, and ac current was produced by a mechanical generator. The unknown inductance, L_u, and unknown resistance, R_u, were determined based on known values of fixed inductor, L_2, and variable resistors R_2, R_3, and R_4. Based on inductance and resistance, the permeability and losses were determined. The bridge method has a very high accuracy at small flux densities. However, at larger flux densities, higher harmonics generated due to nonlinearity of the B-H loop are the major source of error since they cause an additional loss in the bridge elements [108]. Other disadvantages include a need for variable precision resistors, frequency dependence of a resistance, inductance, and self-capacitance of the reference coil.

The circuit diagram of the resonant method is shown in Fig. 2.3. The principle of operation of this method is to measure a Q (quality) factor of the inductor by resonating the inductive part of its impedance with a capacitor. The resonant method was employed for high-frequency measurements by Bady [109]. The principal advantages of this method are:

- no phase error, since both voltage and current are in phase, and
- a better impedance match between a power source and a measured inductor or transformer.

Therefore, the power rating of an amplifier can be much smaller than the reactive power in the circuit, which is especially important at high frequencies. However, this method is very time consuming due to an adjustment to resonance necessary at each measurement point. The accuracy of impedance measurement is low, and measurement of small Q factors is not possible. Commercial instruments achieve basic accuracy of 7%.

The circuit diagram of the I-V method is shown in Fig. 2.4. Current is determined based on the differential voltage on resistor R. In practice, the current-sensing resistor is replaced with a current transformer to avoid the differential voltage measurement and to enhance accuracy.

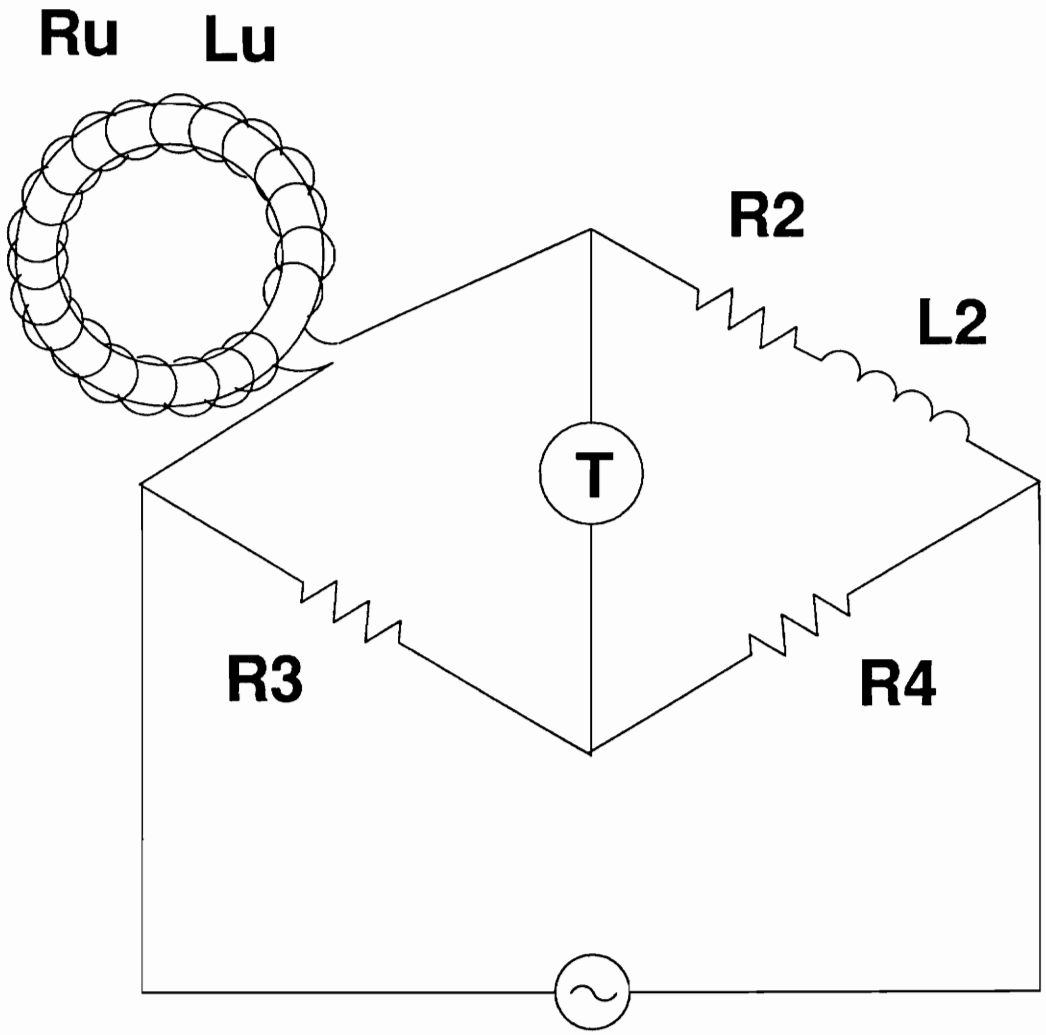

Fig. 2.2. Circuit diagram of the Wien ac bridge. When bridge is balanced, the telephone speaker, T, does not generate sound. Modern bridges use more sophisticated balance detectors.

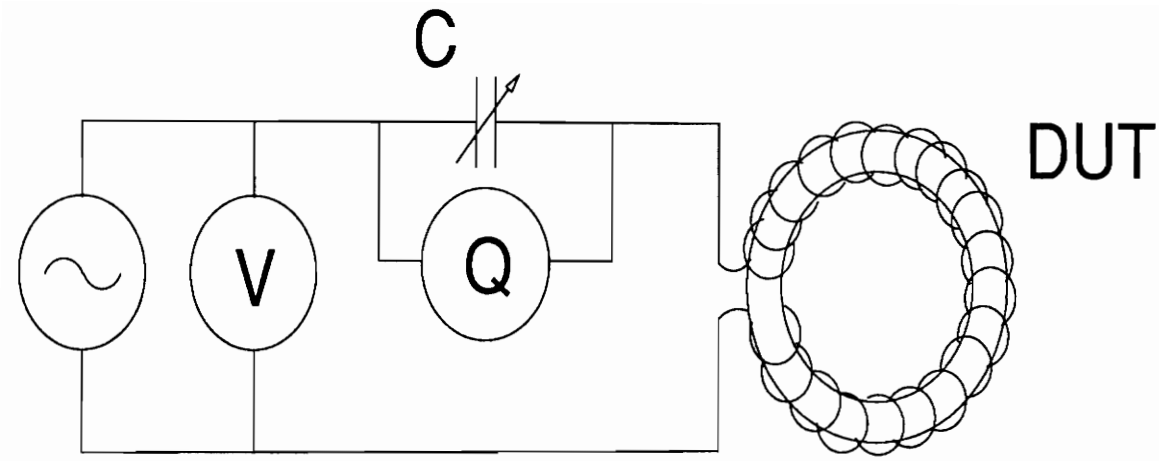

Fig. 2.3. Circuit diagram of the resonant method. Adjustment to the resonance is necessary at each measuring frequency.

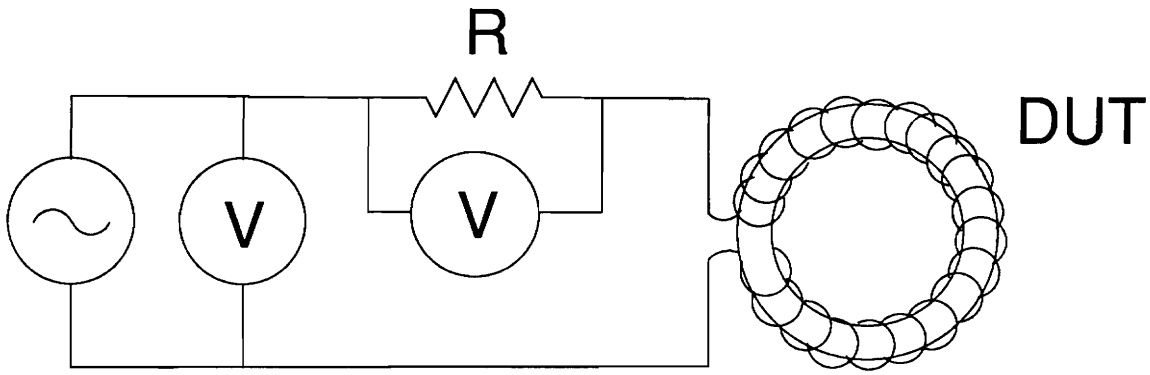

Fig. 2.4. Circuit diagram of the I-V method. The frequency bandwidth is limited by current transformer which is commonly used instead of the resistor R.

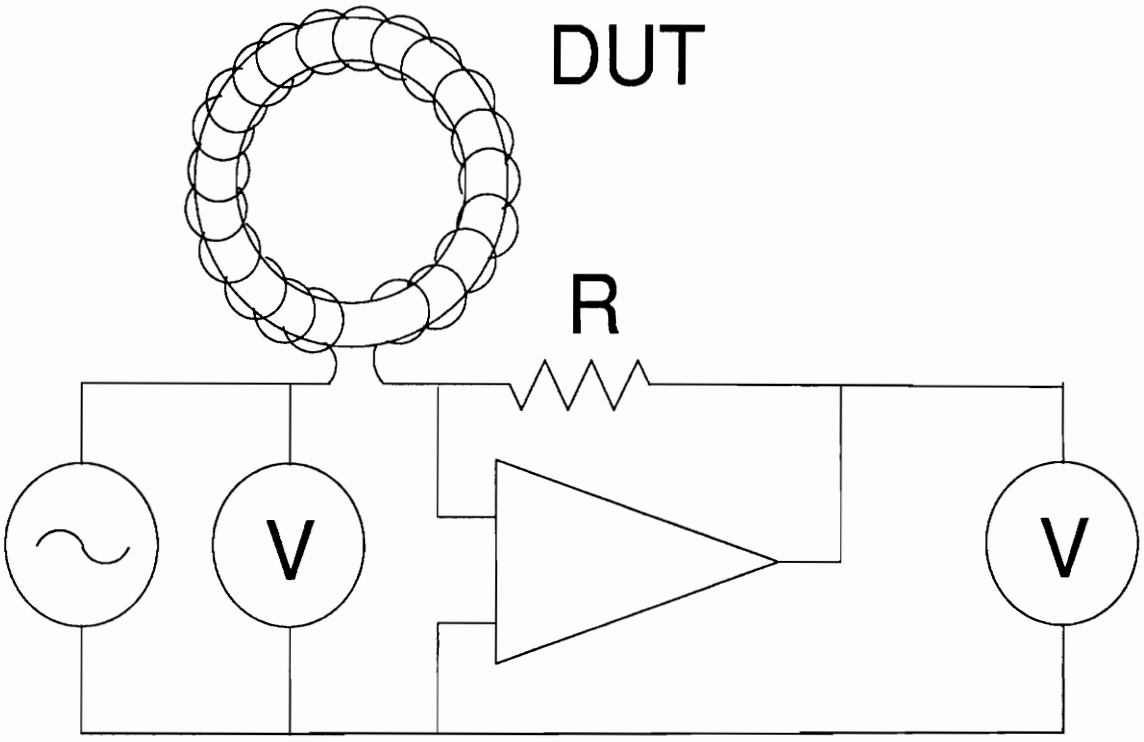

Fig. 2.5. Simplified circuit diagram of the auto balancing bridge method. This is most accurate of all and is usable up to 40 MHz.

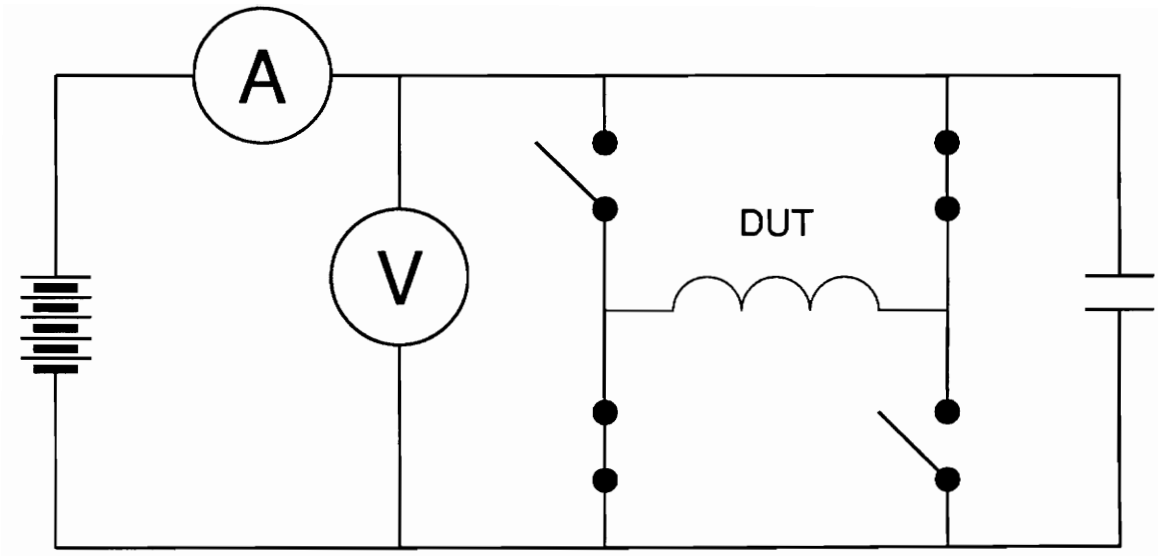

Fig. 2.6. Circuit diagram of the H bridge method. Measurement is conducted under a square wave excitation and includes all circuit-related losses

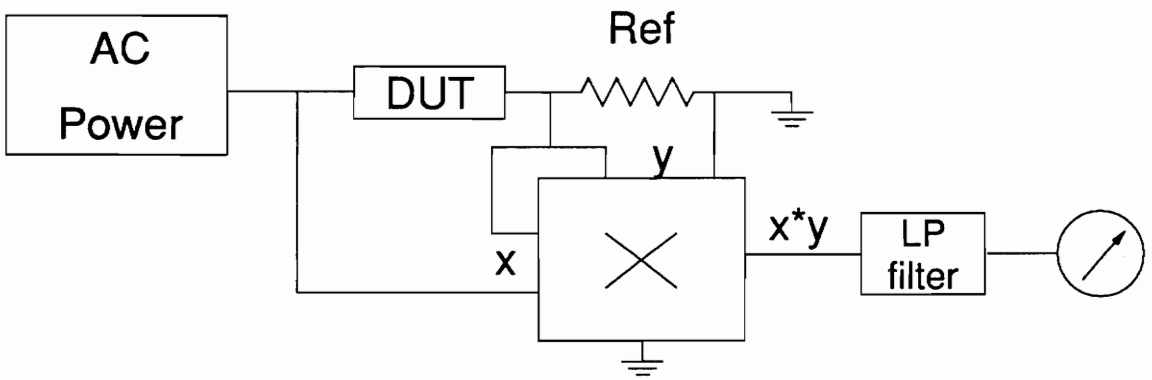

Fig. 2.7. Block diagram of high-frequency wattmeter. Bandwidth limited by analog multiplier and phase errors due to parasitic capacitances and inductances.

However, the transformer limits the lower end of the frequency range. The measurement circuit can be fitted into the probe to enable in-circuit and temperature chamber measurements. Commercial instruments achieve 1.5% basic accuracy.

Both network analysis methods are useful only at high frequencies and at the impedance level restricted to a narrow range around the characteristic impedance of the directional coupler employed. Therefore they are not suitable for magnetic loss measurement.

The principle of operation of the auto balancing bridge method is shown in Fig. 2.5. Since the inverting amplifier has a high gain, its input has potential very close to the ground. Therefore, the same current flows through device under test (DUT) and the resistor R, if the input current of an amplifier is negligible. In practice, a null detector and a modulator are needed in addition to the amplifier in order to cover a wide frequency range. This is the most accurate method with a wide frequency range. Commercial instruments achieve 0.05% basic accuracy.

2.1.3 H Bridge

The circuit diagram of the H bridge proposed by Carsten [110] is shown in Fig. 2.6. The bridge contains four fast transistor switches which drive the DUT with a square wave voltage. The measured dc current and voltage supplied to the circuit are equal to the total loss in the tested core, winding, switches, and capacitor. This method omly allows the determination of core losses and does not yield information on permeability. The square voltage waveform seems advantageous from the standpoint of characterization for power electronics, but is of limited use because the measured permeability and loss depend strongly on the slew rate of the square wave. The major errors are introduced by:

- winding loss,
- transistor conduction and switching loss, and
- capacitor dielectric and conduction losses.

2.1.4 Wattmeter

There are two kinds of wattmeter used for core loss measurement. The first is the electric utility type wattmeter with voltage and current windings. These windings are arranged as a stator and rotor, respectively, in order to obtain a readout proportional to the active power. The frequency range of this wattmeter is limited to, or below 1 kHz due to the large inductance of the instrument. The second type employs an analog multiplier circuit to obtain power loss in the core. The block diagram is shown in Fig. 2.7. Phase errors and bandwidth of the multiplier limit the upper measuring frequency to below 1 MHz. This method is widely used commercially. A major advantage of the method is the ability to measure a power loss due to nonsinusoidal waveforms.

2.1.5 Calorimetry

The method is described by Bowman, *et al.*, [111] for the measurement of total loss in the transformer. However, it can be used also for measurement of core loss when the winding loss is minimized. The major sources of error are due to the heat conducted through the electrical termination of the DUT (device under test) and power dissipation in the windings. Obviously no permeability data can be obtained. Another major drawback of this method is the long measurement time, which depends on the thermal capacity of the calorimeter and the power dissipated in the DUT. If the device is immersed in oil, repeating the measurements is inconvenient due to handling of oiled components.

2.2 Principles of Impedance-Based Magnetic Material Characterization

This automated core loss measurement technique is suitable for a very wide frequency range, from 100 kHz to 100 MHz. It employs a Hewlett-Packard HP4194A impedance analyzer with an HP41941A impedance probe and an Amplifier Research 10A250 wideband power amplifier. The impedance is calculated as the ratio of measured voltage and current using the I-V method described in Section 2.1.2. The Hewlett-Packard 4194A impedance analyzer is used to measure permeability and core loss. The measurement setup is shown in Fig. 2.8. An ac signal produced by the impedance analyzer is applied from a power amplifier through the impedance probe, which can withstand currents up to 0.5 A and voltages up to 150 V, to the inductor under test. The probe returns two signals corresponding to the current and voltage at the device. These signals are attenuated by 30 dB power attenuators with large heatsinks to prevent damage to the impedance analyzer. The measured impedance is converted internally into an equivalent parallel inductance and an equivalent parallel resistance to characterize the permeability and core loss, respectively. The impedance analyzer is controlled with a special application software written in Pascal on a personal computer, through the IEEE-488 interface to maintain constant flux density or constant core loss during the frequency sweep.

2.3 Calibration Procedure

Calibration and offset of the measurement setup are very important because they minimize the errors due to the parasitic components associated with the instrumentation and associated with the test coil. The test coil causes error in the core loss measurement due to the presence of copper losses, and the error in the permeability measurement is due to the presence of a

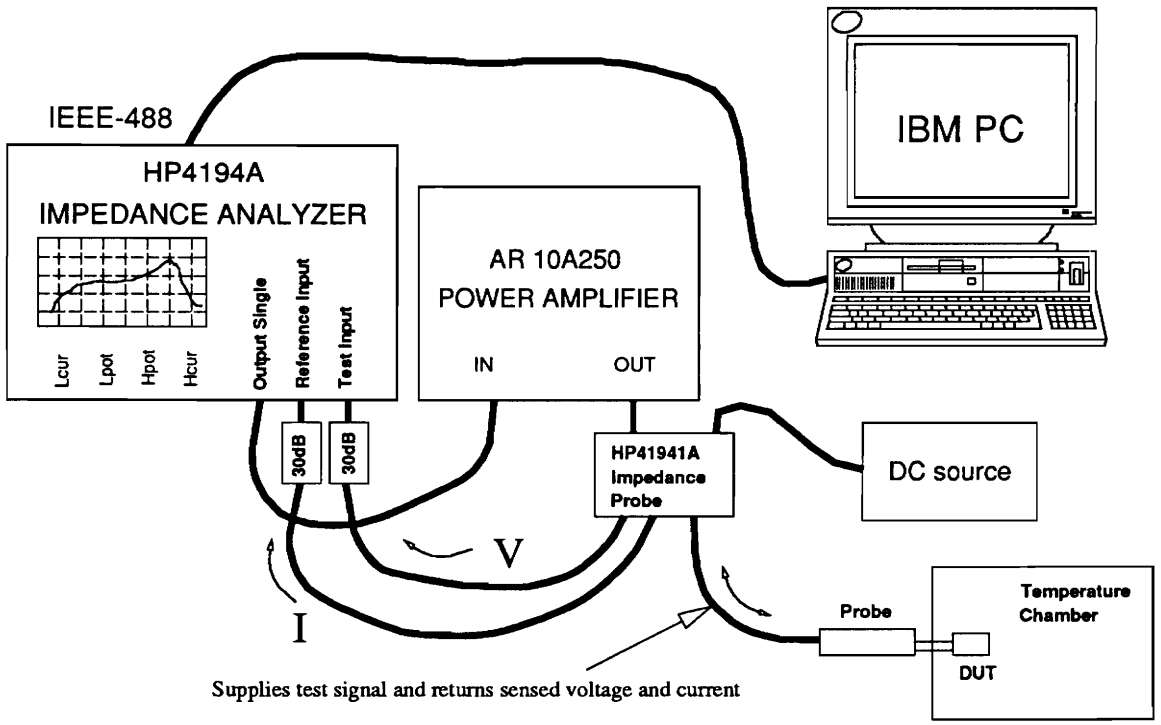

Fig. 2.8. The setup for high-frequency measurements of power ferrites. When frequency is swept, either flux density or power dissipation are set as a parameter.

magnetic field not contained in the magnetic core under test. These errors alter the amplitude and phase of the measured impedance. The following calibration and offset procedure can compensate for these errors.

The 0 Siemens (open circuit), 50 Ohms, and 0 Ohms (short circuit) calibrations are performed with impedance standards provided with the HP41941A impedance probe. During each calibration, the appropriate standard is attached to the measuring tip of the probe. After calibration, a short circuit offset is performed using a test coil without the magnetic core. Both calibration and offset data are stored internally in the instrument. The impedance of the test coil itself is compensated for during the measurement of the core impedance except for the stray capacitance of the coil winding to the core. Since only a few turns of wire are sufficient to obtain the necessary impedance level for the inductor under test to approximately match the output impedance of the power amplifier, the stray capacitance of such a winding is very small. Since the error introduced by parasitic components varies with frequency, the calibration with each impedance standard (0 Ω, 50 Ω, and 0 S) and the offset procedure with the air-core coil is performed automatically at the 70 discrete frequencies within the 10 kHz to 100 MHz range. The device under test is an inductor with a small number of turns wound on an ungapped core to minimize the magnetizing current and ensure that copper loss is much smaller than core loss. Furthermore, the copper loss is compensated for during the offset procedure as described above.

2.4 Measurement Procedure

When the calibration and offset procedures are complete, the device under test is attached. The measurement procedure is shown in Fig. 2.9. Initially, the desired frequency range and flux density levels are specified. The gain of the power amplifier is adjusted to obtain the nec-

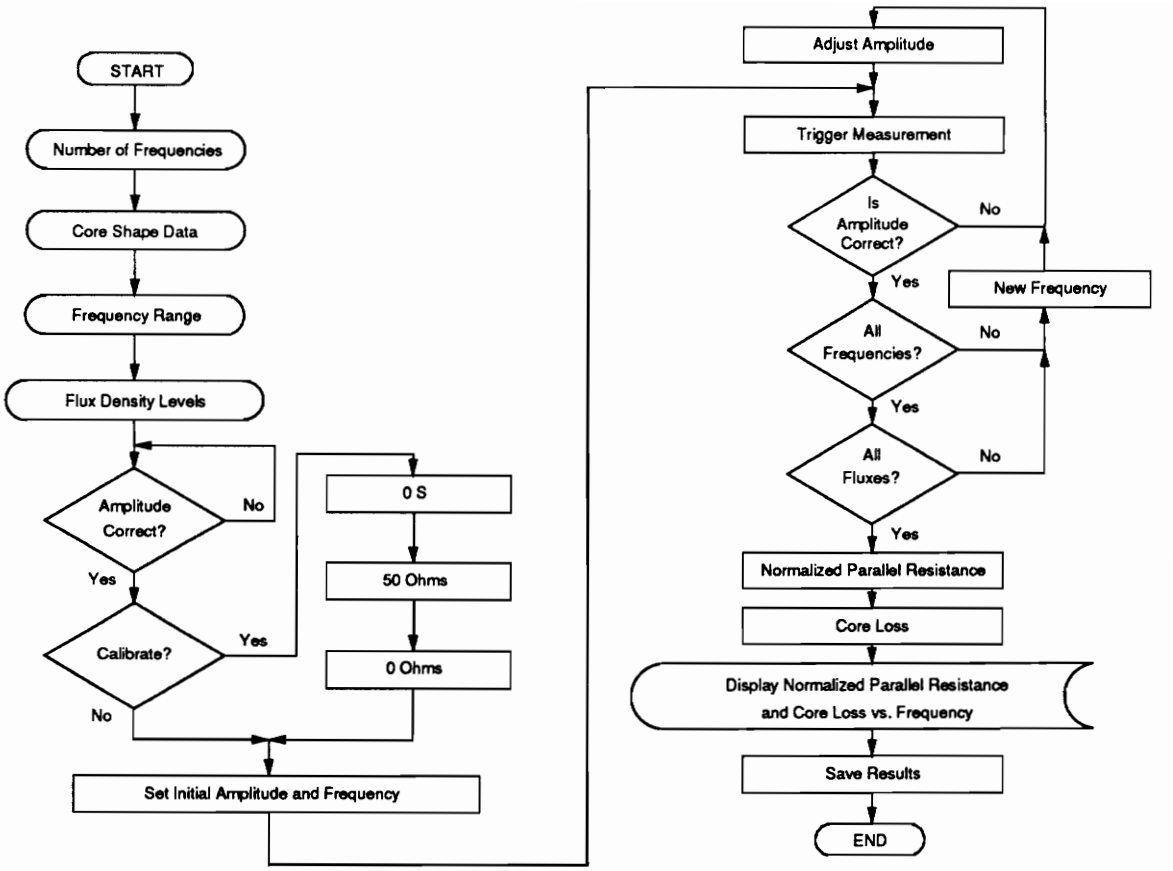

Fig. 2.9. Algorithm for an automated core loss measurement using the HP4194A impedance analyzer. Manual intervention is required initially to set the gain of a power amplifier and attach 0 S, 50 Ω, and 0 Ω impedance references during calibration.

essary flux density level. The frequency and the amplitude of the signal are swept to measure equivalent parallel resistance and equivalent parallel inductance at each desired frequency, with flux density as a running parameter. The instrument automatically interpolates a 70-point calibration and offset data set and uses it to correct measurement results. The ac voltage applied to the DUT is constantly monitored and adjusted to ensure a constant flux density or a constant core loss. After the measurement, an equivalent parallel inductance is converted to permeability and loss, displayed on the computer screen, and saved to a disk. The automated measurement takes approximately 100 seconds for a complete set of core loss characteristics, consisting of 250 points at various flux density levels and frequencies at fixed temperature.

Chapter 3

Characterization and Analysis of Permeability and Losses in Soft Ferrites

3.1 Fundamental Magnetic Characteristics

The principal characteristic of the magnetic material is a hysteresis loop, shown in Fig. 3.1, with an initial magnetization curve and a minor hysteresis loop with a dc bias. Saturation flux density, B_{sat}, is achieved under very strong applied magnetic fields. When the strong applied field is removed, the flux density lowers to remanence, B_r. When the applied field is reversed to value $-H_c$, the flux density returns to zero. This value of the applied field is called coercive force. Hysteresis loop represents the response of the material to the applied magnetic field. Flux density, B, and applied magnetic field, H, are related through the following formula:

$$B = M + \mu_0 H \quad , \tag{3.1}$$

where

M - magnetization of the magnetic material, and

μ_0 - permeability of vacuum = $4\pi \cdot 10^{-7}$ H/m.

The susceptibility of a magnetic material is defined as:

$$\chi \equiv \frac{M}{H} \quad , \tag{3.2}$$

and the permeability,

$$\mu \equiv \frac{B}{H} \quad . \tag{3.3}$$

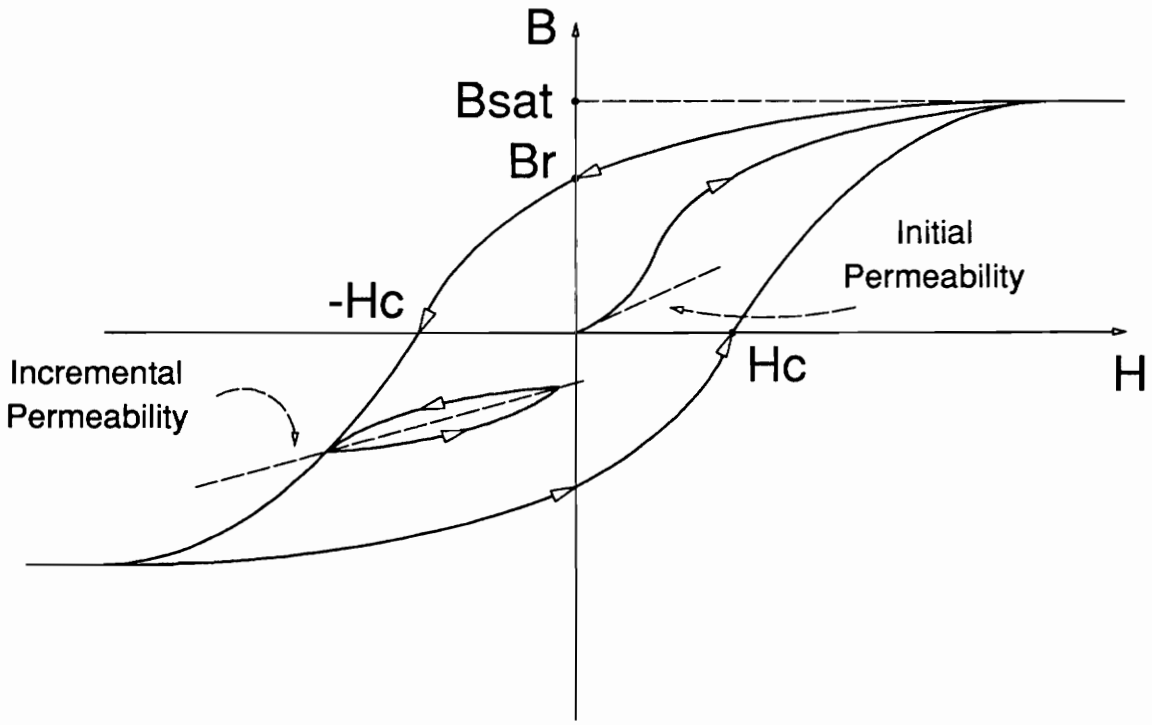

Fig. 3.1. The initial magnetization curve and hysteresis loop of magnetic material.

Relative susceptibility and relative permeability are defined as:

$$\hat{\chi} = \frac{\chi}{\mu_0} \qquad \hat{\mu} = \frac{\mu}{\mu_0} \qquad \hat{\mu} = 1 + \hat{\chi} \quad . \tag{3.4}$$

The initial slope of the magnetization curve is called an initial permeability, μ_i. The average slope of the minor loop with dc bias is called incremental permeability, μ_Δ. In a case of no dc bias, it is called amplitude permeability, μ_a. These classic definitions denote only the slope of the minor hysteresis loop as if it were a straight line, not a loop. The loop is formed because of the delay between an applied field, H, and the flux density in the material, B. If the material is subjected to a sinusoidal excitation, the delay can be interpreted as a phase shift, δ, shown in Fig. 3.2, and a relative complex permeability can be introduced [112]:

$$\bar{\mu} \equiv \frac{B}{\mu_0 H} = \hat{\mu} e^{-j\delta} = \mu_s' - j\mu_s'' = \frac{1}{1/\mu_p' + j/\mu_p''} \quad , \tag{3.5}$$

where

$\hat{\mu}$ - magnitude of relative complex permeability [H/m],

μ_s' - real part of series representation of relative permeability,

μ_s'' - imaginary part of series representation of relative permeability,

μ_p' - real part of parallel representation of relative permeability, and

μ_p'' - imaginary part of parallel representation of relative permeability.

The parallel and series representations of the complex permeability are mutually dependent in the following manner:

$$\mu_s' = \frac{\mu_p'}{1 + (\mu_p'/\mu_p'')^2} \quad , \tag{3.6}$$

$$\mu_s'' = \frac{\mu_p''}{1 + (\mu_p''/\mu_p')^2} \quad , \tag{3.7}$$

$$\mu_p' = \mu_s'[1 + (\mu_s''/\mu_s')^2] \quad , \tag{3.8}$$

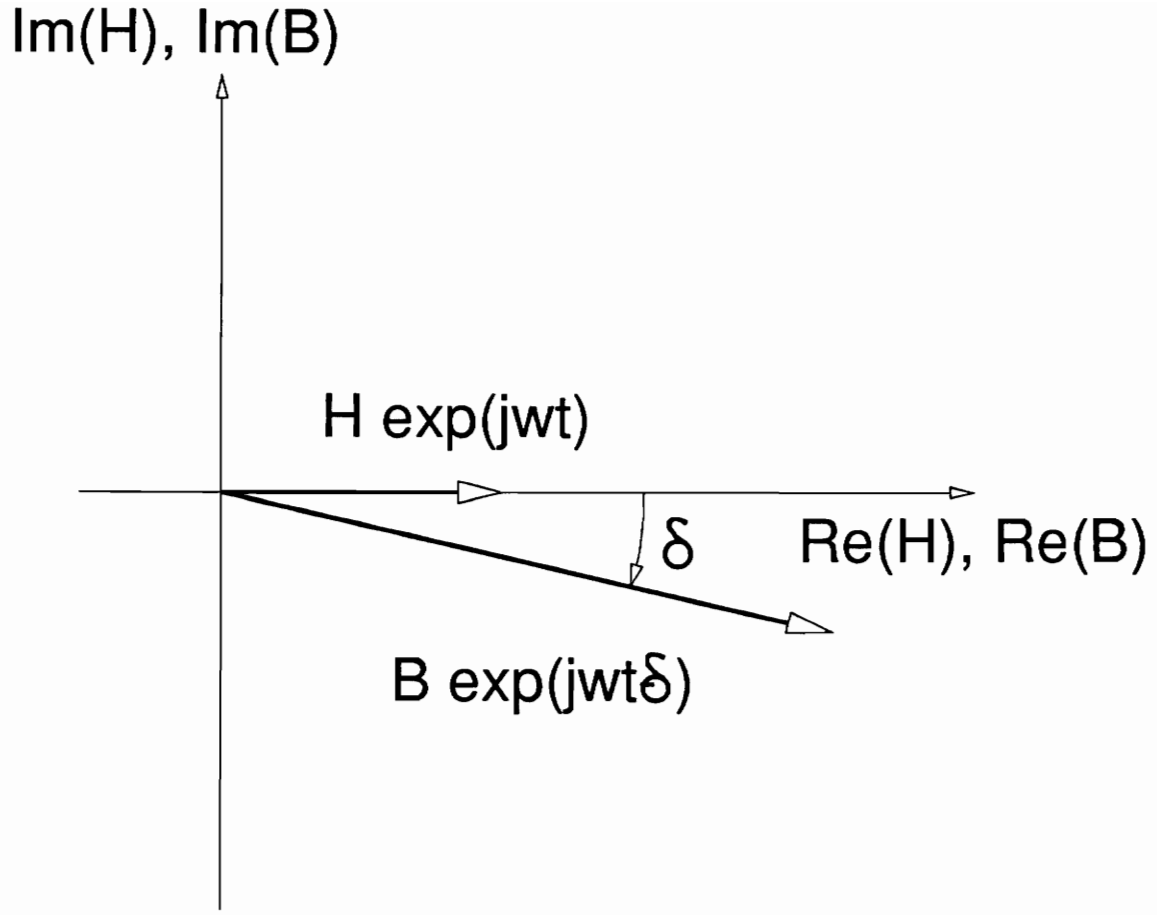

Fig. 3.2. Phase angle between applied magnetic field, H, and the flux density, B.

$$\mu_p'' = \mu_s''[1 + (\mu_s'/\mu_s'')^2] \quad . \tag{3.9}$$

The idealized hysteresis loop, represented by the complex permeability, is an ellipse. Higher harmonics with smaller magnitudes, which constitute the difference between the ellipse and the actual minor hysteresis loop, are neglected. The real part of the permeability is the actual slope of the minor hysteresis loop. The ratio of the length of a minor axis to a major axis of the ellipse is equal to tangent δ, a factor commonly used to describe losses in magnetic materials. This factor has the following relations with real and imaginary parts of the complex permeability:

$$\tan\delta = \frac{\mu_s''}{\mu_s'} = \frac{\mu_p'}{\mu_p''} \quad . \tag{3.10}$$

In practical applications in power electronics the behavior of the component containing magnetic material is represented with a equivalent electrical circuit model. The contribution of the magnetic core to the model can be presented as either a series or parallel connection of inductor and resistor. The inductive components in most power electronics applications are driven by ac voltage sources which establish the ac flux density. Therefore, a parallel model of the component is more favorable, since a known voltage can be readily applied to a parallel resistance in order to determine losses in the core. The parallel model is particularly advantageous in a case of a gapped core, where the size of the gap affects only the parallel inductance, not the parallel resistance. This is because the in the parallel model the voltage applied to the resistance does not change when the inductance changes like in the series model.

Let us consider an inductor, shown in Fig. 3.3, with a number of turns, N, cross-section area, A_e, magnetic path, l_e, carrying peak flux density, $\hat{B}$, induced by the sinusoidal peak magnetic field, $\hat{H}$, at frequency f. The rms (root-mean-square) voltage on the inductor can be determined from the Faraday's law:

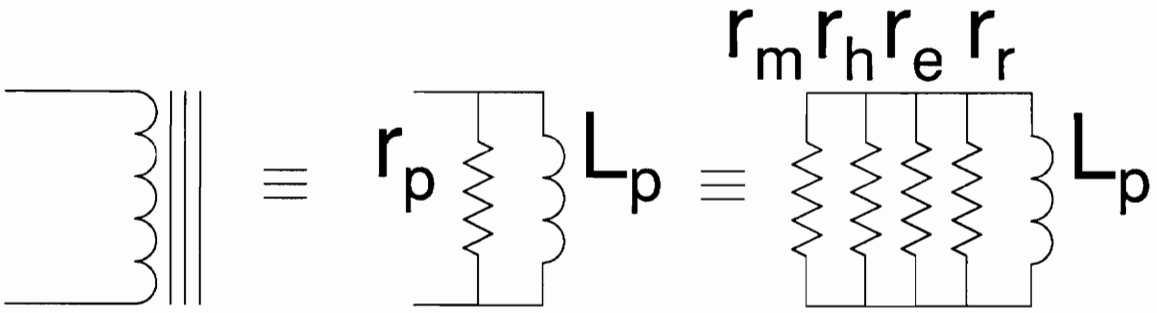

$$R_p = r_p \frac{l_e}{A_e N^2} \qquad R_p = \frac{2\pi^2 f^2 B^2}{P_m}$$

Fig. 3.3. Equivalent circuit of an inductor. Contribution from each magnetic loss is represented by parallel resistances.

$$V = \sqrt{2}\pi B f N A_e \quad , \tag{3.11}$$

and its rms current from the definition of the magnetic field strength,

$$I = H\frac{l_e}{N\sqrt{2}} \quad . \tag{4.12}$$

Therefore, the impedance of the inductor can be expressed as:

$$Z = \frac{V}{I} = 2\pi f \frac{\hat{B}}{\hat{H}} N^2 \frac{A_e}{l_e} = 2\pi j f \bar{\mu}\mu_0 N^2 \frac{A_e}{l_e} \quad . \tag{4.13}$$

An equivalent parallel inductance of a closed magnetic circuit is due to the parallel permeability:

$$L_p = \mu_p' \mu_0 N^2 \frac{A_e}{l_e} \quad , \tag{3.14}$$

$$\mu_p' = \frac{L_p l_e}{\mu_0 N^2 A_e} \quad , \text{ and} \tag{3.15}$$

where

μ_p' - real part of complex relative parallel permeability

Similarly, the equivalent parallel resistance is related to the imaginary part of the parallel permeability:

$$r_p = 2\pi f \mu_p'' \mu_0 N^2 \frac{A_e}{l_e} \quad , \tag{3.16}$$

$$\mu_p'' = \frac{r_p}{2\pi f \mu_0 N^2 A_e} \frac{l_e}{} \quad , \tag{3.17}$$

where

r_p - parallel resistance of the inductor, and

f - frequency.

In order to make the resistance a representation of material properties, a normalized parallel resistance can be defined as:

$$R_p \equiv r_p \frac{l_e}{N^2 A_e} \quad . \tag{3.18}$$

Therefore, the equivalent normalized parallel resistance due to the magnetic material, R_p, is equal to a parallel resistance, r_p, due to the core with an unit cross-sectional area, 1 m^2, unit magnetic path length, 1 m, and unit number of turns, 1.

The normalized parallel resistance can be expressed as a function of the imaginary part of the parallel permeability and a frequency:

$$R_p = 2\pi f \mu_0 \mu_p'' \quad . \tag{3.19}$$

This equation shows that normalized parallel resistance is independent of the physical size and shape of the measured core or the number of turns of the winding. The normalized parallel resistance, R_p, is associated only with magnetic characteristics of the material of the core.

Another parameter characterizing the losses in the magnetic material is a core loss per unit volume, defined as the power dissipation (in Watts) of a core having a volume of 1 m^3. In order to find the relationship between core loss density and previously defined loss parameters, consider an inductor with an effective magnetic path length, l_e, an effective cross-section area of the magnetic path, A_e, wound with N turns of wire, and having an effective peak flux density $\hat{B}$. The voltage, V, induced due to the peak flux density, $\hat{B}$, is:

$$V = N \frac{d\phi}{dt} = 2\pi f \hat{B} A_e N \quad . \tag{3.20}$$

When a sinusoidal voltage with an amplitude V appears on the terminations of the inductor utilizing the core of volume $V_e = A_e l_e$, the core loss per unit volume is equal to:

$$P_m = \frac{V^2}{2V_e r_p} = \frac{V^2}{2A_e l_e N^2 R_p A_e / l_e} = \frac{V^2}{2A_e^2 N^2 R_p} \quad . \tag{3.21}$$

Substitution of Eq. (3.17) in the above equation yields the relationship between the core loss density and the normalized parallel resistance:

$$P_m = \frac{2\pi^2 \hat{B}^2 f^2}{R_p} \quad . \tag{3.22}$$

The tangent of a loss angle related to initial permeability is also often used as a representation of losses:

$$\frac{\tan\delta}{\mu_i} = \frac{2\pi f \mu_0}{R_p} \quad , \quad \text{or} \tag{3.23}$$

$$\frac{\tan\delta}{\mu_i} = \frac{\mu_0 P_m}{\pi f \hat{B}^2} \quad . \tag{3.24}$$

3.2 Mechanisms of Magnetization and Losses in Soft Ferrites

The first theory of ferromagnetism was proposed by Weiss [113] in 1907. He assumed the existence of the molecular magnetic field and domain structure. The domain was a small region uniformly magnetized to saturation. The molecular field was explained later in terms of exchange forces by Heisenberg in 1926.

The fundamentals of a modern theory of ferromagnetism were established by Landau and Lifshitz [114] in 1935. The theory explained the existence and predicted the dimensions of magnetic domains and domain walls as a minimum energy state of the ferromagnetic crystal.

3.2.1 Structure and Magnetization of Soft Ferrites

Soft ferrites used in power electronics have a polycrystalline structure formed during the sintering process. It can be modeled as polyhedral grains separated by polygonal grain boundaries. During sintering, the total surface of grains is minimized in order to minimize the free energy of the system. This is achieved by formation and growth of polyhedral grains. The average number of polygons observed on the two-dimensional cross-section of the body consisting of polyhedrons with N faces is given as [115]:

$$\bar{n} = \sqrt{\frac{\sqrt{3\pi}}{2} N} \quad . \tag{3.25}$$

Experimental cross-sections have $\bar{n}$ = 5 to 6, which yields N = 10 to 14. The grain size may vary from 1 μm [116, 117] to 1 mm [118, 119], depending on initial particle size, sintering temperature, time, and growth controlling additives. The grain size may be described by a logarithmic-normal statistical distribution [120].

The idealized structure of ferrite grains is shown in Fig. 3.4. In reality there are crystal defects, second phases between grains, and porosity in the material. Most impurities and additives which are insoluble in the spinel crystal structure occupy voids at the edges of the polyhedrons. In an oxidizing firing atmosphere during grain growth stage, pores and inclusions can migrate out of crystallites, but otherwise they stay trapped inside [121, 122, 123]. In the latter case, the grain boundary is very thin (3-4 nm [124]), and it creates very small coercive force, high permeability, and small hysteresis loss.

However, an easy penetration of a thin grain boundary by charge carriers enhances eddy current losses due to motion of large aggregates of domain walls extending over many grains. In contrast, the oxidizing atmosphere during grain growth promotes concentration of impurities close to the grain surface and second phases between the grains, particularly at triple grain junctions [125]. If the amount of impurities or additives exceeds the solubility in a spinel lattice, and if their combination can produce an amorphous second phase, then such a second phase is deposited on grain boundaries [126]. This glassy nonmagnetic layer significantly retards the motion of domain walls, increases hysteresis loss, and decreases permeability, but increases bulk resistivity. It is important to note that the glassy layer is not absolutely necessary to increase resistivity. The concentration of some impurities near the grain boundary is sufficient to increase bulk resistivity. Thick grain boundary and the presence of strong pinning centers at triple grain junctions prevent creation of aggregates of domain walls beyond a single grain. Lack of these aggregates and higher resistivity of the grain boundary substantially reduce eddy current losses. Therefore this type of ferrite is used for high-frequency power

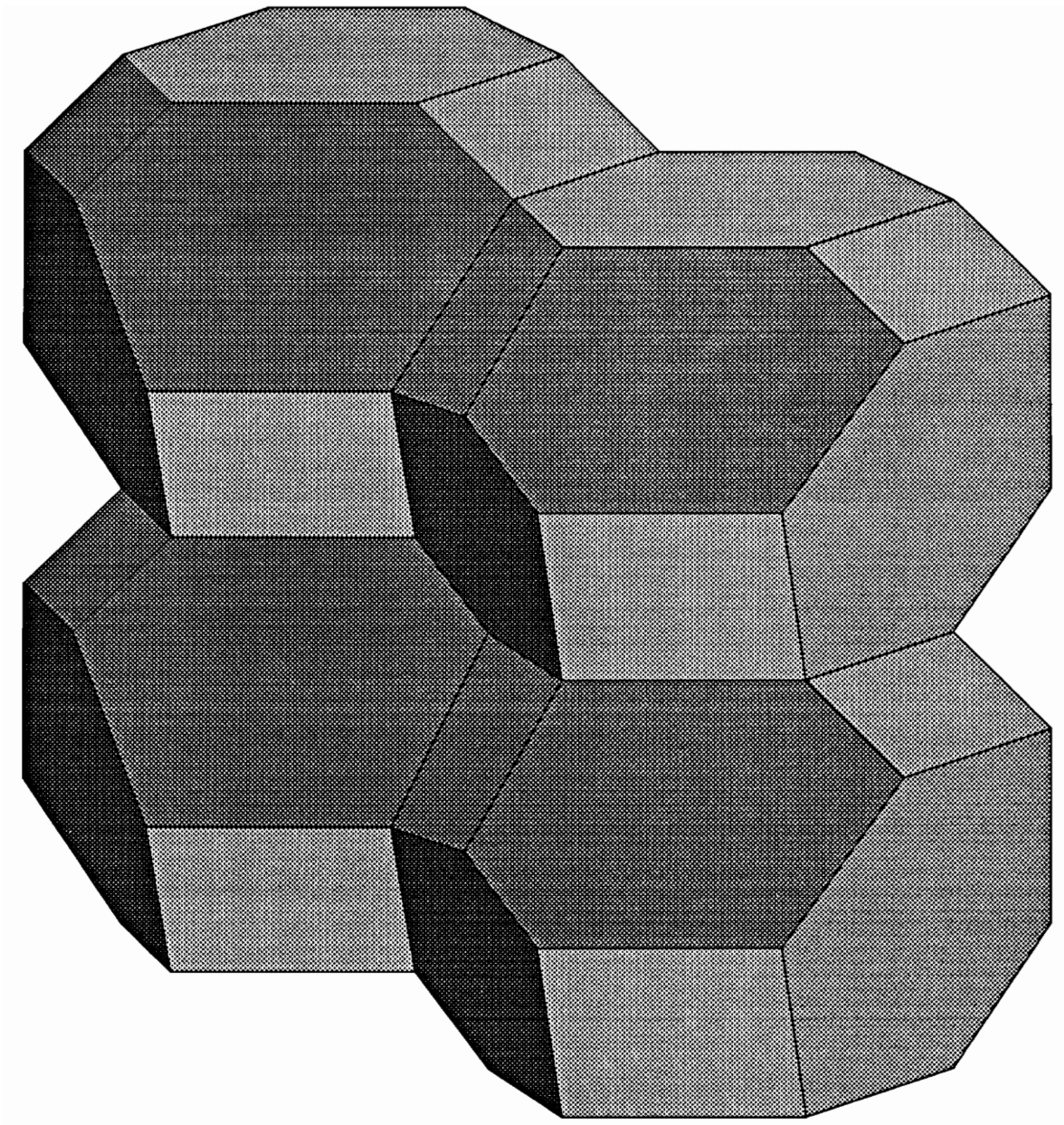

Fig. 3.4. Idealized structure of polycrystalline ferrite material. Practical material contains pores, inclusions, and second phases.

applications.

Kittel [127, 128] and Néel [129] showed that small ferromagnetic particles below a certain critical size cannot support domain walls. Rankis [130] calculated the critical size of the grain for various ferrites. For MnZn ferrite, the critical grain diameter was 98 μm, and for NiZn ferrite, 50 to 54 μm. Both of these values were several times larger than actual grain size. He noted however, that the calculation for a single isolated grain with magnetic poles on the surface due to demagnetization is not relevant for a polycrystalline material with thin grain boundaries where such demagnetizing forces are much weaker due to the magnetic coupling between the grains through a non-magnetic grain boundary. Therefore, even larger critical grain size is expected in a polycrystalline ferrite. He also calculated the thickness of the domain wall to be about 0.2 μm for NiZn ferrites and 0.4 μm for MnZn ferrite.

Since the grain size in a typical soft ferrite is much smaller than the critical grain size required to support a domain wall, the major reason for existence of domain walls is to minimize demagnetizing energy of voids, pores, inclusions, and grain boundaries, minimize anisotropy energy which varies due to nonhomogeneous chemical composition, and minimize magnetostriction energy due to nonhomogeneous mechanical stress created during cooling of the material during the manufacturing process.

Most of the voids and impurities are concentrated on the edges and triple grain junctions of polyhedron grains. Therefore, these edges and points serve as pivots for bending and moving domain walls. Domain walls can be nucleated or pinned at the grain boundaries [131, 132, 133]. Some domain walls can extend through a thin grain boundary and be supported by adjacent grains with similar crystallographic orientation. The simple case of the grain containing two magnetic domains divided by a domain wall is shown in Fig. 3.5.

Initially, the domain wall divides the grain in two domains of similar size (step 0), so the resultant net magnetization is zero. This is not necessarily the case in every grain. Some grains may not support an inside domain wall or may be divided unequally, but that may be averaged out with adjacent grains. When a small external field is applied (Step 1), the domain

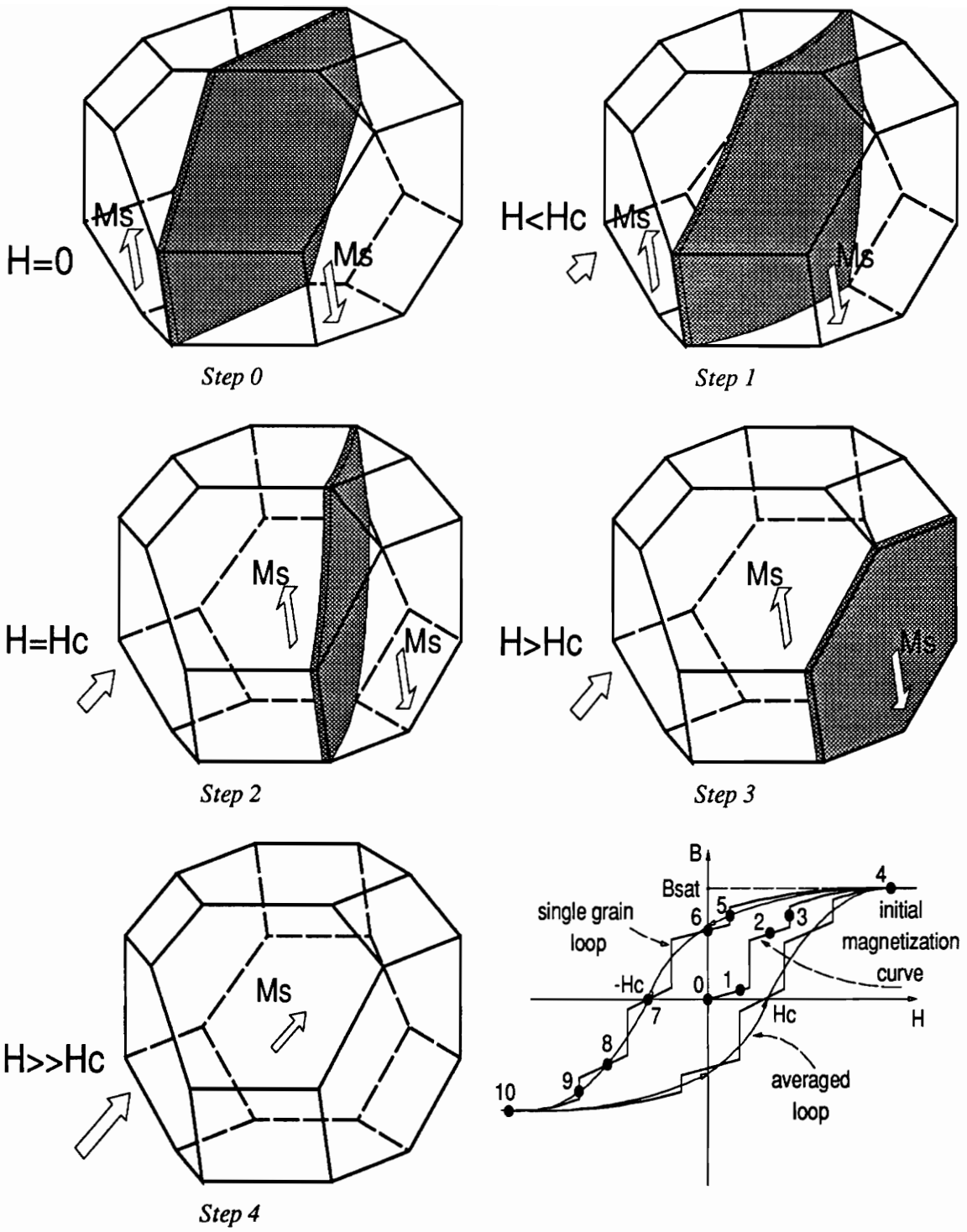

Fig. 3.5. Initial magnetization process of the grain with a single domain wall.

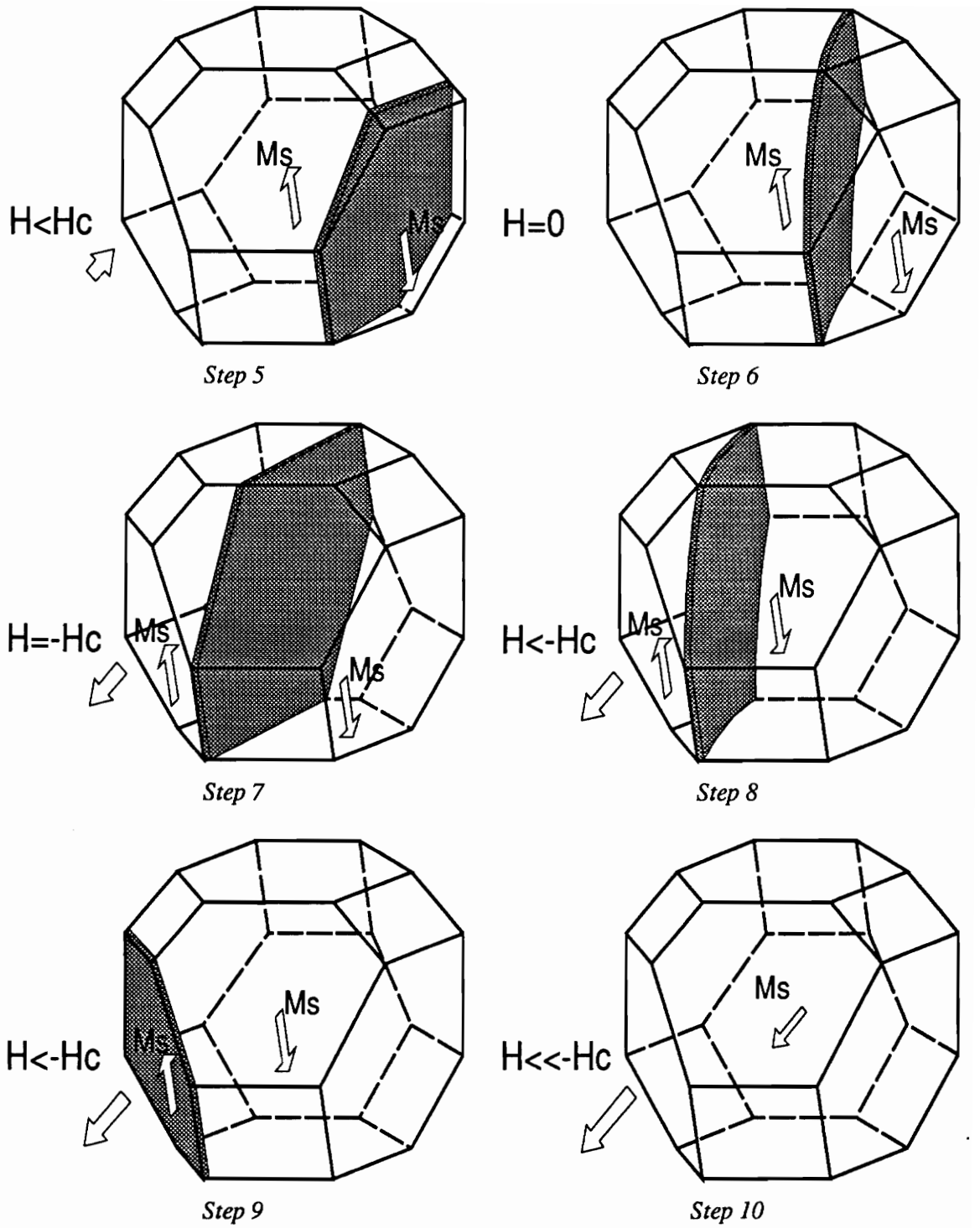

Fig. 3.6. Magnetization process of the grain with a single domain wall.

wall bends cylindrically or spherically [134]. The deviation from an ideal cylindrical or spherical bending is probably due to pinning the edges of the wall on edges of the polyhedron supporting the wall, and a change in a structure of the edge of a domain wall at the grain boundary. This change in the domain wall structure and retardation of the domain wall motion was predicted by Rankis in his theory of initial permeability [135]. He suggested that an non-homogeneous strain at the grain boundary, created during cooling below the Curie temperature, creates a layer of increased crystal anisotropy adjacent to a grain boundary. The domain observations confirm the retardation of the wall motion at a finite distance from a grain boundary [136]. When larger field is applied (step 2), the wall overcomes its coercive force and jumps to a new position. The excessive energy of the wall is dissipated as a hysteresis loss. When the applied field is larger than the coercive force the domain wall jumps and is pinned to the grain boundary (step 3). At very strong fields the domain wall is extinct and the domain is rotated towards the direction of the applied field (step 4). The process described in steps 0 to 4 is called the initial magnetization. The magnetization process that forms the hysteresis loop is shown in Fig. 3.6. When the field is lowered the domain rotates back to the easy axis and the domain wall is nucleated at the grain boundary (step 5). Due to the hysteresis the domain wall arrives at different position when the external field is removed (step 6) compared to the initial state (step 0). The state of zero net magnetization is attained when the negative coercive force, $-H_c$, is applied (step 7). At greater fields the domain wall jumps (step 8), is pinned to the grain boundary (step 9) and extinct (step 10), accompanied by the domain rotation. The other part of the hysteresis loop consists of the magnetization process, similar to steps 5 through 10, with a positive value of the coercive force, H_c.

3.2.2 Mechanisms of Magnetization

Becker [137] suggested that two processes contribute to magnetic permeability:

- increase of volume of domains favorably oriented with respect to applied field at the expense of unfavorably oriented domains, and
- rotation of directions of domain magnetizations towards the direction of the applied field.

Kersten made the great step towards understanding permeability in magnetic materials in 1956. He explain the temperature dependence of permeability in metallic ferromagnets assuming that the domain wall may bend in a cylindrical fashion [138, 139]. In 1962 Globus [140] introduced a model with a single domain wall bisecting a spherical grain to explain linear dependence of permeability on the grain size in ferrites. However, the Globus model failed to take into account the energy of demagnetization which occurs due to the pole formation on the domain wall non-parallel to the magnetization of the domain. That problem had already been pointed out by Kaplan [141] in 1951 and by Smit and Wijn [142] in 1959 when they adapted Kersten's model for ferrites. They showed that the contribution to permeability from spherical bulging of a domain wall can yield a relative permeability about 10, which is much less than the permeability of most ferrites. Hoekstra, *et al.*, [143] proved later that indeed the temperature dependence of permeability in ferrites can be explained assuming cylindrical wall bulging. Hoekstra also showed that the cylindrical bulging can contribute to the permeability on the order of 1000, which is comparable with actual permeability in soft ferrites. He noted, however, that despite the agreement of the shape of the experimental curve with the theory, the absolute magnitude of permeability was much less than predicted by the theory. He attributed that to less-than-ideal cylindrical bulging where the demagnetization energy, predicted by Smit and Wijn, lowers the actual permeability. The accuracy of the cylindrical bulging theory was improved at extreme temperatures (<-100 °C and close to Curie temperature) by Stoppels [144] by adding the second term in the magnetic anisotropy energy constant. The theory of a grain boundary stress layer proposed by Rankis explained the permeability of NiZn ferrites but failed in case of MnZn ferrites [145]. Recently Miroshkin, *et al.*, [146, 147] used the spherical bulging model to interpret the susceptibility and its temperature dependence of low-permeability MnZn and NiZn ferrites. The results were explained using two different formulas for spherical

bulging in materials with different microstructure neglecting either demagnetization or anisotropy energy. Despite a variety of theories of magnetization in ferrites, no commonly accepted quantitive theory exists.

3.2.3 Mechanisms of Losses

In 1924 Jordan [148] separated magnetic losses into three parts: hysteresis, eddy current, and residual losses (Jordan lag) in the following form:

$$\frac{R}{fL} = r + ef + hH \quad , \tag{3.26}$$

where

R - loss resistance of the inductor due to magnetic losses [Ω],

f - frequency [kHz],

L - inductance [H],

r - coefficient of residual viscosity [10^{-3}],

e - eddy current coefficient [μs],

h - hysteresis coefficient [cm/kA], and

H - applied magnetic field.

Jordan used a frequency of 0.8 kHz as a reference, but later 1 kHz was commonly used. Legg [149] used similar equation:

$$\frac{R}{\mu fL} = a\hat{B} + c + ef \quad , \tag{3.27}$$

where

μ - relative permeability,

a - hysteresis resistance coefficient,

c - residual resistance coefficient,

e - eddy current resistance coefficient of core,

$\hat{B}$ - peak of sinusoidal flux density.

The loss can be represented as a sum of tangents of loss angles due to different loss contributions [150]:

$$\tan\delta = \tan\delta_H + \tan\delta_r + \tan\delta_e \quad , \tag{3.28}$$

where

$\tan\delta_H$ - contribution from hysteresis losses,

$\tan\delta_r$ - contribution from residual losses, and

$\tan\delta_e$ - contribution from eddy current losses.

The complex relative permeability can be expressed in terms of tangents of loss angles related to initial permeability using Eqs. (3.5), (3.10), and (3.25):

$$\bar{\mu} = \frac{1}{1/\mu_p' + j(\tan\delta_H/\mu_i + \tan\delta_r/\mu_i + \tan\delta_e/\mu_i)} \quad . \tag{3.29}$$

Then the imaginary part of complex permeability follows:

$$\mu_p'' = \frac{1}{\tan\delta_H/\mu_i + \tan\delta_r/\mu_i + \tan\delta_e/\mu_i} \quad , \tag{3.30}$$

as does the normalized parallel resistance:

$$R_p = \frac{2\pi f\mu_0}{\tan\delta_H/\mu_i + \tan\delta_r/\mu_i + \tan\delta_e/\mu_i} = \frac{1}{1/R_{ph} + 1/R_{pr} + 1/R_{pe}} \quad . \tag{3.31}$$

The mechanisms of specific types of losses are discussed in the following sections.

3.2.3.1 Eddy Current Loss

Classic model

Initially the eddy current loss was calculated assuming uniform magnetization of the magnetic material. In a thin lamination of thickness, d, and resistivity, ρ, the eddy current loss is

[151]

$$P_e = \frac{(\pi \hat{B} f d)^2}{6\rho} \quad . \tag{3.32}$$

The relative loss tangent due to classical eddy current loss is obtained by substituting Eq. (3.21):

$$\frac{\tan \delta_e}{\mu_i} = \frac{\mu_0 \pi f d^2}{6\rho} \quad , \tag{3.33}$$

and substituting Eq. (3.19) into (3.29) the normalized parallel resistance is

$$R_p = 12 \frac{\rho}{d^2} \quad . \tag{3.34}$$

and for a spherical particle of diameter, d, and resistivity, ρ,:

$$P_e = \frac{(\pi \hat{B} f d)^2}{20\rho} \quad , \tag{3.35}$$

$$\frac{\tan \delta_e}{\mu_i} = \frac{\mu_0 \pi f d^2}{20\rho} \quad , \text{ and} \tag{3.36}$$

$$R_p = 40 \frac{\rho}{d^2} \quad . \tag{3.37}$$

Pry and Bean model (existence of domains)

The experimental data indicate higher losses in metallic ferromagnets than predicted from classical theory. The contribution of eddy current losses due to moving domain walls was first calculated by Williams, Shockley, and Kittel [152], and extended for a periodic synchronously oscillating domain structure by Pry and Bean in 1958 [153] who gave the following formula for an eddy current losses in a thin lamination:

$$P_{ePB} = \frac{8q}{\rho} \left(\frac{\hat{B} f d}{\pi} \right)^2 \sum_{n \text{ odd}}^{\infty} \frac{1}{n^3} \left[\coth nq + \frac{2I_1(nq\hat{B}/B_s)}{nq(\hat{B}/B_s)\sinh nq} \right] \quad , \tag{3.38}$$

where

d - thickness of lamination,

L - domain wall spacing,

B_s - saturation flux density,

ρ - resistivity,

$I_1(z)$ - first-order Bessel function of imaginary argument, and

q - $2\pi L/d$.

At $q \rightarrow 0$ this equation reduces to a classical loss. For $\hat{B} \ll B_s$ the ratio of actual loss to a classical loss is:

$$\frac{P_{ePB}}{P_e} = \frac{96}{\pi^3}\frac{L}{d}\sum_{n\ \text{odd}}^{\infty}\frac{\coth(n\pi L/d)}{n^3} \quad . \tag{3.39}$$

The model is only valid when the thickness of the lamination is much smaller than the skin depth. Otherwise, only the part of the domain wall near the surface is mobile, which violates the assumption of uniform speed of the whole wall.

Bozorth model (skin effect)

Using the classical model, the additional loss due to the skin effect in magnetic material was calculated by Bozorth [154]:

$$P_{es} = \frac{\hat{B}^2(\sinh\theta - \sin\theta)}{4\mu(\sinh\theta + \sin\theta)} \quad , \tag{3.40}$$

where

θ - d/δ - ratio of lamination thickness to skin depth, and

δ - $1/\sqrt{\pi\mu f/\rho}$ - skin depth.

Bertotti model (excess loss)

In metallic magnetic materials, the assumption of synchronous oscillation in Pry and Bean's model is only valid in the absence of hysteresis, since it has been known that large changes of magnetization consist of a large number of small random discrete jumps [155, 156, 157] instead of synchronous motion. The eddy currents induced during these jumps create internal magnetic

fields that influence the subsequent jumps of neighboring domain walls or wall clusters in a random manner described in terms of statistically independent Markov chains by Bertotti [158]. This is the origin of the so called excess loss:

$$P_{exc} = 2\hat{B}f\tilde{n}_0 H_B\left(\sqrt{1+\frac{16G^{(w)}A_e\hat{B}f}{\rho\tilde{n}_0^2 H_B}}-1\right) \quad , \tag{3.41}$$

where

$G^{(w)}$ - $(4/\pi^3)\sum_{k=1}^{\infty} 1/(2k+1)^3 \cong 0.1356$,

A_e - cross-section area of the lamination,

$\tilde{n}_0$ - number of simultaneously active magnetic objects (domain walls or wall clusters) in the cross-section when $f \to 0$, and

H_B - Bertotti field (V_0 or W in his notation) equal to an average minimum separation between coercive force values for different magnetic objects in the cross-section.

The excess loss can be expressed as a loss factor:

$$\frac{\tan\delta_{exc}}{\mu_i} = \frac{2\mu_0\tilde{n}_0 H_B}{\pi\hat{B}}\left(\sqrt{1+\frac{16G^{(w)}A_e\hat{B}f}{\rho\tilde{n}_0^2 H_B}}-1\right) \quad , \tag{3.42}$$

and as a normalized parallel resistance:

$$R_{pexc} = \frac{\pi^2\hat{B}f}{\tilde{n}_0 H_B\left(\sqrt{1+[16G^{(w)}A_e\hat{B}f]/(\rho\tilde{n}_0^2 H_B)}-1\right)} \quad . \tag{3.43}$$

The above formula can be simplified for a non-oriented three-percent silicon iron as:

$$P_{exc} \approx 8\sqrt{\frac{G^{(w)}A_e H_B}{\rho}}(\hat{B}f)^{3/2} \quad . \tag{3.44}$$

Bertotti also showed that in a special case when only a single Markov chain exists in the magnetic sample, involving all domain walls, the model reduces to the Pry and Bean's model.

In all above models, the material is assumed to have a low and homogeneous resistivity, typical for metallic ferromagnetic materials. However, ferrites are semiconducting materials with resistivities several orders of magnitude higher than those in metals. In addition, the grain boundaries of ferrites can have substantially higher resistivity due to different chemical compo-

sition. Therefore, in the case of ferrites with insulating grain boundary, the above models are applicable both to a bulk material, and to the individual grain. When bulk resistivity and the sample dimensions are used, the macroscopic eddy currents are calculated. However, when intragranular resistivity and grain size are considered, the microscopic eddy currents inside the grain are accounted for. The interaction of domain walls and eddy currents induced within the grains due to electron diffusion will be treated separately as a residual loss later in this Chapter.

The total eddy current loss is a sum of classical and excess eddy current losses.

3.2.3.2 Hysteresis Loss

Bloch [159] first suggested that the movement of the domain walls can be hindered by an nonhomogeneous stress. That idea was developed later by Kondorsky [160] and Kersten [161] in a theory of a coercive force. The first theory of the effect of inclusions was proposed by Kersten [162]. He suggested a model of small spherical nonmagnetic inclusions distributed uniformly throughout a magnetic material. When a rigid domain wall intersects the nonmagnetic inclusion, the area and the energy of the wall is reduced. Therefore, an additional field (energy) is necessary to free the domain wall from the pinning inclusion. Once freed, the wall dissipates its excess energy through damped motion which causes hysteresis loss. Kersten's theory was criticized by Néel [163, 164], who added the effect of demagnetizing energy due to nonmagnetic inclusions and assumed their random distribution. At medium fields, nucleation and extinction of the domain walls [165] are the major sources of hysteresis loss. At high fields most of the domain walls are extinct, and the main contribution to hysteresis is due to irreversible rotation of magnetization [166, 167].

<u>Néel's model (nonmagnetic inclusions)</u>

Smit and Wijn [168] used the following Néel's formula to model coercive force in NiZn ferrite:

$$H_c \cong \frac{8\,|K_1|\,v}{4\pi M_s}\left[0.39+\frac{1}{2}\ln\frac{2\pi M_s^2}{|K_1|}\right] \quad , \tag{3.45}$$

where

K_1 - first order anisotropy constant,

v - volume fraction of nonmagnetic inclusions, and

M_s - saturation magnetization.

They also provide formulas for a coercive force due to an internal stress, σ, in a volume fraction, v, of the material with magnetostriction constant, λ_s:

$$H_c \cong \begin{cases} \dfrac{1.05v\lambda\sigma}{M_s}\left[2.23+\ln\left(\dfrac{M_s}{\sqrt{\frac{3}{2}\lambda\sigma}}\right)\right] & \text{for}\ \dfrac{3}{2}\lambda\sigma \gg K_1 \\ \dfrac{0.191v\lambda^2\sigma^2}{K_1 M_s}\left[1.79+\ln\left(\dfrac{M_s}{\sqrt{K_1}}\right)\right] & \text{for}\ \dfrac{3}{2}\lambda\sigma \ll K_1 \end{cases} . \tag{3.46}$$

Paul's model (grain boundary)

The contribution of grain boundaries to the hysteresis is predicted by a theory developed by Paul [169, 170]. In his model, the coercive force is equal to the field necessary to move the domain wall through a grain boundary approximated by a planar barrier:

$$H_c = 0.38\frac{K_1}{M_1}\frac{\delta_B}{\delta_w}\left(\frac{A_1}{A_2}-\frac{K_2}{K_1}\right) \quad , \tag{3.47}$$

where

K_i - anisotropy constant of the i-th region,

M_i - magnetization of the i-th region,

A_i - exchange constant of the i-th region,

δ_B - thickness of the grain boundary, and

δ_w - $\sqrt{A_1/K_1}$ is a parameter governing the thickness of the domain wall.

The hysteresis loss is proportional to the coercive force of the magnetic material. All three mechanisms: nonhomogeneous stress, spherical inclusions, and grain boundaries contribute to hysteresis in soft ferrites.

Rayleigh model (empirical)

Lord Rayleigh found that at low magnetic fields susceptibility is linearly dependent on the applied field [171]:

$$\chi_a = \chi_i + \nu\hat{H} \quad , \tag{3.48}$$

where

χ_a - amplitude susceptibility,

χ_i - initial susceptibility,

ν - Rayleigh constant, and

$\hat{H}$ - peak applied magnetic field.

He also found that the hysteresis loop could be approximated by two parabolas, and he expressed the magnetization as:

$$M = \chi_a + \frac{\nu}{2}\hat{H}^2 \quad . \tag{3.49}$$

The hysteresis loss can be found by an integration of the hysteresis loop [172]:

$$P_h = \frac{4\nu\hat{B}^3 f}{3\mu_0^2\mu_a^3} \quad . \tag{3.50}$$

Substituting in Eq. (3.24) the hysteresis loss factor is:

$$\frac{\tan\delta_h}{\mu_a} = \frac{4\nu\hat{B}}{3\pi\mu_0\mu_a^3} \equiv \eta_B\hat{B} \quad , \tag{3.51}$$

where η_B is a hysteresis coefficient [173]. Using Eq. (3.22) the normalized parallel resistance due to hysteresis is:

$$R_{ph} = \frac{3\pi^2\mu_0^2\mu_a^3 f}{2\nu\hat{B}} = \frac{2\pi f\mu_0}{\eta_B\hat{B}} \quad . \tag{3.52}$$

It can be also expressed as a function of core loss for modeling and optimization purposes:

$$R_{ph} = \sqrt[3]{\frac{8\pi^4\mu_0^2 f^4}{\eta_B^2 P_h}} = \sqrt[3]{\frac{8\pi^4\mu_0^2}{\eta_B^2}} f^{4/3} P_h^{-1/3} \quad . \tag{3.53}$$

3.2.3.3 Residual Losses

Thermal after-effect (Néel)

The first theory of a residual loss was suggested by Néel [174]. According to Néel, the thermal agitation of spins leads to a fluctuation of the spontaneous magnetization, producing a small fluctuating internal field, which adds up to the applied field and produces hysteresis loss. Therefore, the loss due to this fluctuations does not depend on frequency. However, the fluctuating field is time dependent:

$$H_F(t) = S_v(Q + \log t) \quad , \tag{3.54}$$

where Q is a constant of the order of 40 to 50; t is time since the application of the external field; and S_v is a material constant dependent on temperature. In practice residual loss of thermal after-effect can be represented as a material constant in terms of the H_F field averaged in the direction of applied field:

$$B_F = \mu_0 \mu_i < H_F > \quad . \tag{3.55}$$

The residual loss is not, however, a physical phenomenon based exclusively on the single mechanism. There are other mechanisms contributing to the residual loss, and the above mechanism is referred as a thermal after-effect.

The following phenomena contribute to residual loss:

- thermal after-effect,
- ferromagnetic resonance,
- magnetostriction,
- domain wall resonance or relaxation, and
- relaxation of electron and ion diffusion processes (diffusion after-effect).

Ferromagnetic resonance

Ferromagnetic resonance occurs when a spin is subjected to both constant and variable magnetic field. If an electron is put in a constant magnetic field , H, it behaves like a gyroscope, preserving its momentum. Therefore instead of instantaneous alignment with the applied field, it precesses around the direction of the applied field with an angular frequency:

$$\omega_{r0} = \gamma \mu_0 H \quad , \tag{3.56}$$

where $\gamma \cong 1.7588 \cdot 10^{11}$ C/kg is the e/m ratio of an electron. Therefore each change in the applied field causes spin precession which is damped due to the interactions with the crystal lattice. This is the origin of domain rotation loss [175].

Snoek investigated the frequency dependence of the permeability and losses and suggested that the ferromagnetic resonance can be a source of loss in ferrites [176]. Kittel [177] extended Snoek's model by deriving the expressions for complex susceptibility due to domain rotation:

$$\chi_r(\omega) = \chi_{r0} \frac{\omega_r^2 + (\lambda/\chi_{r00})[j\omega + (\lambda/\chi_{r00})]}{\omega_r^2 + [j\omega + (\lambda/\chi_{r00})]^2} \quad , \tag{3.57}$$

where

χ_{r0} - static value of rotational susceptibility,

χ_{r00} - average rotational susceptibility $\approx \chi_{r0}$, and

λ - relaxation frequency.

Assuming a significant domain rotation ($\chi r \cong \mu r$), the normalized parallel resistance due to domain rotation is found using Eqs. (3.5), (3.19), and (3.57):

$$R_{pr} = \chi_{r0} \frac{\lambda^2 \chi_{r00}^2 \omega^2 + \lambda^4 + 2\lambda^2 \omega_r^2 \chi_{r00}^2 + \omega_r^4 \chi_{r00}^4}{\lambda \chi_{r00} (\chi_{r00}^2 \omega^2 + \lambda^2 + \omega_r^2 \chi_{r00}^2)} \quad . \tag{3.58}$$

Magnetostriction

Magnetostriction affects permeability and loss through static and dynamic contributions. First, when the mechanical stress is applied to the core (for example by using a mechanical clamp), the domain structure and orientation changes in order to minimize overall energy [178, 179]. The thickness of domain walls is reduced due to increase of stress-induced crystalline

anisotropy. Therefore, in agreement with Paul's theory, the coercive force due to interaction of domain walls with grain boundaries increases and so does the hysteresis loss and hysteresis-based residual loss. Second, even in an absence of external mechanical stress, an internal stress is created due to magnetostriction when an external magnetic field is applied. If the time-varying applied magnetic field has a harmonic component with a frequency close to one of the frequencies of a mechanical resonance of the core, the magnetic field energy is converted into mechanical energy and dissipated in the core and its surroundings as heat. The magneto-mechanical resonance was described first by Pierce in 1929 [180]. The magnetomechanical resonance in ferrites was described by van der Burgt, *et al.*, [181, 182, 183, 184]. The modern theory of magnetostriction was founded by Callen and Callen [185, 186]. Following van der Burgt notation, the motional susceptibility of the toroid due to magnetostriction can be expressed for a single resonance as:

$$\chi_{mot} = k^2 \frac{\chi^{\sigma}}{1-(f/f_0)^2(1-jQ_E^H)} \quad , \tag{3.59}$$

$$f_0 = \frac{\sqrt{E'^H/\rho}}{2\pi R} \quad , \tag{3.60}$$

$$E'^H = E'^H \left[1 + \frac{(W/R)^2}{12} \right] \quad , \tag{3.61}$$

where

χ^{σ} - susceptibility of mechanically free sample,

ρ - density,

R - radius of the central circle,

W - radial width,

E'^H - Young's modulus,

f_0 - resonant frequency,

Q_E^H - elastic quality, and

E'^H - apparent Young's modulus.

More detailed analysis of modes of vibration and corresponding frequencies was done by Boyd [187]. The equivalent circuit of the magnetic core including magnetostriction is shown in Fig. 3.7. The magnetic properties of the core influence its inductance and losses are represented in a parallel form, where L_p is a parallel magnetizing inductance which depends on the magnetization of the material in the applied magnetic field; R_h, R_e, and R_r are parallel resistances due to hysteresis, eddy currents, and residual losses, respectively. The magnetostrictive parameters can be represented by electric components corresponding to mechanical parameters of the core where C_c depends on a core density, L_c, on Young's modulus, and R_c on elastic quality. Similarly related are quantities for mechanical mounting of the core: C_m, L_m, and R_m.

Assuming $\mu \approx \chi \gg \mu_0$ the magnetostriction loss factor can be expressed as:

$$\frac{\tan \delta_x}{\mu_i} = \left(\frac{f}{f_0}\right)^2 \frac{Q_E^H}{k^2} \quad , \tag{3.62}$$

the core loss due to magnetostriction as:

$$P_x = \frac{\pi Q_E^H \hat{B} f^3}{\mu_0 f_0^2 k^2} \quad , \tag{3.63}$$

and normalized parallel resistance due to magnetostriction as:

$$R_{px} = \frac{2\pi \mu_0 k^2 f_0^2}{f Q_E^H} \quad . \tag{3.64}$$

The losses due to the thermal after-effect, ferromagnetic resonance, and magnetostriction have a common origin despite different mechanisms. Akhieser [188] introduced the theory of interaction between spin waves and lattice waves, where the waves denote variations from the equilibrium. The atomic magnetic moments are coupled by the exchange interaction, dipole-dipole, and spin-orbit interactions. Since all these interactions strongly depend on the interatomic spacing, the thermally or mechanically induced lattice waves may convert their energy into spin waves, giving rise to a thermal after-effect. Similarly, an external magnetic field can

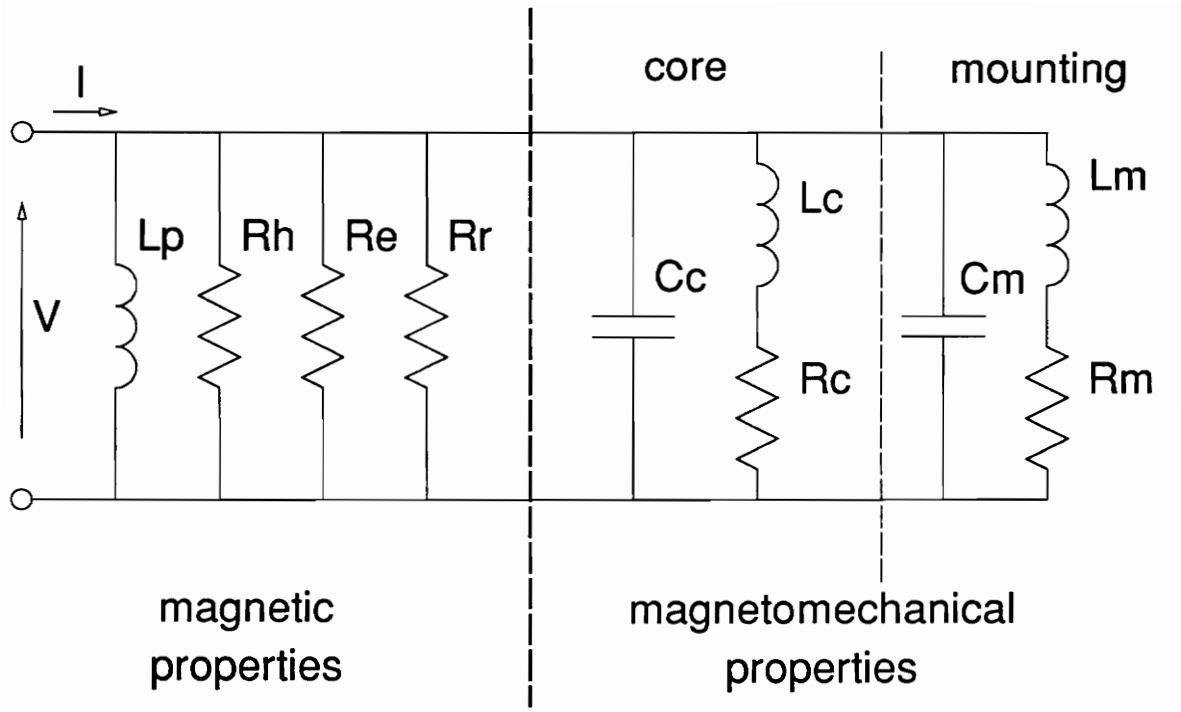

Fig. 3.7. *Equivalent circuit of a magnetostrictive core. The magnetoelastic contributions are shown separated by vertical dashed lines.*

excite spin waves, which can convert the energy to lattice wave producing mechanical vibration. This loss of energy will cause attenuation of spin oscillations and thus a loss in a ferromagnetic resonance.

Domain wall resonance

Domain wall resonance was suggested by Döring [189] in 1948. He assumed that a domain wall can be treated as a harmonic oscillator with its effective mass, m_w, its viscous damping, β, and its stiffness, α, following the equation of motion:

$$m_w\ddot{x} + \beta\dot{x} + \alpha x = M_s H \quad , \tag{3.65}$$

where

x - wall displacement,

M_s - domain magnetization, and

H - time varying applied field.

The complex susceptibility due to domain wall displacement is [190]:

$$\chi_w(\omega) = \frac{\chi_{wo}}{1 - (\omega/\omega_{wr})^2 + j\omega/\omega_w} \quad , \tag{3.66}$$

where

χ_{wo} - static value of susceptibility due to domain wall displacement,

ω_w - relaxation frequency of a domain wall, and

ω_{wr} - resonance frequency of a domain wall.

The mechanism for domain wall damping was explained by Hagedorn and Gyorgy [191] who investigated the mobility of domain walls in yttrium-iron garnet (YIG). When the domain wall moves, it causes a reversal of spins. For a short time the spins are excited to a high energy level, and they dissipate their energy in a form of spin waves after the domain wall passes through. The amount of energy absorbed and later dissipated by spin is proportional to crystal anisotropy. The time it takes for the spin to return to equilibrium depends on the a spin damping factor. The experimental data [192, 193] proved the loss contributions in ferrites from

both domain wall resonance and ferromagnetic resonance.

Electron and ion diffusion

When the issue of losses in ferrites was addressed first in 1946 by Snoek [194], he pointed out that eddy current losses are much smaller in ferrites due to their high resistivity, and therefore, that the residual losses are of great importance. He found that the presence of Fe^{2+} ions in the spinel lattice increased both residual loss and permeability. Relaxation losses due to electron diffusion were identified by Wijn and van der Heide [195], who found correlation between electric conductivity and magnetic loss spectra. Smit and Wijn [196] proposed a phenomenological model assuming that the change of magnetization is proportional to deviations from an equilibrium:

$$\dot{M} = \frac{M_\infty - M}{\tau} \quad , \tag{3.67}$$

where

M - magnetization,

M_∞ - equilibrium magnetization, and

τ - relaxation time constant.

Under sinusoidal excitation $H = H_0 e^{j\omega t}$, the complex permeability ($\mu \approx \chi$) due to domain rotation is:

$$\mu_r \approx \frac{\mu_i}{1 + j\omega\tau} \quad , \tag{3.68}$$

where

μ_i - initial permeability due to domain rotation.

The corresponding residual loss factor is found using Eqs. (3.5) and (3.10):

$$\frac{\tan\delta_r}{\mu_i} = \frac{2\pi f\tau}{\mu_i} \quad , \tag{3.69}$$

the core loss density due to residual loss is found substituting the above equation into (3.24):

$$P_r = \frac{2\pi^2 \hat{B}^2 f^2 \tau}{\mu_0 \mu_i} \quad , \tag{3.70}$$

and normalized parallel resistance due to residual loss is found from Eq. (3.22):

$$R_{pr} = \frac{\mu_0 \mu_i}{\tau} \quad . \tag{3.71}$$

A more elaborate phenomenological description of a relaxation process including quantum exchange interaction and relativistic terms is given by Bar'ykhtar [197, 198].

There are two physical mechanisms of the electron diffusion. The magnetically induced electron diffusion occurs in ferrites which have minimized anisotropy energy during a manufacturing process by substitutions of cations [199] in the crystal lattice. If the substituted cation is of the same element as the principal cation, the difference is only in valency (for example Fe^{2+} and Fe^{3+}). The complexity of mechanisms of electron relaxations may vary depending on the content of Fe^{2+} [200, 201, 202, 203]. In ferrites, electrons can diffuse between cations occupying certain locations in the crystal lattice when a magnetic field is applied. Electrons diffuse in order to minimize the anisotropy energy of the crystal during domain wall motion and domain rotation [204]. Since the relaxation process is thermally activated, it is slower at low temperatures, yielding more phase lag and loss. The second mechanism of electron diffusion, induced by an electric field, is the foundation of ferrite conductivity [205, 206]. The hopping electrons are called polarons. Thermally activated electron exchange between Fe^{2+} and Fe^{3+} ions was observed in Zn-Ti-Fe ferrites by van Diepen and Lotgering through Mössbauer spectroscopy [207]. They also provided formula for the polaron hopping frequency ($1/\tau$):

$$f_{hop} = f_0 \frac{e^{-(U_0+q)/kT}}{1+e^{-U_0/kT}} \quad , \tag{3.72}$$

where

U_0 - activation energy for the hopping electron (polaron),

q - energy barrier due to lattice deformation of electrical polarization,

k - Boltzmann constant,

T - absolute temperature, and

f_0 - polaron relaxation frequency at infinite temperature.

The activation energy of polaron hopping in MnZn and NiZn ferrites was recently found by Berzhanskii, *et al.*, based on the quantum exchange interaction between the $3d$ and $4s$ orbitals of iron ions [208]. Relaxations of ions and ion vacancies are much slower than electrons (minutes vs. nanoseconds at room temperature). Therefore, they contribute less to high frequency losses than electron relaxation at room temperature. Instead, they cause variations of permeability and loss with time [209]. Immediately after the change in magnetic field that leads to a change in the domain configuration, the ions in the crystal lattice try to find a minimum energy positions corresponding to a new domain configuration. The mechanism of interaction of ions with a domain wall was explained by Néel in his theory of diffusion after-effect [210].

3.2.3.4 Electric Field in Ferrite Grain Subject to AC Magnetic Field

When Kittel and Galt [211] found that the contribution of eddy current losses to domain wall damping in metallic ferromagnets is proportional to conductivity, they assumed that the electric field is produced only by a moving domain wall. Such an assumption is justified for metal ferromagnetic materials, but not for ferrites with an nonhomogeneous grain boundary [212, 213]. Researchers tried to apply the results of classical eddy current theory or Pry and Bean's model to explain additional losses in ferrites at high frequencies [214], which remain after subtraction of a hysteresis loss, by a modification of a frequency exponent to fit experimental data [215, 216]. The other common approach was to neglect residual losses except domain rotation and domain wall resonance and disregard the effect of a grain boundary [217, 218, 219, 220, 221].

In this work the effect of the grain boundary on the distribution of the electric field is investigated and the interaction of grain boundaries and domain walls with the electric field is studied. Consider a polyhedron grain with a single domain wall bulging in a spherical or cylindrical fashion. These are the two kinds of domain wall bulging mechanisms assumed in the reversible magnetization processes described in Section 3.2.2. The cross-section of both types of walls in a plane perpendicular to the domain easy axis of magnetization yields an arc. Analysis of the geometrical relationships of the arc fixed at its ends, shown in Fig. 3.8 yields the following set of equations:

$$\begin{cases} (x-x_0)^2+y^2=r^2 \\ x_0^2+\dfrac{d^2}{4}=r^2 \\ (x_p-x_0)^2=r^2 \end{cases} . \tag{3.73}$$

The displacement x of any point on the wall can be found after eliminating r and x_0:

$$x=\frac{\sqrt{d^4+8d^2x_p^2+16x_p^4-64x_p^2y^2}-d^2+4x_p^2}{8x_p} . \tag{3.74}$$

The normalized displacement for small deviations from equilibrium is:

$$\frac{x}{x_p}=\lim_{x_p\to 0}\frac{\sqrt{d^4+8d^2x_p^2+16x_p^4-64x_p^2y^2}-d^2+4x_p^2}{8x_p^2}=1-4\left(\frac{y}{d}\right)^2 . \tag{3.75}$$

If the wall is moving with a speed $v = dx_p/dt$ at the center, as shown in Fig. 3.9, it induces an electric field due to a change of the flux density $dB = 2\,M_s$. According to the Faraday's law:

$$E_y dy=-\frac{d\Phi_z}{dt}=-\frac{dB\,dx\,dy}{dt}=2dyM_s v\left[1-4\left(\frac{y}{d}\right)^2\right], \quad \text{or} \tag{3.76}$$

$$E_y=2M_s v\left[1-4\left(\frac{y}{d}\right)^2\right] . \tag{3.77}$$

The maximum electric field is in the middle of the grain, for $y = 0$. Maximum eddy currents are also expected to appear around the center of the domain wall. Eddy currents, flowing approximately in the direction of y axis, charge up the capacitive grain boundary if its

resistance is substantially higher than that of the inside of the grain. The charged grain boundary creates an electric field opposing the field generated by the domain wall and reduces eddy currents.

However, at very high frequencies, the impedance of the capacitive grain boundary decreases below the resistance of the inside material. Then the moving domain wall induces eddy currents inside and outside of the grain because the grain boundary ceases to exist for the electric field. Since the electric field has the same direction along the entire wall, the extreme potentials appear at the pinning edges of the domain wall. The sharp discontinuity of the potential at these locations create current crowding and additional losses at high frequencies. Insulating grain boundaries prevent the flow of such currents at low frequencies. In contrast to metallic ferromagnets, the grain boundary in ferrites has the capability to store the energy, and therefore the domain wall interacts with a complex impedance.

The first equivalent circuit of the ferrite grain impedance consisting of series connection of two RC parallel circuits was proposed by Koops [222]. He assumed that the grain boundary resistivity is much higher than an intragranular resistivity. Miroshkin, *et al.*, added another series RC branch [223] to better fit experimental data. However, if considerations are restricted only to a high frequency range, where the impedance of the grain is low enough to introduce eddy current losses, a simpler model can be used. Since the eddy current path through the grain boundary is different from the path of internal eddy currents, a schematic diagram in Fig. 3.10 can represent a simplified equivalent electrical circuit representing the currents generated by the domain wall at high frequency. The resistance, R_{in}, represents the inside of the grain where the principal contribution comes from the center of the grain, whereas R_{gb} represents the resistance of a grain boundary and areas around the edges of the domain wall where the heaviest current concentration occurs at high frequencies. Capacitance, C_{gb}, represents effective capacitance of the grain boundary, which is lower than the total capacitance due to a nonuniform distribution of the electric field on the grain boundary. Based on the equivalent circuit the admittance of the grain can be expressed as:

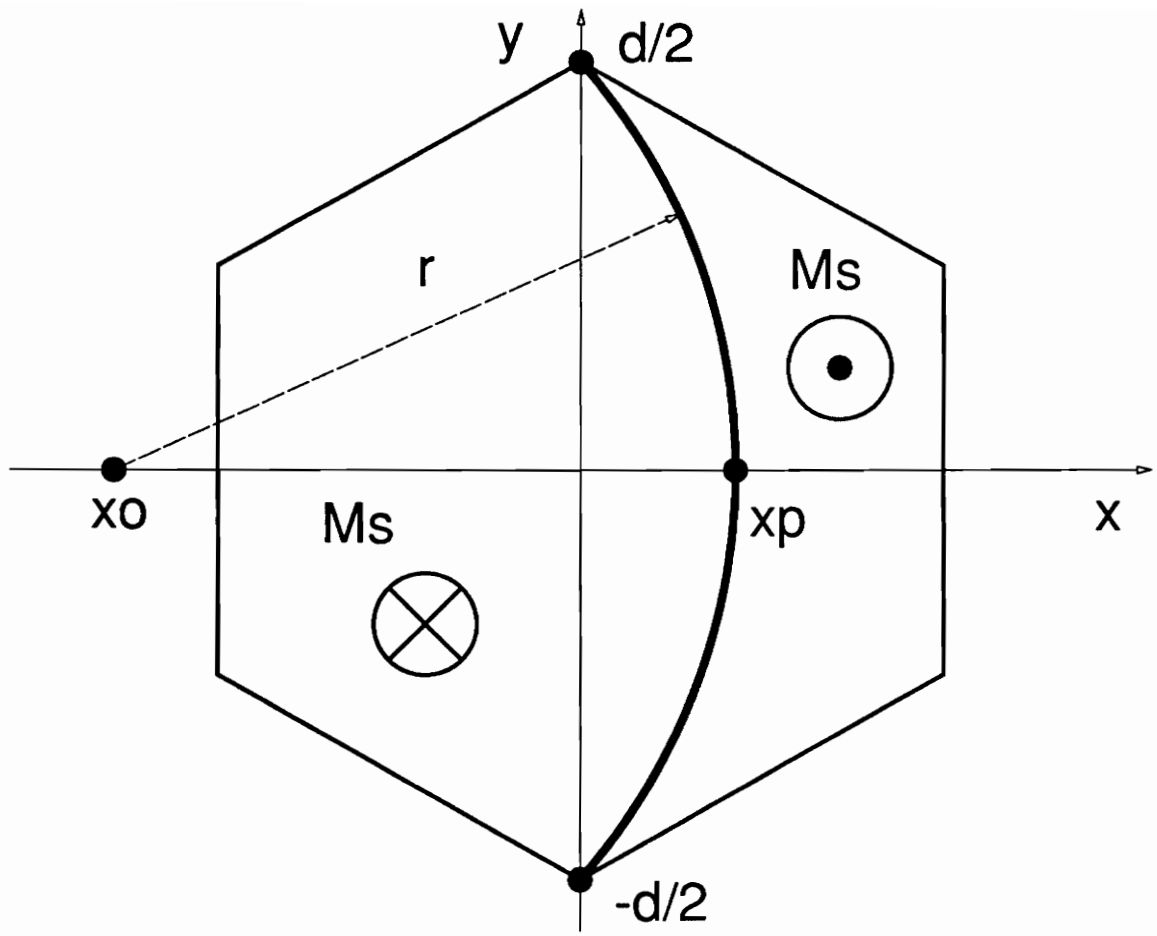

Fig. 3.8. Geometry of cylindrically or spherically bulging domain wall.

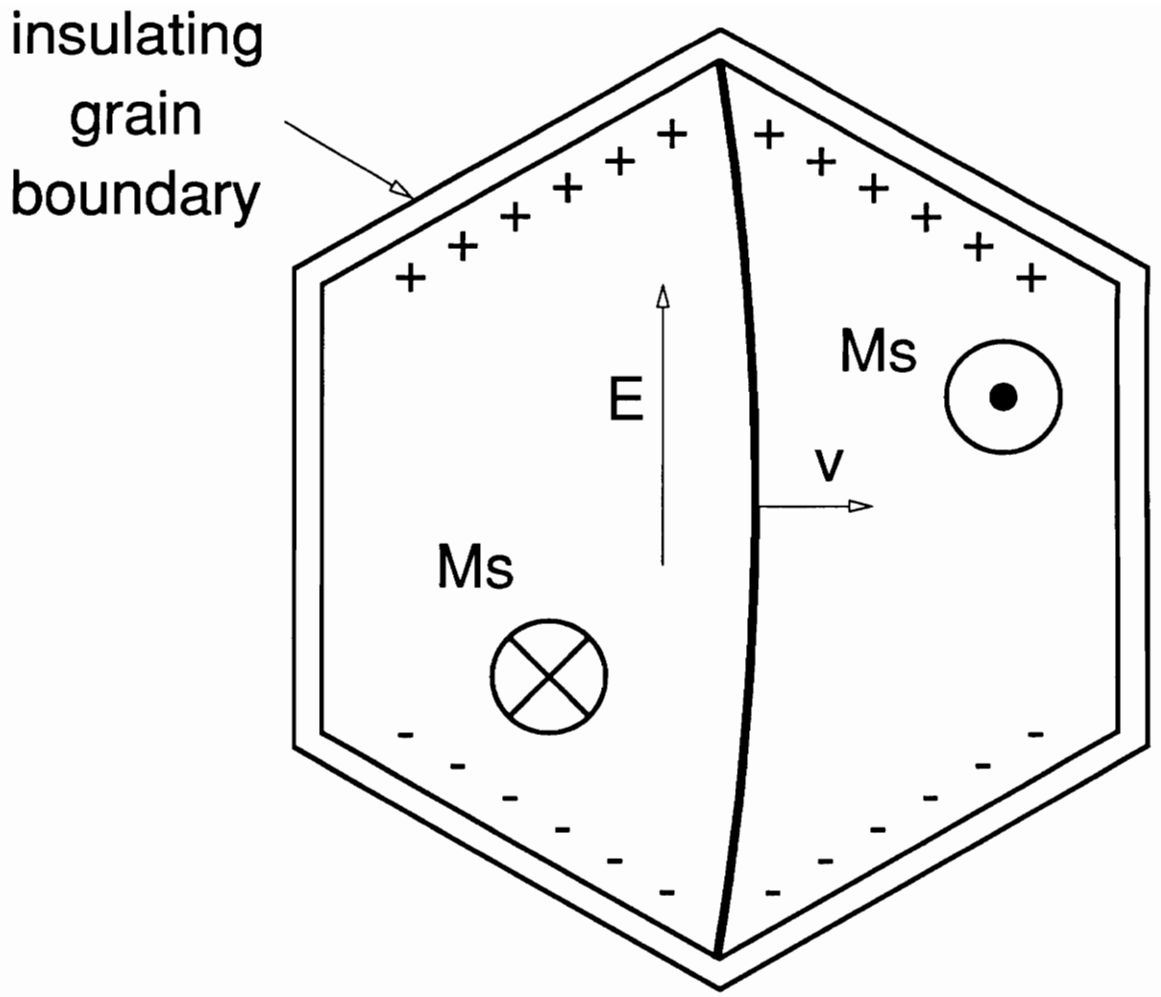

Fig. 3.9. Electric field and a space charge due to a single moving domain wall.

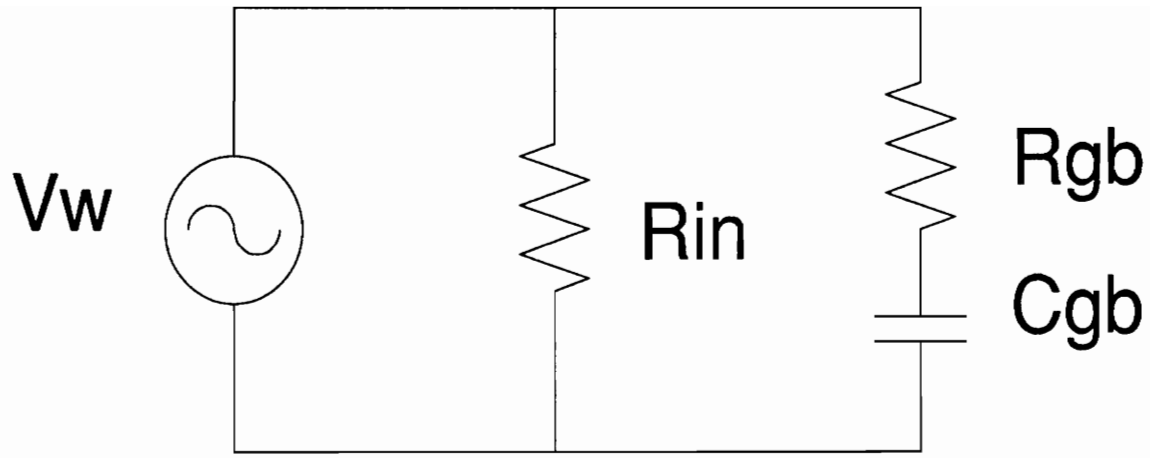

Fig. 3.10. Equivalent circuit diagram of a single domain wall in a grain with an insulating boundary.

$$Y = \frac{1}{R_{in}} + \frac{1}{R_{gb} - j/2\pi f C_{gb}} = \frac{1}{R_{gb}}\left(\frac{R_{gb}}{R_{\epsilon}} + \frac{1}{1 - j/2\pi f R_{gb} C_{gb}}\right) = \frac{1}{R_{gb}}\left(\frac{R_{gb}}{R_{in}} + \frac{1}{1 - j f_{gb}/f}\right) \quad . \tag{3.78}$$

Considering Eq. (3.66) in high permeability material ($\mu \approx \chi$) , consisting of identical grains with randomly oriented single domain walls and damping described by Eq. (3.78), the permeability spectrum can be expressed using a following formula:

$$\bar{\mu} = \frac{1}{1/\mu_i + j[\eta_{gin} + 1/(1 - j f_{gb}/f)]f/f_w} \quad , \tag{3.79}$$

where

μ_i - initial permeability,

η_{gin} - R_{gb}/R_{in}, is a ratio of internal to boundary related loss,

f_w - wall damping frequency, and

f_{gb} - grain boundary cutoff frequency,

The values of the parameters η_{gin} and f_w depend on the domain structure of the material. In the single domain configuration just considered, there are three cases, shown in Fig. 3.11, which produce different boundary related losses. When domain wall is confined solely to the inside of the grain and does not extend through the pinning edge of the grain, the electric potential difference between the inside and outside of the grain is equal to the potential at pinning point, V_p, since the outside has, on the average, a zero potential. However, when the domain wall extends through the pinning site to another grain, then the potential on the other side of the pinning site can be either V_p or $-V_p$, depending on the domain orientation of the other grain. If the domain orientation is opposite to the first grain then the walls move in the opposite direction. Therefore, both sides of the pinning site have the same potential and the potential difference is close to zero. In such case losses due to the current through a grain boundary will be negligible even at high frequencies when the grain boundary has low impedance. However, if the domain orientation is identical in both grains, the walls in both grains move in the same direction. Then the potential difference at the pinning site is $2V_p$, which greatly increases boundary related losses and wall damping.

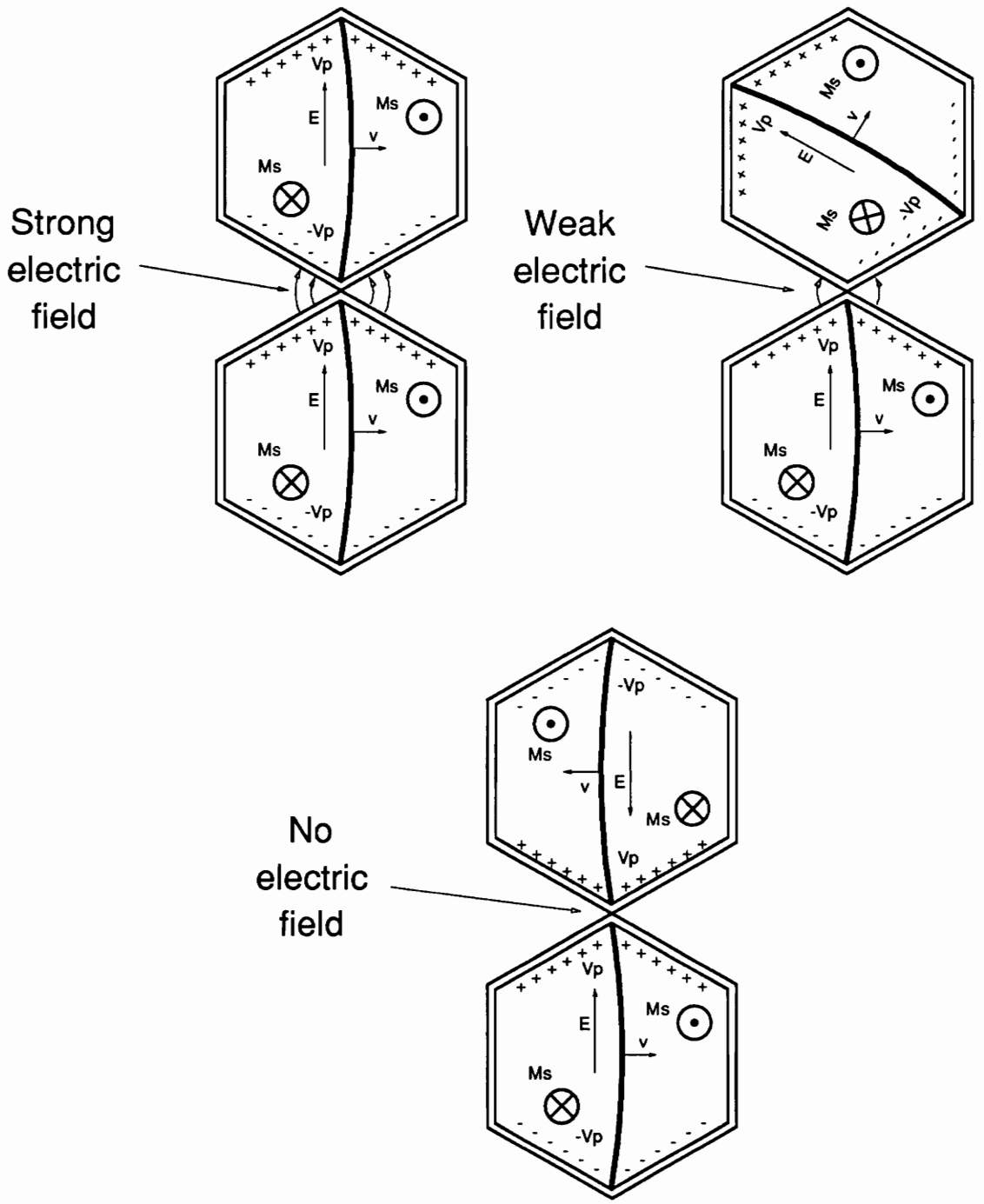

Fig. 3.11. Electric field between the grains for three different grain orientations.

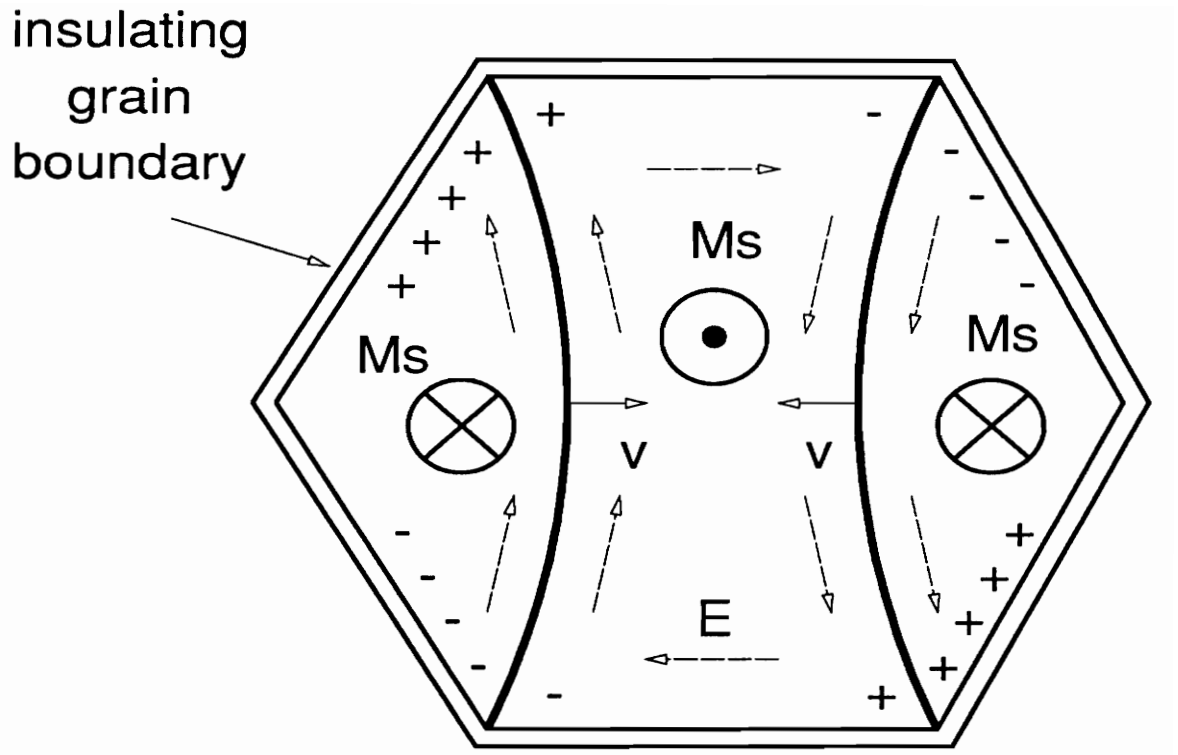

Fig. 3.12. Electric field due to a pair of moving domain walls.

If there are more domain walls inside a single grain, the neighboring domain walls move in opposite directions, creating opposite electric fields. The area between the walls is subjected to two opposite electric fields which induce circular currents, as shown in Fig. 3.12.

The electric field between two or more domain walls cannot be canceled by a charged grain boundary because the walls move in the opposite directions, creating opposite electric fields. Therefore, in the grains with multiple domain walls, even a highly insulating grain boundary does not reduce losses. For that reason, the losses in the grains with multiple domain walls are substantially higher than in single domain grains below the grain cutoff frequency. At higher frequencies the grain boundary does not influence the distribution of an electric field. Therefore, the losses in grains with single domain wall and the grains with multiple domain walls are similar if the wall spacing is the same.

The mechanism of a domain wall damping described above can explain the difference (usually 20-60%) between measured and calculated classical eddy current losses in ferrites which have bulk resistivity below 0.1 Ωm, as shown by Yamada, *et al.*, [224]., i.e. when the associate R_{gb} is small. In such materials, the boundary is very thin and capacitance, C_{gb}, is very large, such that it can be considered a short circuit at the frequencies of interest. The current crowding will appear at any frequency because of a poor insulating grain boundary. However, in ferrites with higher resistivity and smaller grain size, eddy current losses are negligible [225, 226]. Therefore, a residual loss mechanism must be employed to account for additional losses besides eddy current losses and hysteresis.

3.3 A Proposed Theory of Residual Losses Due to Magnetoelectric Effect

Sato, *et al.*, [227] and Yamada, *et al.*, pointed out that the calculated eddy current losses, using (3.29), show similar frequency dependence to these of experimental values, except the

magnitudes of calculated losses are 10 to 20 times too small. In Yamada's analysis, the difference between the frequency exponent of the measured losses and the frequency exponent of the conductivity varied between 1.81 and 2.22. Therefore, excess eddy current losses are ruled out since they are proportional to $f^{3/2}$ (3.41). Furthermore, we can assume that the new kind of loss is related to an electric field because the unknown loss is proportional to f^2 like eddy current losses. The electric field can interact with three objects in the grain: the grain boundary, the inside of the grain, and the domain wall. The first two are ruled out since they contribute to eddy current losses which are negligible in this case. Unknown loss cannot be created due to the interaction of an electric field with the whole volume of the grain. If it is so it would be even more pronounced in material with the large grain which is not observed. Thus, the only possible source of an unknown loss is the interaction between a domain wall and the electric field due to the domain wall motion. Such a mechanism is possible due to spin-polaron interactions in the domain wall. A similar problem was solved recently in a semiconducting ferromagnet indicating the mechanism of interaction with the crystal lattice [228]. Solving the problem in a semiconducting ferrimagnet may be considerably more difficult due to more complex magnetic and electronic structure.

The magnetoelectric effect (ME) was theoretically predicted by Landau and Lifshitz [229]. Later Dzyaloshinskii predicted ME in Cr_2O_3 [230], and Astrov verified it experimentally [231, 232]. The first ferrite which showed ME was $GaFeO_3$ [233]. ME produced dc voltage during ferromagnetic resonance in Mg-Mn and lithium ferrites [234], recently explained by a quantum mechanical theory [235, 236]. The change in anisotropy energy due to ME in magnetite (Fe_3O_4) was observed at 4.2°K by Rado and Ferrari [237, 238]. Aubert [239, 240] proposed a thermodynamic model for a paraelectric ferro- and ferrimagnets, and showed that the change of the crystal anisotropy due to ME involves not only the terms directly proportional to an electric field but also dependence of the angle of anisotropy of the electric field. The note on the contribution of Fe^{2+} ions was made by Babkin and Cherkunova [241], who measured the change of uniaxial anisotropy in magnetite due to ME at temperatures up to 160°K. The mag-

netoconductivity of ferrites was studied by Berzhanskii, *et al.*, [242]. The evidence of a change of the electron hopping frequency between Fe^{2+} and Fe^{3+} ions was provided by Rozin, *et al.*, [243] who observed Mössbauer spectra on MnZn ferrite in a static electric field. The dynamic change of hopping frequency was observed in MnZn ferrite under illumination of coherent laser light in photomagnetic experiments by Kastnelson and Karoza [244]. The hopping frequency decreased with increasing frequency of the illuminated light, and the effect was enhanced by an external bias magnetic field. The phenomenon was explained by a formation of clusters of polarons with increased binding energy and thus lower hopping frequency. It is reasonable to assume that ac electric field causes similar polaron clusters, but their energy should not be frequency dependent as it is in the optical band, since frequencies considered here are much lower than cluster oscillation frequency, which is on the order of $2 \cdot 10^{12}$ Hz [245].

As discussed in Section 3.2.3.3, electron diffusion occurs in certain ferrites under a change in magnetic field in order to minimize crystal anisotropy energy. Consider a moving domain wall in a crystallite grain and assume that the electric field produced by a domain wall is negligible. The polaron (an electron associated with a cation pair) resides at location favorable for the direction of easy axis of magnetization. When the domain wall sweeps through the grain, the spins of the associated cations rapidly reverse their orientation in a 180° turn to align again with an easy axis. Therefore the polaron is in the same location before and after the wall sweeps through. It is only during the moment of wall crossing the location of this electron when it is thrown out of a minimum energy state, trying to adjust the anisotropy to rotating spins in the lattice. However, soon after the domain wall passes through, the polaron settles down to its original state, dissipating the excess energy through the interaction with a lattice (phonon). Since the amplitude of the energy jump of the electron in this process depends on the magnetoelectric effect, the ion pairs that have a low activation energy introduce low residual losses. The process described so far is the origin of the residual loss due to electron diffusion. Note that this process is similar to the domain wall damping due to ferromagnetic (spin) resonance described in section about residual losses. Both processes compete with each other

during magnetization reversal. Perhaps in materials with a low crystalline anisotropy the spin can reverse entirely due to a change in an energy state of the polaron.

Now consider motion of a domain wall with a significant electric field. Assume the existence of polaron clusters with higher energy barrier than a single polaron has. When the domain wall sweeps through, the polarons are excited to an even higher energy level, corresponding to a higher energy barrier. After the wall passes through, the clustered polarons return to their minimum energy state, dissipating more energy than in the absence of an electric field. Therefore, the residual loss due to polaron relaxation is proportional to an electric field in the domain wall. It has identical frequency and flux density dependence like classical eddy current loss. It is also proportional to a concentration of hopping electrons and thus to conductivity.

The frequency dispersion of an electric field in the grain can be found based on the dielectric properties of ferrite. At low frequencies, the electric field in a small ferrite grain with a low permittivity can store much less charge than the grain boundary with a high capacitance. Therefore, the total eelectric field inside the grain is small but increases rapidly at the grain boundary. At high frequencies, when the capacitive grain boundary has low impedance, the charge cannot be accumulated at the grain boundary. The intensity of an electric field inside the grain is then much greater. The transition between the two different electric field distributions is a relaxation frequency of ferrite conductivity, f_c. Assuming uniform polarization in the grain and its boundary, $\boldsymbol{P} = \varepsilon \boldsymbol{E}$ = const, the electric field inside the grain can be expressed as:

$$E = \frac{\varepsilon_G}{\varepsilon^*} E_\infty \quad , \tag{3.80}$$

where

ε^* - apparent permittivity of the grain,

ε_G - intrinsic permittivity of the grain, and

E_∞ - electric field in the grain at $f \gg f_c$.

Recently Largeteau, *et al.*, investigated dielectric relaxations in NiZn ferrite [246, 247] and used space charge model to find microstructural parameters governing its dielectric properties [248]. The apparent permittivity of the grain can be expressed as [249]:

$$\varepsilon^* = \varepsilon_G \frac{1 + j\omega\varepsilon_G\rho_G}{\tanh Y/Y + j\omega\varepsilon_G\rho_G} \quad , \tag{3.81}$$

$$\delta_G = \frac{D_G}{2\sqrt{ne^2/\varepsilon_G kT}} \qquad \text{and} \qquad Y = \delta_G\sqrt{1 + j\omega\varepsilon_G\rho_G} \quad , \tag{3.82}$$

where

D_G - grain diameter,

δ_G - ratio of a grain diameter to a thickness of the charge layer at grain boundary,

ρ_G - intrinsic resistivity of the grain, and

n - concentration of charge carriers,

e - charge of electron.

The ferrites of interest are semiconductors with well defined space charge ($\delta_G >> 1$) due to a low concentration of charge carriers. If we define an intrinsic relaxation frequency of the grain as:

$$f_G = \frac{1}{2\pi\rho_G\varepsilon_G} \quad , \tag{3.83}$$

at frequencies $f \gg f_G/\delta_G$ the term $j\omega\varepsilon_G\rho_G = jf/f_G$ is much greater than $\tanh Y/Y \cong 1/\delta_G$, so the later term can be neglected at high frequency. The apparent permittivity can be approximated then as:

$$\varepsilon^* = \varepsilon_G \frac{1 + jf/f_G}{jf/f_G} \quad , \tag{3.84}$$

and the expression for the intragranular electric field can be rewritten as:

$$E = E_\infty \frac{jf/f_G}{1 + jf/f_G} = \frac{E_\infty}{1 + (f_G/f)^2} + \frac{jE_\infty f_G/f}{1 + (f_G/f)^2} \quad . \tag{3.85}$$

The energy barrier for a polaron cluster can be expressed as a sum of contributions from a crystal anisotropy and a magnetoelectric effect which depends on intragranular electric field:

$$q = q_0 + \frac{q_E}{1+(f_G/f)^2} \quad . \tag{3.86}$$

Substituting the above equation in the formula for the hopping frequency (3.72):

$$f_{hop} = f_0 \frac{e^{-\left[U_0+q_0+q_E/1+(f_G/f)^2\right]/kT}}{1+e^{-U_0/kT}} = f_1 e^{-\left[q_E/1+(f_G/f)^2\right]/kT} \quad , \tag{3.87}$$

where

$$f_1 = f_0 \frac{e^{-(U_0+q_0)/kT}}{1+e^{-U_0/kT}} \quad . \tag{3.88}$$

Using two first terms of a Taylor series expansion around infinite frequency of an electric field, the hopping frequency can be approximated as:

$$f_{hop} \approx f_1 e^{-q_E/kT}\left[1+\frac{q_E}{kT}(f_G/f)^2\right] = f_p[1+(f_c/f)^2] \quad , \tag{3.89}$$

$$f_p = f_1 e^{-q_E/kT} \quad , \quad \text{and} \quad f_c = f_G\sqrt{\frac{q_E}{kT}} \quad , \tag{3.90}$$

where

f_c - space charge relaxation frequency, and

f_p - polaron relaxation frequency.

According to the above formulas, the space charge relaxation frequency depends essentially on the intrinsic permittivity and resistivity of the grain, the temperature and the energy barrier due to magnetoelectric effect. The polaron relaxation frequency, in addition to these factors, depends on the energy barrier, q_0, due to crystal and stress anisotropy, and the polaron potential difference, U_0. U_0 depends on the mutual ordering in the lattice of cation pairs which create polarons. Since it is desirable to minimize the electric field in the grain, the space charge relaxation frequency should be as high as possible. This leads, however, to contradicting requirements: high magnetoelectric potential, q_E, and low resistivity, ρ_G. If the concentration of

Fe^{2+} ions is increased, the intrinsic resistivity is lower, and the intrinsic grain relaxation frequency increases. However, due to a larger concentration of Fe^{2+}-Fe^{3+} ion pairs, the magnetoelectric effect is stronger and residual losses increase. In order to resolve this problem, a paramagnetic ion can be added in a concentration comparable to Fe^{2+} ions, for example tetravalent titanium, Ti^{4+} [250]. The paramagnetic ion decreases magnetoelectric effect of the neighboring Fe^{2+} ion because Ti^{4+} does not favor changing its valency when the magnetic field changes. Therefore, polarons associated with Ti^{4+}-Fe^{2+} ion pairs keep relatively low intragranular resistivity of the grain but substantially decrease magnetoelectric relaxation, due to a higher activation energy. This mechanism reduces residual losses.

Using Eq. (3.68), the frequency dispersion of permeability can be written as:

$$\bar{\mu} = \frac{1}{1/\mu_p' + jf/f_w[1+(f_c/f)^2]} \quad . \tag{3.91}$$

Corresponding residual loss factor is found from Eq. (3.10):

$$\frac{\tan\delta_{ME}}{\mu_i} = \frac{f}{f_w}\frac{1}{1+(f_c/f)^2} \quad , \tag{3.92}$$

the residual core loss density is calculated from Eq. (3.21):

$$P_{ME} = \frac{\pi \hat{B}^2 f^2}{\mu_0 f_w}\frac{1}{1+(f_c/f)^2} \quad , \tag{3.93}$$

and the residual normalized parallel resistance from Eq. (3.20):

$$R_{pME} = 2\pi\mu_0 f_w[1+(f_c/f)^2] \quad . \tag{3.94}$$

The result of this theory is used as a part of the model of ferrite losses described in Section 3.5.

3.4 Interpretation of Loss Characteristics

In order to identify the loss mechanisms in magnetic materials, consider a few cases of theoretical magnetic materials and their normalized parallel resistance vs. frequency characteristics under constant flux excitation.

Case 1 Ferromagnetic resonance

The first material has no moving domain walls, and the only contribution to permeability is from domain rotation. Such conditions may occur in ferrites exposed to a strong static magnetic field which nucleates domain walls. The relative permeability is 100, the damping parameter varies is equal to a 100, and the frequency of ferromagnetic resonance varies from 0.1 MHz to 1 GHz in response to applied static bias field.

The normalized parallel resistance (NPR), calculated from Eq. (3.58), and shown in Fig. 3.13, depends strongly on the damping parameter. For a large damping factor, NPR is proportional to f^2 at high frequencies. As the static magnetic bias increases the low-frequency losses decrease and the high frequency losses increase.

Case 2 Domain wall resonance

The permeability of a second material is only due to reversible displacement of domain walls. Its permeability of 1000, domain wall resonance frequency of 10 MHz, and a wall relaxation frequency is a parameter varying from 1 to 100 MHz. The NPR characteristic, based on Eq. (3.66) and shown in Fig. 3.14, is flat and independent of frequency up to 100 MHz.

Case 3 Irreversible domain wall motion

The permeability in this case originates from irreversible wall displacement. The wall domain wall relaxation frequency is f_w = 10 MHz, and the hysteresis parameter, $\eta = 1$. The flux density is varied from 0 to 0.3. The resonance frequency is assumed much higher than the relaxation frequency, $f_{wr} >> f_w$. The complex permeability is obtained combining Eqs. (3.52) and (3.66):

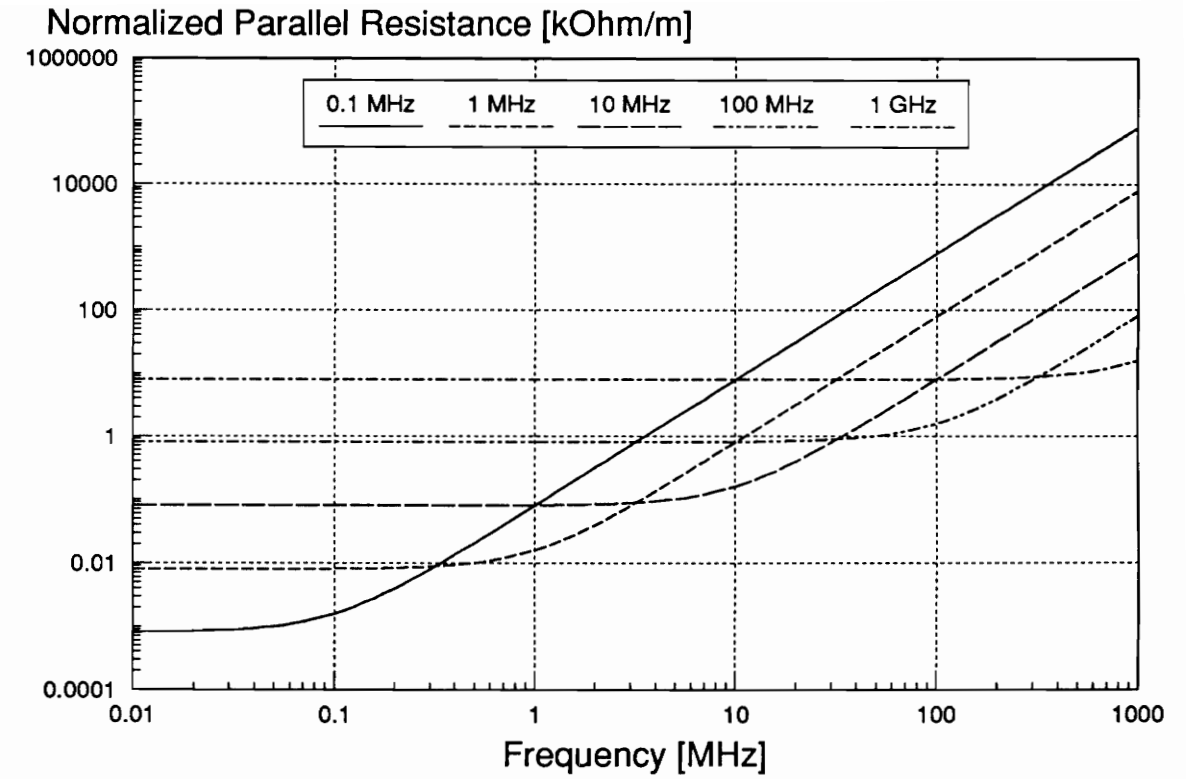

Fig. 3.13. Case 1. Loss characteristics due to a ferromagnetic resonance. The frequency of a resonance is the parameter dependent on the applied bias field as shown in the Eq. (3.56).

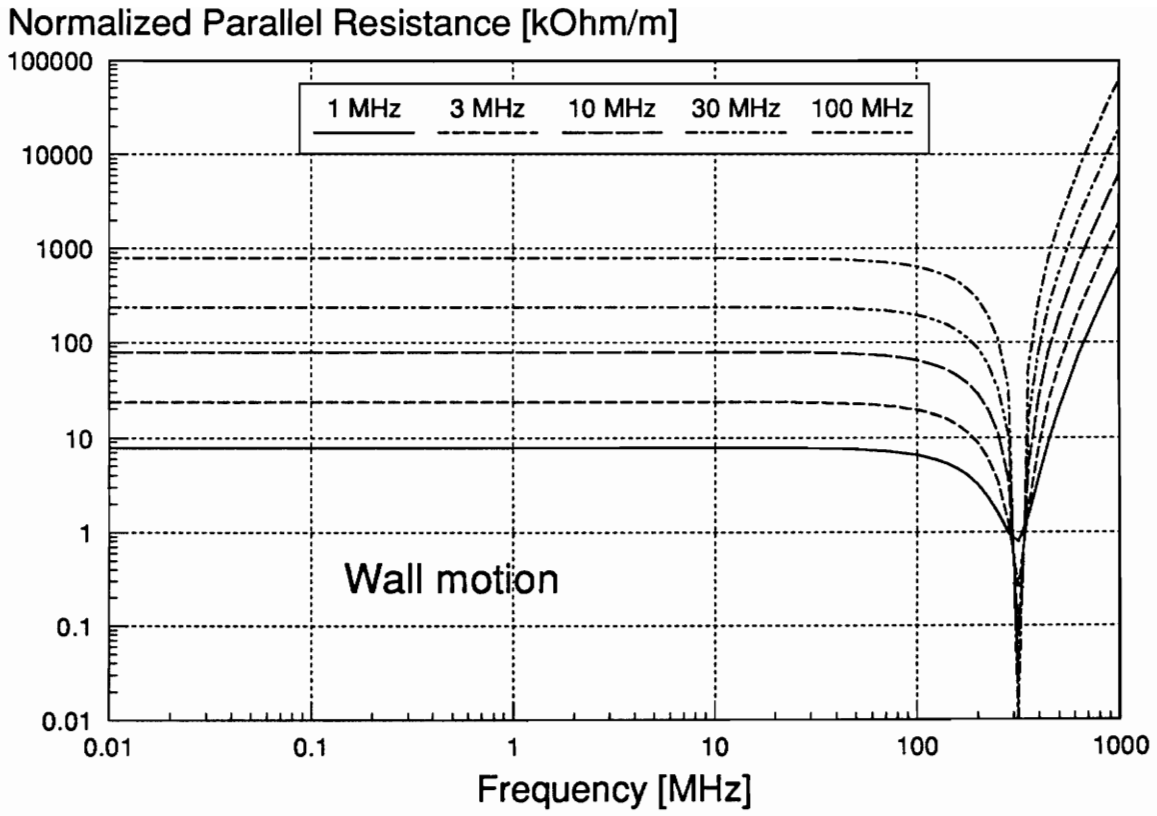

Fig. 3.14. Case 2. Loss characteristics due to reversible domain wall motion. The parameter is the relaxation frequency inversely proportional to damping losses (3.66).

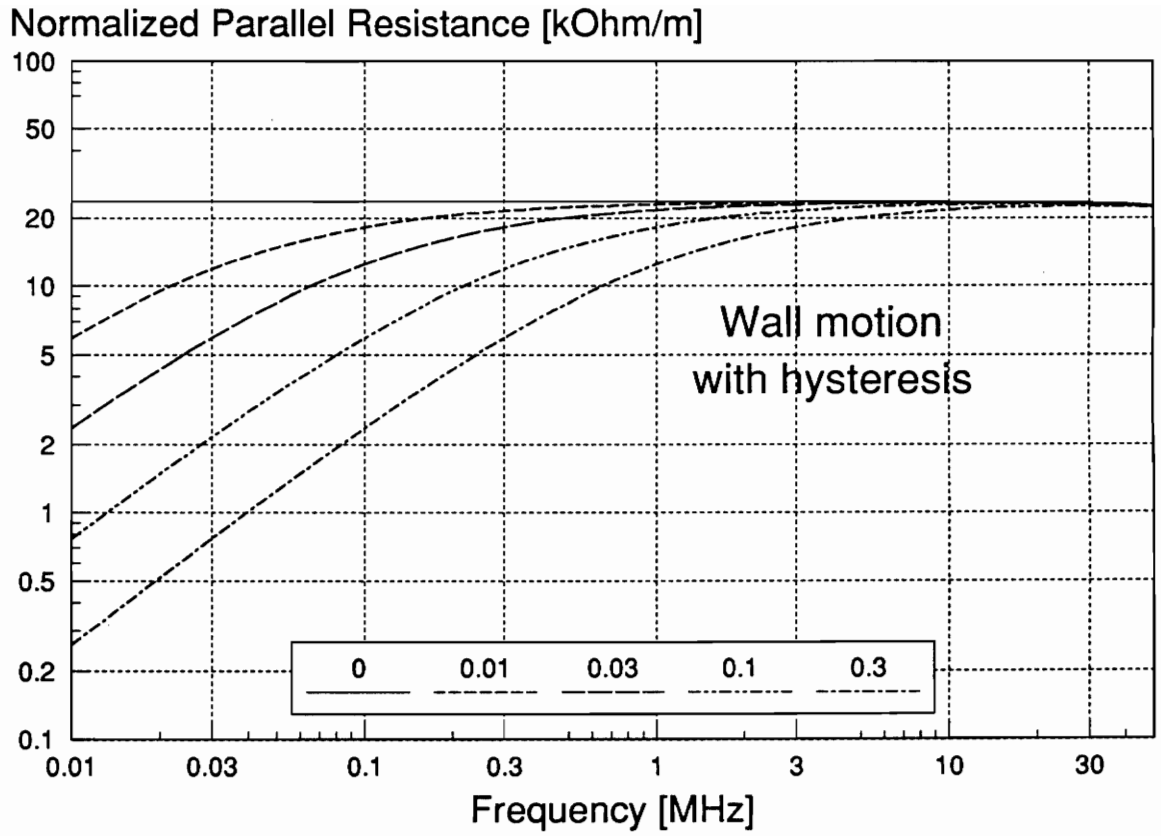

Fig. 3.15. Case 3. Loss characteristics due to irreversible domain wall motion. The parameter is $\eta_B B$ in Eq. (3.52). At low frequency hysteresis loss dominates, while at higher frequencies residual losses.

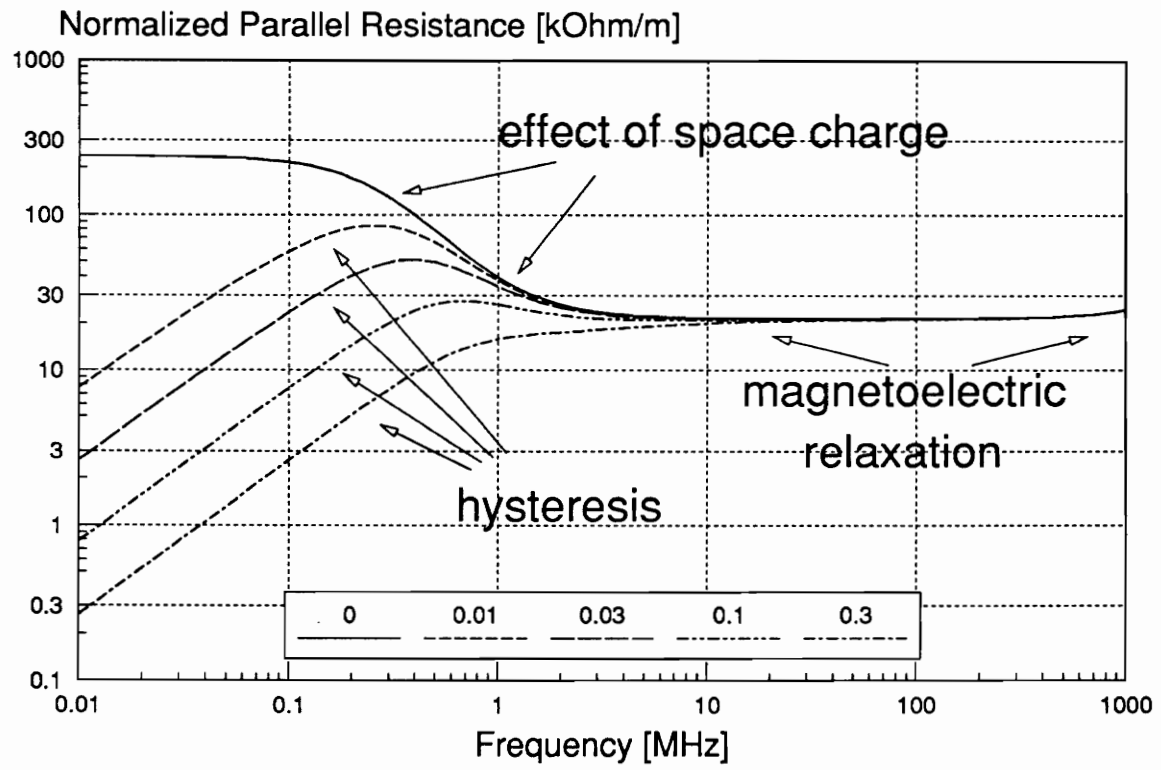

Fig. 3.16. Case 4. Loss characteristics due to irreversible domain wall motion with the space charge effect. The hysteresis loss combined with the space charge effect produces a peak in the normalized parallel resistance characteristics. At high frequencies the residual losses are greater due to the magnetoelectric effect discussed in section 3.3.

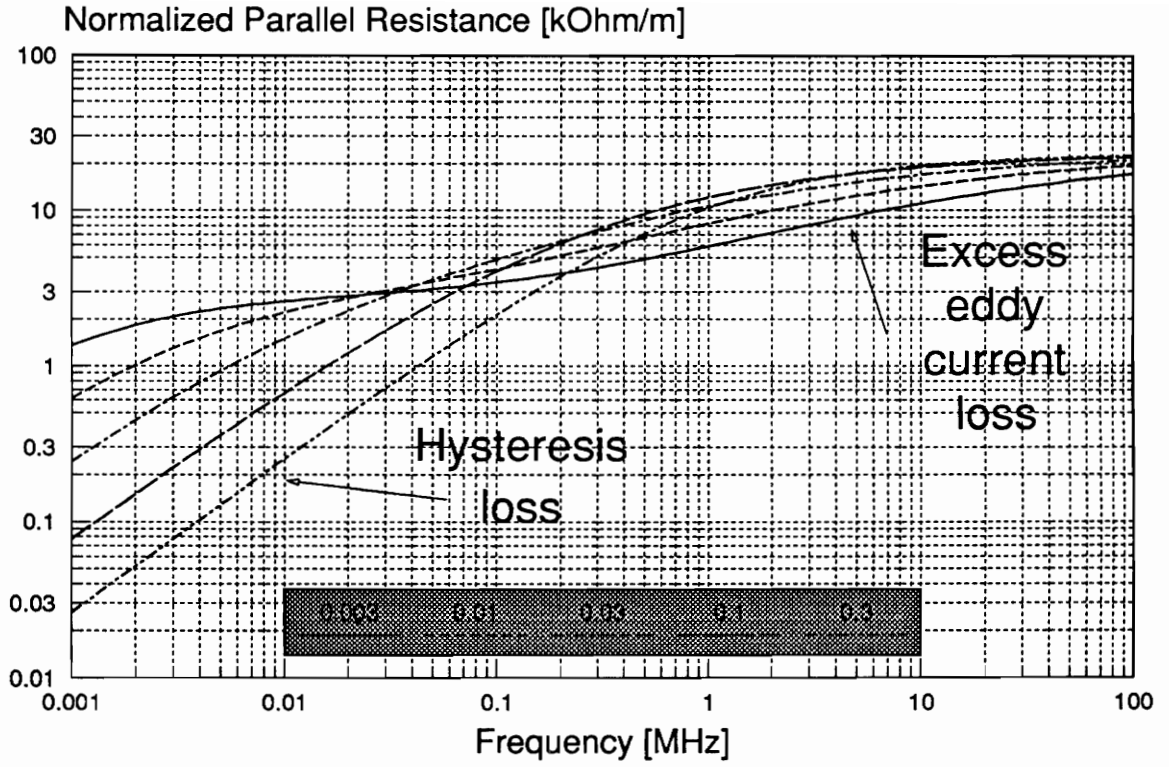

Fig. 3.17. Case 5. Loss characteristics due to hysteresis and excess eddy current losses. The parameter is $\eta_B B$ in Eq. (3.52). The excess eddy current losses are based on the Bertotti model (3.43). This is the only type of loss for which the normalized parallel resistance increases with the flux density.

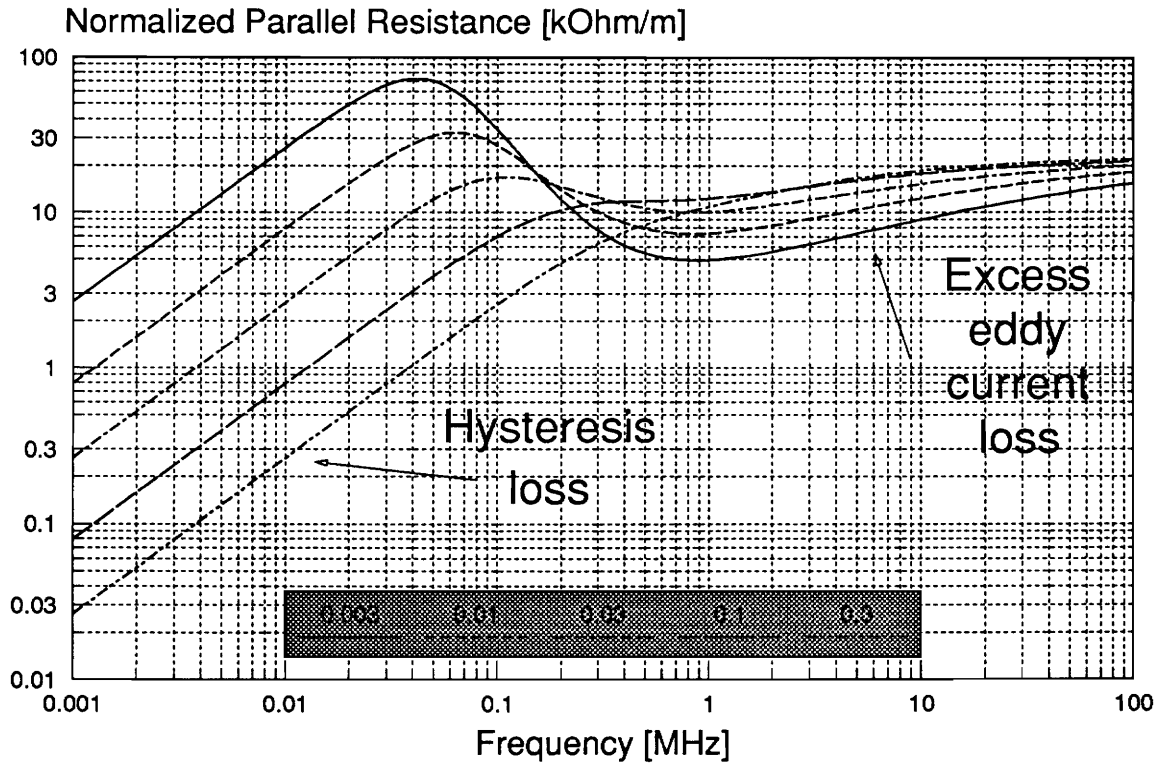

Fig. 3.18. Case 6. Loss characteristics due to hysteresis and excess eddy current losses with a space charge effect. The parameter is $\eta_B B$ in Eq. (3.52). The excess loss dominates at high frequencies but is negligible at low frequencies. The space charge effect appears due to the insulating grain boundary.

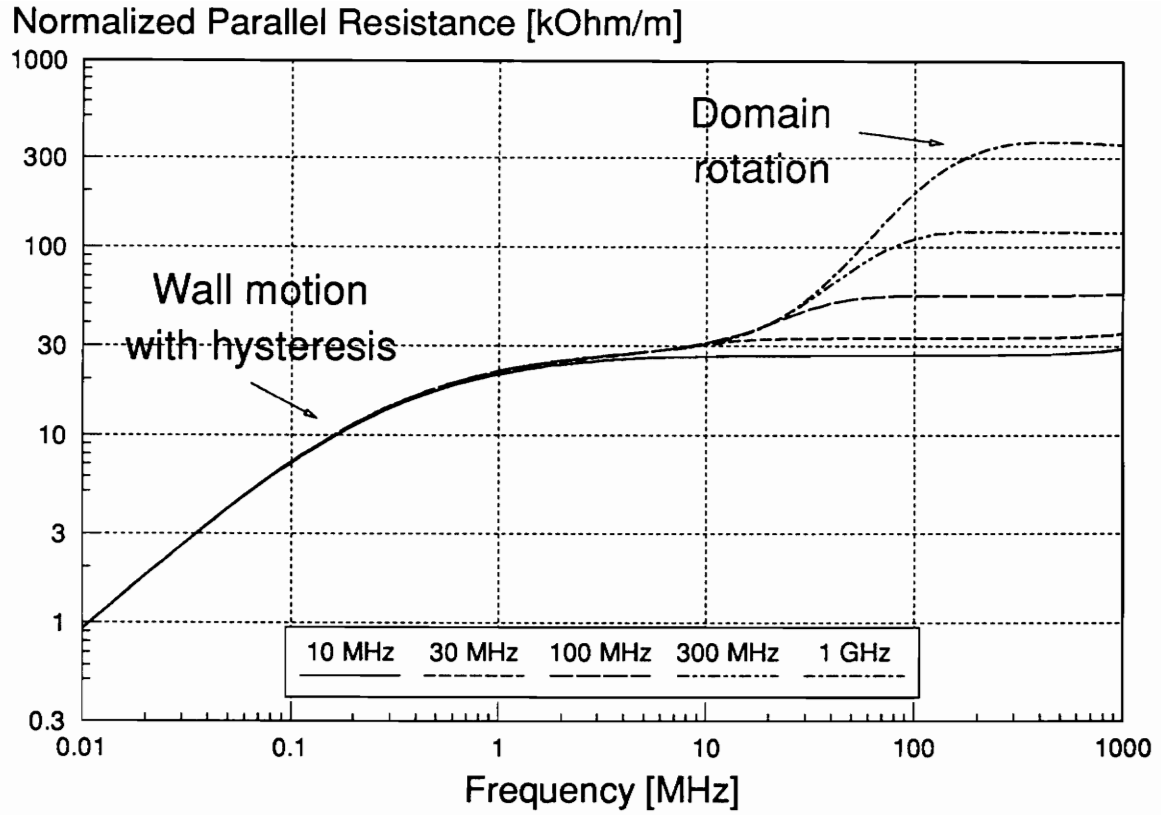

Fig. 3.19. Case 7. Loss characteristics due to hysteresis, domain wall resonance and domain rotation. The parameter is the ferromagnetic resonance frequency in Eq. (3.64). At low frequencies the irreversible domain wall motion is dominant. At high frequencies the domain rotation contributes to the permeability and losses.

$$\mu = \frac{1}{1/\mu_i + j(\eta_B \hat{B} + f/f_w)} \tag{3.95}$$

At low frequencies NPR, shown in Fig. 3.15, is proportional to frequency and inversely proportional to flux density. At high frequencies, both dependencies disappear due to domination of a relaxation losses.

Case 4 Irreversible domain wall motion in an insulated grain

The fourth material is similar to the third one, except it has an insulating grain boundary. Therefore, the relaxation loss is decreased at lower frequencies. Compared to previous case, it produces a peak in NPR characteristics, based on Eqs. (3.52) and (3.94) and shown in Fig. 3.16, below the space charge relaxation frequency, f_c. The height of the peak depends on the value of the hysteresis loss below f_c. At high frequencies, the characteristics are similar.

Case 5 Irreversible domain wall motion with excess eddy current losses

The material in the fifth case has hysteresis loss, eddy current loss, and excess eddy current loss. At low frequencies, hysteresis loss dominates, while at high frequencies the excess loss is higher. Constant flux density characteristics, based on Eqs. (3.43) and (3.52) and shown in Fig. 3.17, cross each other as the NPR dependence on flux density changes from $1/\hat{B}$ to $\sqrt{\hat{B}}$. Such crossing appears only in the presence of excess eddy current losses, since no other losses make the NPR flux density exponent positive.

Case 6 Irreversible domain wall motion with excess eddy current losses in an insulated grain

The sixth material is almost identical with the fifth one, except it has polycrystalline structure, and the grains have insulating boundaries and contain space charge. The characteristics, based on Eqs. (3.43), (3.52), and (3.94), and shown in Fig. 3.18, have similar crossing to the fifth case due to excess eddy currents.

Case 7 Irreversible domain wall motion and domain rotation

The last material has hysteresis, domain wall resonance, and domain rotation losses. At low frequencies the NPR characteristics, shown in Fig. 3.19, appear proportional to frequency due to hysteresis losses until they are dominated by domain wall resonance, yielding a flat portion at medium frequencies. At high frequencies, the wall permeability decreases substantially, and rotational permeability and losses prevail. The characteristics are based on the Eqs. (3.52), (3.57) and (3.66).

All above characteristics can be also used with a constant core loss as a parameter instead of a flux density. The only change in frequency slope is for hysteresis loss which is proportional to $f^{4/3}$ instead of f. Therefore the isoloss characteristics (with a core loss as a parameter) are very similar to those with flux density parameter. The hysteresis is proportional to $1/P_h^{1/3}$, according to (3.53), instead of $1/\hat{B}$ and thus yields much closer branches than with flux density as a parameter. Such characteristics, analyzed in detail in the next chapter, are ideally suited for optimization of operating frequency of the power transformer, since a single curve corresponds to identical thermal conditions for the core at any frequency. This is not the case of conventional characteristics where a constant flux density curve does not enable fair comparison of materials with frequency dependent losses.

In the following Section, the above loss analysis is applied to measured ferrite characteristics.

3.5 Modeling of Loss Characteristics of Soft Ferrites

In actual ferrites there is always a combination of loss mechanisms. The purpose of this section is to analyze the losses that appear in three types of soft ferrites electronics applications and provide a reasonably accurate yet simple model suitable for optimization algorithms.

3.5.1 Manganese-Zinc Ferrite

This is the most commonly used material for transformers in switched-mode power supplies. Many grades differing by chemical composition and sintering conditions are manufactured. The 3F4 material provided by Philips Components was used for measurements and modeling of loss characteristics of manganese-zinc ferrites. This material is a good subject for modeling due to its small grains, homogeneous structure, and high resistivity [251]. The ferrite was used in a form of a toroid with an outer diameter of 12.44 mm, an inner diameter of 7.50 mm, and a height of 5.00 mm. The winding consisted of six turns of 175×AWG#44 litz wire. The core was measured at five flux density levels of 1, 3, 10, 30, and 100 mT, at 40 discrete frequencies distributed exponentially in the frequency range from 100 kHz to 10 MHz at 100°C, and at four flux density levels at fifty frequencies from 100 kHz to 20 MHz at 25°C. The errors due to parasitic inductance and capacitance of the interconnections in the temperature chamber prevented measurements above 10 MHz. The ferrite was subjected to a static magnetic bias field by means of a dc current from the power supply set in current regulation mode through the impedance probe to the winding of a test inductor. The bias characteristics are very important, since such bias often occurs in power electronics transformers and inductors. The instrumentation and calibration procedures are described in Chapter 2. After dc bias was applied, the sample was demagnetized with a 10 kHz saturating excitation. In order to avoid a temperature change of the core during measurement, each measurement series was stopped when the core loss per unit volume reached 1 W/cm^3. During the measurement, the flux density was maintained with a 3% accuracy. The measured and fitted data and the fitting error at the temperature of 100°C and bias fields of 0 to 100 A/m is shown in Figs. 3.20-3.30. Similar set of characteristics are shown in Figs. 3.31, 3.32, 3.33, and 3.34 at static bias magnetic field of 0, 10, 30 , and 100 A/m respectively and at 25°C. When no bias is applied the hysteresis losses dominate at frequencies below 1 MHz, while above 3 MHz residual losses prevail.

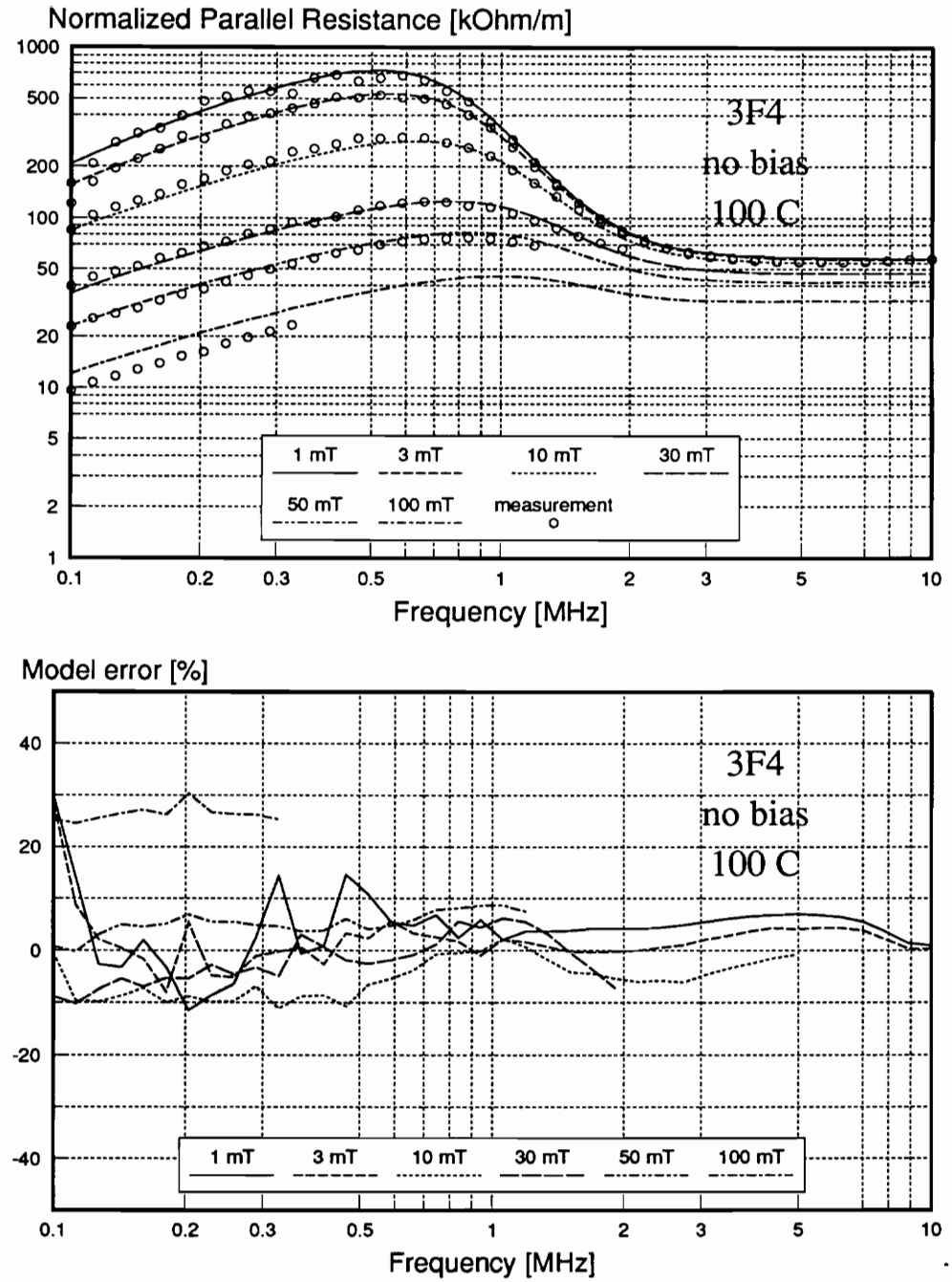

Fig. 3.20. Normalized parallel resistance and model error for 3F4 ferrite without bias and at 100 ℃ temperature.

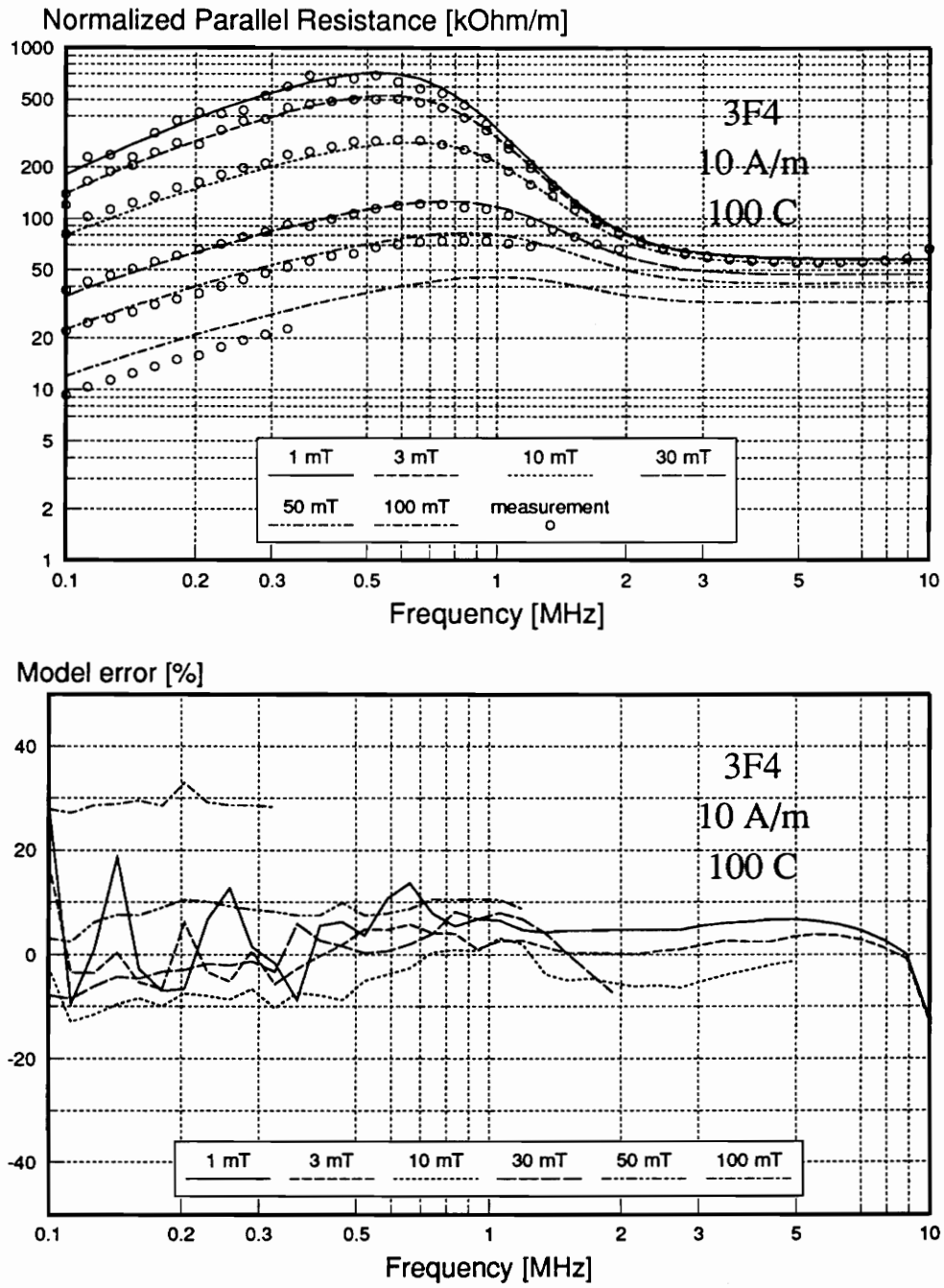

Fig. 3.21. Normalized parallel resistance and model error for 3F4 ferrite at 10 A/m static bias and at 100 ℃ temperature.

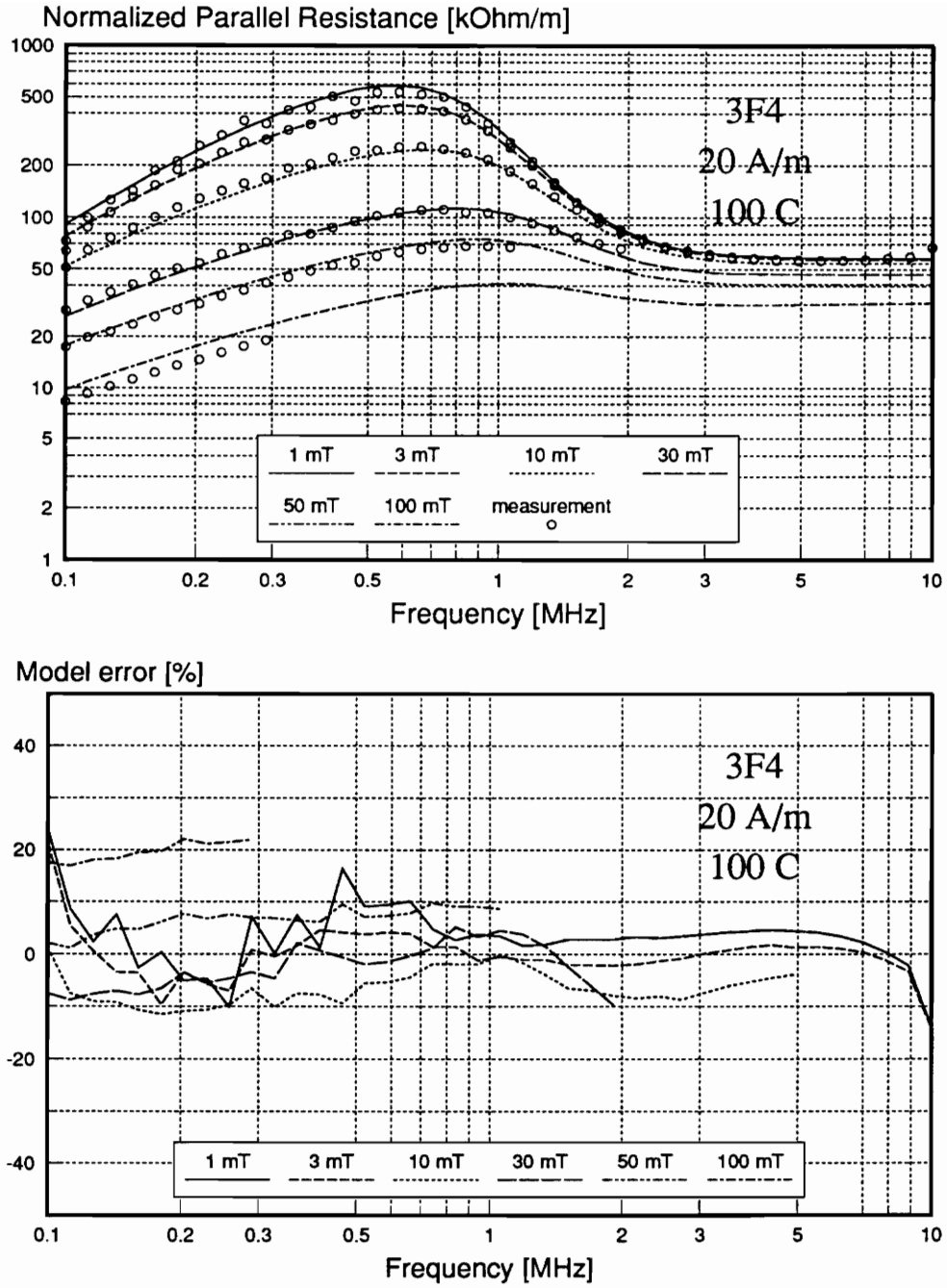

Fig. 3.22. Normalized parallel resistance and model error for 3F4 ferrite at 20 A/m static bias and at 100 ℃ temperature.

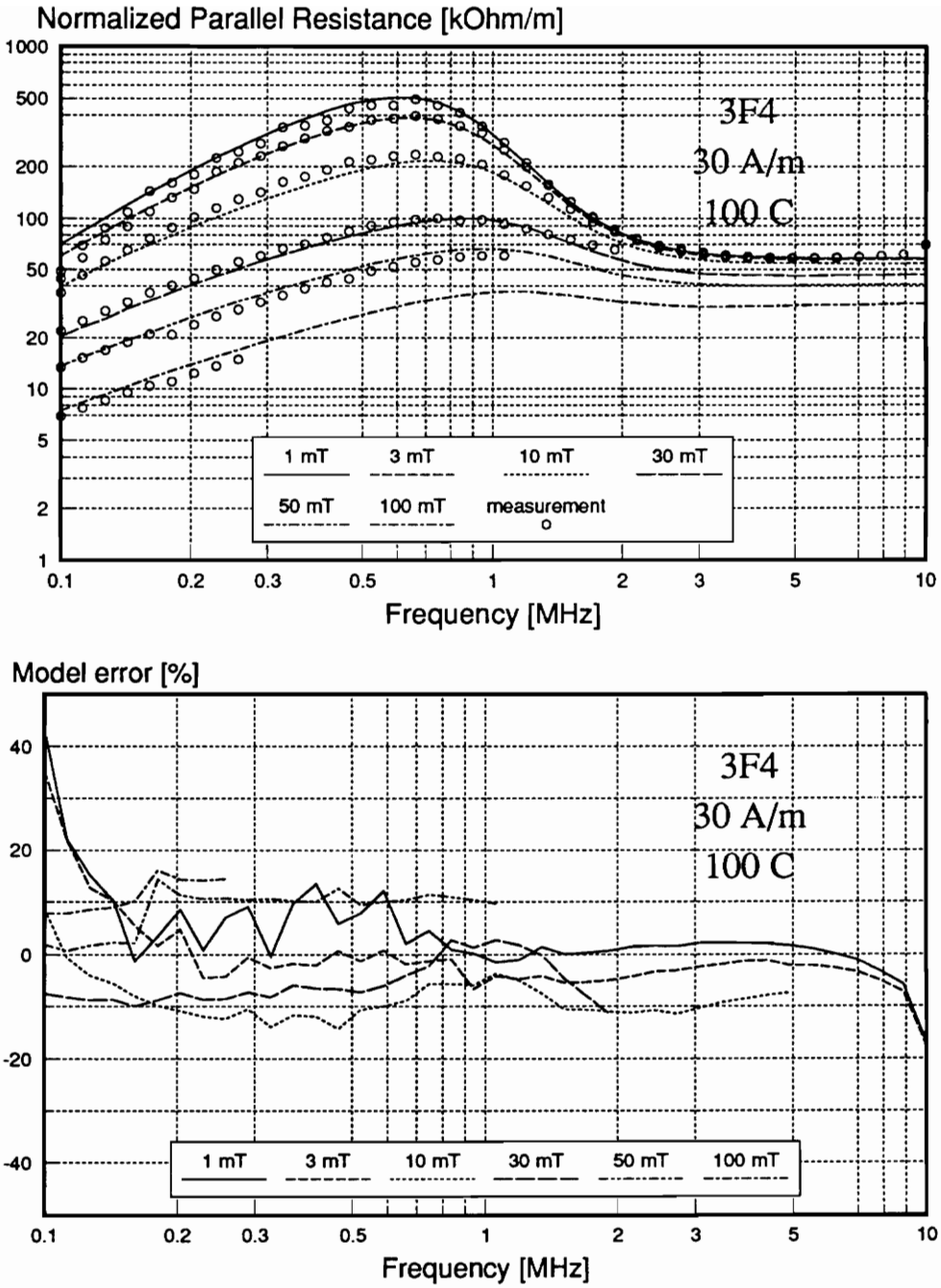

Fig. 3.23. Normalized parallel resistance and model error for 3F4 ferrite at 30 A/m static bias and at 100 ℃ temperature.

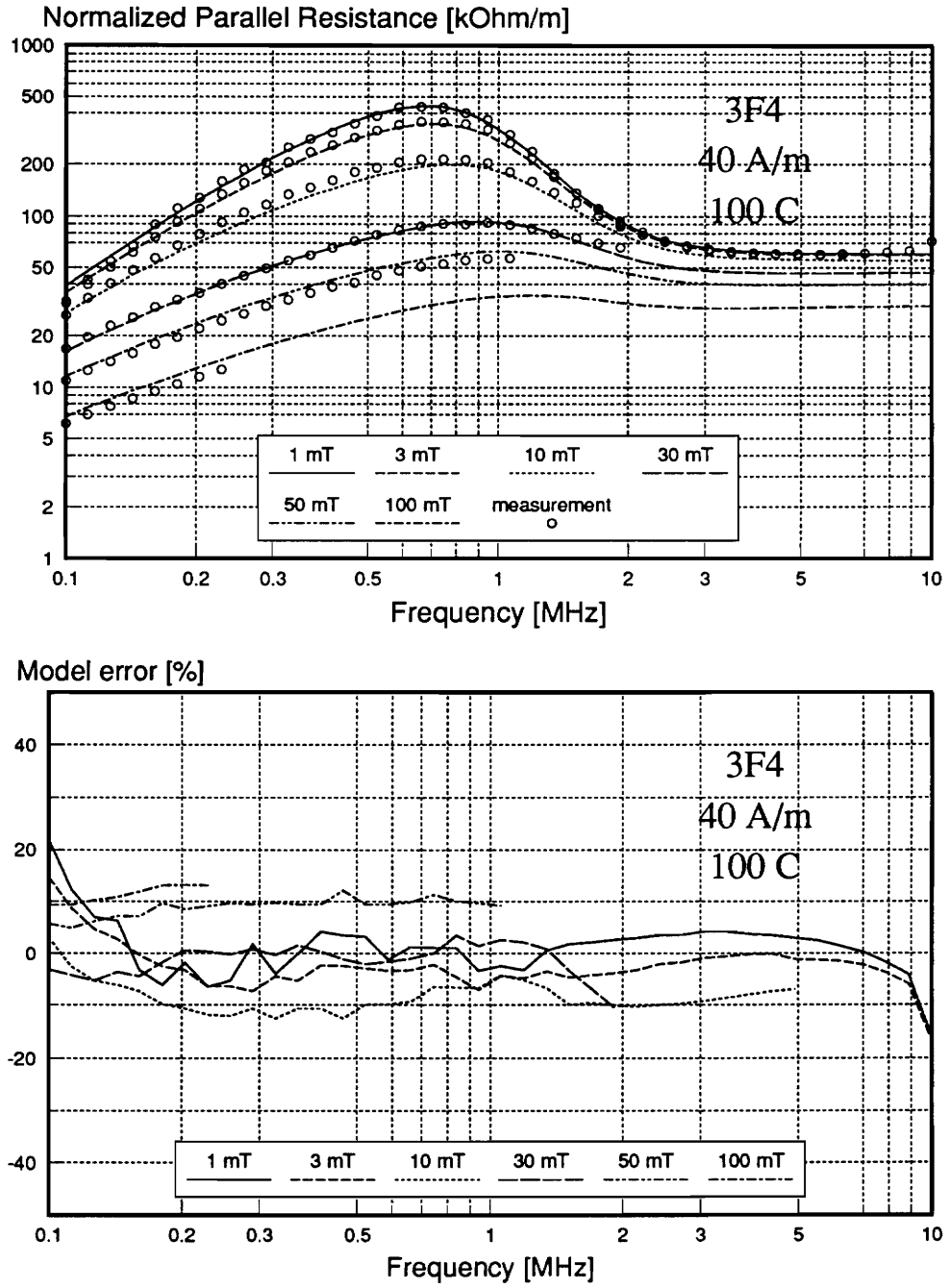

Fig. 3.24. Normalized parallel resistance and model error for 3F4 ferrite at 40 A/m static bias and at 100 ℃ temperature.

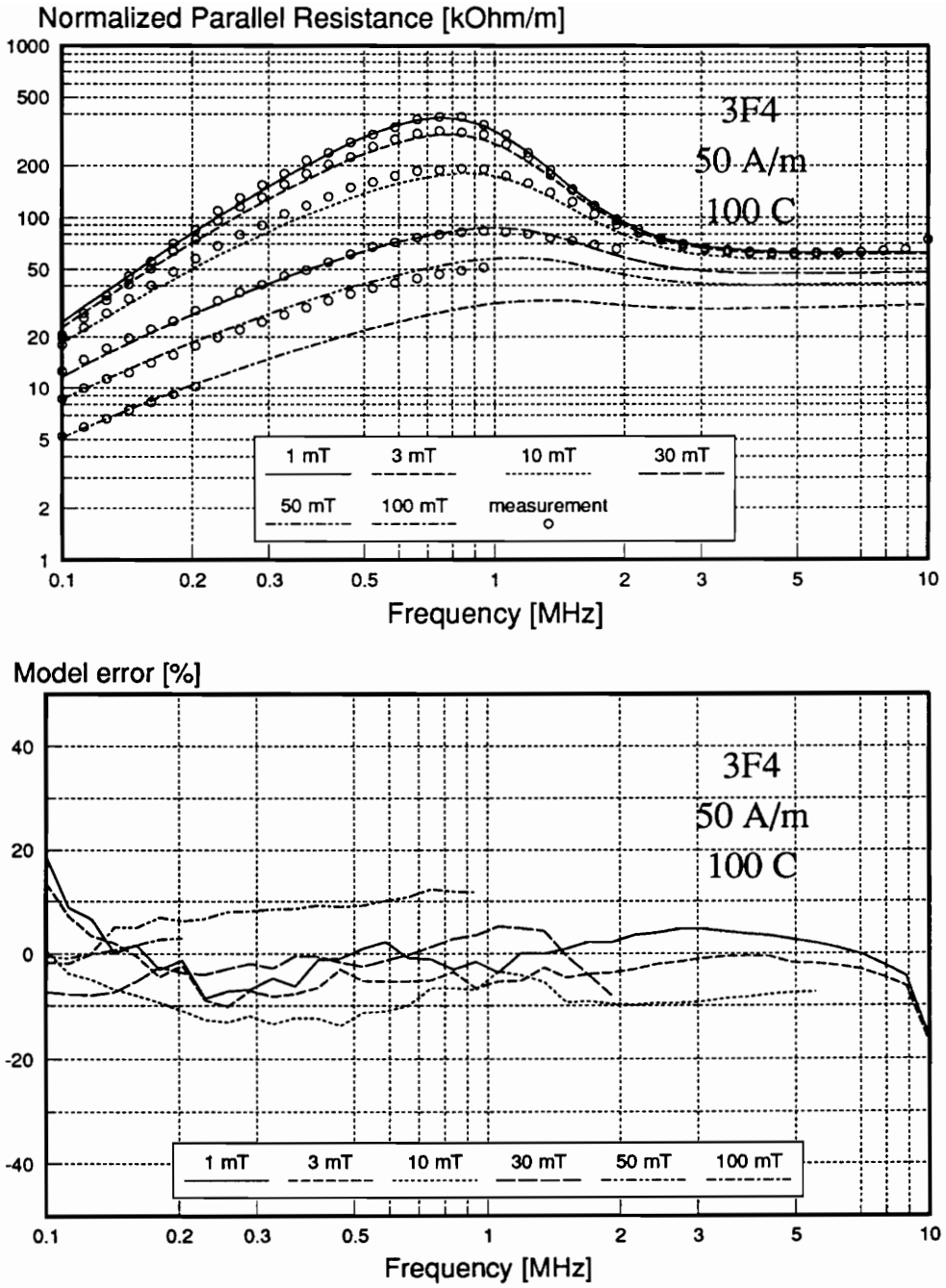

Fig. 3.25. Normalized parallel resistance and model error for 3F4 ferrite at 50 A/m static bias and at 100 ℃ temperature.

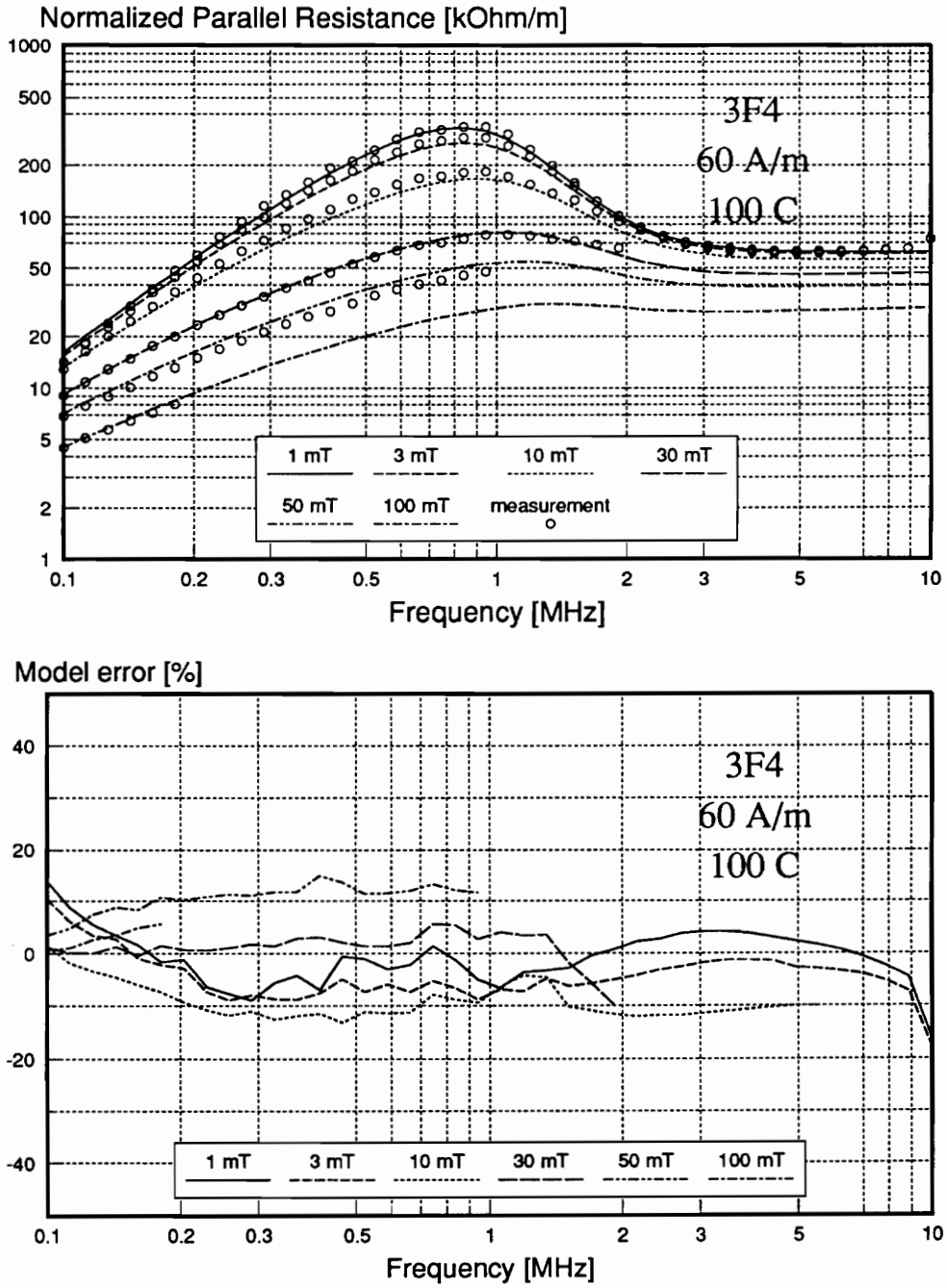

Fig. 3.26. Normalized parallel resistance and model error for 3F4 ferrite at 60 A/m static bias and at 100 ℃ temperature.

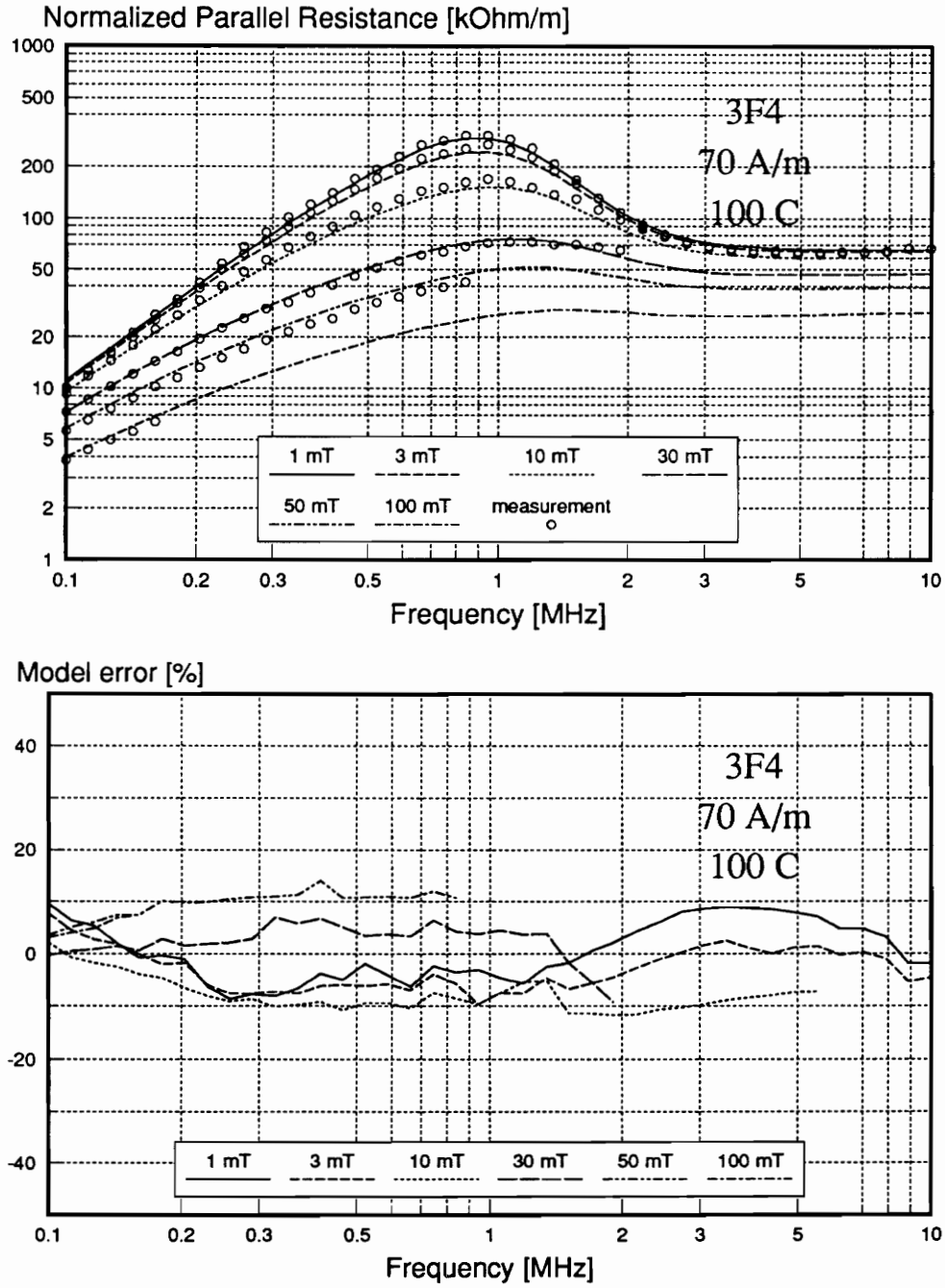

Fig. 3.27. Normalized parallel resistance and model error for 3F4 ferrite at 70 A/m static bias and at 100 ℃ temperature.

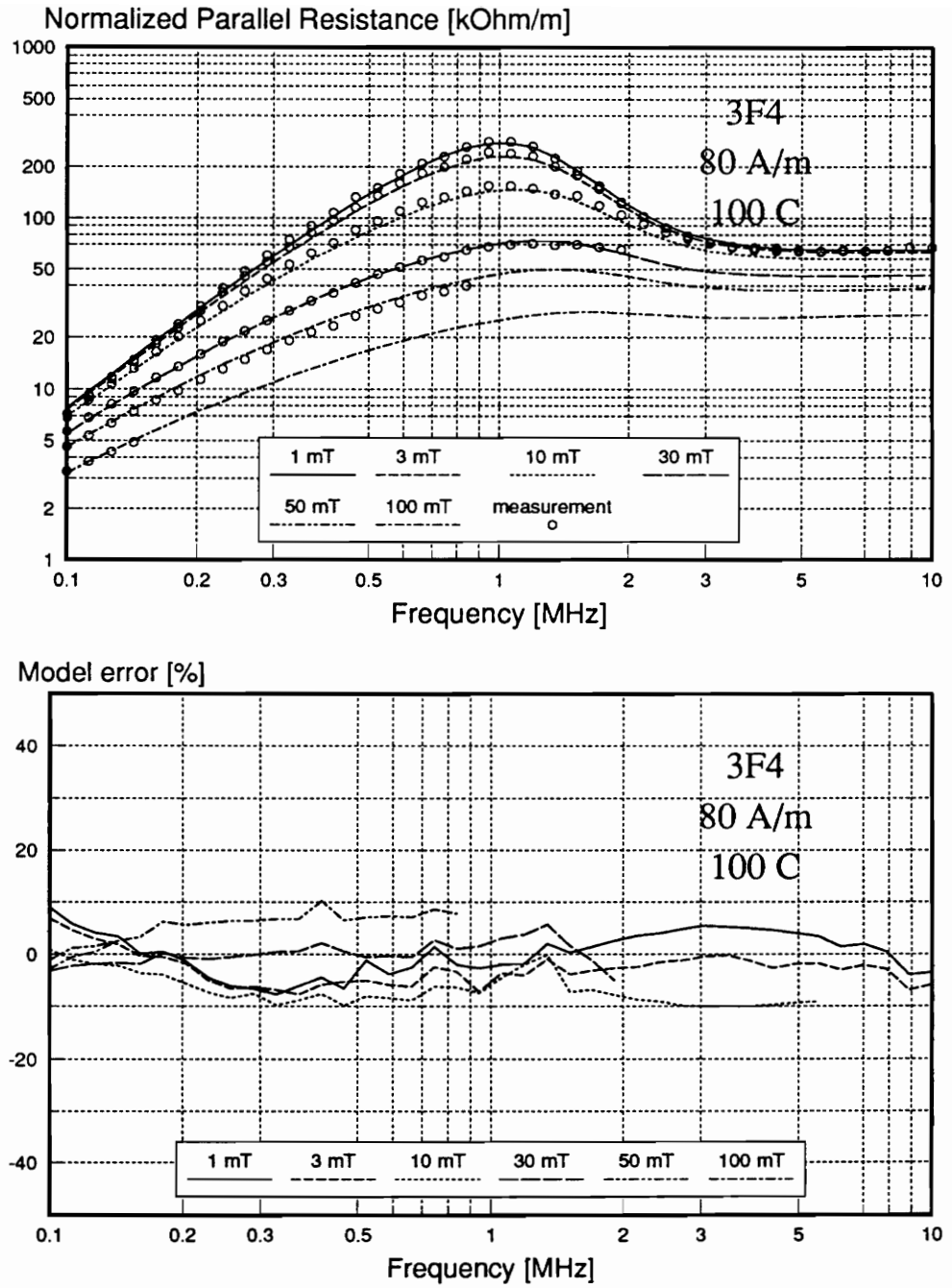

Fig. 3.28. Normalized parallel resistance and model error for 3F4 ferrite at 80 A/m static bias and at 100 ℃ temperature.

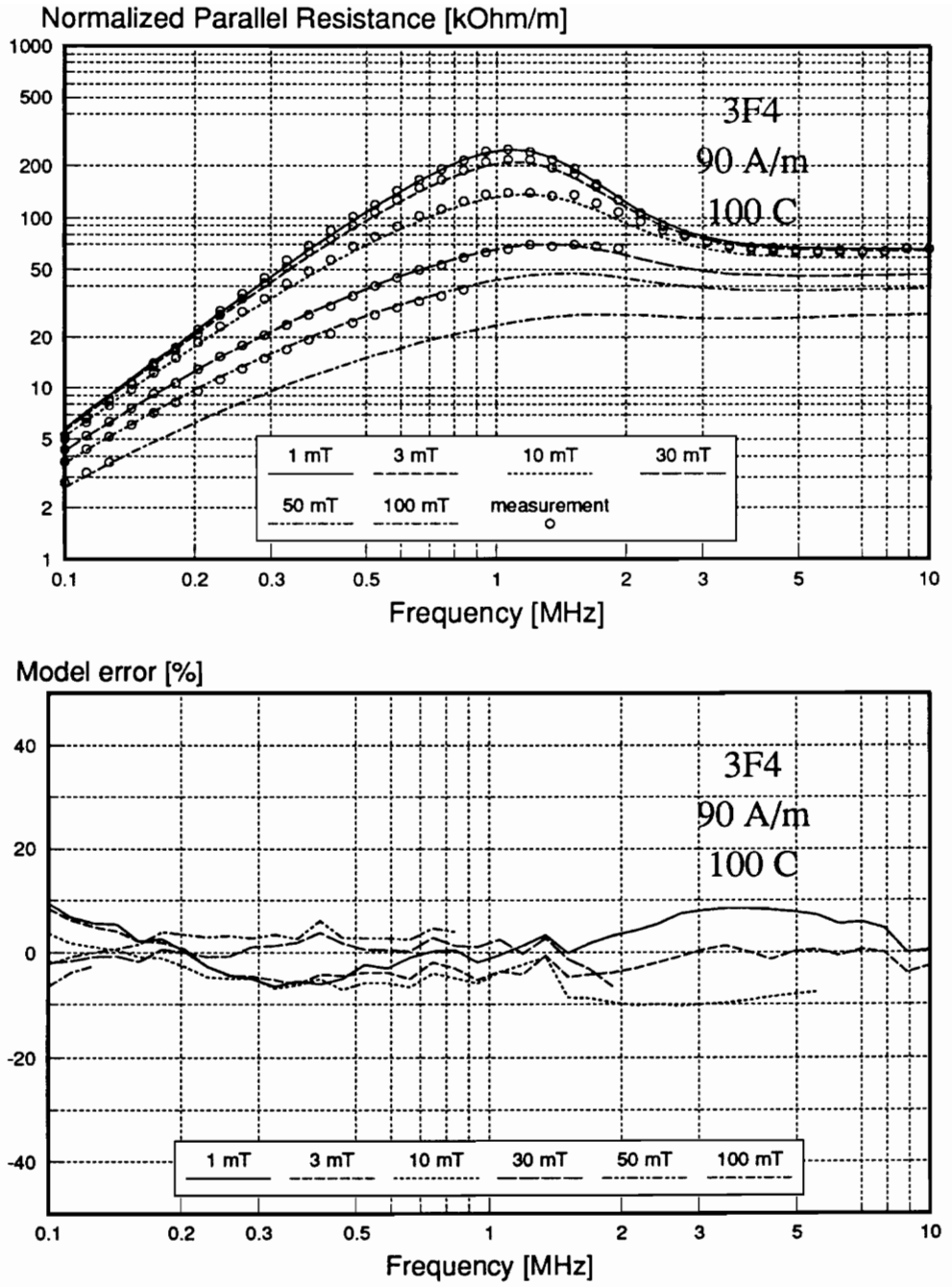

Fig. 3.29. Normalized parallel resistance and model error for 3F4 ferrite at 90 A/m static bias and at 100 ℃ temperature.

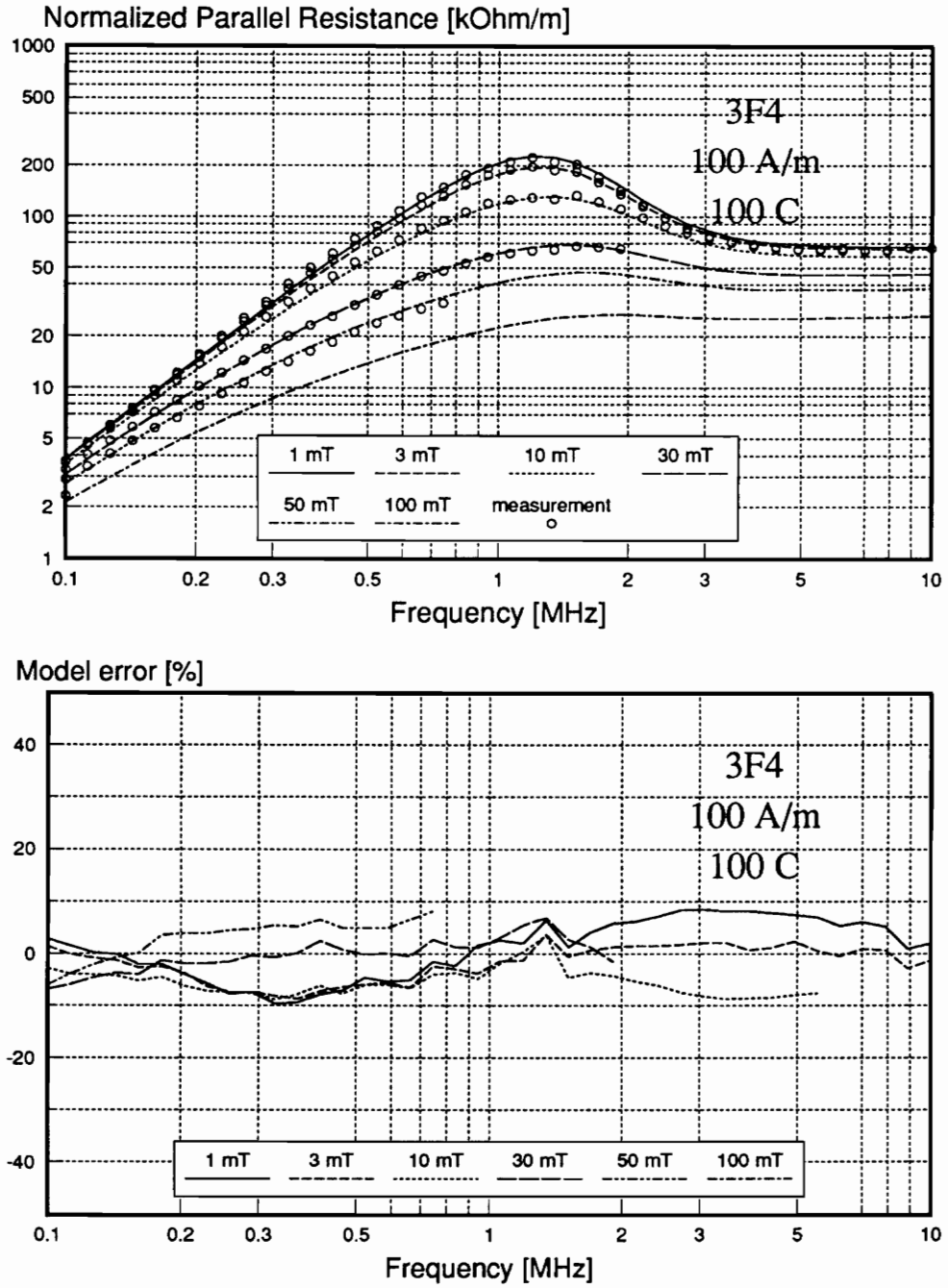

Fig. 3.30. Normalized parallel resistance and model error for 3F4 ferrite at 100 A/m static bias and at 100 ℃ temperature.

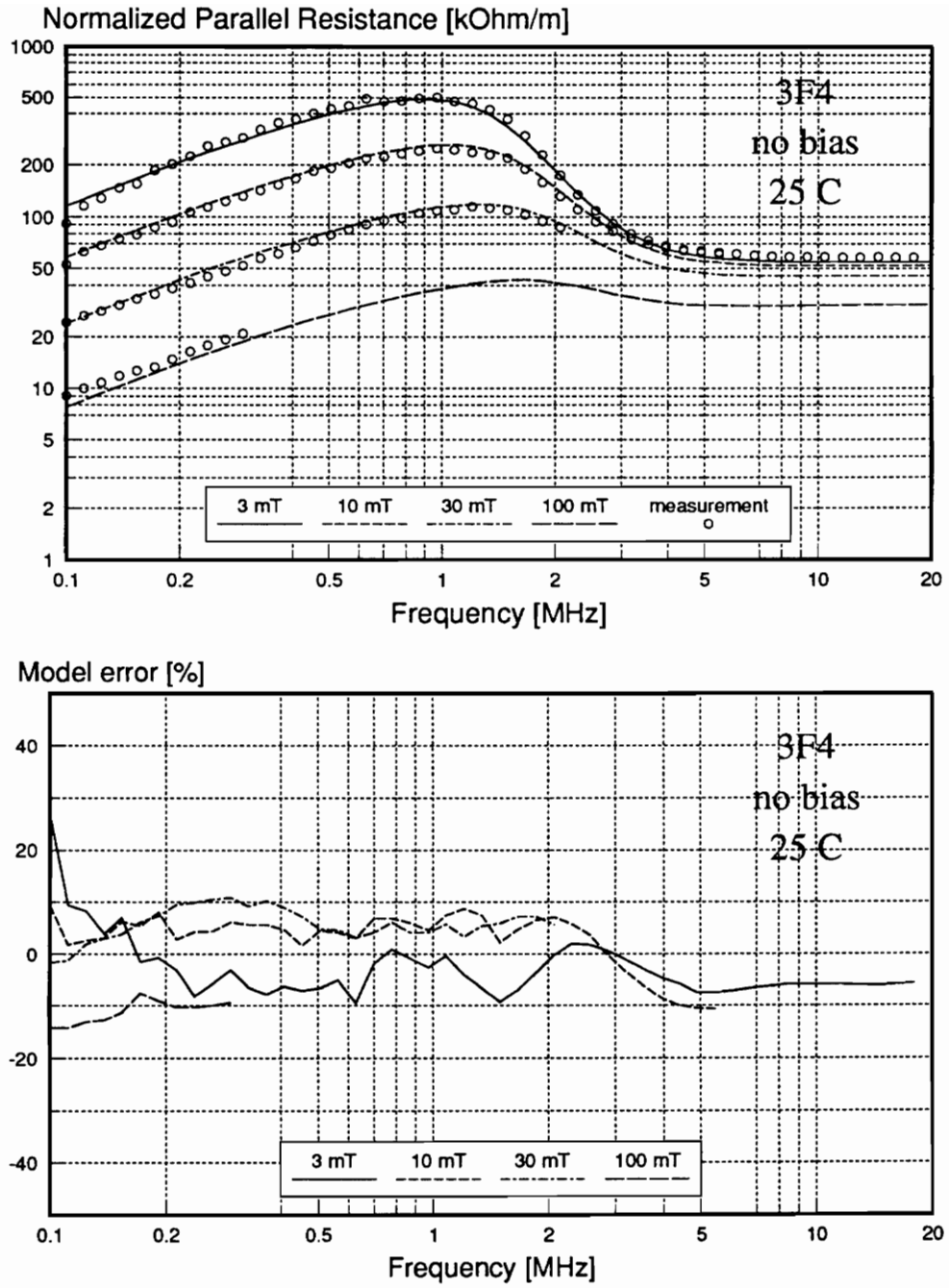

Fig. 3.31. Normalized parallel resistance and model error for 3F4 ferrite with no static bias and at 25 ℃ temperature.

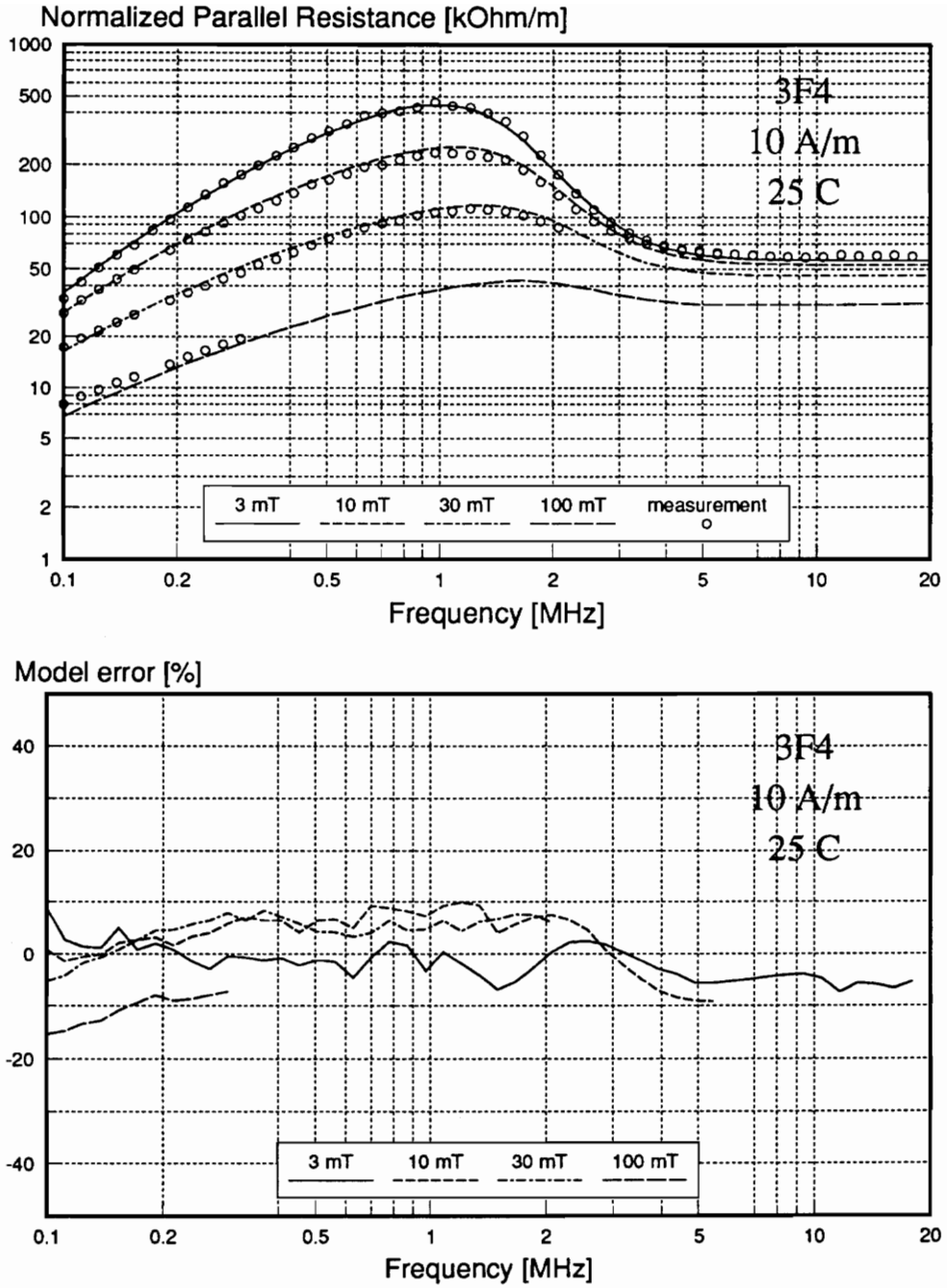

Fig. 3.32. Normalized parallel resistance and model error for 3F4 ferrite at 10 A/m static bias and at 25 ℃ temperature.

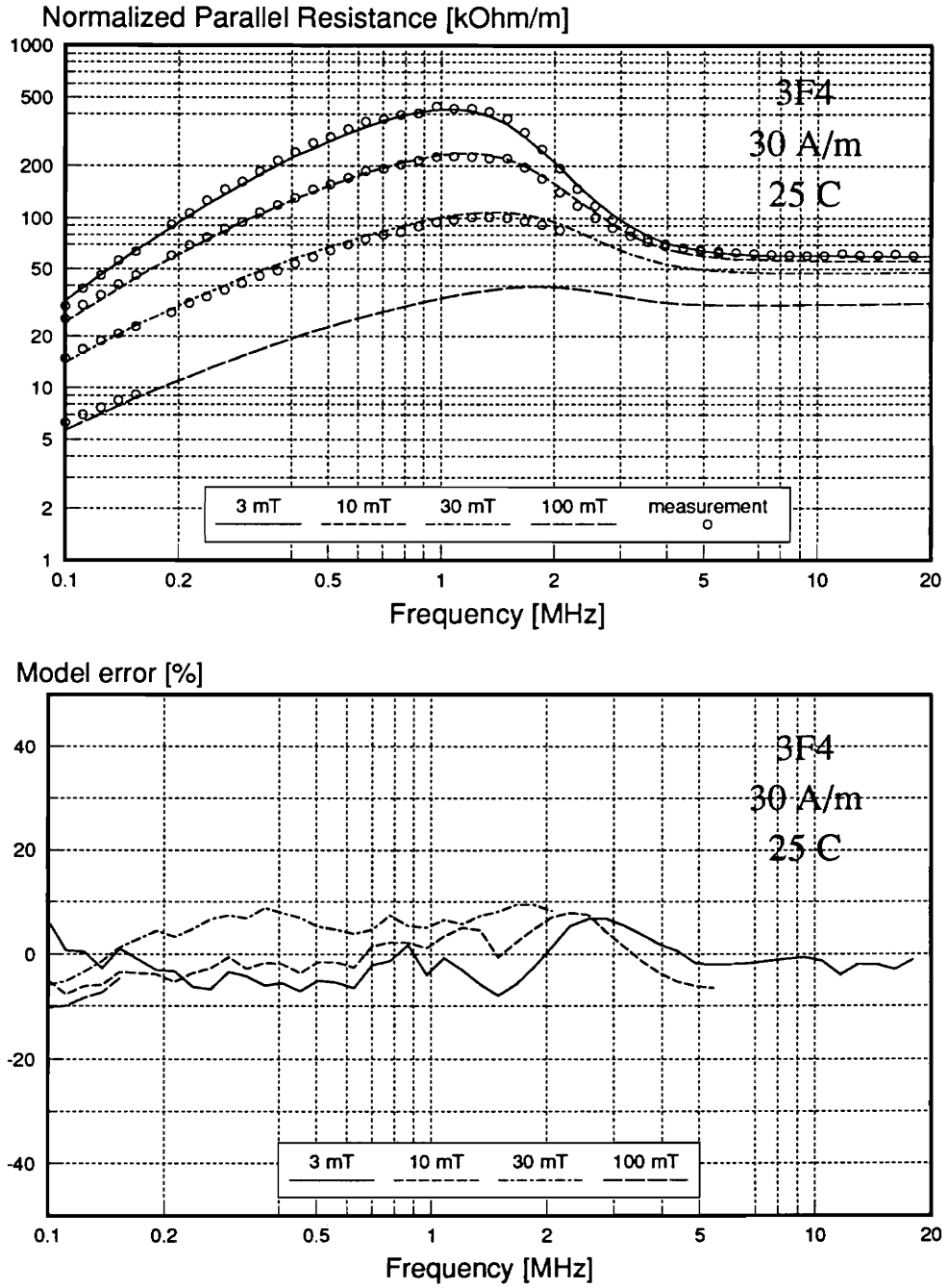

Fig. 3.33. Normalized parallel resistance and model error for 3F4 ferrite at 30 A/m static bias and at 25 ℃ temperature.

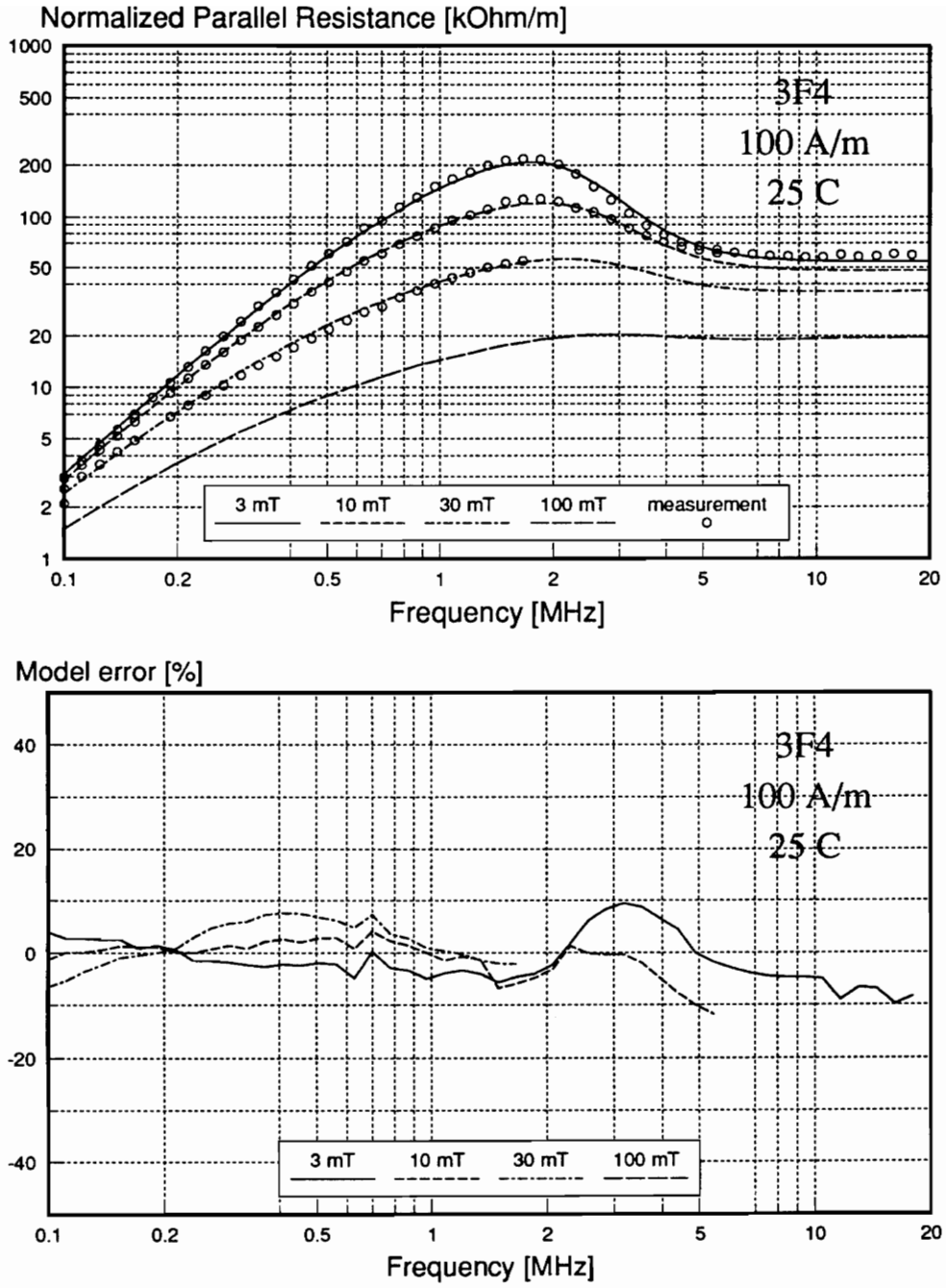

Fig. 3.34. Normalized parallel resistance and model error for 3F4 ferrite at 100 A/m static bias and at 25 ℃ temperature.

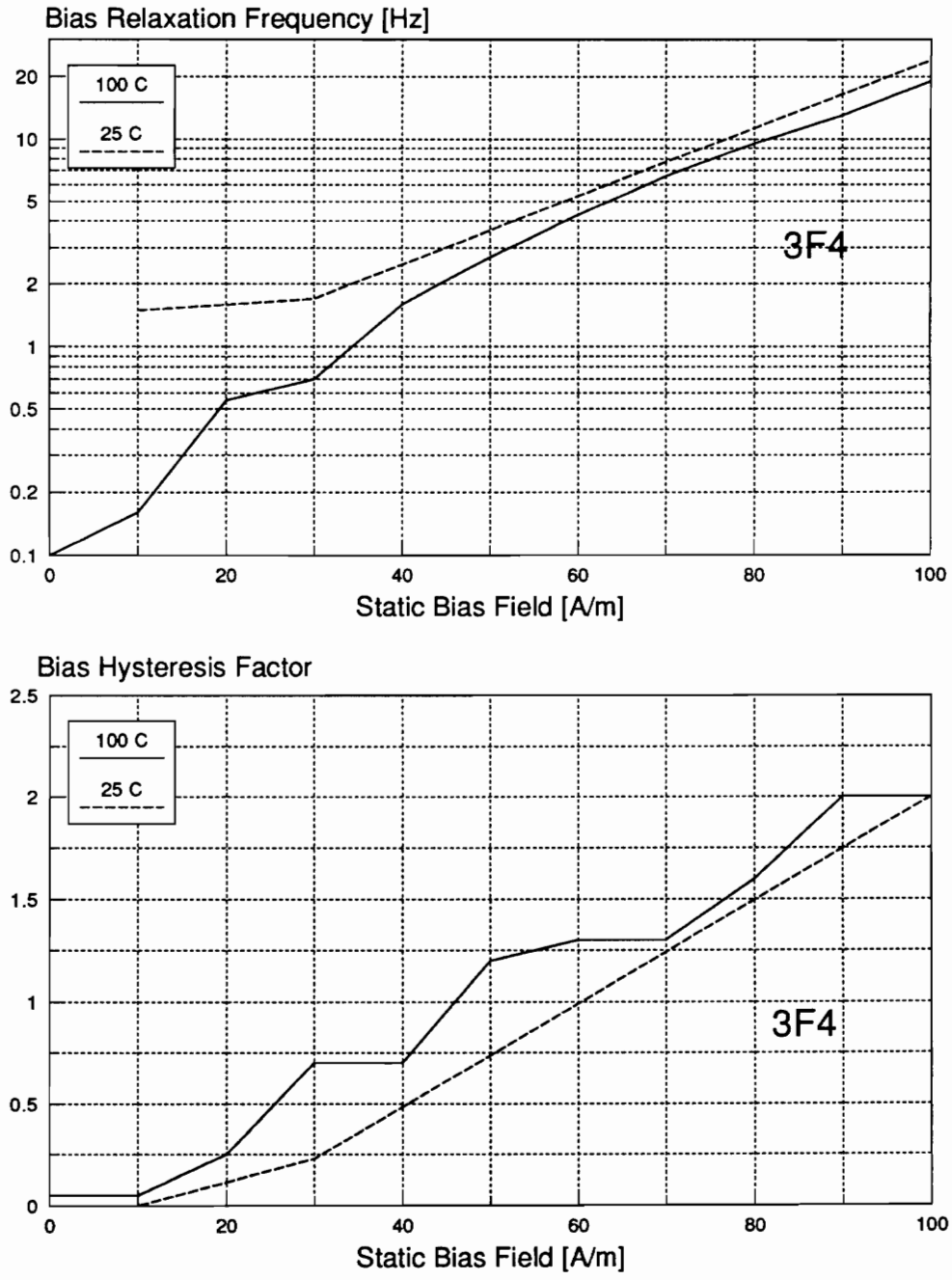

Fig. 3.35. Dependence of bias relaxation frequency, f_H, and bias hysteresis factor, η_H, on the static bias field in a 3F4 ferrite.

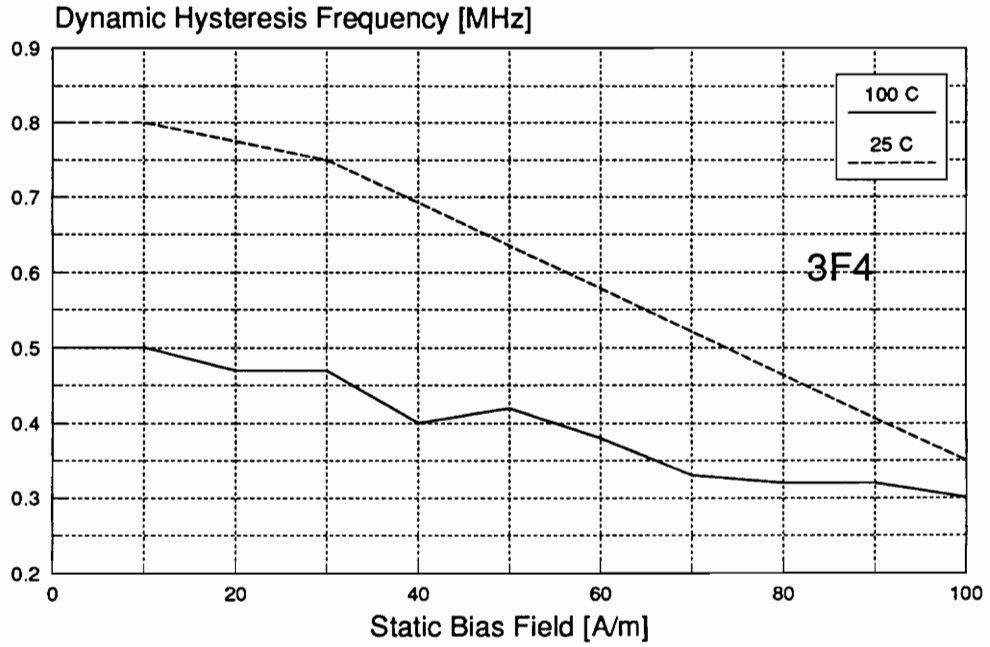

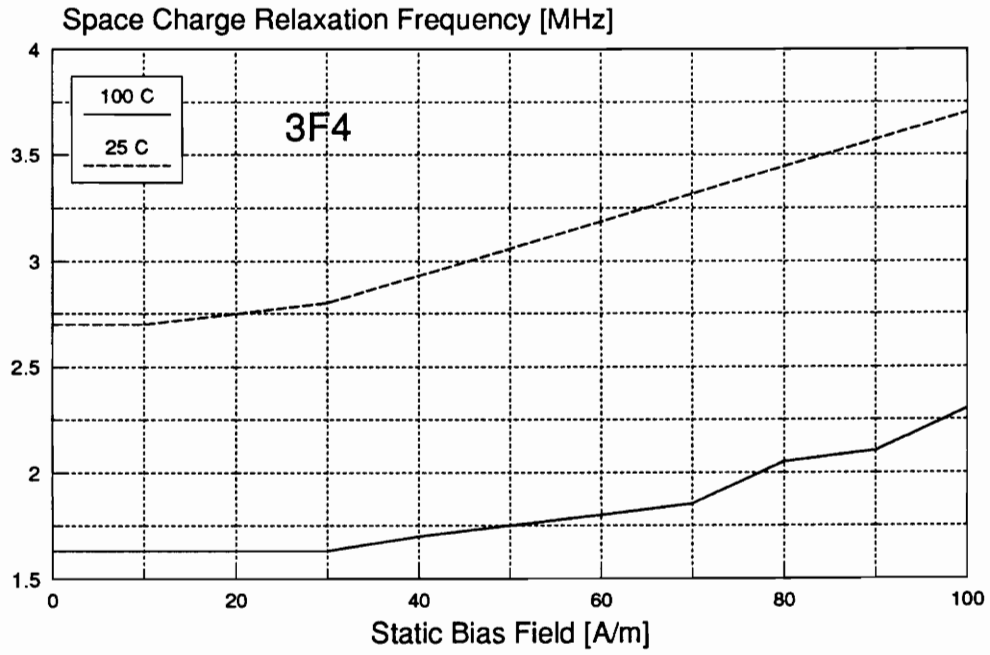

Fig. 3.36. Dependence of space charge parameters on the static bias field in a 3F4 ferrite.

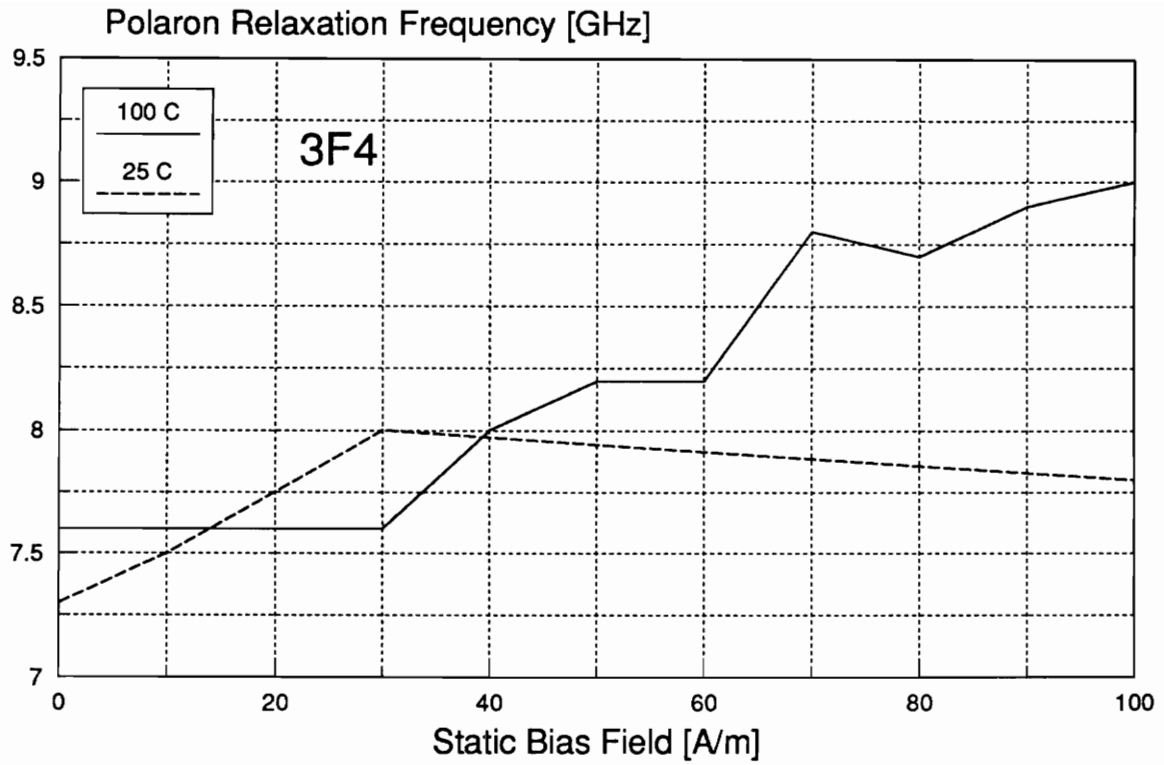

Fig. 3.37. Dependence of a polaron relaxation frequency on the static bias field in a 3F4 ferrite.

At intermediate frequencies the peak due to the space charge effect appears. Under strong bias and small ac flux density at low frequencies, the normalized parallel resistance is proportional to f^2 due to the heavily damped ferromagnetic resonance, as shown in Fig. 3.30. A similar theoretical f^2 dependence is shown in Fig. 3.13. Eddy current losses are negligible due to a high resistivity of this ferrite (10 Ωm [252]) and a small size of the test specimen. The following model combines hysteresis loss (3.52), thermal after-effect (3.55), ferromagnetic resonance loss (3.58), and the domain wall relaxation due to magnetoelectric effect (3.94):

$$R_p = \frac{1}{1/R_{ph} + 1/R_{pr} + 1/R_{pME}} = \frac{2\pi\mu_0}{\eta_B(\hat{B} + B_F)(1 + f/f_B + \eta_H)/f + f_H/f^2 + 1/f_w[1 + (f_c/f)^2]} \quad (3.96)$$

Since Rayleigh hysteresis model is used the model is expected to introduce some error at high flux densities. An additional term, f/f_B, is necessary to more accurately account for the frequency-dependent hysteresis loss, perhaps due to shrinking of the thickness of domain walls when the crystal anisotropy increases due to a magnetoelectric effect at high frequencies.

Two additional terms are necessary to account for an increased residual loss and a hysteresis loss under ac excitation with a static bias magnetic field. The increase in the hysteresis loss represented by bias factor, η_H, can be explained by an increase in the coercive force due to pinning domain walls to grain boundaries enhanced by the static bias field. The f^2 dependence of the additional residual loss factor can be interpreted as a loss contribution from a heavily damped spin relaxation of rotating domains. The stronger the bias field, the more domain walls are pinned to grain boundaries or extinct, increasing contribution from rotational permeability and loss. Concurrently the spin damping increases above a certain critical applied bias field [253]. Figure 3.35 shows the bias relaxation frequency, f_H, and the bias hysteresis factor, η_H. The dynamic hysteresis frequency, f_B, and the space charge relaxation frequency, f_c, are shown in Fig. 3.36. The polaron relaxation frequency is shown in Fig. 3.37.

The bias relaxation frequency, f_H, which determines additional residual losses due to static magnetic bias field, exhibits a very strong dependence on the bias field. For that reason it is

plotted in semi-logarithmic scale, and it appears as an almost straight line. Therefore, the residual loss due to static bias field exponentially increases with the bias field. It also slightly decreases with temperature. The bias hysteresis factor, η_H, is a measure by what amount the hysteresis loss increases under static magnetic bias. At small bias, η_H is equal to zero. It is proportional to the bias field above a certain critical field and slightly depends on temperature. The dynamic hysteresis frequency, f_B, is the frequency above which the frequency-dependent hysteresis loss has a significant contribution. It decreases with bias field when more domain walls interact with grain boundaries where stronger electric field due to a space charge reduces domain wall thickness and thus increases loss. At higher temperature, the crystal anisotropy decreases, and domain walls are thicker. A strong decrease of this loss at higher temperature proves that this loss is related to a change of domain wall thickness. The space charge relaxation frequency, f_c, increases slightly with a magnetic bias. The only field related parameter governing this dependence is the energy barrier due to the magnetoelectric effect, q_E, which must depend on the static magnetic field. The space charge relaxation frequency, f_c, decreases with increasing temperature according to the Eq. (3.90). The polaron relaxation frequency, f_p, slightly increases with temperature in agreement with the Eq. (3.90) because above 25°C the activation energy of polarons due to Fe^{2+} ions is comparable with kT [254]. According to the governing equation, the value of f_p should decrease slightly with an applied bias field due to increase in q_E, but in the experimental data the bias dependence is inconclusive.

3.5.2 Nickel-Zinc Ferrite

Nickel-zinc ferrites are used only at high frequencies. Currently, these ferrites are not manufactured for applications in power electronics, but they will be necessary for resonant power supplies operating in the megahertz range. For that reason the model had to be verified on an existing material not specifically designed for power applications. The modeling of loss char-

acteristics of nickel-zinc ferrite was performed using 4C4 material provided by Philips Components. The tested core (P/N 1041T060) had a form of a toroid with an outer diameter of 5.88 mm, an inner diameter of 3.01 mm, and a height of 1.56 mm. The winding consisted of 13 turns of AWG#24 wire. The core was measured at six flux density levels of 0.3, 1, 3, 10, 30, and 50 mT, at 60 discrete frequencies distributed exponentially in the frequency range from 100 kHz to 100 MHz at 25°C. The errors due to parasitic inductance and capacitance of the interconnections prevented measurements in the temperature chamber. Other test conditions were similar to those when MnZn ferrite was tested. The measured and fitted data, and the model error are shown in Figs. 3.38-3.44 at static bias magnetic field of 0, 50, 100, 200, 300, 400, and 500 A/m, respectively, and at 25°C. In an absence of bias, the hysteresis losses dominate at frequencies below 10 MHz, while above 20 MHz residual losses prevail. The combination of both appears at intermediate frequencies, but the transition is sharper than in the tested MnZn ferrite. However, under a strong bias and a small ac flux density, the normalized parallel resistance is proportional to f^2, similarly to MnZn ferrite.

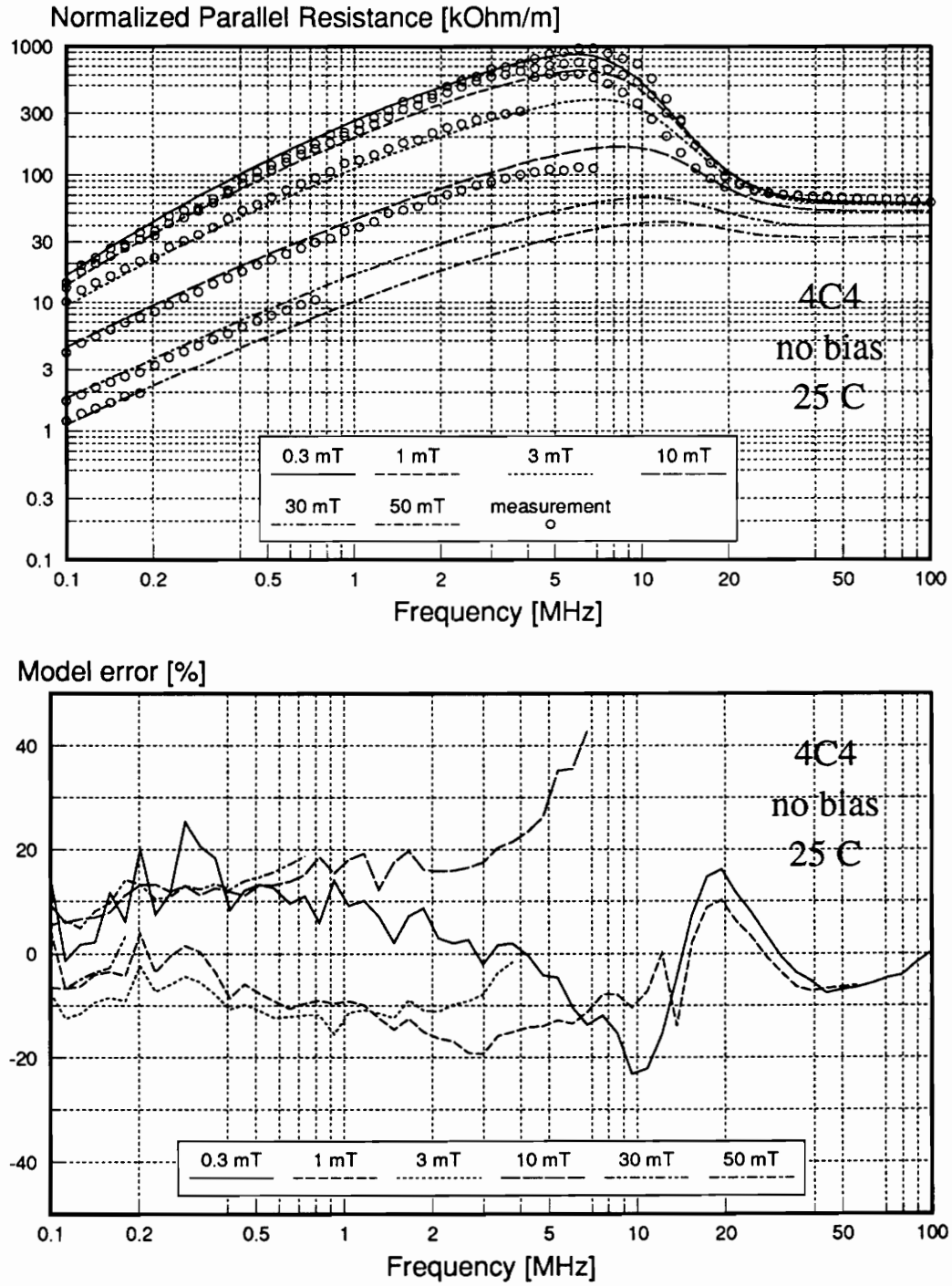

Fig. 3.38. Normalized parallel resistance and model error for 4C4 ferrite with no bias and at 25 ℃ temperature.

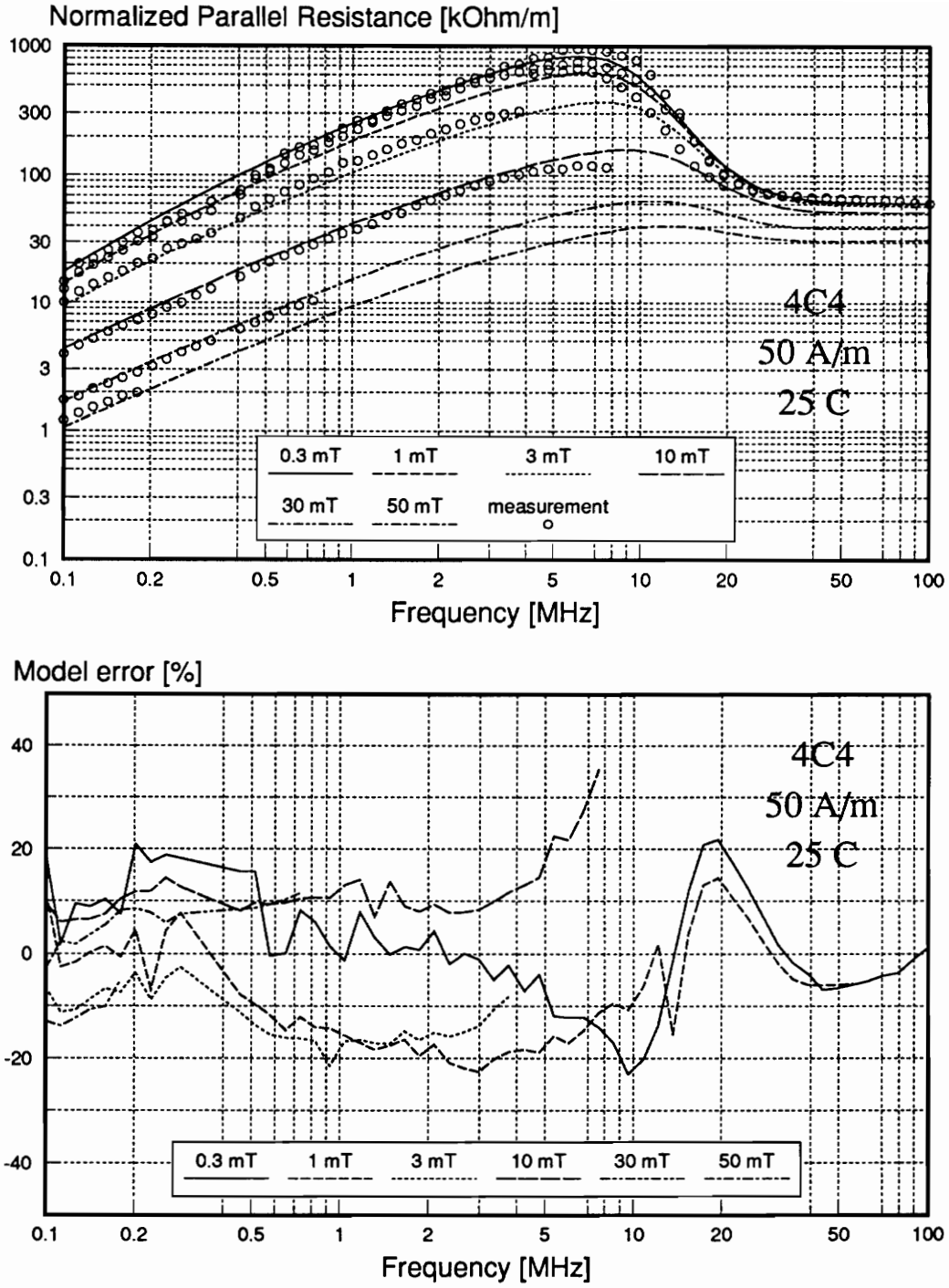

Fig. 3.39. Normalized parallel resistance and model error for 4C4 ferrite at 50 A/m static bias and at 25 ℃ temperature.

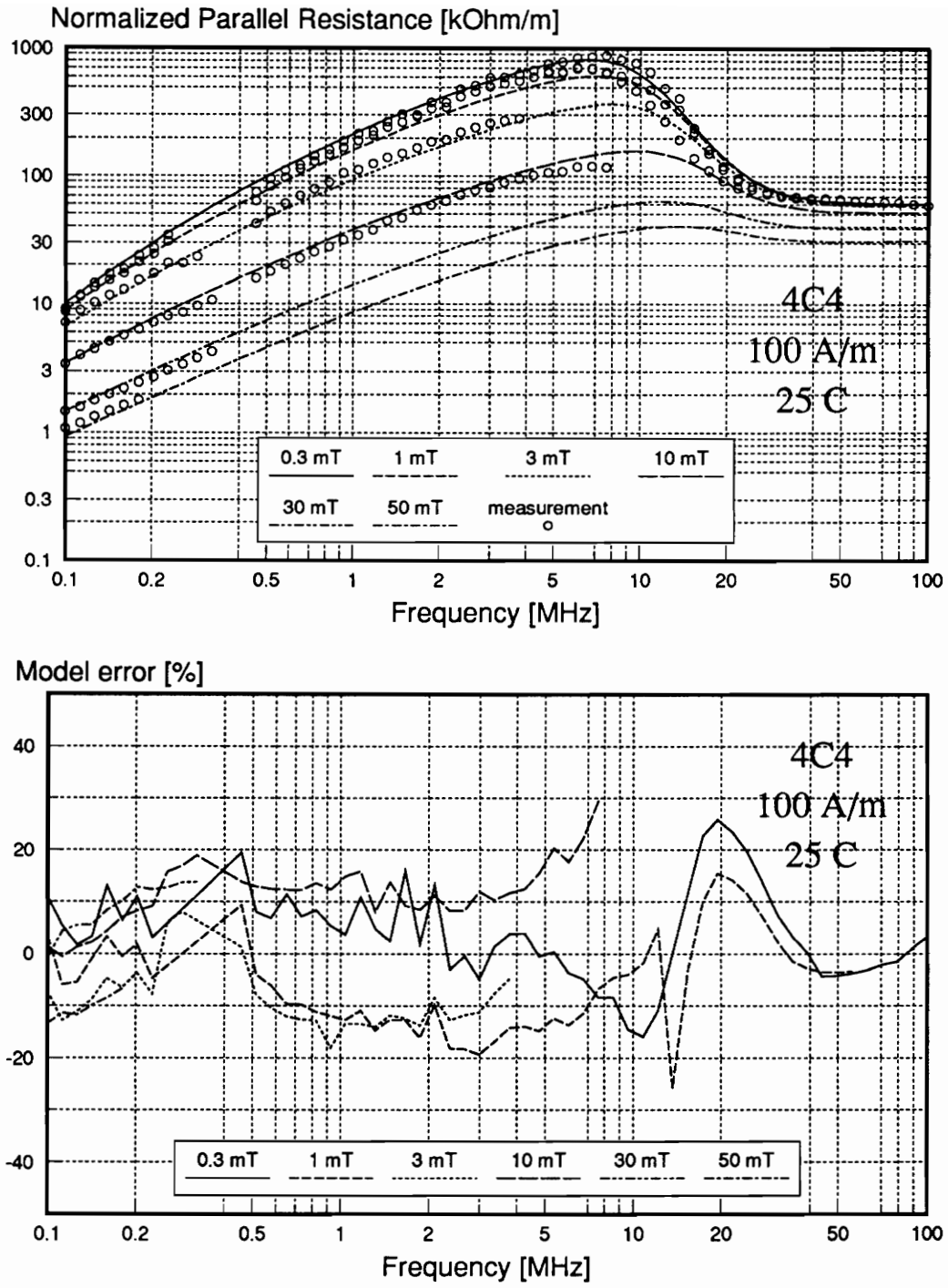

Fig. 3.40. Normalized parallel resistance and model error for 4C4 ferrite at 100 A/m static bias and at 25 ℃ temperature.

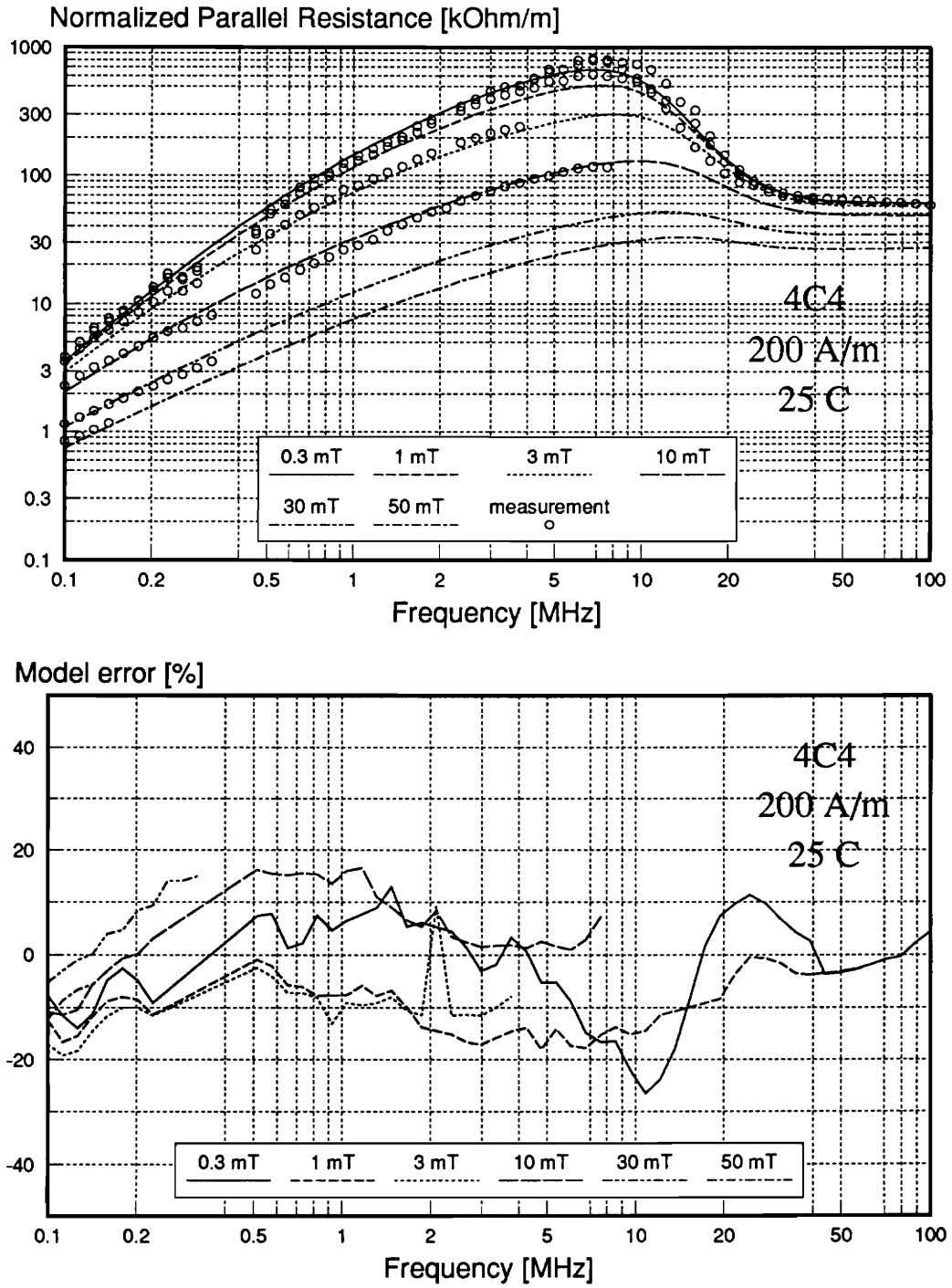

Fig. 3.41. Normalized parallel resistance and model error for 4C4 ferrite at 200 A/m static bias and at 25 ℃ temperature.

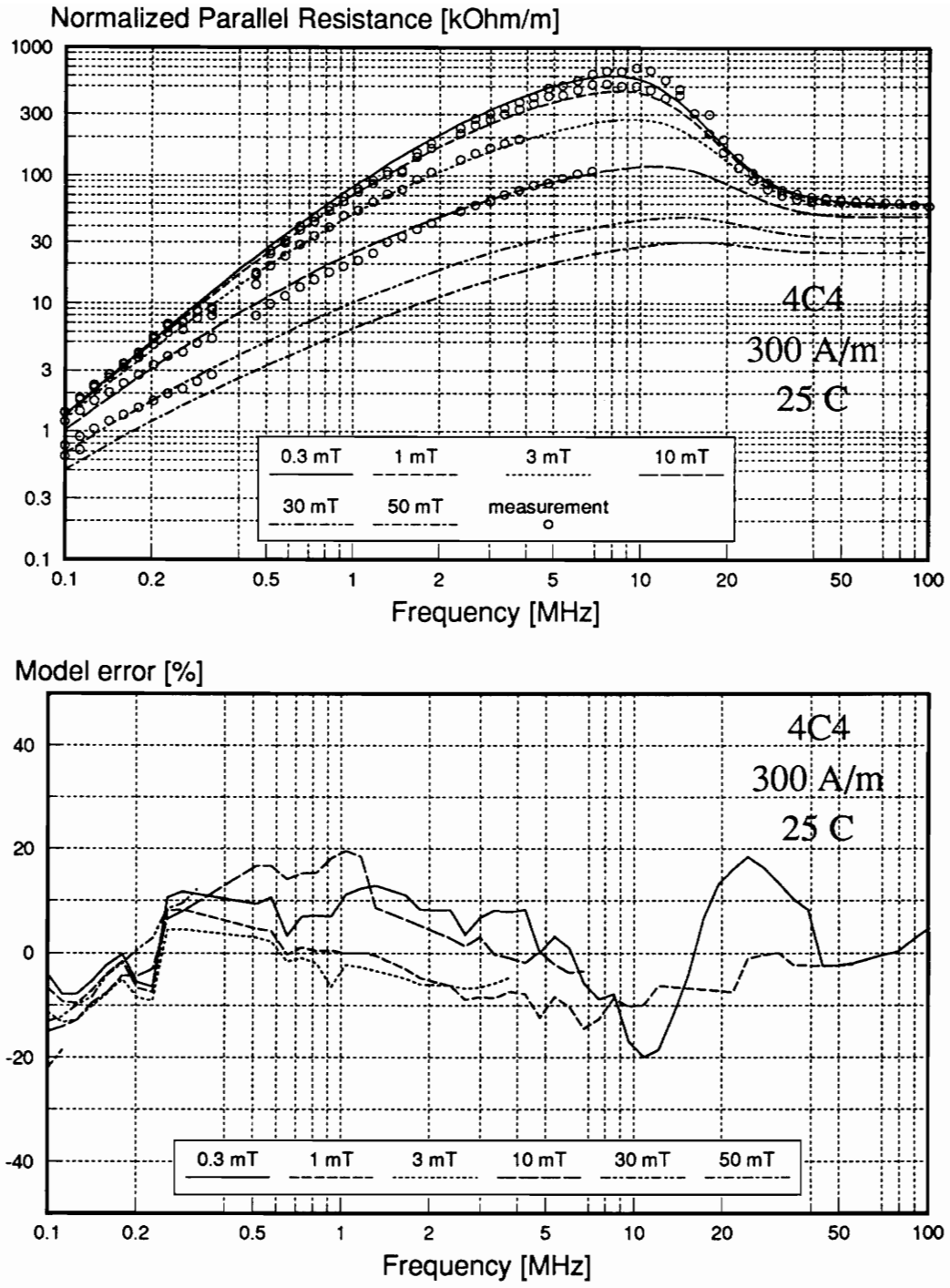

Fig. 3.42. Normalized parallel resistance and model error for 4C4 ferrite at 300 A/m static bias and at 25 ℃ temperature.

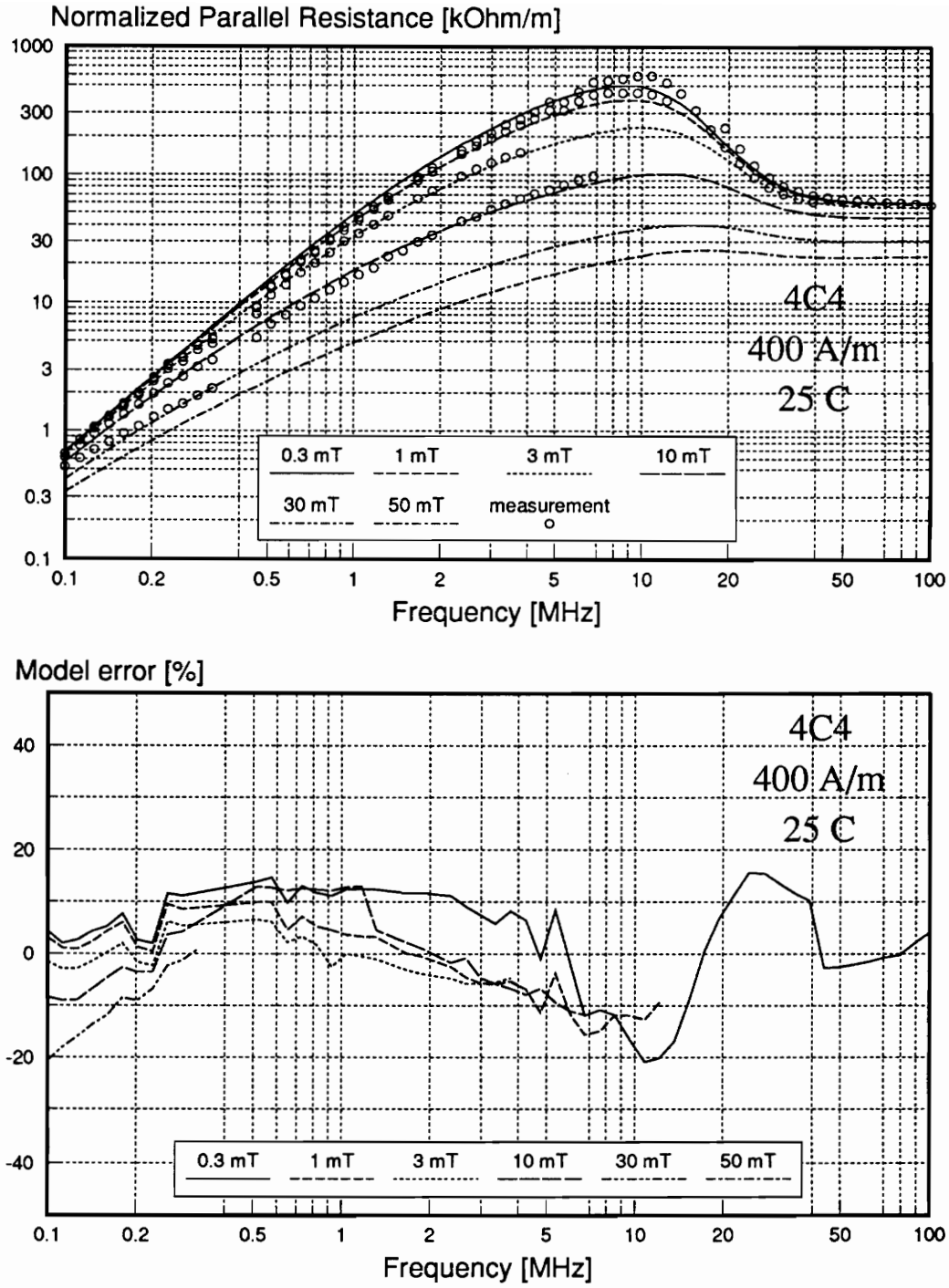

Fig. 3.43. Normalized parallel resistance and model error for 4C4 ferrite at 400 A/m static bias and at 25 ℃ temperature.

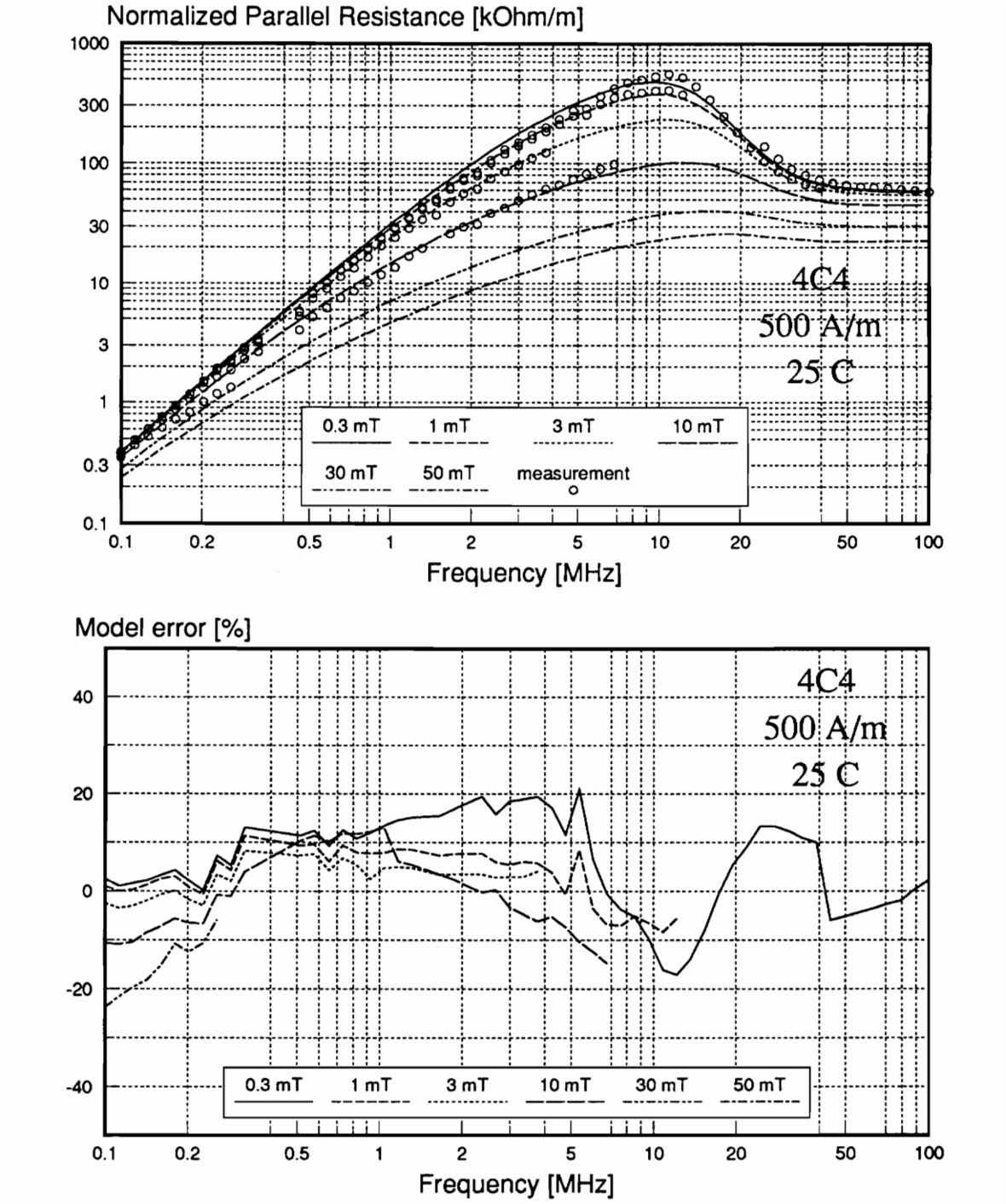

Fig. 3.44. Normalized parallel resistance and model error for 4C4 ferrite at 500 A/m static bias and at 25 ℃ temperature.

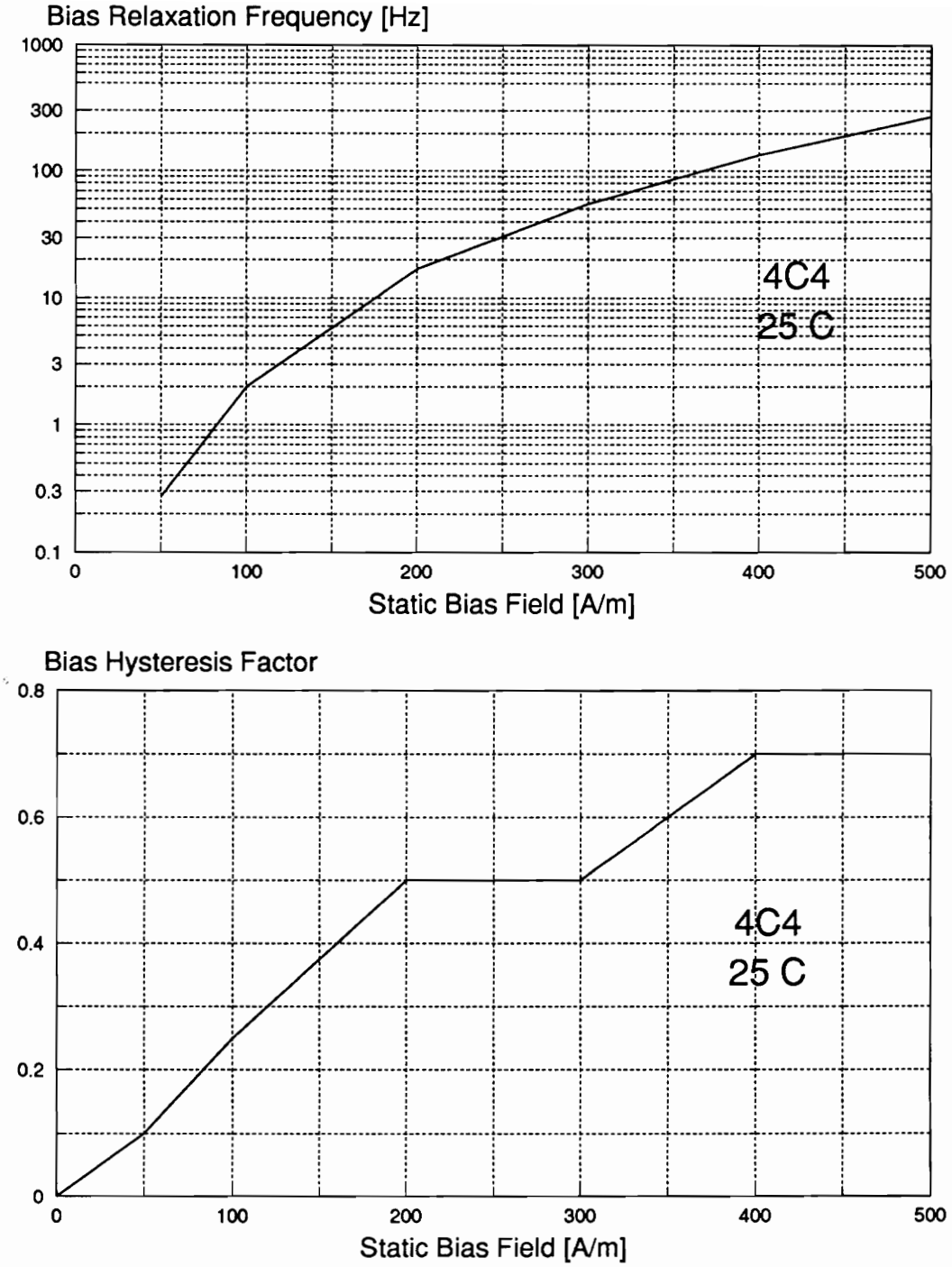

Fig. 3.45. Dependence of bias parameters on the static bias field in a 4C4 ferrite.

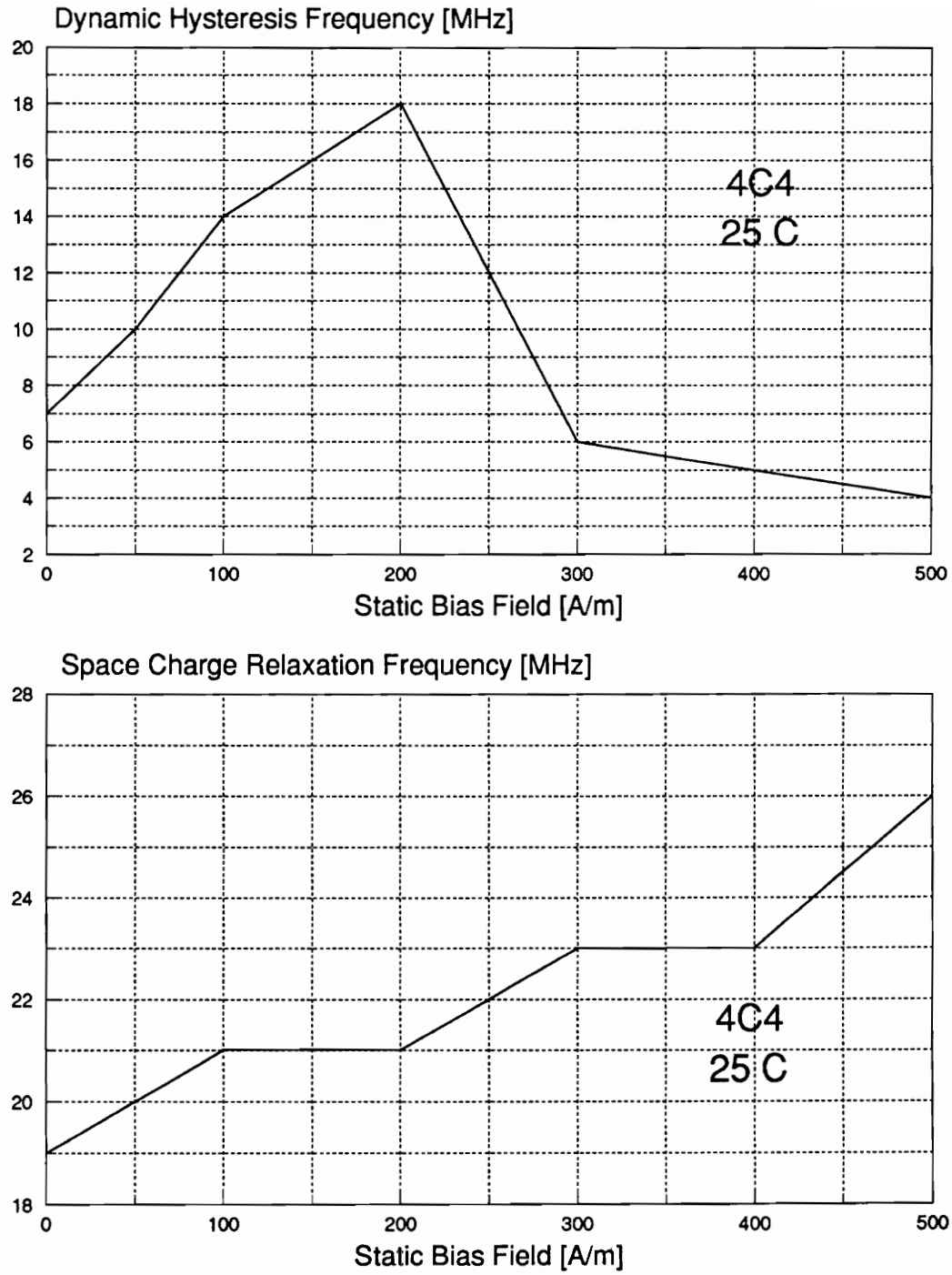

Fig. 3.46. Dependence of space charge parameters on the static bias field in a 4C4 ferrite.

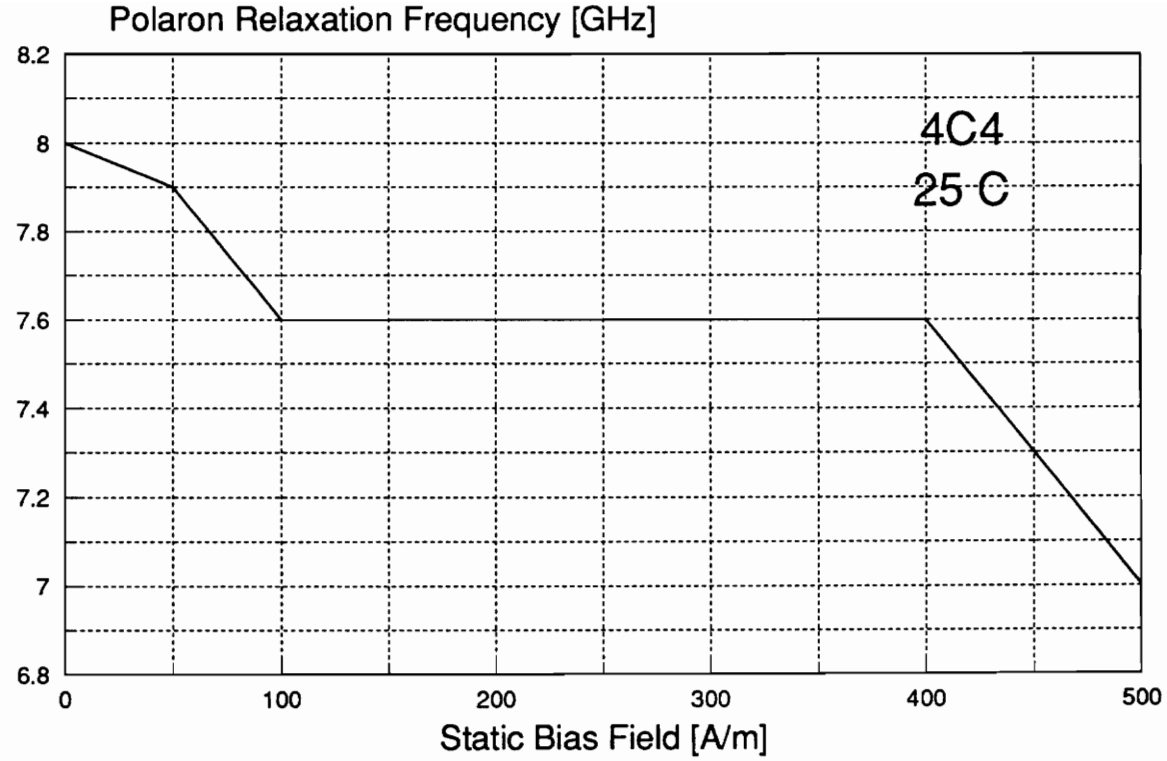

Fig. 3.47. Dependence of a polaron relaxation frequency on the static bias field in a 4C4 ferrite.

Eddy current losses are neglected due to a very high resistivity of this ferrite (10^5 Ωm) and a small size of the test specimen. The model used for data fitting is the same as for MnZn ferrite. The model parameters are shown in Figs. 3.45, 3.46, and 3.47.

In a nickel-zinc ferrite, the bias relaxation frequency, f_H, similarly depends on the applied static bias but does not obey the exponential law at small fields. The difference can be attributed to a stronger anisotropy field in NiZn ferrite which is superimposed on the applied field. The bias hysteresis factor is similar to that of MnZn ferrite, indicating a similar hysteresis mechanisms at low frequencies. However, the dynamic hysteresis frequency has a different shape than that for MnZn ferrite, which can be attributed to a simplicity of the model of dynamic hysteresis, leading to an error over 40% at 10 mT and 7 MHz. More detailed analysis and better model are necessary, especially for NiZn ferrite. The space charge relaxation frequency increases with a bias field similarly to the MnZn ferrite due to the magnetoelectric effect. The polaron relaxation frequency slightly decreases with an increase of a static bias field as predicted from the magnetoelectric effect.

3.5.3 Manganese-Magnesium Ferrite

The manganese-magnesium ferrite has a square hysteresis loop. For that reason it was used in computer memories in 1960s. Today it enjoys revival in magnetic amplifiers in multiple-output switched-mode power supplies. The modeling of loss characteristics of nickel-zinc ferrite was performed using 3R1 material provided by Philips Components. The tested core had a form of a toroid with an outer diameter of 9.37 mm, an inner diameter of 5.36 mm, and a height of 3.38 mm. The winding consisted of 5 turns of AWG#17 wire. The core was measured at six flux density levels of 0.1, 0.3, 1, 3, 10, and 30 mT, at 60 discrete frequencies distributed exponentially in the frequency range from 100 kHz to 100 MHz at 25°C. The errors

due to parasitic inductance and capacitance of the interconnections prevented measurements in the temperature chamber. Other test conditions were similar to those when MnZn ferrite was tested. The following model based on Eqs. (3.5), (3.29), (3.58), (3.68), and (3.96) was used to fit the experimental data:

$$\bar{\mu} = 1 + \frac{1}{1/\chi_w + j[\eta_B(\hat{B} + B_F)(1 + f/f_B + \eta_H) + f_H/f + f/f_w]} + \frac{1}{1/\chi_p + jf/f_p} + \frac{1}{1/\chi_r + jf/f_r}, \tag{3.97}$$

where

χ_w - domain wall susceptibility,

χ_p - domain rotation susceptibility due to polarons,

f_p - polaron relaxation frequency,

χ_r - domain rotation susceptibility due to spins, and

f_r - spin relaxation frequency.

The measured and fitted data, and the fitting error are shown in Figs. 3.48 and 3.49 at static bias magnetic field of 0 and 100 A/m, respectively, and at 25°C. In an absence of a bias field, the following types of losses dominate at respective frequencies: the hysteresis losses below 1 MHz, residual losses due to polaron relaxation between 2 and 20 MHz, and ferromagnetic resonance above 30 MHz. Combinations of losses appear at intermediate frequencies, but there is no peak in the characteristics. A chemical composition of this ferrite [255] suggests that no Fe^{2+} ions are present. However, loss characteristics show that there is a polaron relaxation at frequencies between 2 and 20 MHz, but without a space charge effect. This could be explained by an electron reaction between neighboring atoms in a spinel lattice [256, 257, 258, 259]:

$$Mn^{2+} + Fe^{3+} \leftrightarrow Mn^{3+} + Fe^{2+} \quad . \tag{3.98}$$

Since this process has the activation energy much higher compared to polaron associated with the Fe^{2+}-Fe^{3+} ion pair, the intrinsic conductivity and space charge relaxation frequency are much lower than in MnZn or NiZn ferrites with Fe^{2+} content. Therefore, the space charge effect occurs in a frequency range dominated by hysteresis loss and residual loss due to a thermal after-effect, so the space charge has only a minor influence on losses. Under a strong

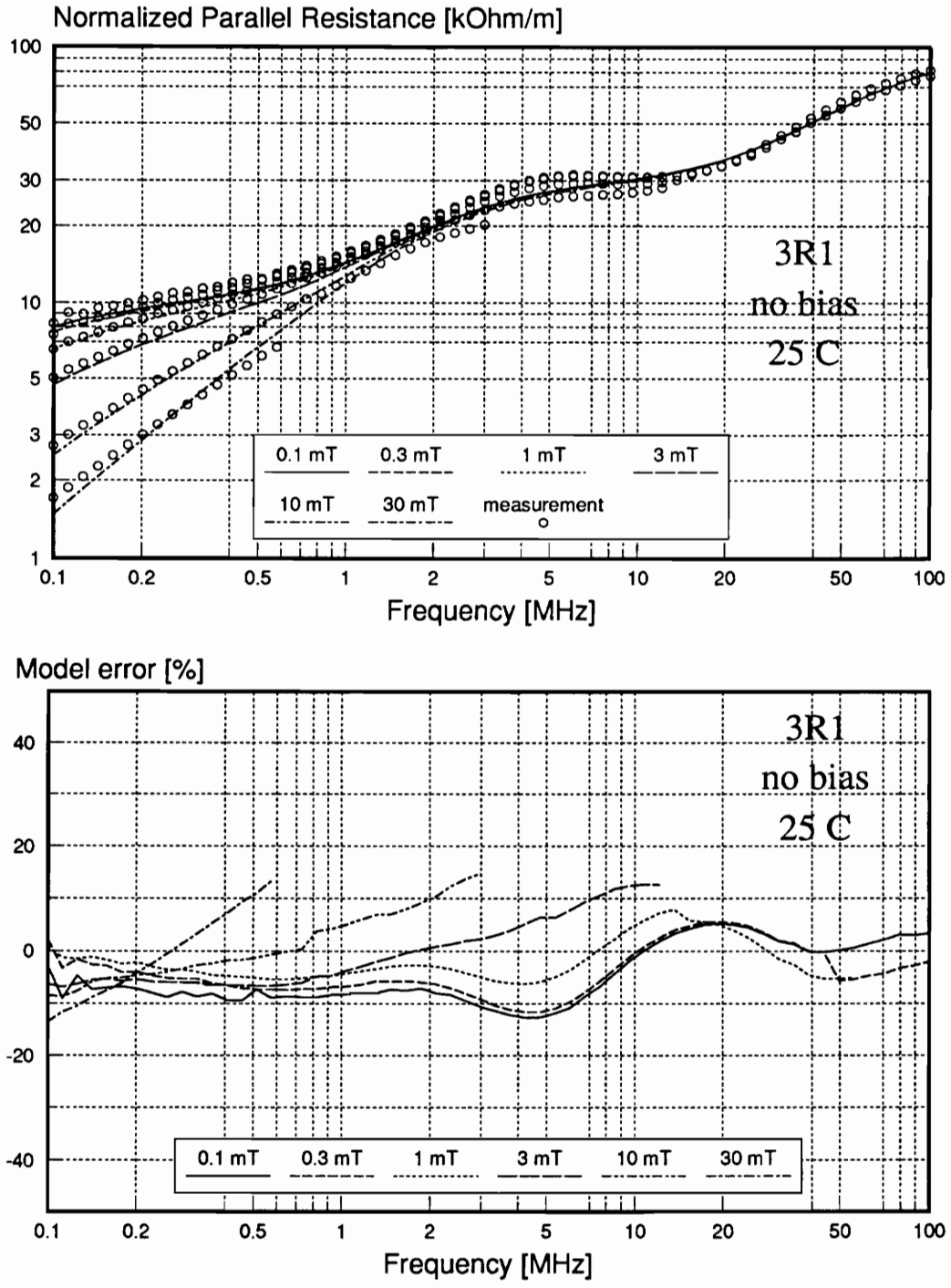

Fig. 3.48. Normalized parallel resistance and model error for 3R1 ferrite with no static bias and at 25 ℃ temperature.

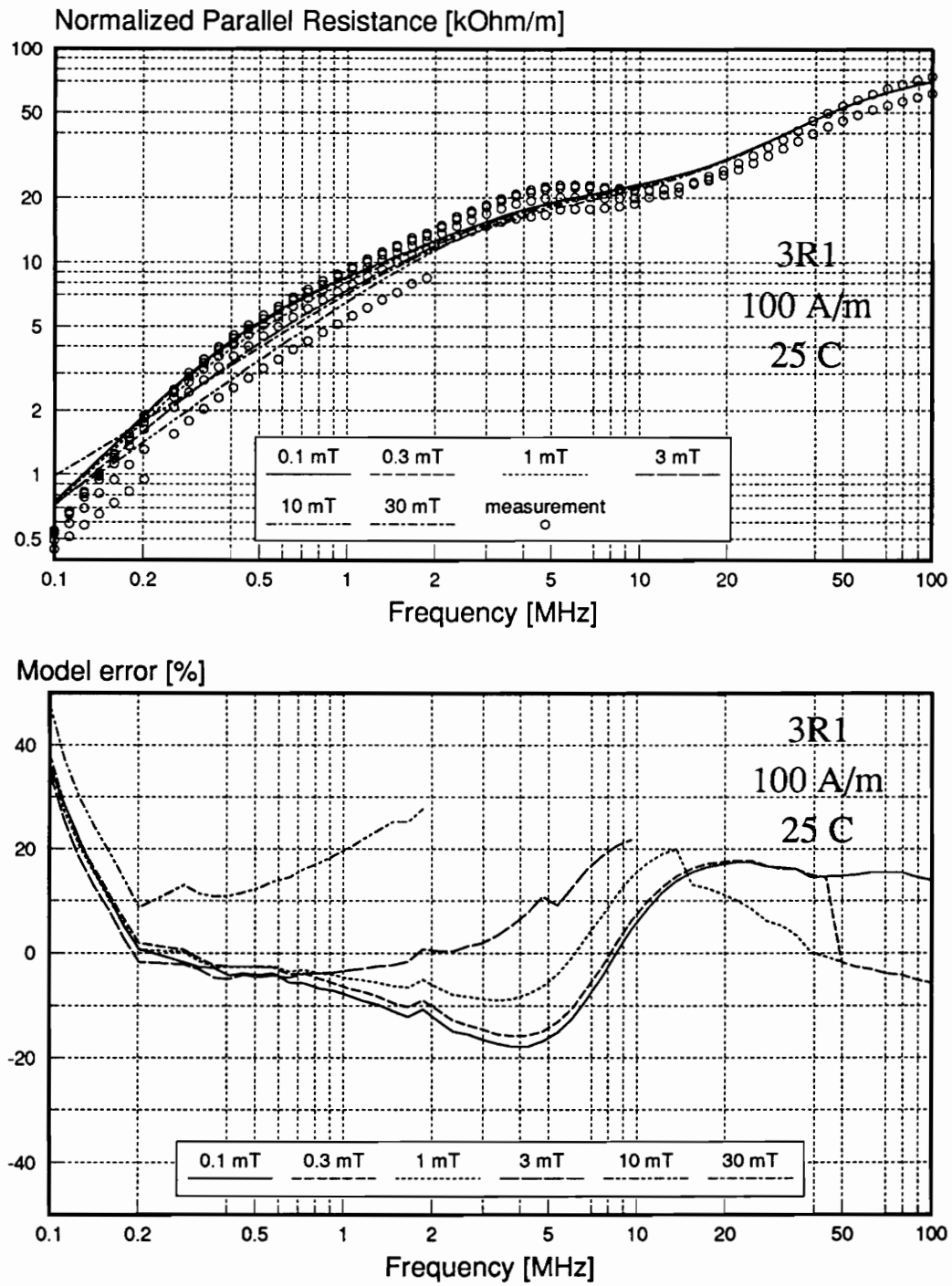

Fig. 3.49. Normalized parallel resistance and model error for 3R1 ferrite at 100 A/m static bias and at 25 ℃ temperature.

Table 3.1. Model parameters for 3R1 MnMg ferrite vs. bias field

H [A/m]	f_H [Hz]	η_H	f_w [GHz]	f_p [GHz]	f_r [GHz]	χ_p
0	0	0	0.8	2.4	9	600
100	200	3	0.8	1.4	8	300

bias and a small ac flux density, the normalized parallel resistance is proportional to f^2, similarly to MnZn and NiZn ferrite due to the domain rotation losses. Eddy current losses are neglected due to a very high resistivity of this ferrite and a small size of the test specimen. The model used for data fitting is different from the models used for MnZn and NiZn ferrites because of an additional contribution of domain rotation loss and an absence of the space charge effect. The fitting parameters are shown in Table 3.1.

Other parameters do not depend on applied bias field: $\chi_w = 2000$, $\chi_r = 80$, $B_F = 1$ mT, $\eta_B = 45 \cdot 10^{-3}$ T^{-1}. The wall motion in square-loop ferrites was analyzed in detail by Knowles [260, 261, 262, 263, 264, 265, 266], who concluded that it is essentially governed by a porosity of the grain and an energy of the domain wall. Therefore the wall relaxation frequency, f_w, depends mainly on the crystalline anisotropy and does not change with an applied field. The polaron relaxation frequency, f_p, and spin relaxation frequency, f_r, decrease due to a strong spin damping in response to the static magnetic bias field.

3.6 Magnetoelastic Resonances in Ferrites

The residual loss due to magnetostriction is not important in most power transformers and inductors employing ferrite. In fact, metallic magnetic materials show greater magnetostriction, particularly in amorphous cores [267, 268, 269, 270]. There are circumstances when the magnetomechanical resonance may cause a failure of not only the magnetic component but the rest of the circuit. Even if the circuit utilizes core at high frequency not coinciding with a resonance, a low frequency magnetoelastic resonance may influence transient response or cause an instability of a closed loop system. The greatest risk of instability occurs in variable frequency circuits like self-oscillating and frequency modulated power converters. The following sections contain loss characteristics measured with an extreme resolution up to 10^4 data points

per curve in order to reveal the most narrow magnetomechanical resonances due to magnetostriction of ferrite materials. Such narrow resonances are possible because of a very high elastic quality of ferrite cores.

3.6.1 Influence of the Core Material

Two grades of ferrites are tested: 4C4 (nickel-zinc, Philips P/N 213T050 with 6 turns of AWG#23) and 3F3 (manganese-zinc, Philips P/N 768T188 with 6 turns of AWG#18), both in the form of toroid. 3F3 material is also tested in the form of an EE core (Philips part no. 814E250 with 10 turns of AWG#23). The 4C4 ferrite is characterized at 10 mT ac flux density under different dc bias conditions. Bias current is applied through the impedance probe. The measured permeability and core loss of the 4C4 ferrite is shown in Fig. 3.50. Even without dc bias, the characteristics contain a large number of strong peaks, causing the core loss to increase up to thirty times more compared with the base line - contrary to the typical smooth curves given in the manufacturer data books. External dc bias field increases both the base line and the peaks of the core loss characteristics. In stronger fields, new peaks occur and some old ones disappear due to the change in the magnitude of the magnetostriction [271]. The largest peaks after a dc bias is applied increase core loss up to fifty times over the corresponding value before a dc bias is applied. The base line core loss doubles at the largest bias. After the bias is removed, the base line core loss remains permanently about 50% larger than the initial loss before the dc bias. The 4C4 ferrite is also tested under a strong high-frequency ac magnetic field. The permeability and core loss are plotted in Fig. 3.51. The first set of characteristics is obtained from a core never before exposed to the magnetic field. The core is measured with a flux density of 10 mT. The same test is repeated on the same core after it has been exposed to a magnetic field with peak flux density of 200 mT and frequency of 1 MHz. As shown in Fig.

3.52, when 4C4 ferrite is exposed to a strong high-frequency ac magnetic field, an increase in core loss, accompanied by a slight drop in the permeability, occurs similarly to the previous case when a dc field is applied.

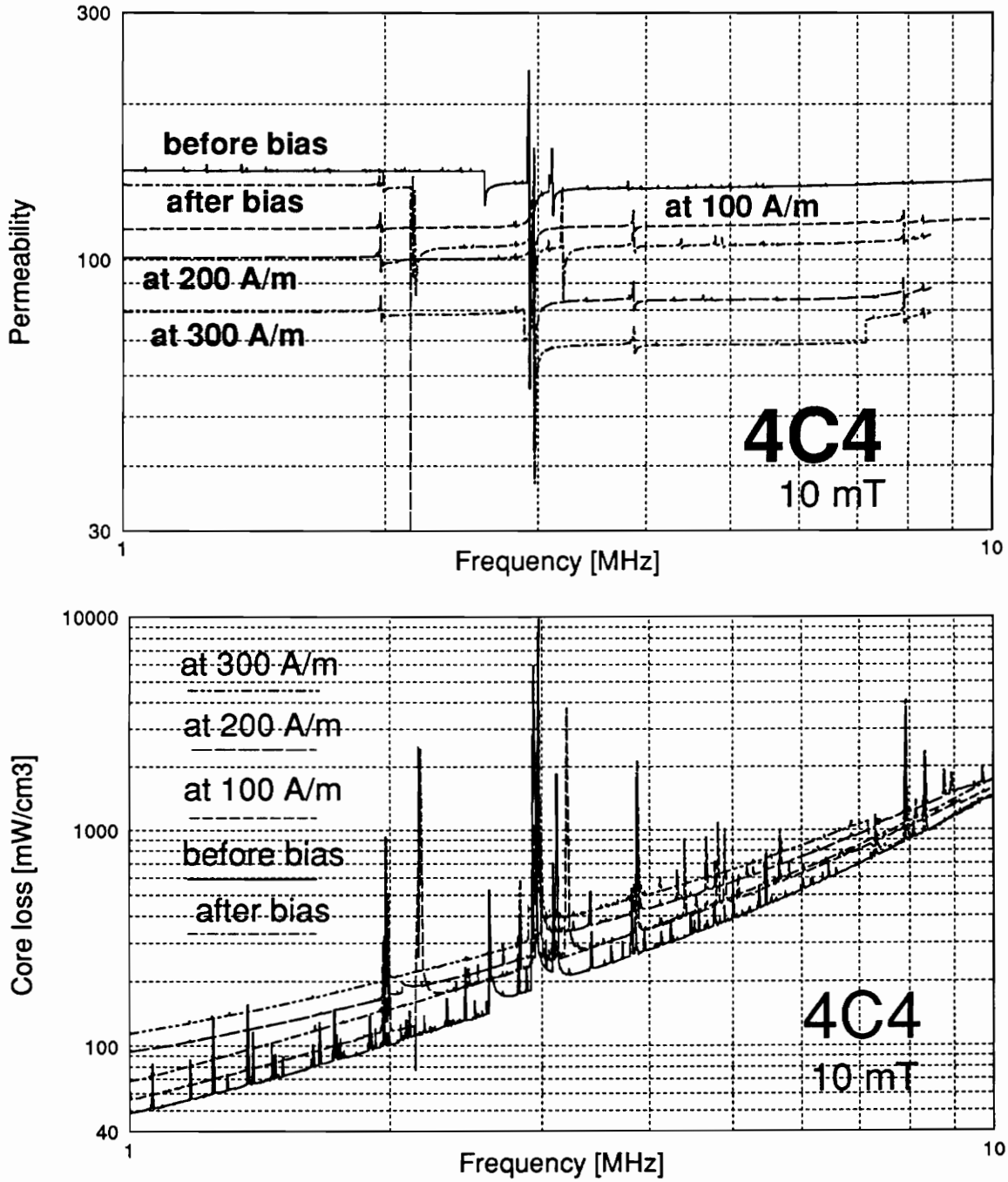

Fig. 3.50. Influence of static bias on magnetoelastic resonances in 4C4 ferrite at 10 mT ac flux density.

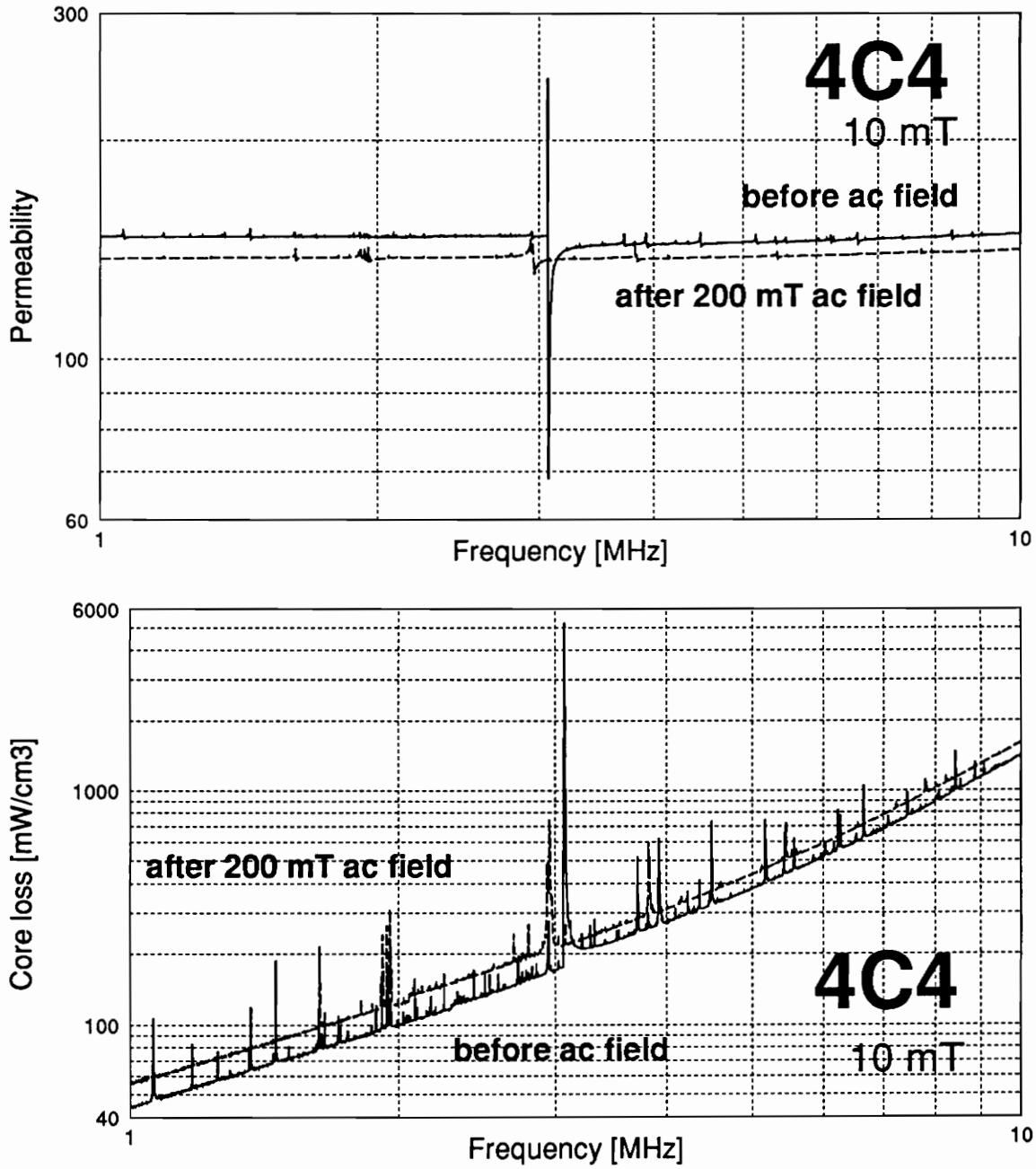

Fig. 3.51. Influence of demagnetization on magnetoelastic resonances in 4C4 ferrite at 10 mT ac flux density. The plots show permeability and core loss before and after treatment with 200 mT, 1 MHz magnetic field.

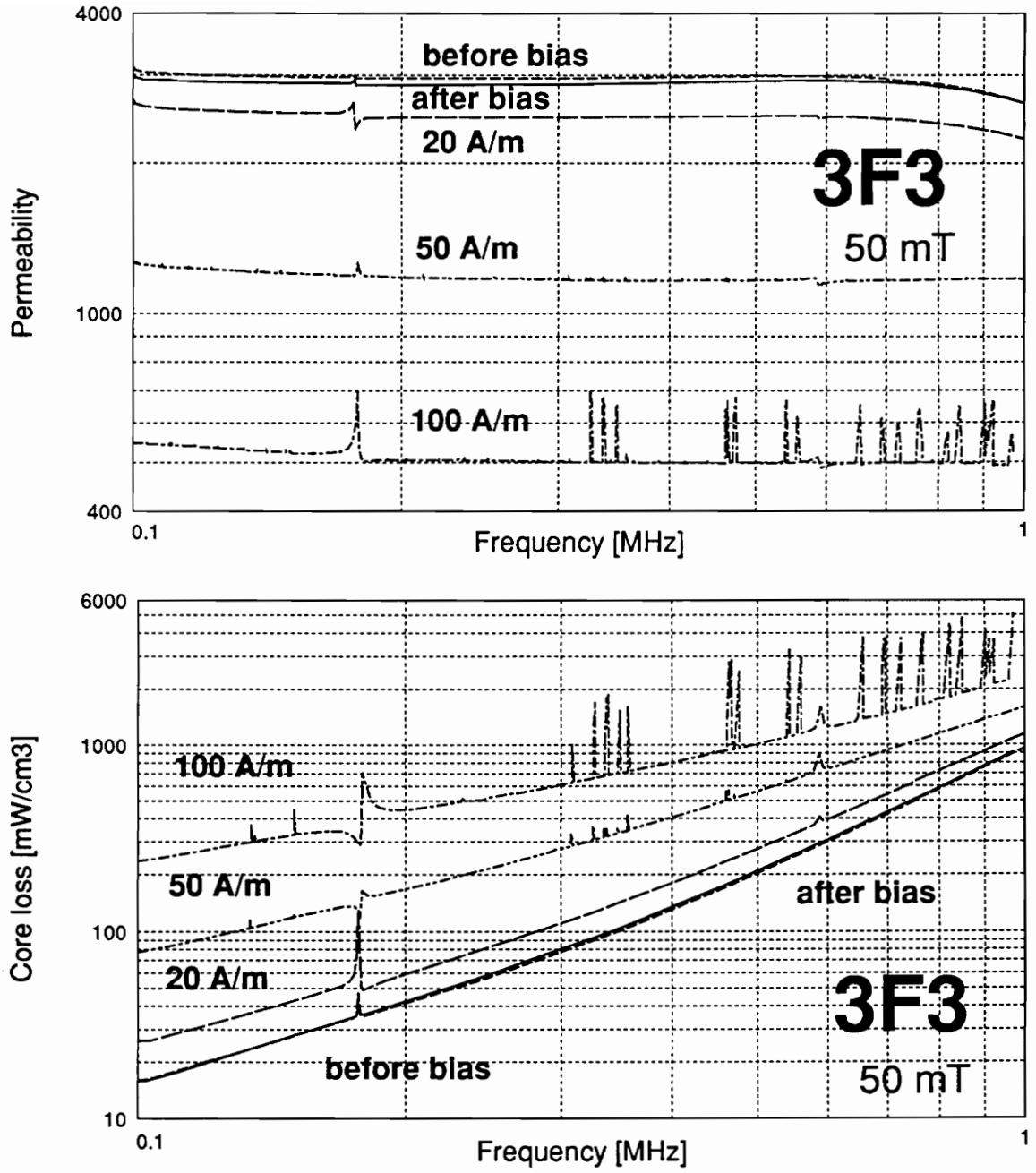

Fig. 3.52. Influence of static bias on magnetoelastic resonances in 3F3 ferrite at 50 mT ac flux density.

About 20% increase of base line core loss is observed. The number of resonant peaks, due to the magnetostriction, decreases because the large external ac field alters the local anisotropy fields of the virgin core. Therefore, the magnetostriction characteristics are altered permanently after treatment with a strong ac magnetic field.

Another ferrite tested, 3F3, made by Philips, is a low-loss ferrite for high-frequency power conversion applications. Since it is a manganese-zinc ferrite, it does not have local anisotropy fields. The only field that can exist in this ferrite without an external dc bias field is a small magnetic remanence. The 3F3 ferrite is characterized at 50 mT ac flux density under different dc biases. The permeability and core loss characteristics for a toroid are shown in Fig. 3.53. Since the 3F3 ferrite does not have strong uniaxial anisotropy, the magnetization of the core is much more uniform than that of 4C4 in the previous tests. Therefore, the characteristics of 3F3 ferrite have far fewer peaks due to the magnetostriction. Also, many smaller resonances might have been masked by the hysteresis or residual losses which are substantial in manganese-zinc ferrites. When 100 A/m bias field is applied, the core loss increased up to twenty times in the peaks due to the magnetostriction over the corresponding values without a bias. The base line core loss increased up to fifteen times under these conditions. The core loss characteristic almost returns to the original shape after dc bias is removed.

The influence of the mechanical damping on the permeability and loss characteristics of MnZn ferrite is shown in Fig. 3.55.. Damping entirely eliminates narrow resonances and substantially softens the major resonant peak, but increases the baseline losses at high frequencies. In NiZn ferrite, damping eliminates all resonances and decreases the baseline losses particularly at lower frequencies. This is perhaps due to negative magnetostriction of NiZn ferrites.

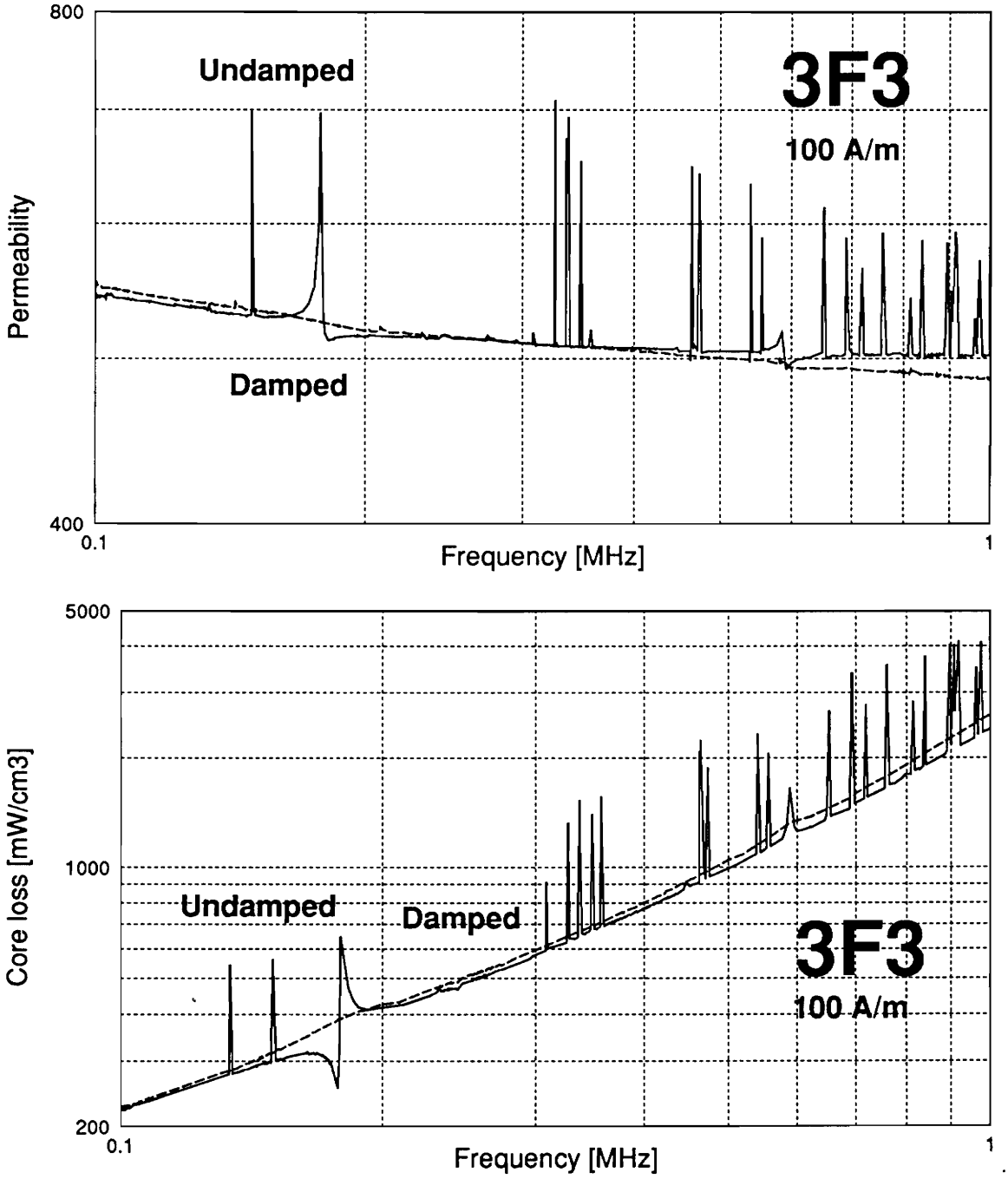

Fig. 3.53. Influence of mechanical damping on the permeability and core loss of 3F3 ferrite at 50 mT ac flux density under dc bias.

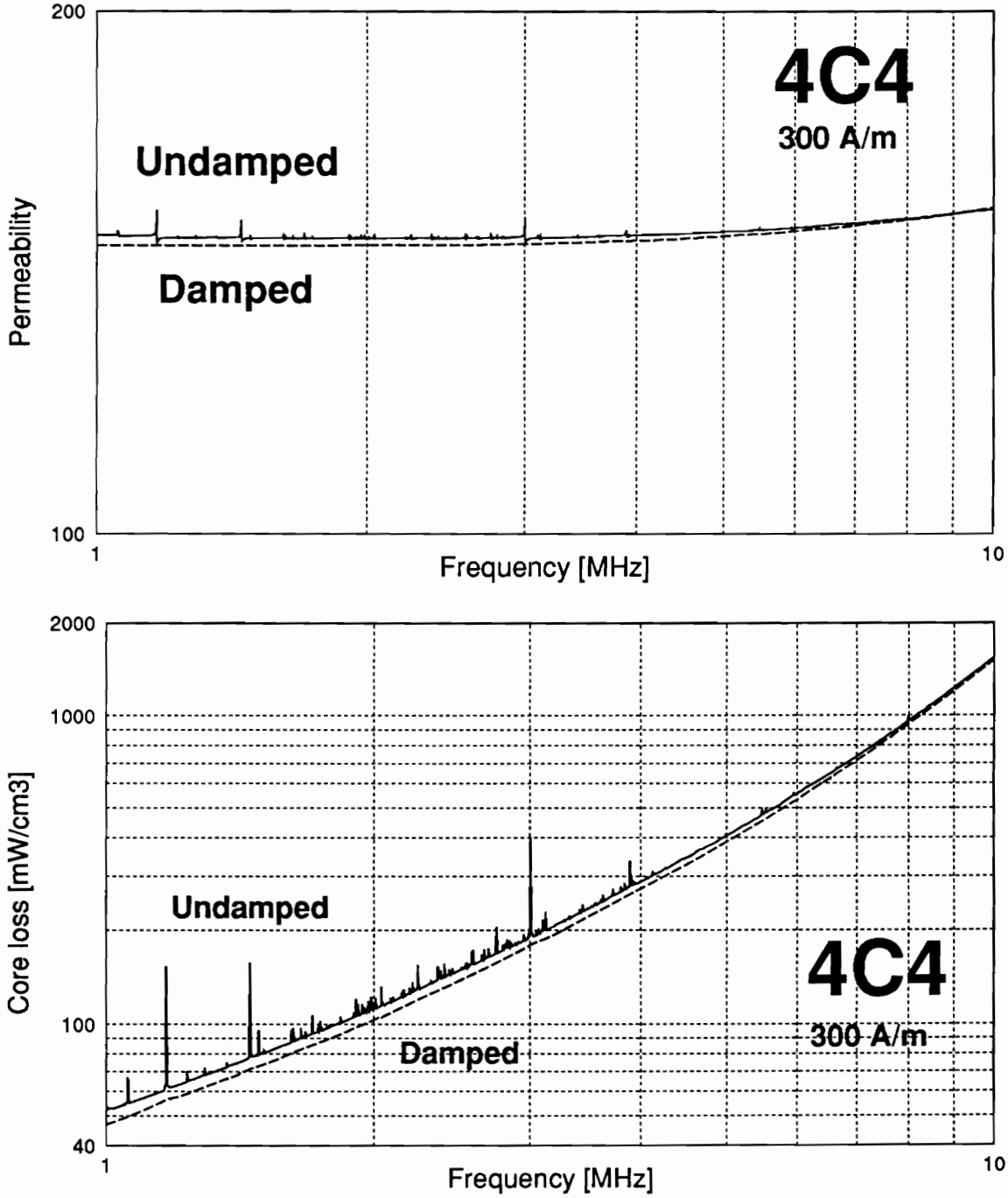

Fig. 3.54. Influence of mechanical damping on the permeability and core loss of 4C4 ferrite at 10 mT ac flux density under dc bias.

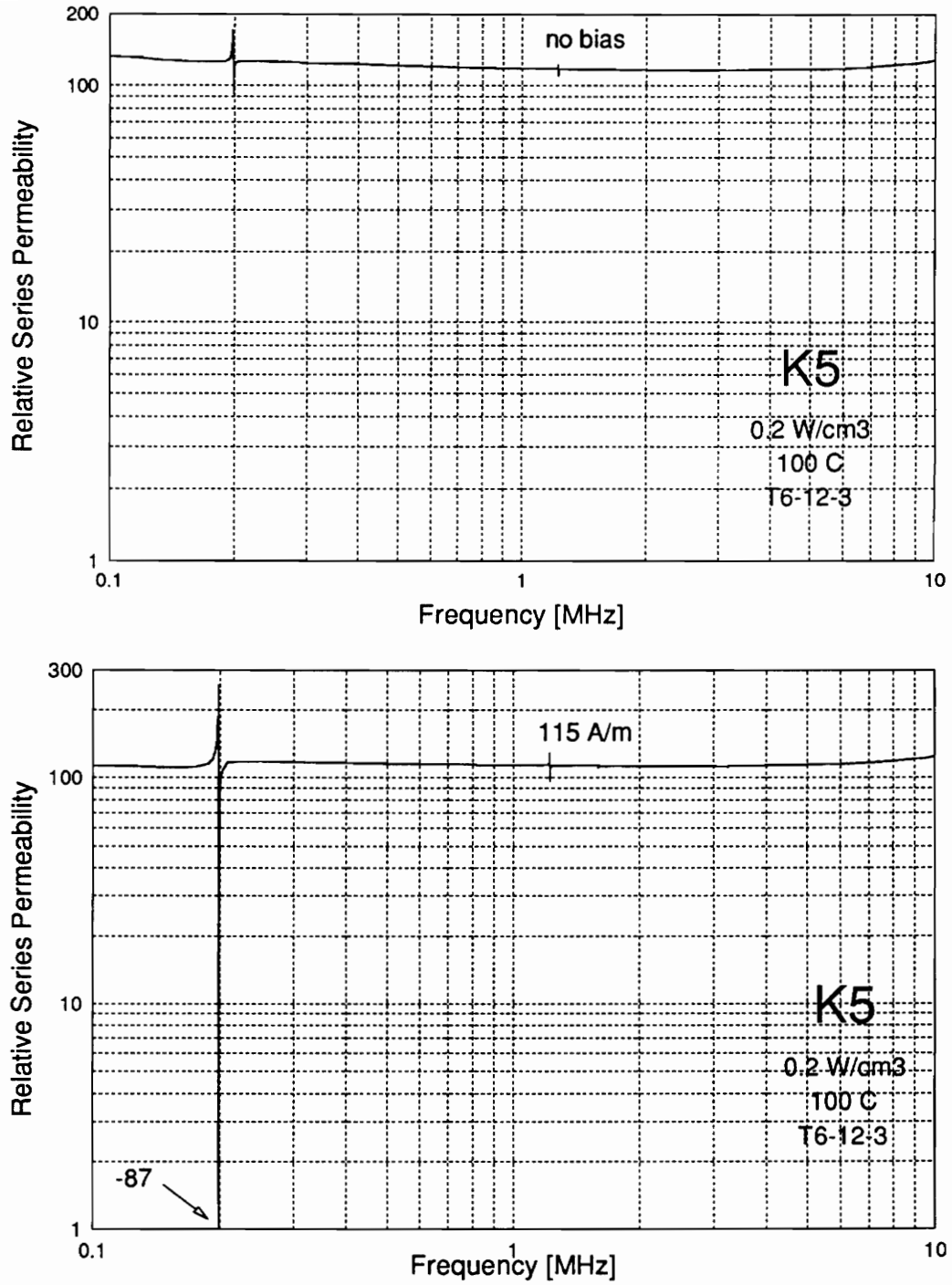

Fig. 3.56. Permeability due to magnetoelastic resonances in K5 ferrite at 0 and 115 A/m static bias and at 100 ℃ temperature.

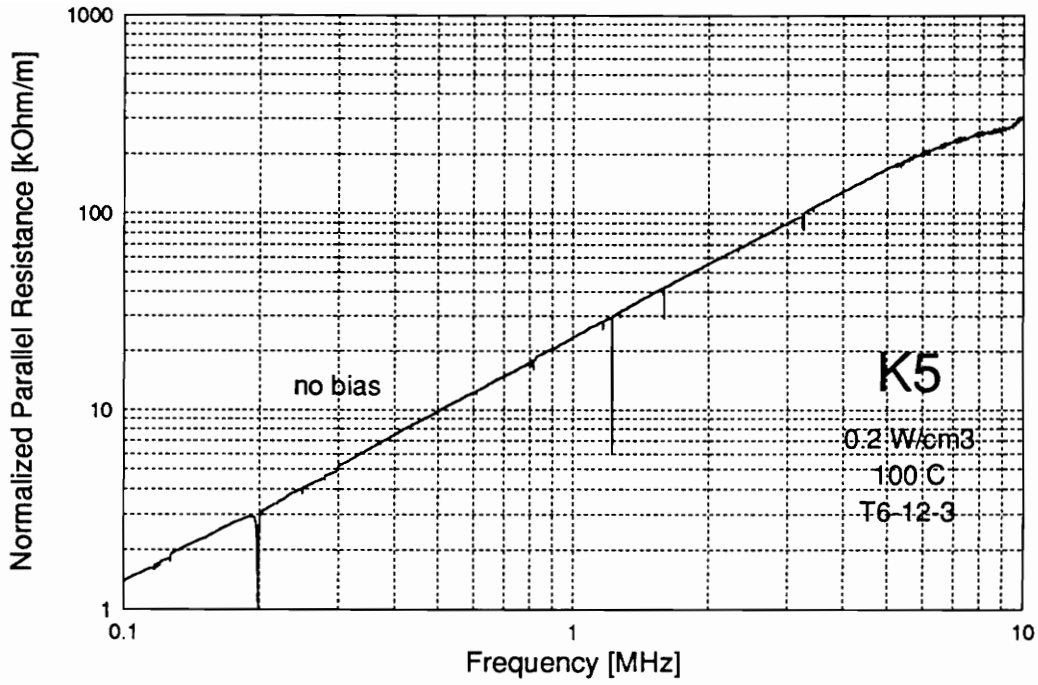

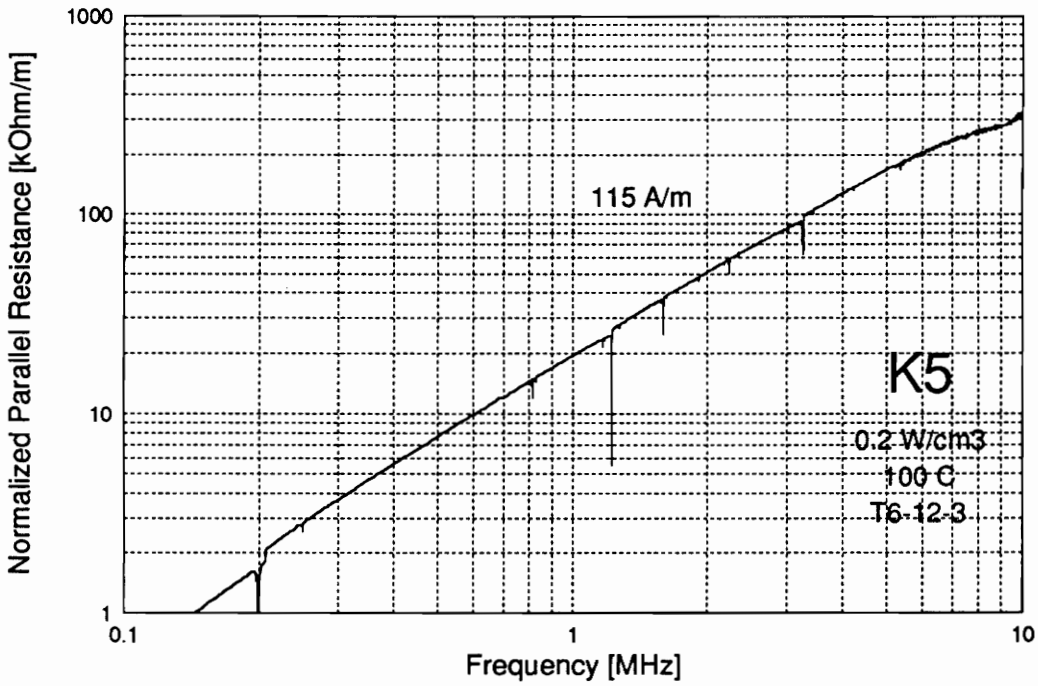

Fig. 3.57. Normalized parallel resistance due to magnetoelastic resonances in K5 ferrite at 0 and 115 A/m static bias and at 100 ℃ temperature.

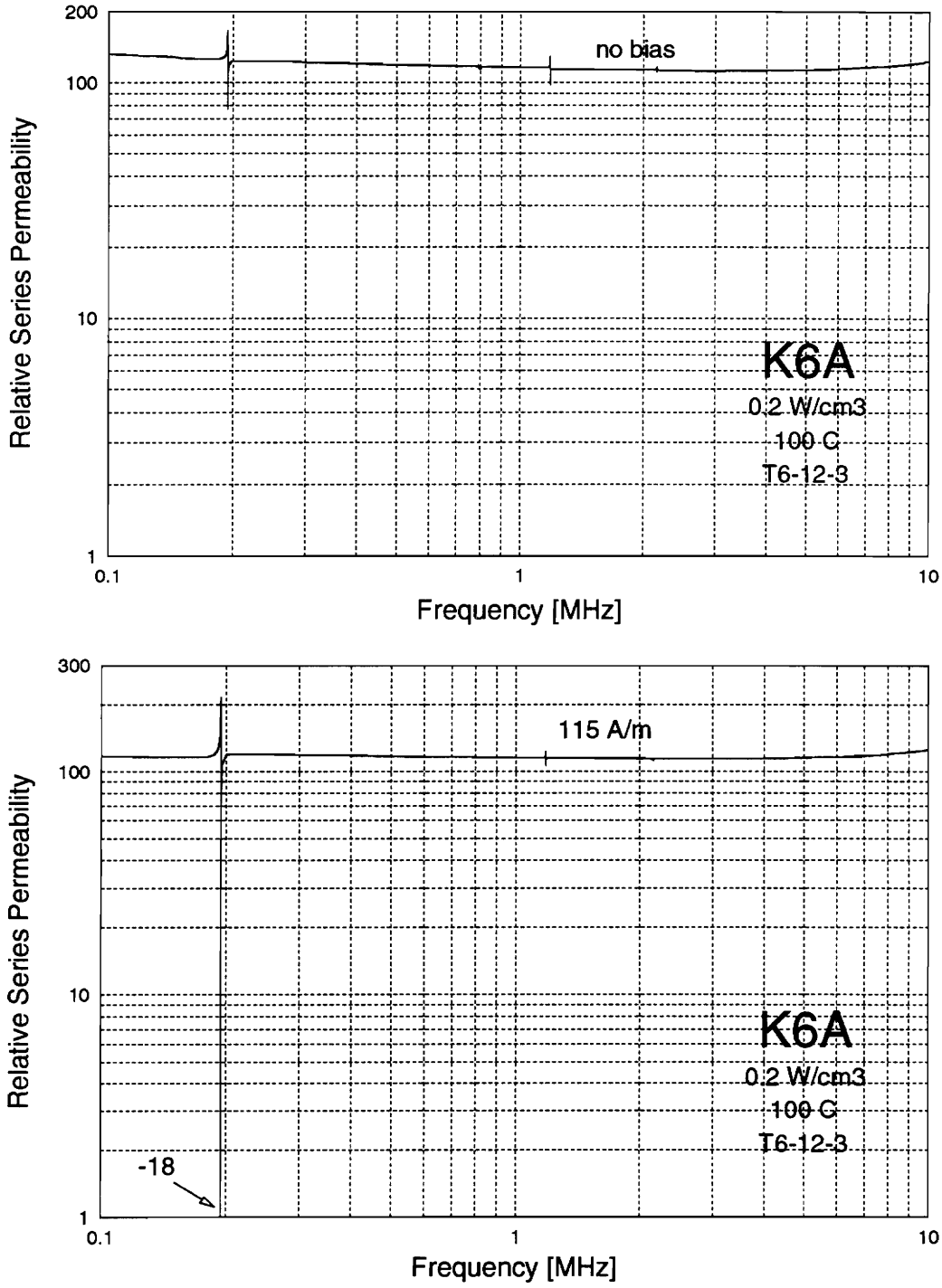

Fig. 3.58. Permeability due to magnetoelastic resonances in K6A ferrite at 0 and 115 A/m static bias and at 100°C temperature.

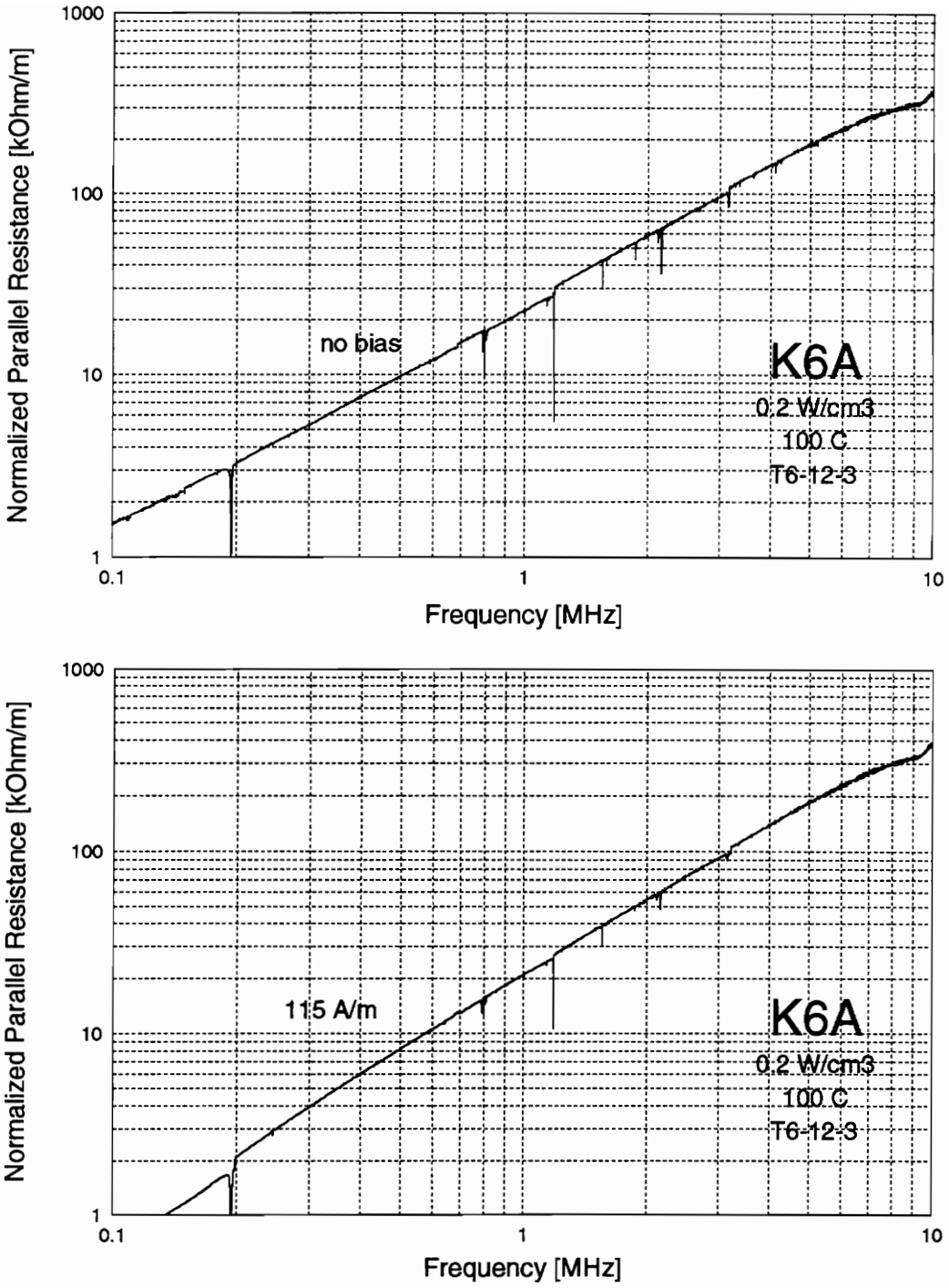

Fig. 3.59. Normalized parallel resistance due to magnetoelastic resonances in K6A ferrite at 0 and 115 A/m static bias and at 100°C temperature.

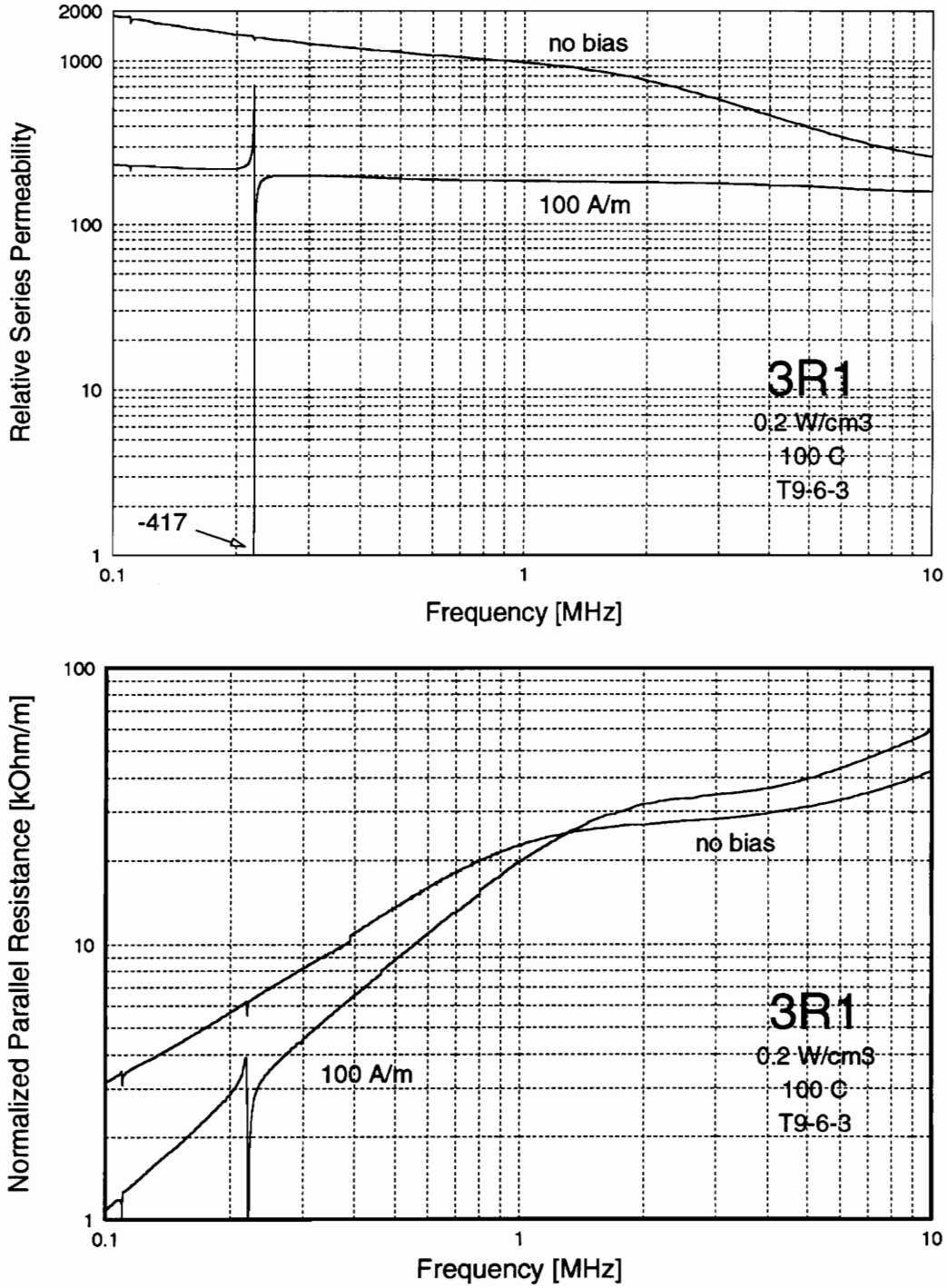

Fig. 3.60. Permeability and normalized parallel resistance due to magnetoelastic resonances in 3R1 ferrite at 0 and 100 A/m static bias and at 100°C temperature.

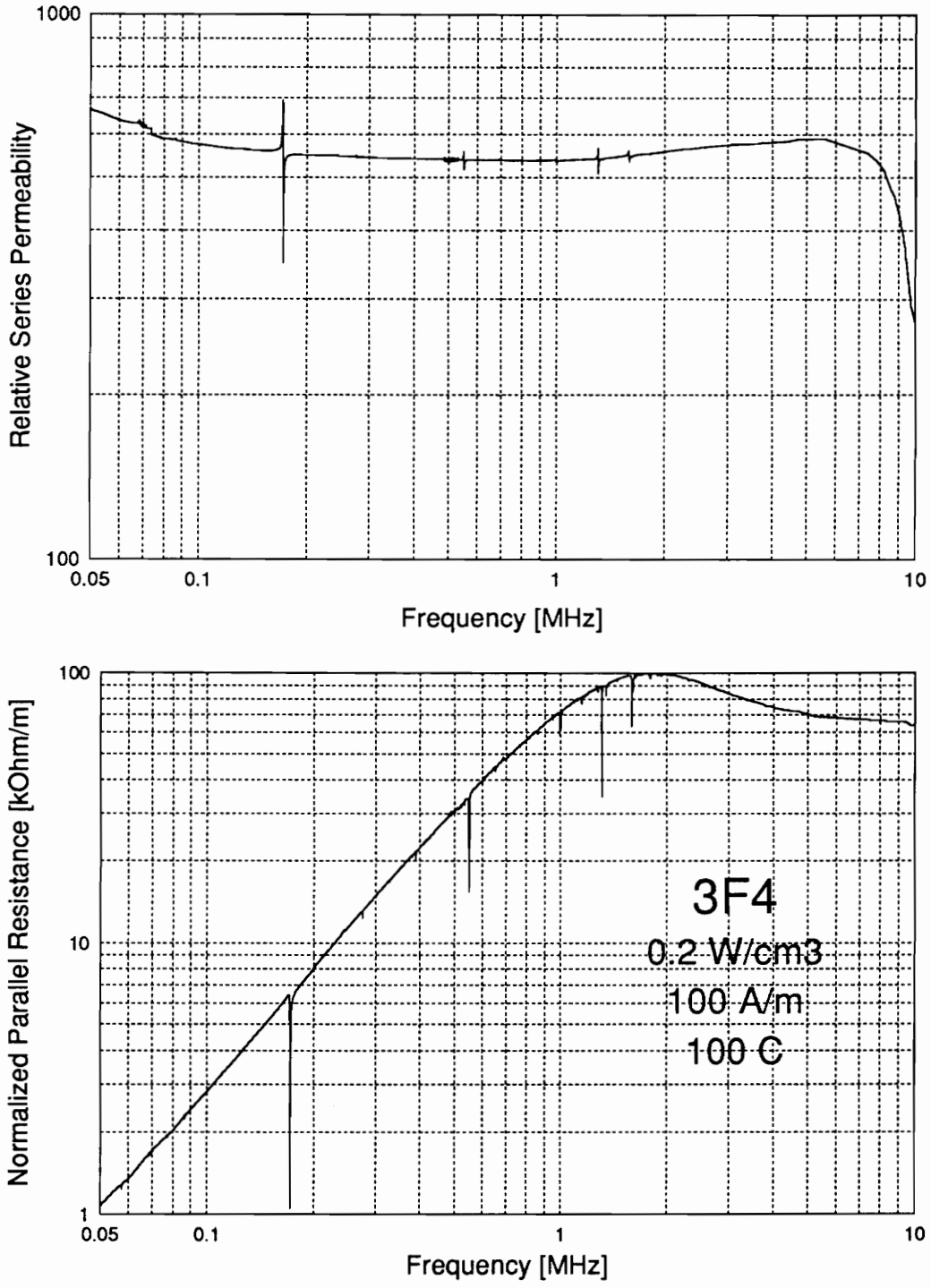

Fig. 3.61. Permeability and normalized parallel resistance due to magnetoelastic resonances in for 3F4 ferrite at 0 and 100 A/m static bias and at 100 ℃ temperature.

Fig. 3.54 a toroid made of NiZn ferrite (type K5, P/N T6-12-3) manufactured by TDK shows four strong resonances at 200 kHz, 1.3 MHz, 1.6 MHz, and 3.2 MHz and a number of weaker ones. A few more appear when bias is applied, the major resonance broadens, and the apparent permeability drops to -87 at resonance. Another NiZn ferrite made by TDK designated K6A and shown in Fig. 3.55, with identical dimensions has even more resonances. However, when tested with a superimposed static bias field, the number of resonance decreased, but the main resonance broadened. Therefore, resonant frequencies are characteristic of a particular shape, but depending on the ferrite composition and static bias only some resonances are active. This does not mean that the other resonances disappear. They are not observable only because the loss they contribute is less than other losses in the material. Corresponding changes in permeability due to magnetostriction resonance in K6A ferrite are shown in Fig. 3.56. Under bias condition the resonance is so strong that the apparent permeability reaches a negative peak of -18.

The next material tested was MnMg ferrite for magnetic amplifiers. This case is particularly important because toroidal shape is used almost exclusively in high-frequency magnetic amplifiers. The tested sample is a toroid with an outer diameter of 9.37 mm, an inner diameter of 5.36 mm, and a height of 3.38 mm. The characteristics, shown in Fig. 3.57, exhibit only one major resonance at 220 kHz, enhanced by the application of bias and reaching minimum apparent permeability of -417. Also, a minor subharmonic resonance exists at 110 kHz. Unfortunately these frequencies are within a typical application frequency range. It is interesting to note that there are no higher modes of vibration in the 3R1 ferrite ring. This is probably due to an oval cross-section of the toroid instead of a rectangular one of previously described NiZn rings.

The last case is a MnZn ferrite toroid (K ferrite, P/N 40601-TC, Magnetics, Inc.) with an outer diameter 5.80mm, inside diameter 2.99 mm, and height of 1.49 mm. The characteristics, shown in Fig. 3.58, reveal a small principal resonance occurring at 400 kHz with a subharmonic oscillation at 200 kHz. When the static bias field is increased, a number of new strong

resonances appear up to 1.4 MHz, including two additional subharmonic oscillations. This is characteristic feature of MnZn ferrites, confirmed by observation of more materials. Figure 3.59 shows resonances in a toroid made of 3F4 ferrite. The resonances are so strong because the MnZn ferrites have low hysteresis and residual losses, which make almost every magneto-mechanical resonance visible. However, the change in the apparent permeability due to magnetomechanical resonance is much smaller in MnZn ferrites than in NiZn or MnMg ferrites, and it does not reach negative values. This is because MnZn ferrites have small magnetostriction [272].

3.6.2 Influence of a Core Shape

In many applications shapes other than the toroid are utilized. The characteristics containing resonances were observed in the following cores: RM6 in Fig. 3.60, PQ20/16 in Fig. 3.61, P2616 in Fig 3..62, LP22/13 in Fig. 3.63, EPC25 in Fig. 3.64, and 782E272 in Fig. 3.65. All cores were fully assembled before testing.

The resonances appear between 110 kHz and 1.5 MHz, but the majority are concentrated in the 200 to 500 kHz frequency range. This is of a particular concern since most new designs of power converters are in this range. The cores with a high degree of symmetry (pot core) or with thin flat parts (EPC) have a greater number of resonances than other cores. The resonant frequencies are extremely difficult to calculate because of the complex shapes of the cores. Therefore, it would be very desirable if ferrite core manufacturers could provide data on resonant frequencies on every core they manufacture, so designers could avoid magnetoelastic resonances and make more reliable and stable devices.

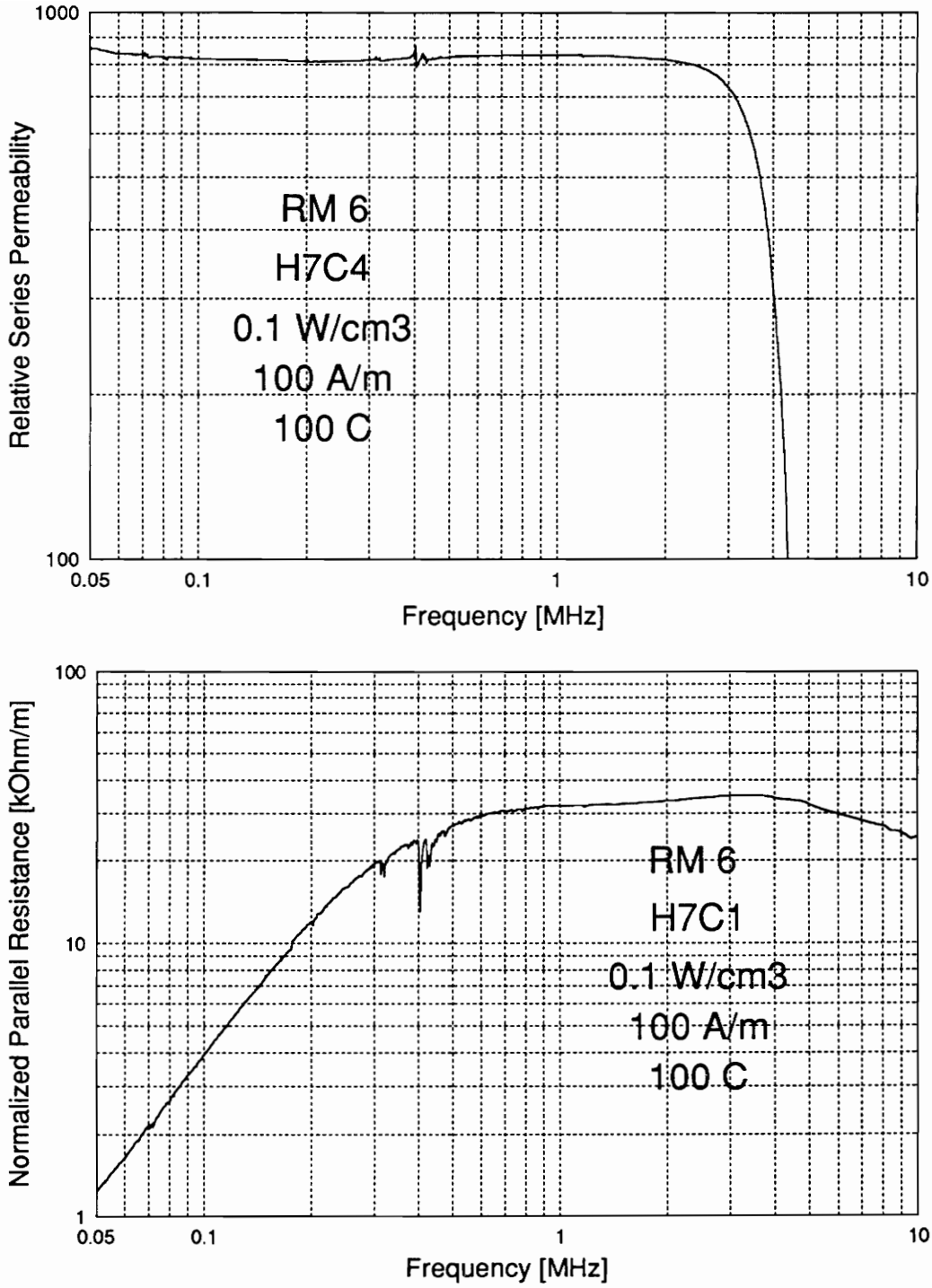

Fig. 3.62. Normalized parallel resistance due to magnetoelastic resonances in RM6 core (TDK) at 100 A/m static bias and at 100 ℃ temperature.

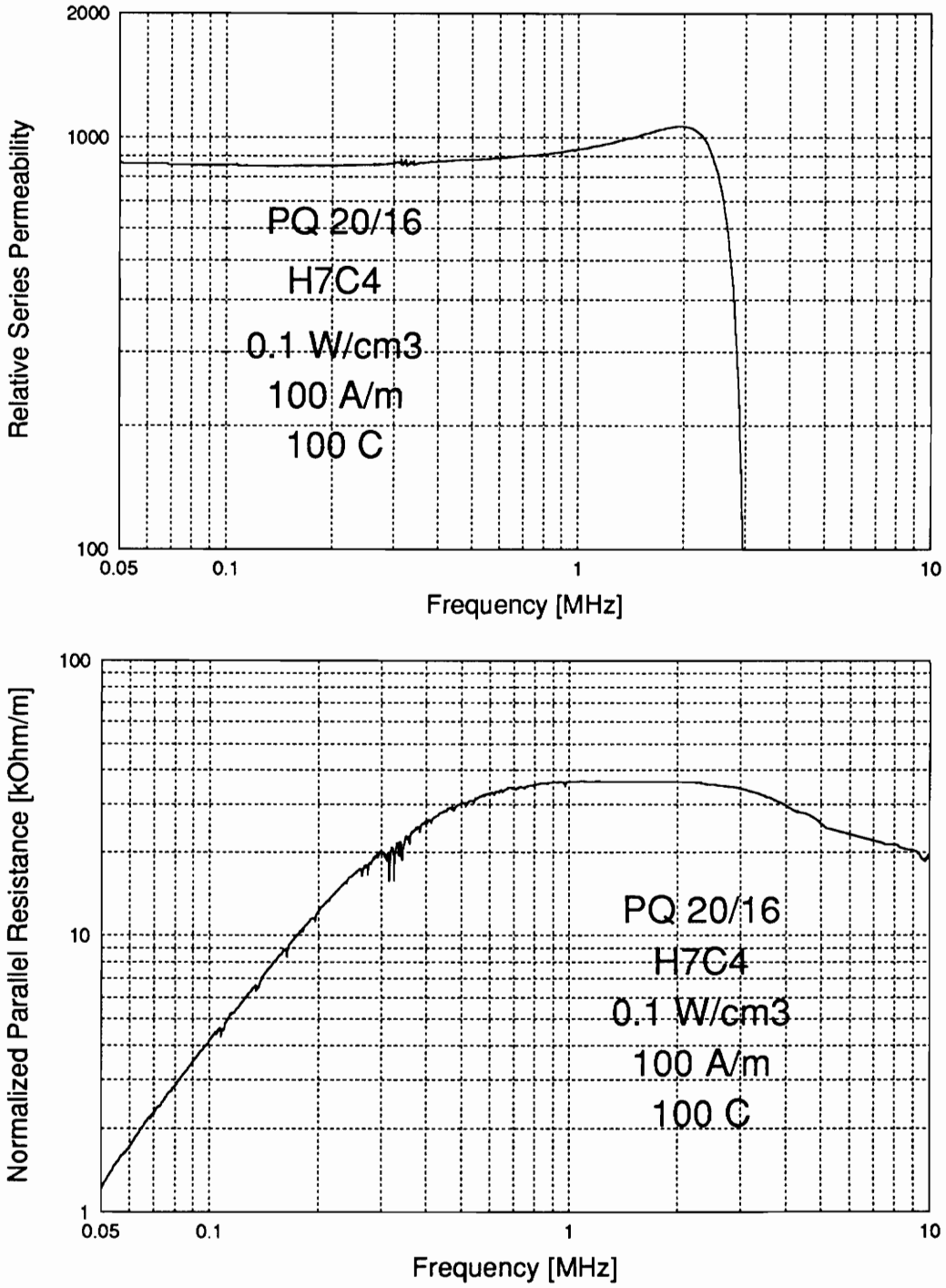

Fig. 3.63. Normalized parallel resistance due to magnetoelastic resonances in PQ20/16 core (TDK) at 100 A/m static bias and at 100 ℃ temperature.

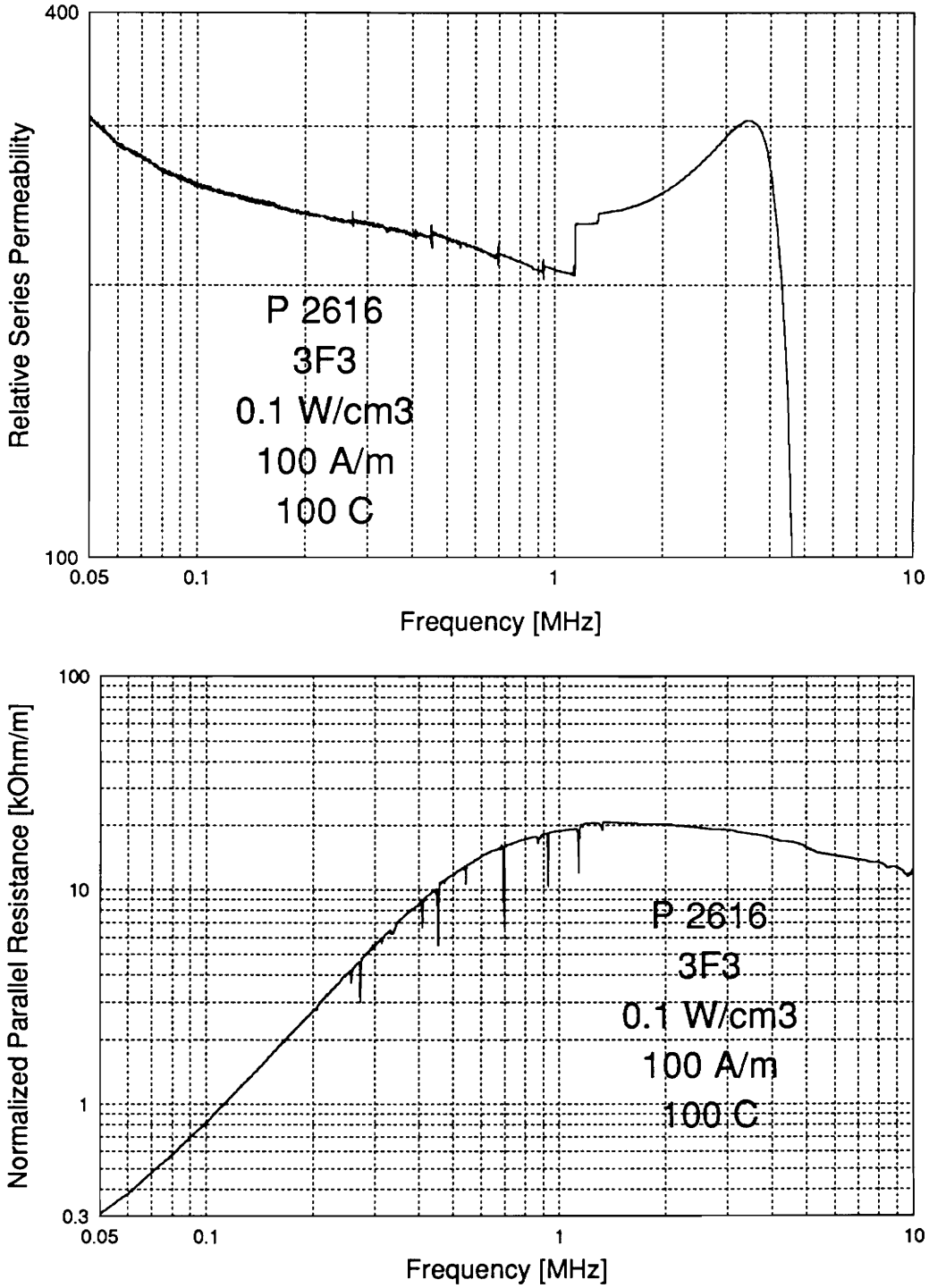

Fig. 3.64. Normalized parallel resistance due to magnetoelastic resonances in P2616 pot core (Philips) at 100 A/m static bias and at 100 ℃ temperature.

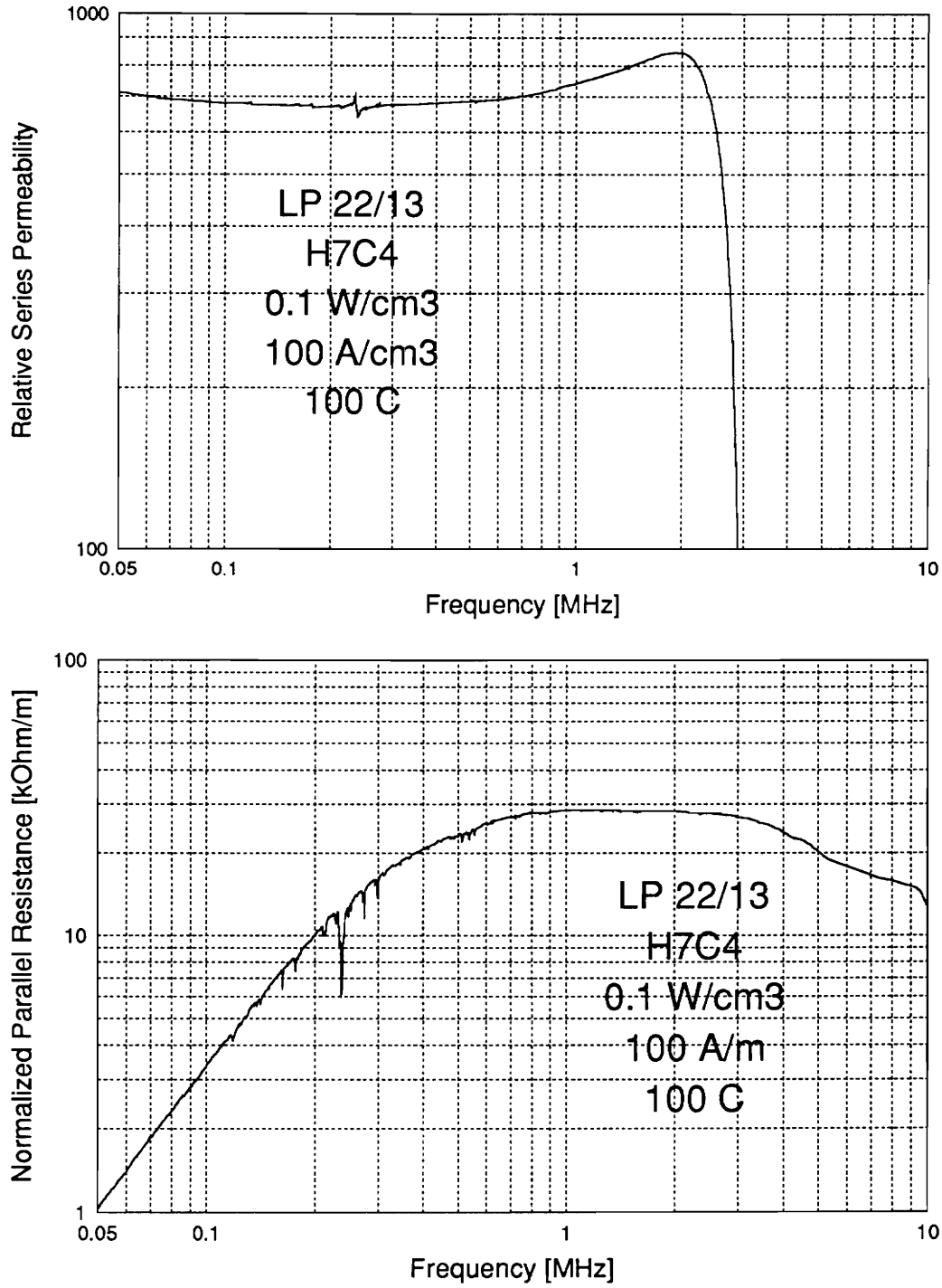

Fig. 3.65. Normalized parallel resistance due to magnetoelastic resonances in LP22/13 core (TDK) at 100 A/m static bias and at 100 ℃ temperature.

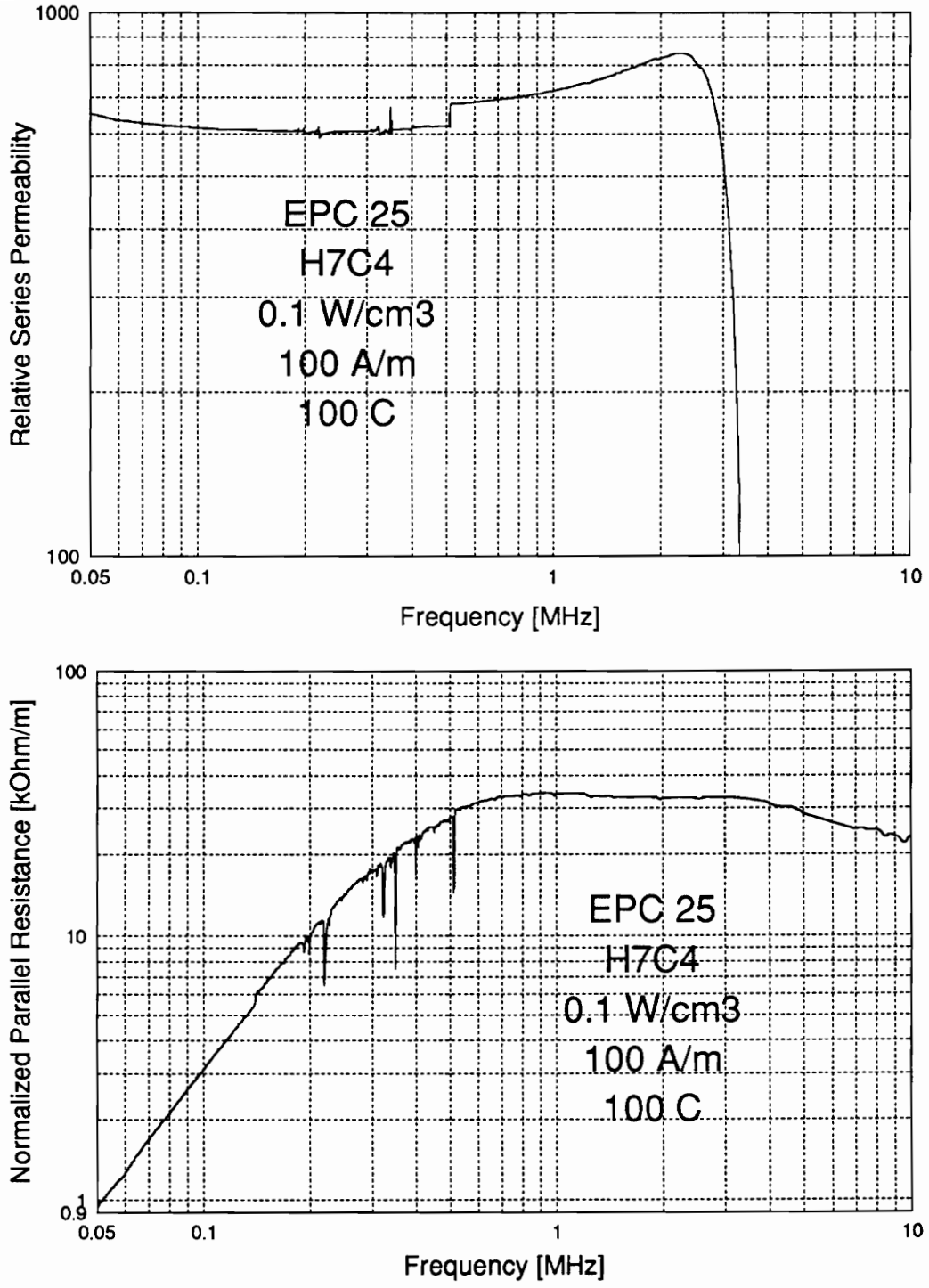

Fig. 3.66. Normalized parallel resistance due to magnetoelastic resonances in EPC25 core (TDK) at 100 A/m static bias and at 100 ℃ temperature.

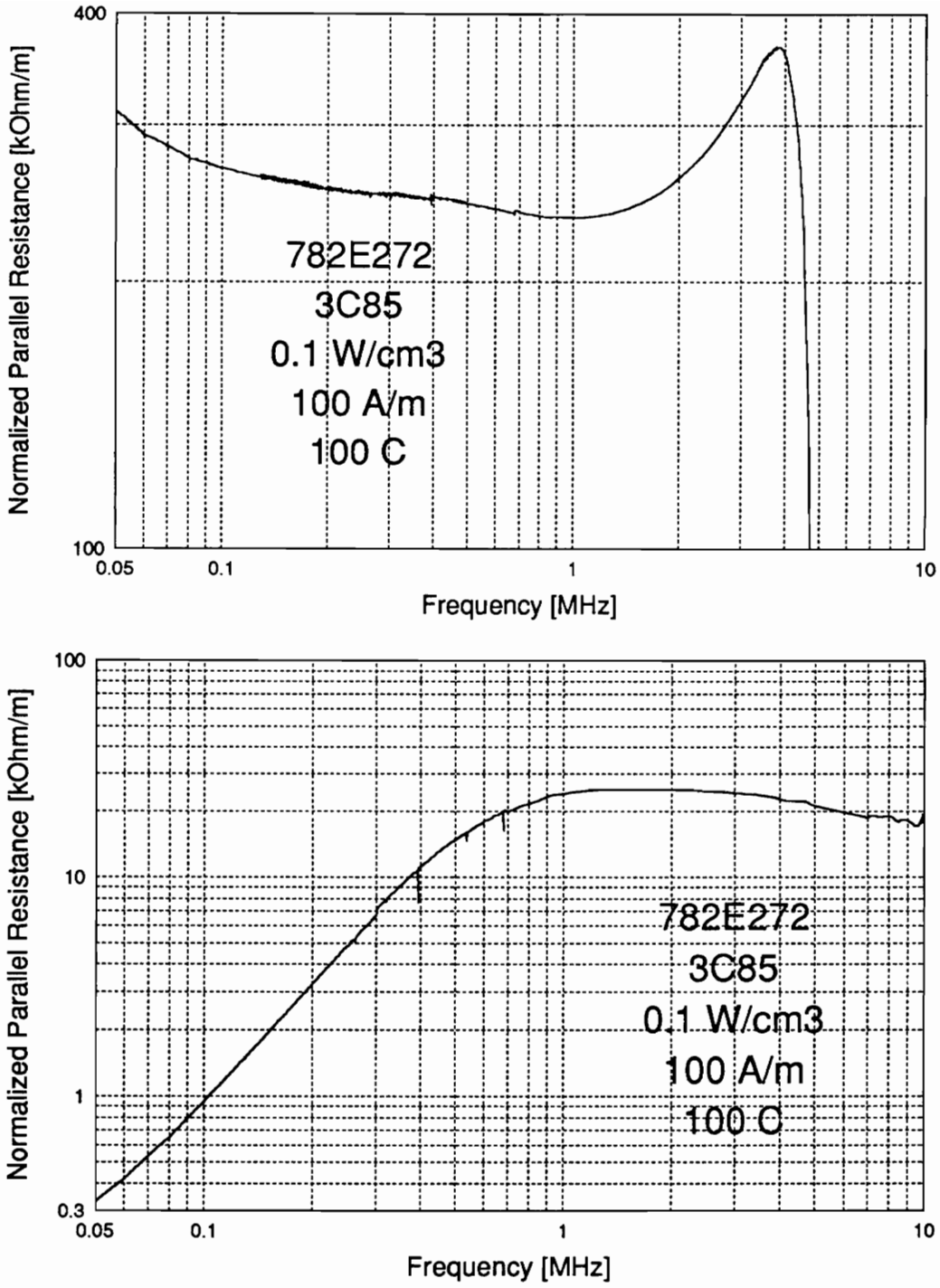

Fig. 3.67. Normalized parallel resistance due to magnetoelastic resonances in 782E272 EE core (Philips) at 100 A/m static bias and at 100 ℃ temperature.

3.7 Dynamic Changes of Core Loss under Time-Varying Bias

When the magnetic material is subjected to a change in the field, leading to a change of positions of domain walls, its properties change but not immediately. The delay originates from the ion diffusion after-effect described in Section 3.2.3.3. The best known manifestation of this effect is disaccommodation or time decrease in permeability [273, 274]. In power electronics applications, the permeability is usually not as critical as losses. In order to investigate how diffusion after-effect influences losses, several experiments were performed with a toroid made of MnZn ferrite with the following dimensions: outer diameter 5.80mm, inside diameter 2.99 mm, and height of 1.49 mm (K ferrite P/N 40601-TC, Magnetics, Inc.). The core was wound with 5 turns of AWG#23, and its normal parallel resistance was measured at 1 MHz 25 mT ac field at the temperature of 100°C. Then, without removing from the temperature chamber, the core was subjected to a capacitor discharge through the winding resulting in a 75 kA/m peak magnetic field. Immediately afterwards, an impedance probe was connected with the original ac excitation to monitor the changes in core loss with time. The results of three hour measurement are shown in Fig. 3.66. The additional loss due to the diffusion after-effect is about 10%, and the core needs at least several hours to return to the original condition. In the next experiment, the changes of losses were examined under squarewave periodic bias changing between 0 and 50 A/m. The frequency of the bias was 0.2 Hz, and the rise time and fall time were set to 0.1 s. The ac excitation was 25 mT at 1 MHz at 100°C. The permeability and the normalized parallel resistance are shown in Fig. 3.67 as a function of time. The permeability changes in a square-wave fashion following the bias field. After each change there was a small negative droop in permeability. The losses depended not only on the bias level but also on the rate and the direction of the bias change. The greatest losses, about 14% over base, occurred

during the fall of bias, but they were not much smaller during the bias rise. The experiment was repeated with larger high-frequency excitation of 50 mT at lower frequency of 500 kHz. The results are shown in Fig. 3.68.

The permeability droops negative after each bias change similarly to the case with a 25 mT excitation. The changes in losses, however, are mainly due to the difference in bias level. The additional loss during the fall of bias amounted to 10% of the base loss.

In the last experiment a triangle bias was used instead of a squarewave to observe the change in losses at slower bias changes. The permeability and loss characteristics, shown in Fig. 3.69, measured at 0.5 MHz and 50 mT, essentially follow the changes in bias except for some distortion in the permeability waveform caused by the delay due to an after-effect. The loss characteristics shows a decrease of about 8% of the base loss when the bias reaches zero. The characteristics at 25 mT and 1 MHz ac excitation, shown in Fig. 3.70, the permeability changes in time very similarly to the 50 mT case. However, the loss characteristic is entirely different. During each slope of the triangle bias, there occur two peaks in diffusion after-effect losses. These peaks are related to two different ion diffusion processes with different activation energy levels and thus different time constants. The amplitude of the peaks is below 4% of the base loss.

In conclusion, the losses due to the diffusion after-effect depend on the frequency and flux density of the ac excitation. They increase with an increase of the rate of change of bias and may reach 14% of the base loss at 500 A/m·s rate of bias change. The diffusion after-effect loss is especially important in magnetic components in circuits where bias conditions change rapidly with time. These include power factor correction circuits and switched-mode power supplied with pulsed load, for example a radar or a computer disk drive.

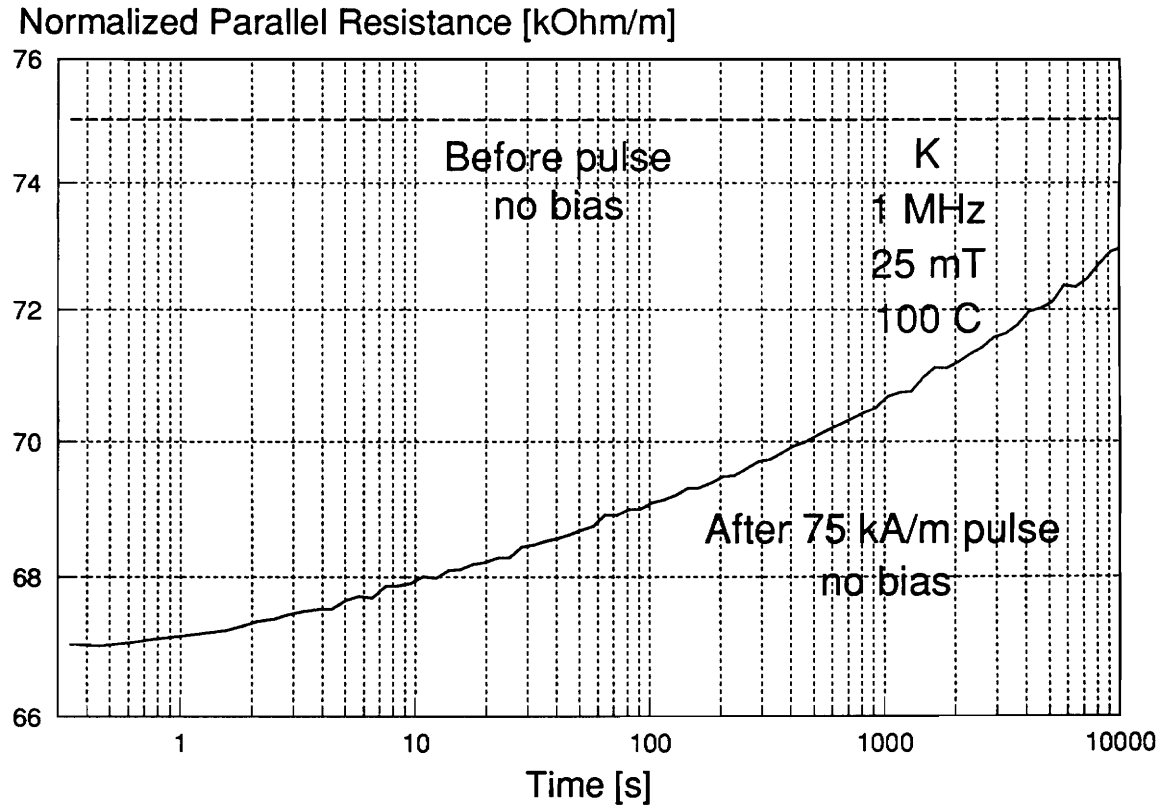

Fig. 3.68. Normalized parallel resistance due to diffusion after-effect in K ferrite (Magnetics, Inc.) after 75 kA/m pulse at 100 ℃ temperature.

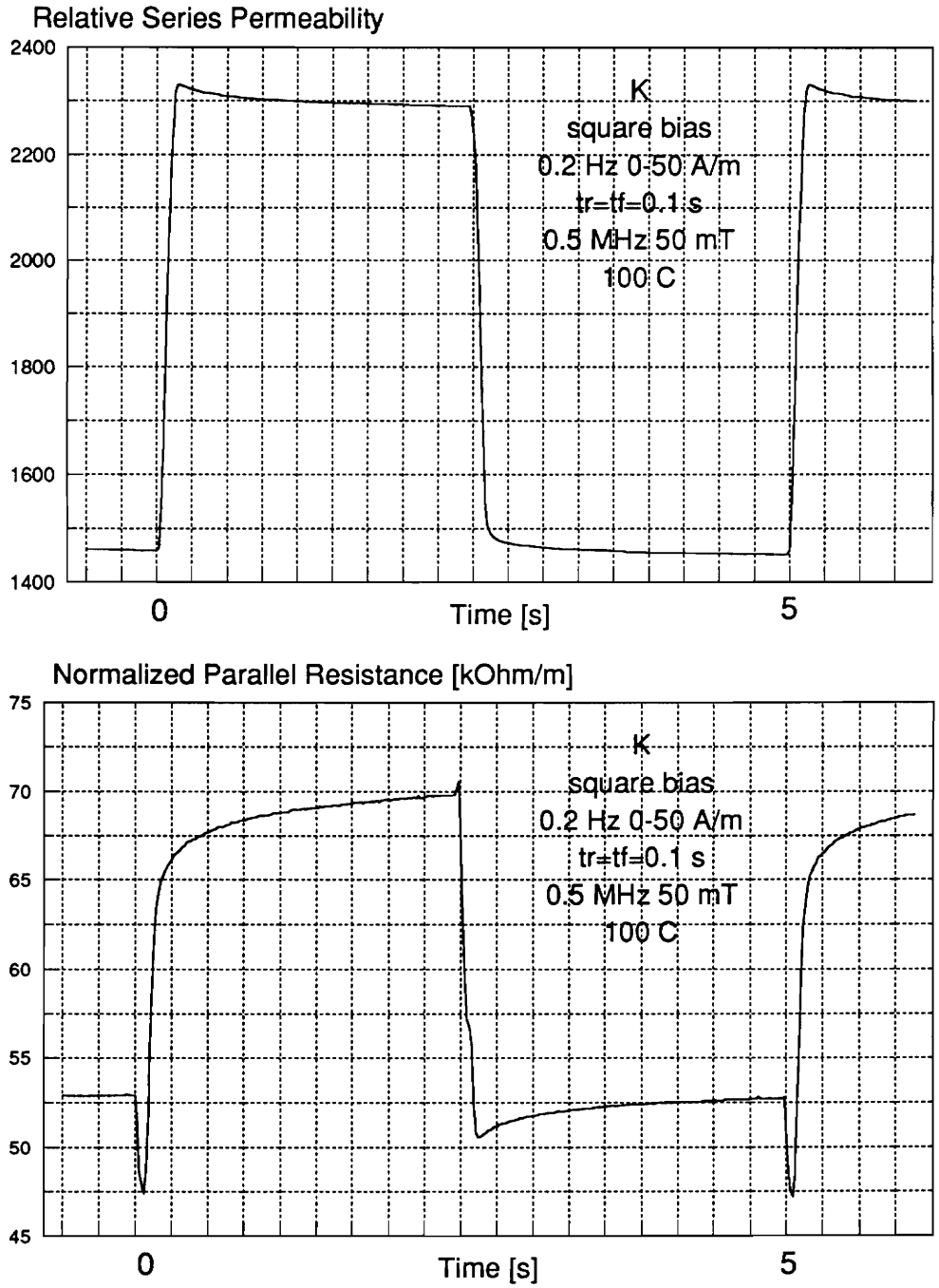

Fig. 3.69. Permeability and normalized parallel resistance due to diffusion after-effect in K ferrite (Magnetics, Inc.) under square wave bias conditions at 50 mT, 500 kHz, and 100 °C temperature.

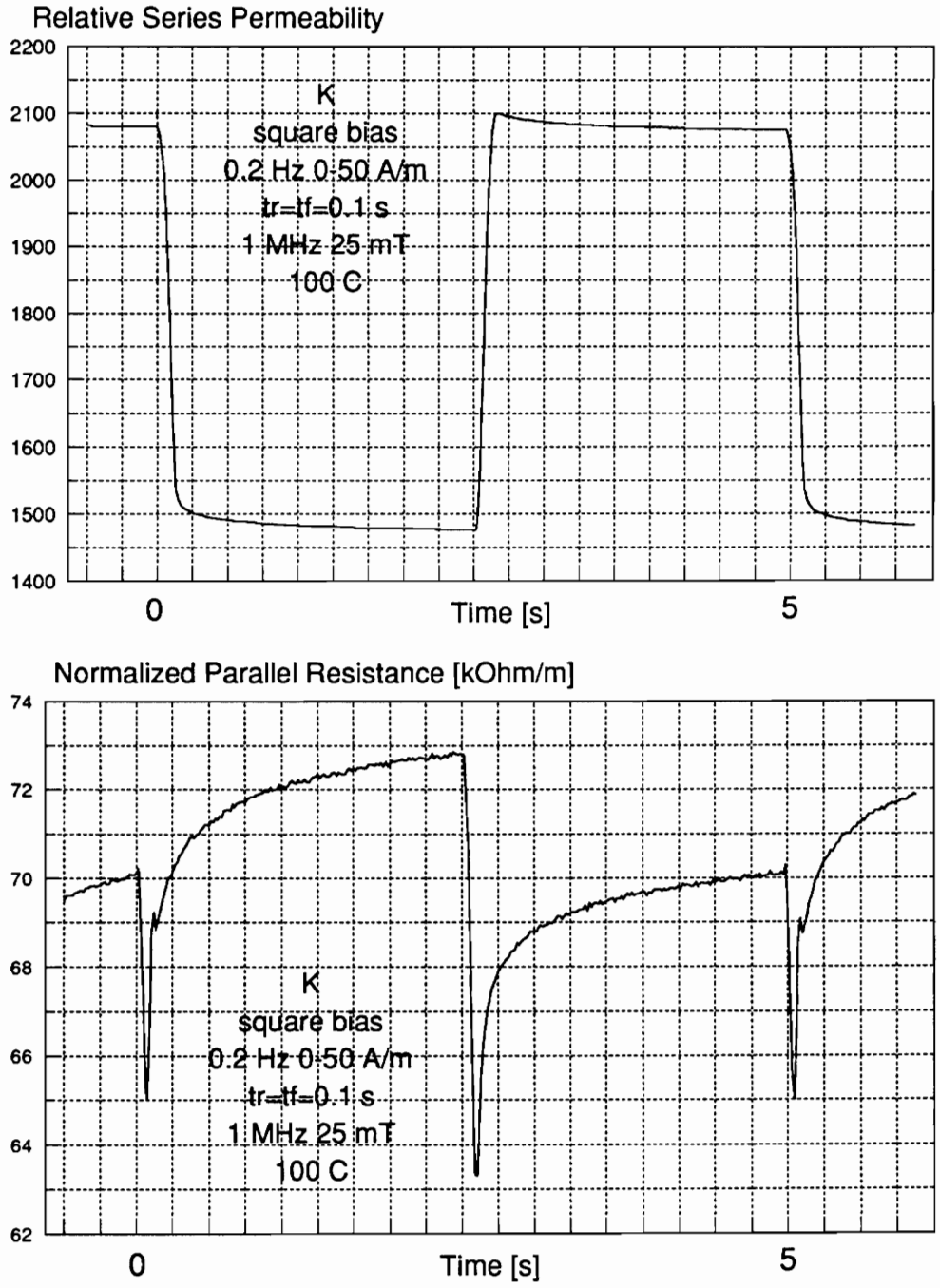

Fig. 3.70. Permeability and normalized parallel resistance due to diffusion after-effect in K ferrite (Magnetics, Inc.) under square wave bias conditions at 25 mT, 1 MHz, and 100 °C temperature. The losses under bias are lower due to an increase of the space charge relaxation frequency (compare Figs. 4.26 and 4.31).

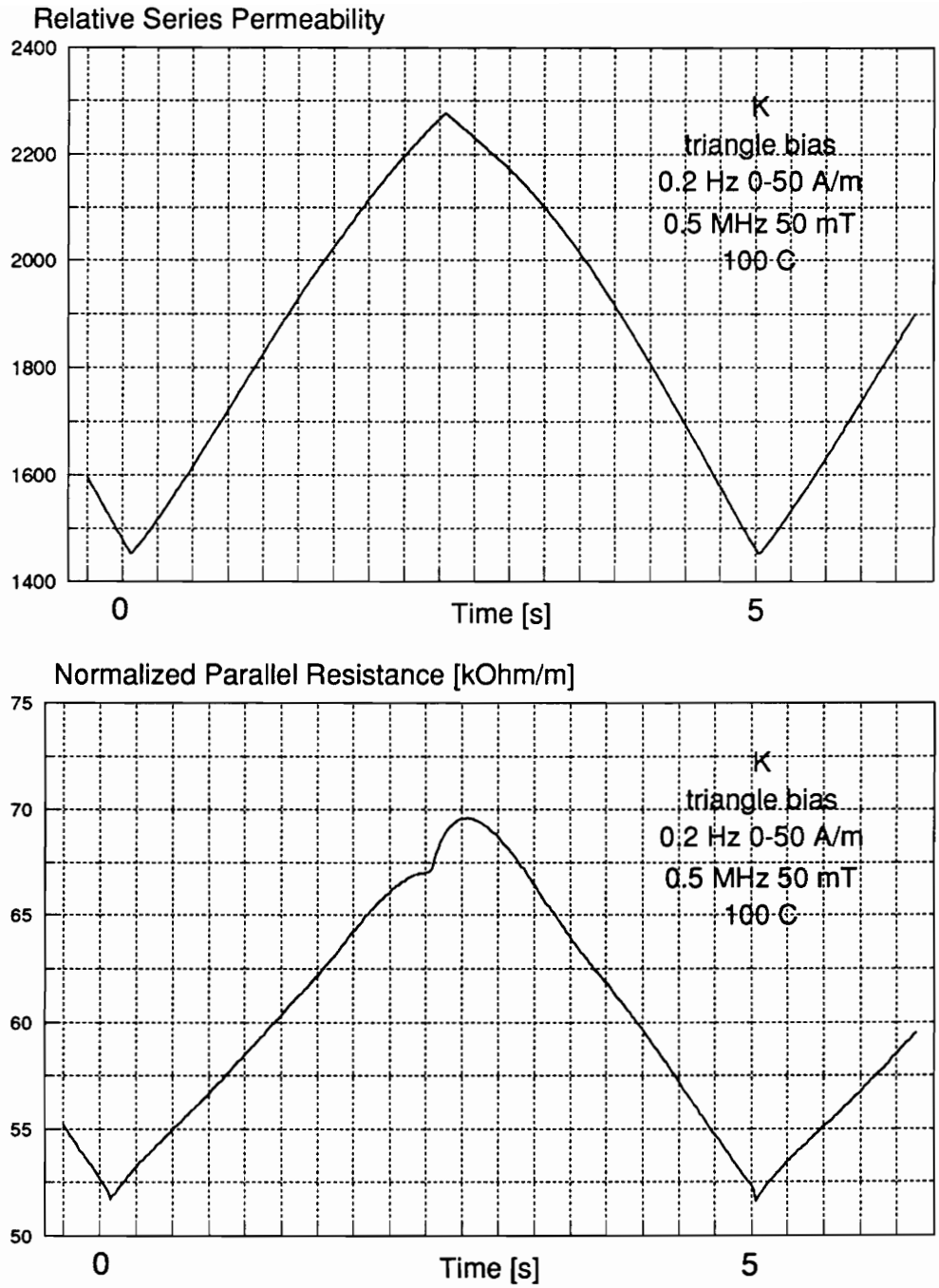

Fig. 3.71. Permeability and normalized parallel resistance due to diffusion after-effect in K ferrite (Magnetics, Inc.) under triangle wave bias conditions at 50 mT, 500 kHz, and 100 °C temperature.

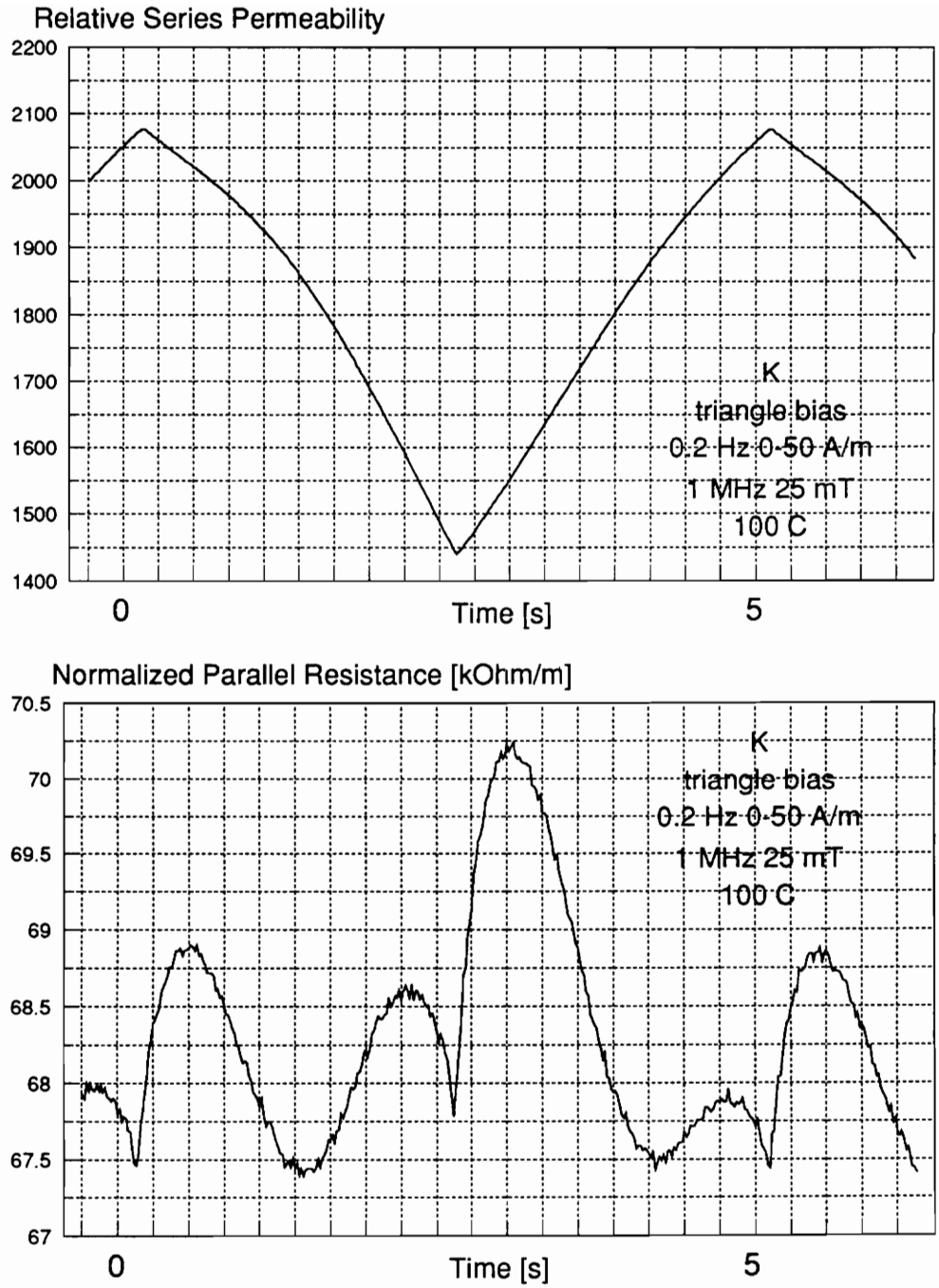

Fig. 3.72. Permeability and normalized parallel resistance due to diffusion after-effect in K ferrite (Magnetics, Inc.) under triangle bias conditions at 25 mT, 1 MHz, and 100 ℃ temperature.

3.8 Comparison of Core Loss in Commercial Ferrites

Losses in ferrites differ substantially depending on chemical composition and microstructure. Seven types of ferrites were characterized at a constant power dissipation of 200 mW/cm^3 and are compared in Fig. 3.71. The eighth type (not shown) was a NiZn ferrite K5 (TDK) with very similar losses compared to those of K6A. The highest normalized parallel resistance (and thus the lowest losses) below 200 kHz has 3F3 ferrite. K material is the best from 200 to 600 kHz, and 3F4 ferrite from 600 kHz to 2.4 MHz. Above 2.4 MHz K6A is the best choice. Neither H7C1 nor 3R1, score well in any frequency range. 3R1 is a square loop material for magnetic amplifiers. Its losses are higher due to the shape of a hysteresis loop necessary in such material. H7C1 was developed over 10 years ago and can not compete with newer ferrites. The conclusions from the comparison are as follows

- there is no best material which covers the whole high frequency range,
- MnZn ferrites are best below 2.4 MHz,
- NiZn ferrites are best above 2.4 MHz,
- square loop ferrites have about 3 to 5 times more losses than low-loss ferrites.

This comparison may serve only as a guideline, because the losses vary between different samples of the same ferrite due to slightly different sintering conditions or chemical composition. In addition the presence of a bias field alters the loss characteristics, as was shown in Section 3.5, and therefore the above conclusions may change in such cases.

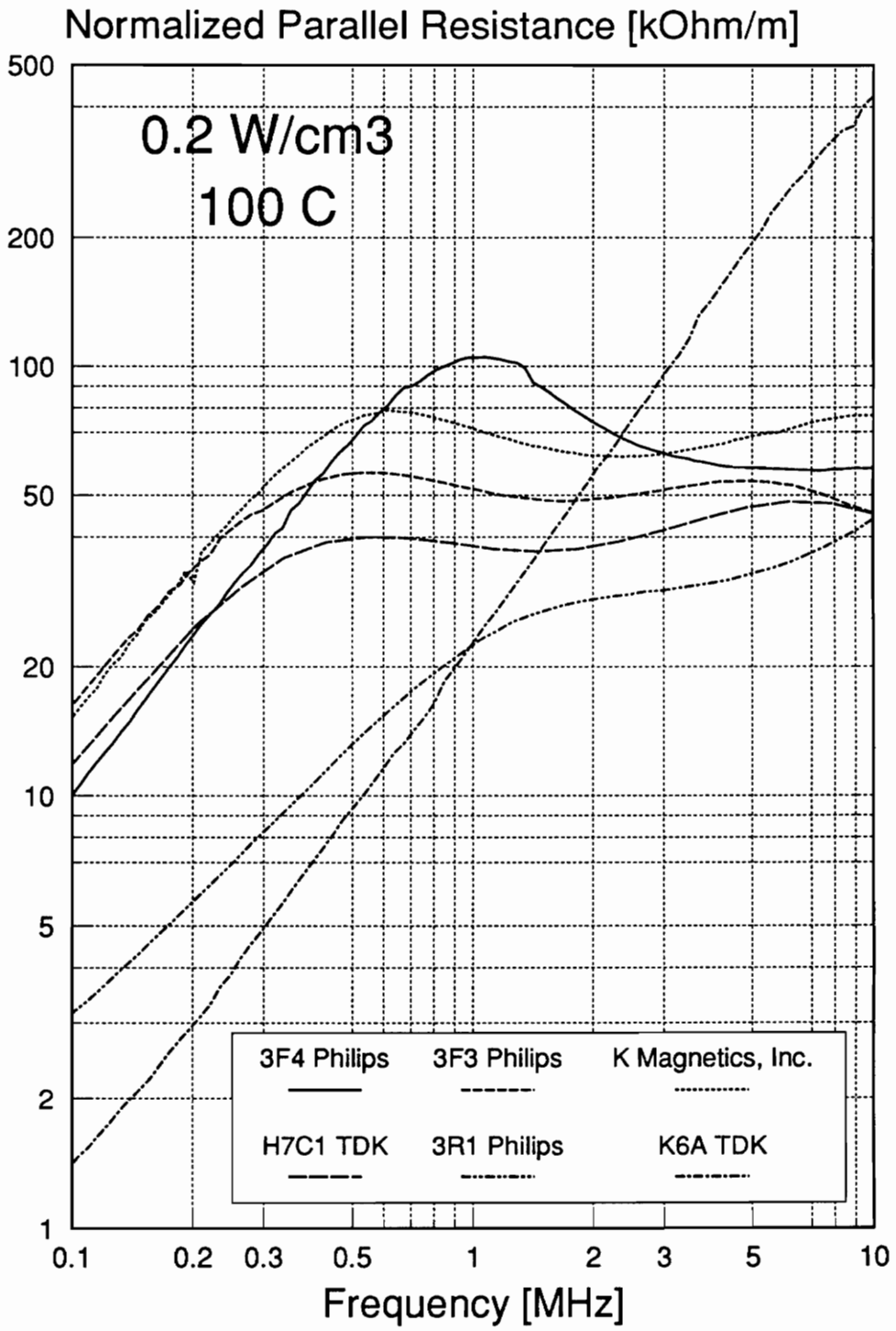

Fig. 3.73. Comparison of normalized parallel resistance in MnZn, MnMg, and NiZn ferrites without bias field at 100 ℃ and 200 mW/cm³.

Chapter 4

Optimization of Power Transformer and Inductor Design

4.1 Design Considerations

Some limiting factors in the design of the high frequency magnetic components include:

- maximum operating temperature,
- maximum flux density in the magnetic material at the operating temperature,
- power handling capability.

The temperature has a damaging effect on a winding insulation and thus on the reliability of the component. Another temperature effect is related to the magnetic properties of the core. Every magnetic material can be magnetized only to a finite magnetization characterized by saturation flux density. It is not practical to operate up to saturation, because in the vicinity of saturation, permeability decreases dramatically, and saturation flux density decreases with temperature. Both factors combined may lead to thermal runaway, saturation of the core, and permanent damage to the magnetic component and other components in the circuit, particularly semiconductors. Assume that the magnetic component is excited with a certain ac voltage that heats up its core due to the induced magnetic flux changes, and that the winding carries a certain current that causes power dissipation in the conductors. Furthermore, for simplicity of the analysis let us assume that the voltage and current excitations depend entirely on the external circuit, and the changes in voltage and current due to the temperature of the magnetic component are negligible.

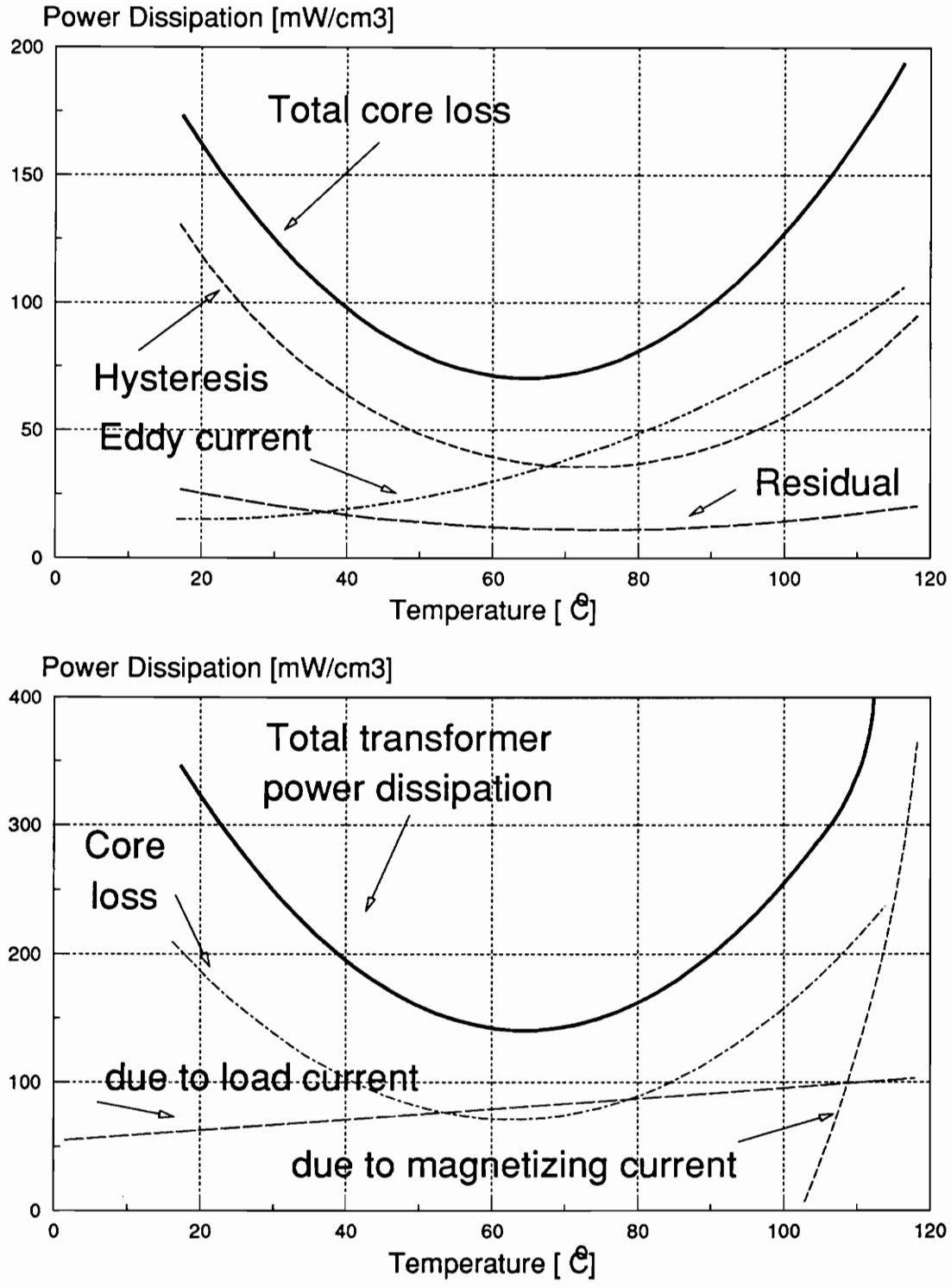

Fig. 4.1. Temperature dependence of the core loss and total loss in the transformer.

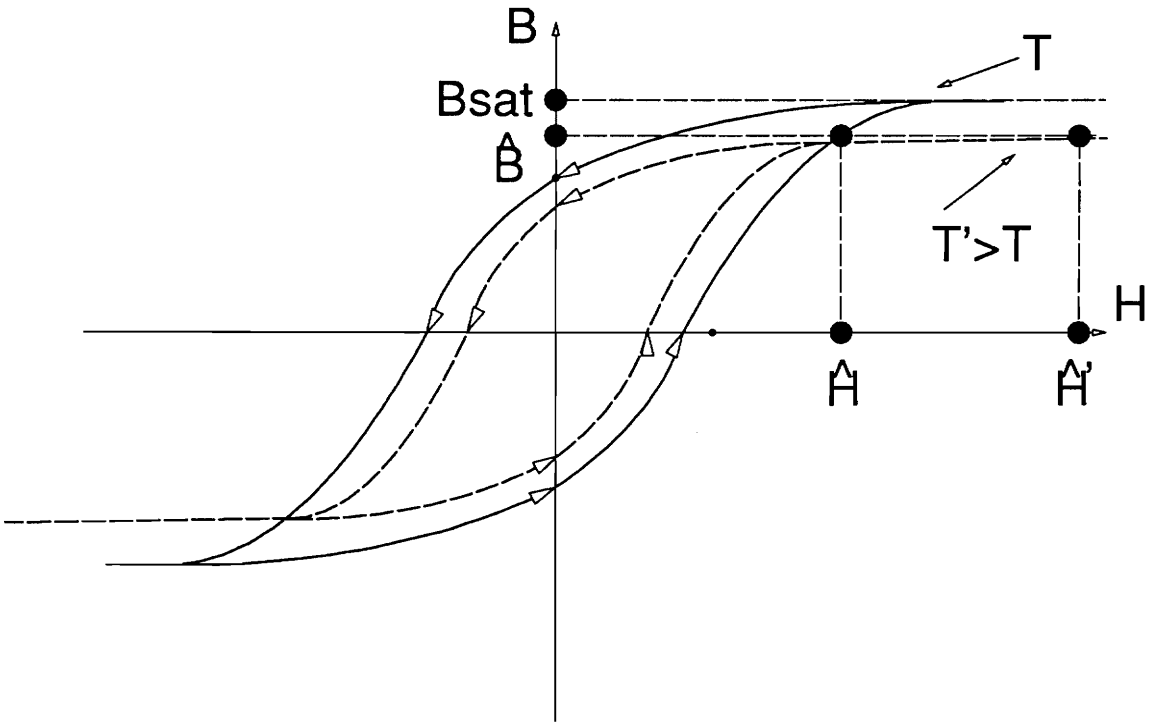

Fig. 4.2. Temperature dependence of the B-H loop. If the core operates at constant flux density close to saturation, the elevated temperature increases required magnetic field and, thus, magnetizing current.

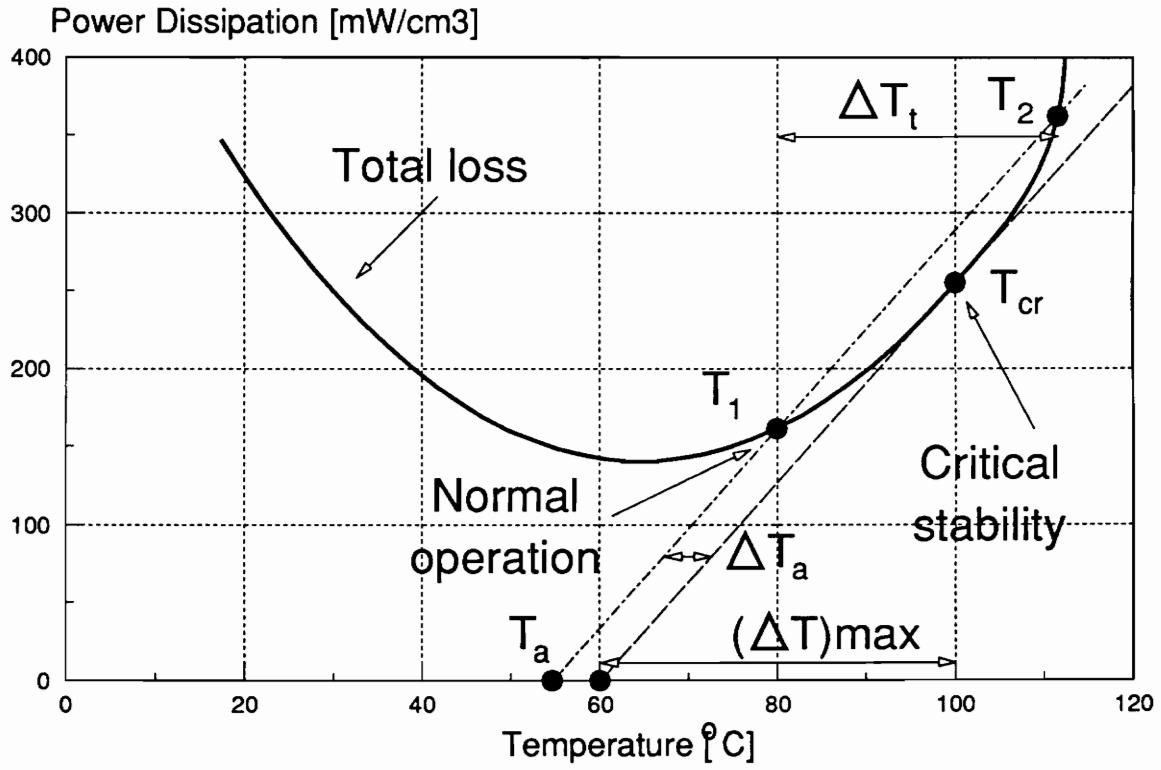

Fig. 4.3. *Thermal stability of the power transformer. A temporary increase of the transformer loss and its temperature above T_2 results in thermal runaway. Similarly, an increase in ambient temperature causes much greater increase in the transformer temperature. If the transformer temperature exceeds T_{cr}, thermal runaway occurs. The maximum stable temperature difference between the core and the ambient, ΔT_R, can be determined from the slope of the loss curve.*

This is a reasonable assumption since most power magnetic components (except resonant inductors) are driven by an ac voltage source. A temperature dependence of a core and total losses in the power transformer is shown in Fig. 4.1. The losses in the magnetic materials can be represented by a U-shaped curve with a minimum at the temperature of minimum crystal anisotropy. The losses in the winding are due to a load current and the magnetizing current. Since the load current is assumed to be independent of the temperature of the transformer, the related conduction losses are proportional to the temperature of the transformer due to a linear increase of a copper resistivity with the temperature at any frequency. When skin and proximity effects are substantial, the winding loss dependence on temperature is nonlinear due to variation of skin depth with temperature.

If the core is large and ferrite resistivity low, then there may be considerable contribution from eddy current losses. Due to the semiconducting properties of ferrites, eddy current losses increase rapidly with temperature. An increased temperature reduces also saturation flux density of the magnetic material, as shown in Fig. 4.2. If the flux excitation due to an applied voltage is constant, the magnetizing current increases rapidly at flat portions of the B-H curve and thus contributes an additional conduction loss to the transformer and other components. The saturation flux density decreases with temperature and reaches zero at the Curie temperature. Therefore, manufacturers usually specify a maximum permissible flux density, which should not be exceeded for reliable operation at certain temperature [275]. All discussed losses are added together and plotted against the thermal resistance of the core in Fig. 4.3.

During normal operation the transformer reaches temperature T_1. If the ambient temperature is constant and the transformer temperature increases temporarily due to transient voltage or current, the transformer temperature returns to the equilibrium T_1, unless it exceeded T_3 during the course of the transient. In the latter case the temperature increases even after transient because above T_3 the power dissipated in the transformer (thick line) exceeds its dissipation capability (chain line). The maximum allowed temperature difference due to transient, $\Delta T_t = T_3 - T_1$, thermal capacity of the transformer, duration of the transient, and the excessive

power dissipated during transient determine stability of the transformer.

The second instability may arise under a nominal power dissipation in the transformer when the ambient temperature is elevated by ΔT_a. In such case the equilibrium temperature T_1 increases towards T_{cr}. When $T_1 = T_{cr}$, any further increase of ambient temperature leads to the thermal runaway because the transformer loss is greater than its heat dissipation capability at any temperature. The flatness of temperature characteristics of transformer loss can be expressed by ΔT_{max}. The greater the ΔT_{max}, the flatter the temperature characteristics and lower risk of thermal runaway. In order to avoid thermal runaway the transformer design specification must include the worst case of voltage and currents, including transient conditions.

At high frequencies the core cannot be driven to the maximum permissible flux density since the losses in the core increase with operating frequency. For small convection cooled transformers, the frequency above which the flux density has to be derated depends on the volume of the core and core material properties. Inductors with a negligible core loss due to an ac component of the magnetic flux do not need derating of the flux density. Only devices with a derated flux density due to a thermal limitation will be considered in the remainder of this chapter. The design procedure for saturation-limited devices was presented by Mulder [276].

The important factor in the design of the magnetic component is its power rating. Since the core and copper losses depend individually on the voltage and current rather than on their product, the power magnetic components need to be designed to handle a total power including both active and reactive parts. Therefore, the power factor of a load driven by the transformer is of a great importance, especially in resonant converters where magnetic components must handle a substantial amount of a reactive power. If the output of the power circuit employs rectification, the type of rectifier also influences the power factor, and an efficiency of the rectifier determines the amount of the active power that has to be delivered by the transformer.

The balance of the core and copper loss can be adjusted by changing the number of turns. Larger number of turns yields lower flux density in the magnetic core, but higher current density in the windings. Therefore, if winding losses exceed core losses, the number of turns must

be reduced.

In the following sections the modeling of the winding and the design procedure for the transformer and inductor will be given.

4.2 Winding Loss Calculation

Low frequency conduction losses are determined by the amount of current and the resistivity of the copper. At higher frequencies, skin effect and proximity effect introduce additional losses. The skin effect loss is due to the current crowding at the surface of the conductor at high frequency. Proximity loss is due to the currents induced in the conductor by a magnetic field from neighboring conductors.

4.2.1 Dowell One-Dimensional Model

The winding losses in the transformer were analyzed by Bennet, *et al.*, [277] and Dowell [278] using a one-dimensional model. In order to use the one-dimensional model, Dowell assumed that the magnetic field is parallel to the winding layers due to the presence of the high-permeability core. He converted a layer of round wires to a layer of square wires of the same cross-section and then to a conducting sheet of equal width and resistance. In the process he modified conductivity and a skin depth of the original conductors. The conversion is shown in Fig. 4.4. The resulting ratio of ac to dc resistance of a multilayer winding is [279]:

$$F_R = F_{RS} + F_{RP} \quad , \tag{4.1}$$

where the skin factor can be expressed as:

$$F_{RS} = \frac{\xi}{2} \frac{\sinh\xi + \sin\xi}{\cosh\xi - \cos\xi} \quad , \tag{4.2}$$

and the proximity factor of a winding with n layers carrying the same current in each layer is

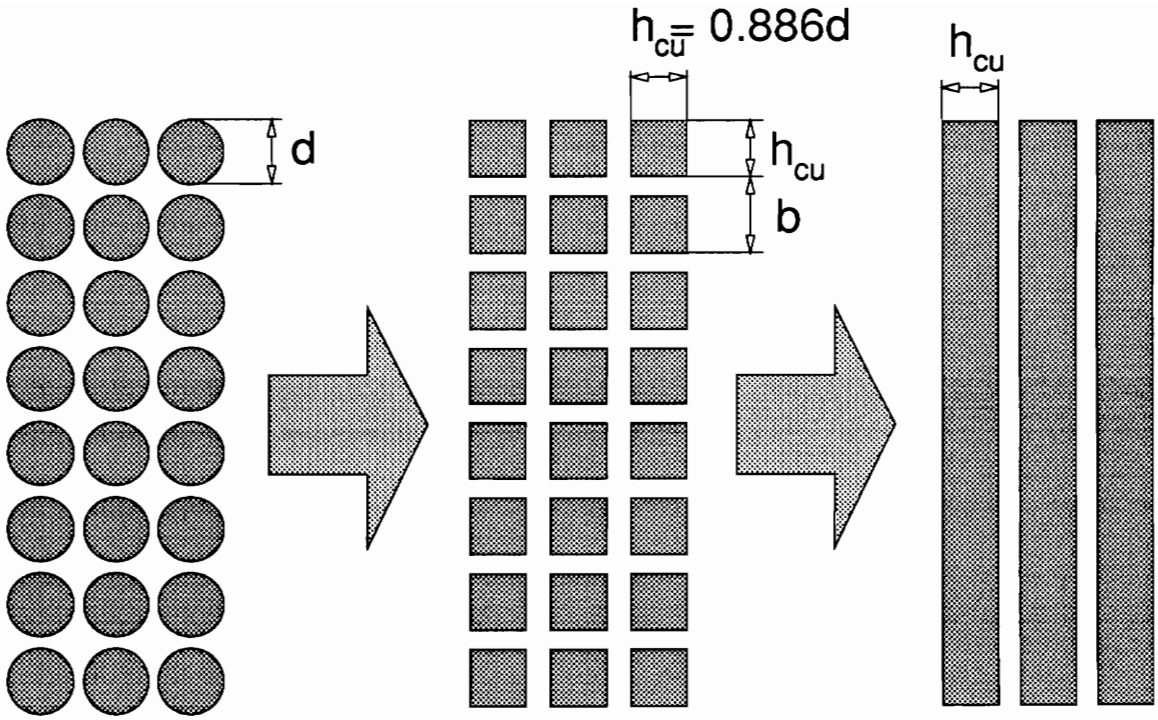

Fig. 4.4. *Conversion of round wires into conducting sheets. The area of square wires is equal to that of round wires. The sheet thickness is equal to the size of the square conductors. The resistivity of the sheet conductor is higher than that of square conductors to compensate for increased cross-section area in the last step of the transformation.*

$$F_{RP} = \frac{\xi}{6}\left(4n^2 \frac{\alpha^2+\alpha+\beta^2+1}{\alpha^2-2\alpha+\beta^2+1} - 1\right)\frac{\sinh\xi - \sin\xi}{\cosh\xi + \cos\xi} \quad , \quad \text{and} \tag{4.3}$$

$$\xi = \frac{\sqrt{\pi\eta}\,d}{2\delta} = \frac{\pi d}{2}\sqrt{\eta f \mu_0/\rho} \quad , \tag{4.4}$$

where

α - real part of the field ratio at the inner and outer surfaces of the winding,

β - imaginary part of the field ratio at the inner and outer surfaces of the winding,

n - number of layers in the winding.

The derivation is shown in the Appendix A. The field ratios for each winding can be determined from magnetomotive force (MMF) diagrams. In all inductors and two-winding transformers, $\alpha = \beta = 0$. In the transformers with multiple windings and negligible magnetizing current, the factor α is different for each winding, but $\beta = 0$. If the magnetizing current in the transformer is significant, then β is not equal to zero even in the transformer with only two windings. Eddy current losses consist of two parts. The first part is independent of the number of layers and represents the skin effect. The second part represents the proximity effect and depends on the number of layers and the external field. Such division occurs because the current density distributions due to skin and proximity effect are orthogonal as shown by Manneback [280].

4.2.2 Phenomenological One-Dimensional Model

Undoubtedly the conversion from round to square conductors employed by Dowell leads to a change in the magnetic field distribution and introduces an error in the estimation of losses. It is possible to analyze losses in the windings without any assumption about magnetic field distribution within the layer. The only assumption that is made in this one-dimensional model is that the magnetic field is parallel to winding layers. Under such assumption, skin and

proximity factors can be found experimentally by analysis of the ac to dc resistance in multi-layer transformer windings. Consider a two-winding transformer with no external field ($\alpha = \beta = 0$). Then the losses may be expressed in the following form (A.19):

$$F_R = F_{RS} + F_{RP} = F_{RS} + \frac{4n^2 - 1}{3} F_{RP0} \quad , \tag{4.5}$$

where F_{RP0} is an ac to dc resistance due to proximity effect in the first layer of an outside winding where the magnetic field on one surface is zero. Since functions F_{RS} and F_{RP0} are not functions of the number of layers, they can be found experimentally by comparing the windings with different number of layers. The following set of equations was used to find skin and proximity factors:

$$\begin{cases} F_{Ri}(f) = F_{RS}(f) + \dfrac{4n_i^2 - 1}{3} F_{RP0}(f) \\ F_{Rj}(f) = F_{RS}(f) + \dfrac{4n_j^2 - 1}{3} F_{RP0}(f) \end{cases} , \tag{4.6}$$

where i and j denote two different transformers wound with the same wire, on identical bobbin, but with different number of layers. Since the wire size is the same for both transformers the skin effect factor, F_{RS}, and the proximity effect factor of the first layer, F_{RP0}, are the same for both transformers.

Using this method and the measurement results shown in Fig. 4.5, the skin and proximity factors and their models were found and are shown in Fig. 4.6 and 4.7, respectively. The dc resistance is assumed equal to ac resistance at 1 kHz. The skin factor and proximity factor have asymptotes at low and high frequencies. The skin effect is constant at low frequencies due to a dc resistance, and proportional to $f^{1/2}$ at high frequencies because the skin depth is inversely proportional to $f^{-1/2}$. The proximity effect is proportional to f^2 as shown by Butterworth [281, 282] and to $f^{1/2}$ at higher frequencies due to reduction of skin depth. Using a combination of asymptotes, the following model was fitted to experimental data to minimize errors:

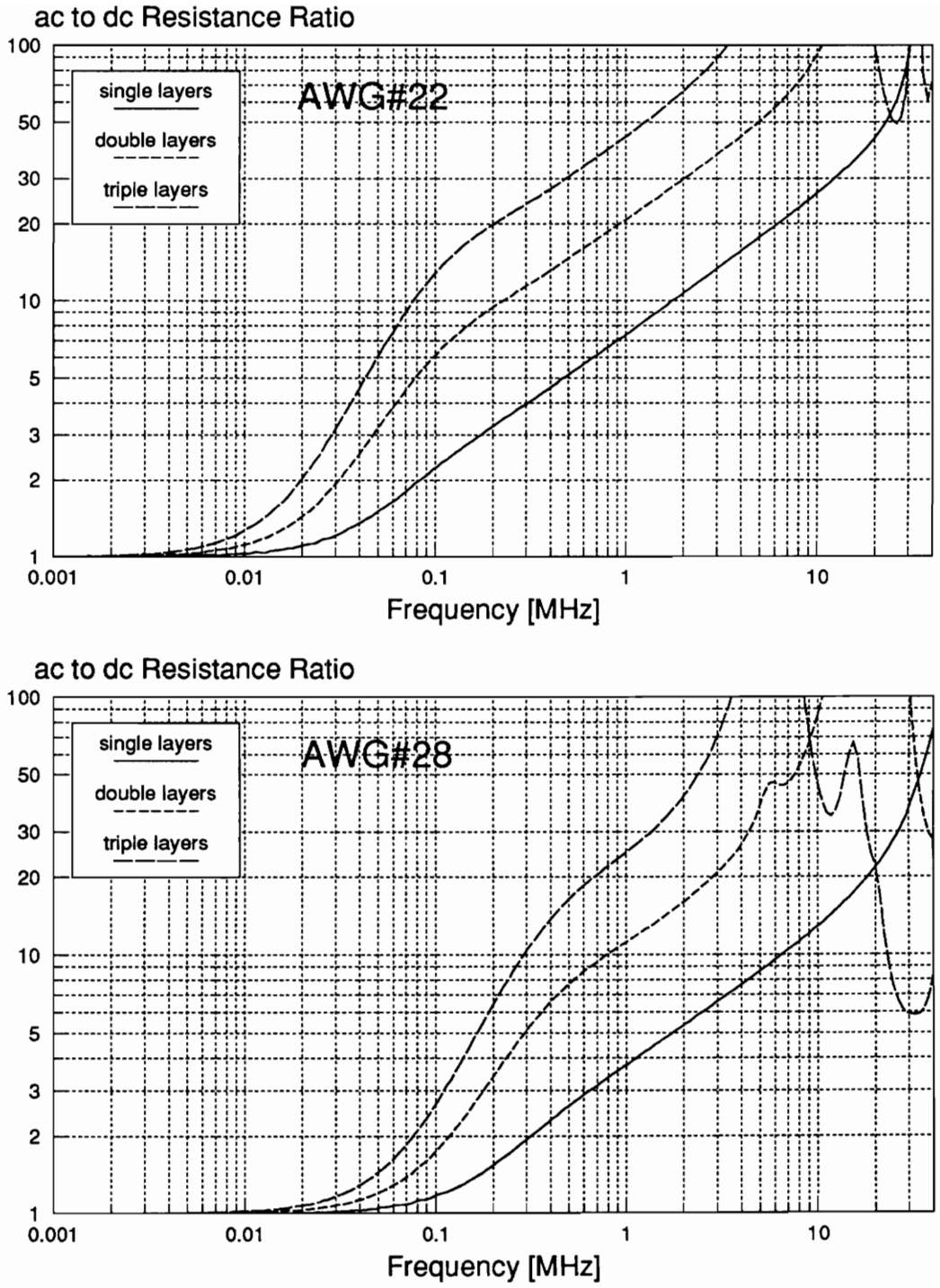

Fig. 4.5. AC to dc resistance of solid wire windings. The measurements were performed on transformers with identical primary and secondary windings.

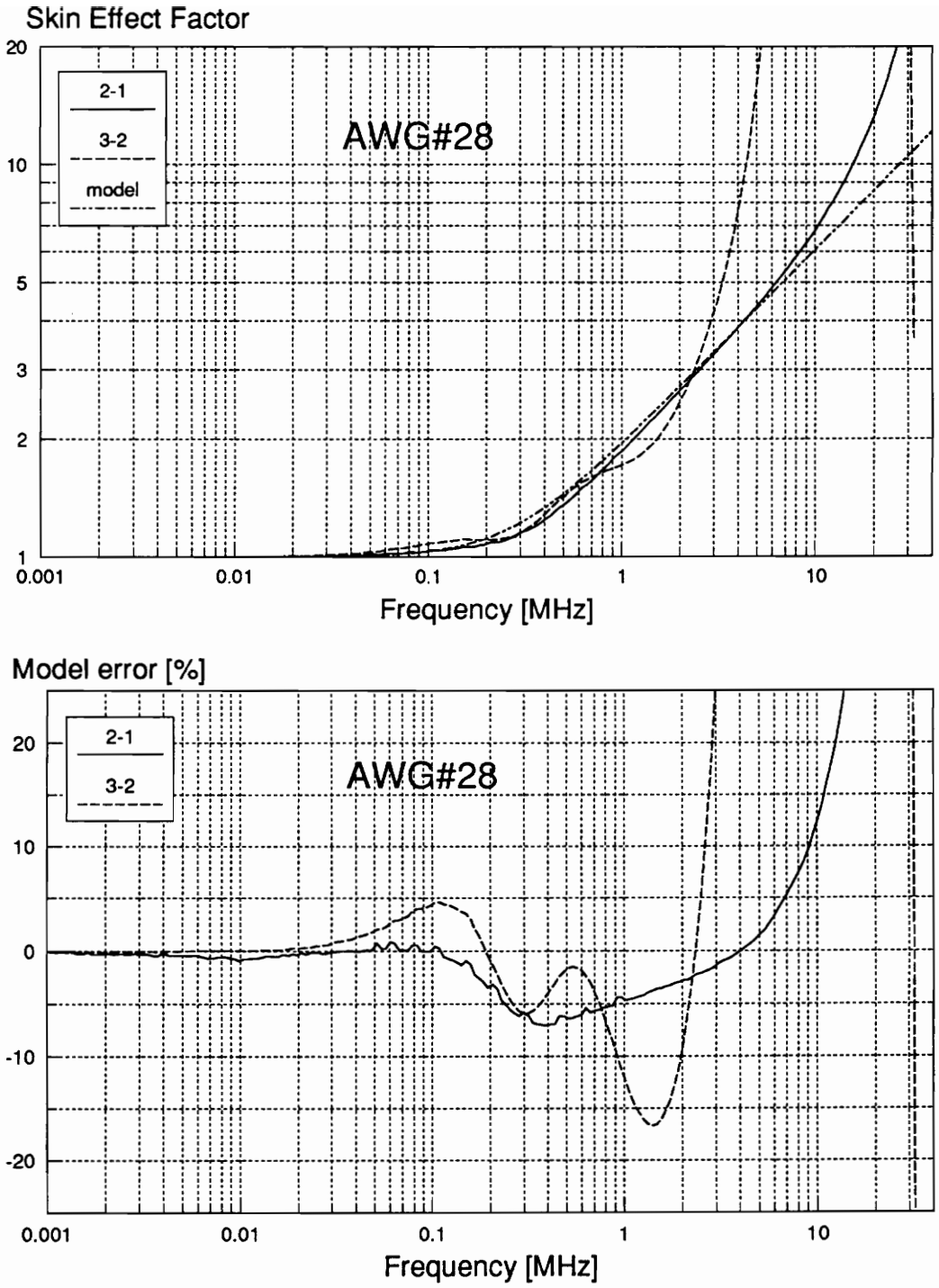

Fig. 4.6. Skin effect calculated from combinations of characteristics of different transformers and the skin model error. 2-1 indicates calculation by comparing two-layer windings with single-layer windings.

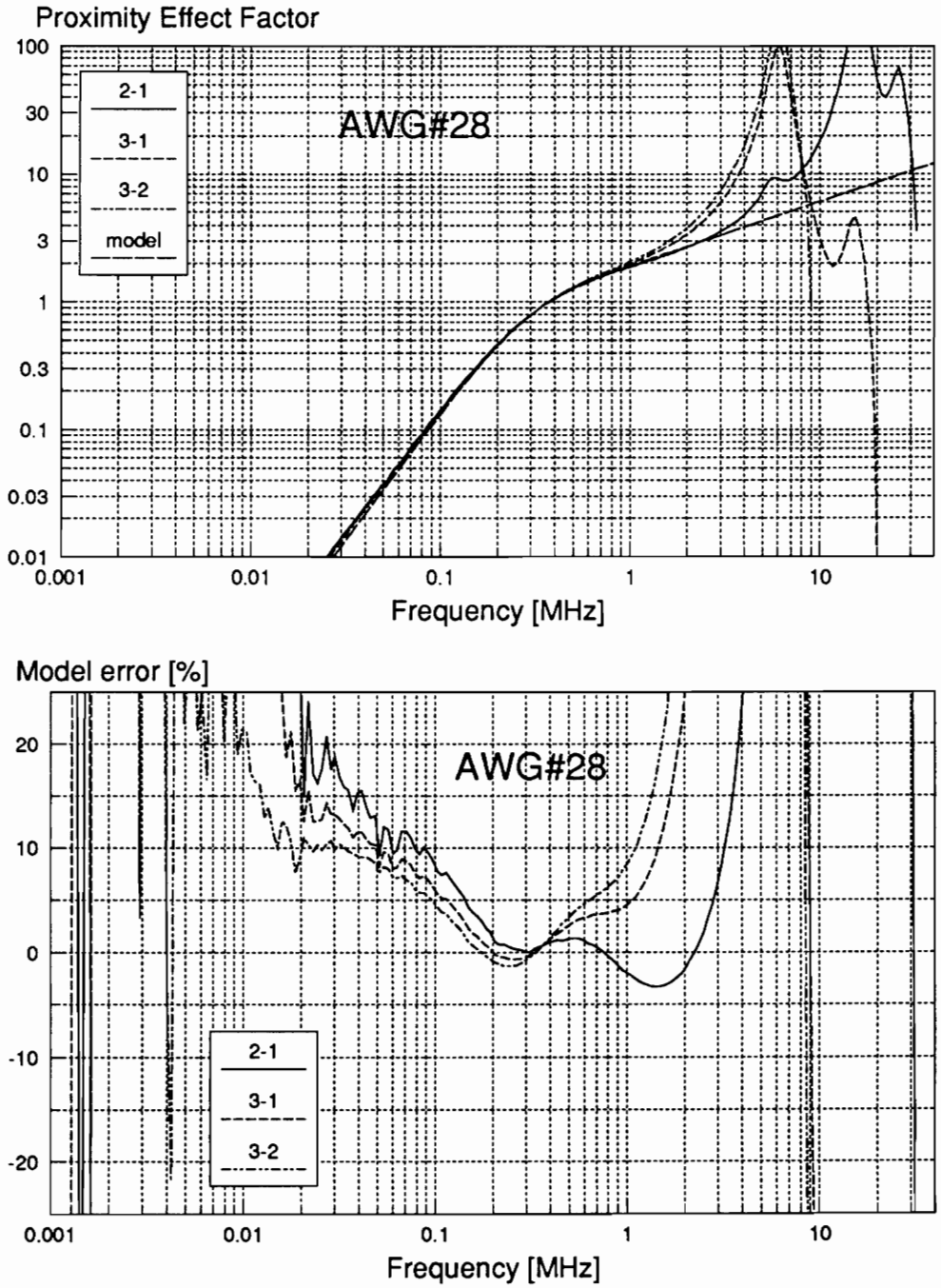

Fig. 4.7. *Proximity effect calculated from combinations of characteristics of different transformers and the proximity model error. Numbers indicate number of layers in each winding.*

$$F_{RS} = \sqrt[4]{1 + 1/\phi^4} \quad , \tag{4.7}$$

$$F_{RP} = \frac{1}{\sqrt[4]{\phi^8 + \phi^2}} \quad , \quad \text{and} \tag{4.8}$$

$$\phi = \frac{8\delta}{\pi d \eta_R} \quad , \tag{4.9}$$

where η_R is spacing factor of round wires, or as a function of frequency:

$$F_{RS} = \sqrt[4]{1 + (f_\delta / f)^2} \quad , \tag{4.10}$$

$$F_{RP} = \frac{1}{\sqrt[4]{(f_\delta / f)^4 + f_\delta / f}} \quad , \quad \text{and} \tag{4.11}$$

$$f_\delta = \frac{64}{\pi^3 d^2 \mu_0 \sigma \eta_R^2} \quad . \tag{4.12}$$

The errors at high frequencies where the leakage inductance resonates with winding capacitance where not minimized since the model does not account for this resonance. Modeling of the resonance region has no practical value because the winding losses in that region are prohibitively large for any application.

Since this model does not assume the structure of the winding layer but is based solely on the one-dimensional assumption and fitted to the experimental data, it is referred to as phenomenological model. This model is employed in Section 4.3 to verify accuracy of the one-dimensional magnetic field approximation.

4.2.3 A Uniform Field Two-Dimensional Model

Ferreira [283] suggested that a two-dimensional model is better for an analysis of the transformer windings with round conductors than one-dimensional models. The expression for ac resistance of a layer of round conductors which he derived can be used to find a formula for an ac to dc resistance ratio of the *n*-layer winding, substituting in Eq. (4.8):

$$F_R = \frac{\gamma}{2}\left[\frac{\mathrm{ber}\gamma\,\mathrm{bei}'\gamma - \mathrm{bei}\gamma\,\mathrm{ber}'\gamma}{\mathrm{ber}'^2\gamma + \mathrm{bei}'^2\gamma} - \frac{2\pi}{3}\left(4n^2 \frac{\alpha^2+\alpha+\beta^2+1}{\alpha^2-2\alpha+\beta^2+1} - 1 \right) \frac{\mathrm{ber}_2\gamma\,\mathrm{ber}'\gamma + \mathrm{bei}_2\gamma\,\mathrm{bei}'\gamma}{\mathrm{ber}^2\gamma + \mathrm{bei}^2\gamma} \right], \tag{4.13}$$

where $\gamma = d/\delta\sqrt{2}$, and $\mathrm{ber}_m(z)$ and $\mathrm{bei}_m(z)$ are the Kelvin functions which can be calculated from the Bessel functions of the complex argument $\mathrm{ber}_m(z)+j\,\mathrm{bei}_m(z) = J_m(j^{3/2}z)$ and $\mathrm{ber}'(z)+j\,\mathrm{bei}'(z) = -j^{3/2}J_1(j^{3/2}z)$.

The accuracy of the model is verified in the following section.

4.3 Experimental Verification of Winding Modeling

In order to assess the practical value of one- and two-dimensional winding models, and analyze the sources of modeling errors, all models described in Section 4.2 were verified experimentally.

A total of seven transformers were wound and tested. The measurements were done with the Hewlett-Packard 4194A impedance analyzer equipped with the HP16047C high-frequency impedance fixture. The integration time was set to medium, and the averaging was set to eight. Each measurement consisted of two hundred data points between frequencies of 1 kHz and 40 MHz equally distributed on the logarithmic scale. The dc resistance was assumed equal to the ac resistance at 1 kHz. The basic measurement error of the instrument was 0.17 percent.

4.3.1 Solid Wire Windings

Three transformers were wound on a LP23/8 bobbin with a winding breadth of 15.2 mm and a diameter of 7.7 mm. The primary and secondary windings were identical and each consisted of one, two, or three layers of 42 turns of AWG #28 wire insulated with 1-mil thick insulation tape. The corresponding outer diameters of the windings were 9.3 mm, 10.8 mm, and 12.2

mm. Another three transformers were wound on a LP22/13 bobbin with a winding breadth of 14.1 mm and a diameter of 10.8 mm. The primary and secondary windings were identical and each consisted of one, two, or three layers of 20 turns of AWG #22 wire insulated with 1-mil thick insulation tape. The corresponding outer diameters of the windings were 13.3 mm, 16.3 mm, and 19.1 mm. The measurement results and model predictions are shown in Fig. 4.8-4.11. Both one-dimensional and phenomenological models carry about 4 percent error when compared to the measured data of transformers with AWG #28 wire, and 8 percent in transformers with AWG #22 wire. In single layer windings the error is small but it increases with the number of layers. Therefore, the principal source of error is an incorrect modeling of the proximity effect. By comparing the transformers with a thin and thick wire, it is reasonable to conclude that the error is inversely proportional to the number of wires in a layer and proportional to the number of layers. The dependence on both factors can be combined into a dependence on the aspect ratio (*i.e.*, height divided by breadth) of the winding. The error can be expressed by an empirical formula:

$$\frac{\Delta F_R}{F_R} \cong \frac{h_w}{4\, b_w} \quad , \tag{4.14}$$

where

h_w - total height of all windings, and

b_w - breadth of the windings.

The dependence of error on the aspect ratio suggests that the error originates at the ends of the windings. The magnetic field there abandons the direction parallel to the winding layers. Therefore, the path of the flux lines is shorter than the geometrical path. The shorter path carrying a fixed amount of current produces a stronger magnetic field than predicted with one-dimensional model. This leads to excessive losses at lower frequencies, resulting in negative model error.

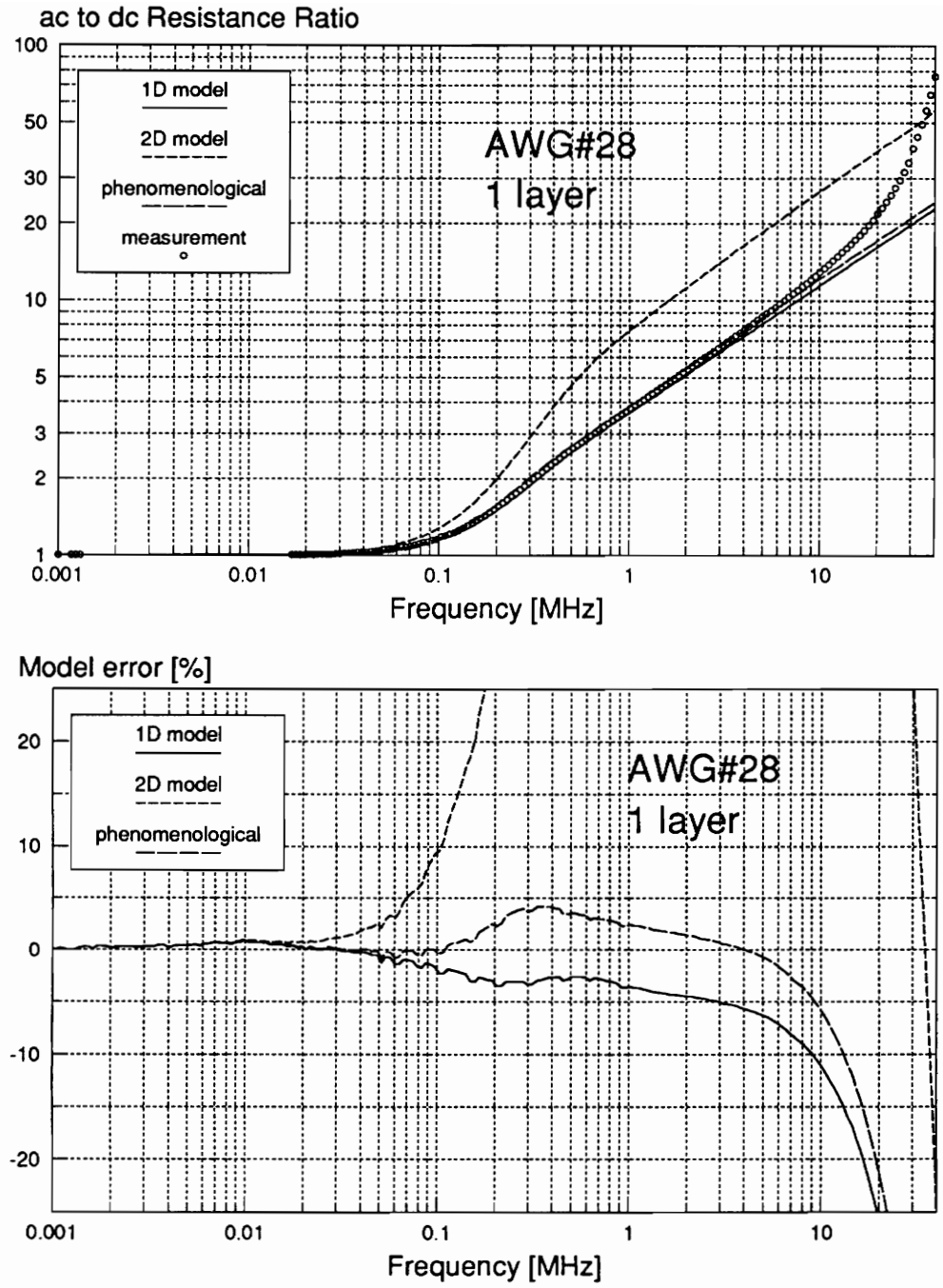

Fig. 4.8. AC to dc resistance ratio and model errors in a transformer with a single layer primary and secondary windings made of AWG #28 wire.

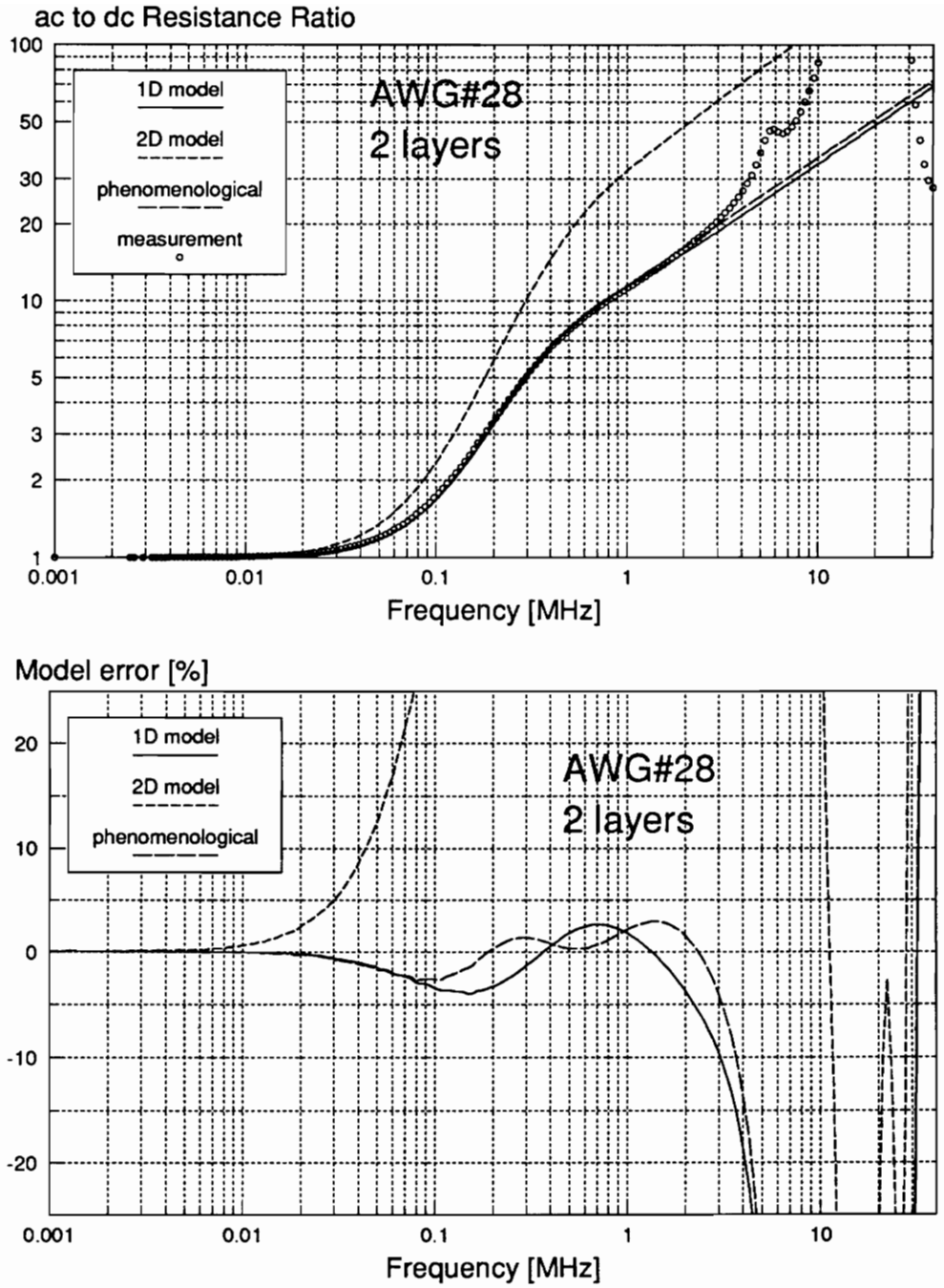

Fig. 4.9. AC to dc resistance ratio and model errors in a transformer with a double layer primary and secondary windings made of AWG #28 wire.

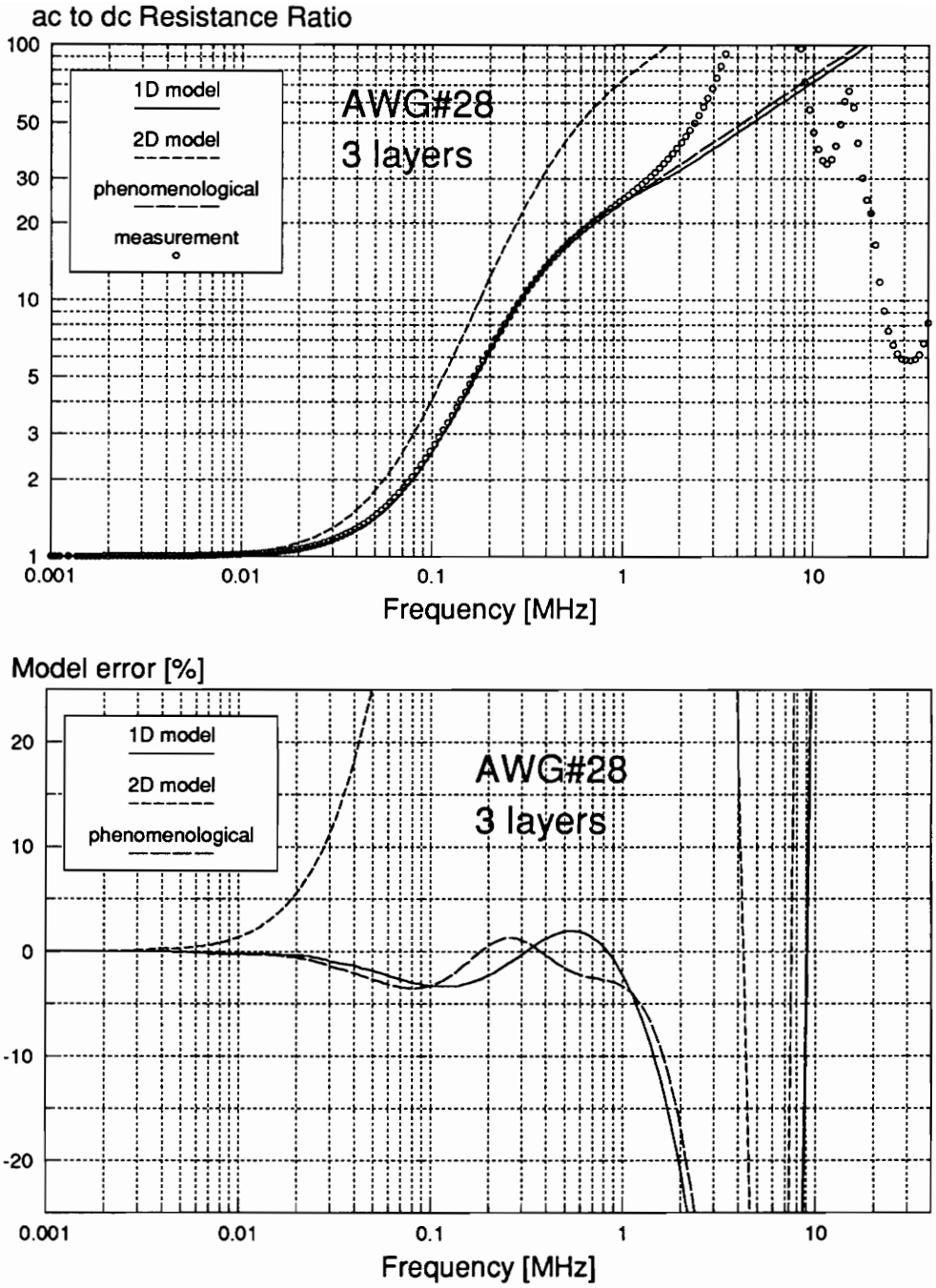

Fig. 4.10. AC to dc resistance ratio and model errors in a transformer with a triple layer primary and secondary windings made of AWG #28 wire.

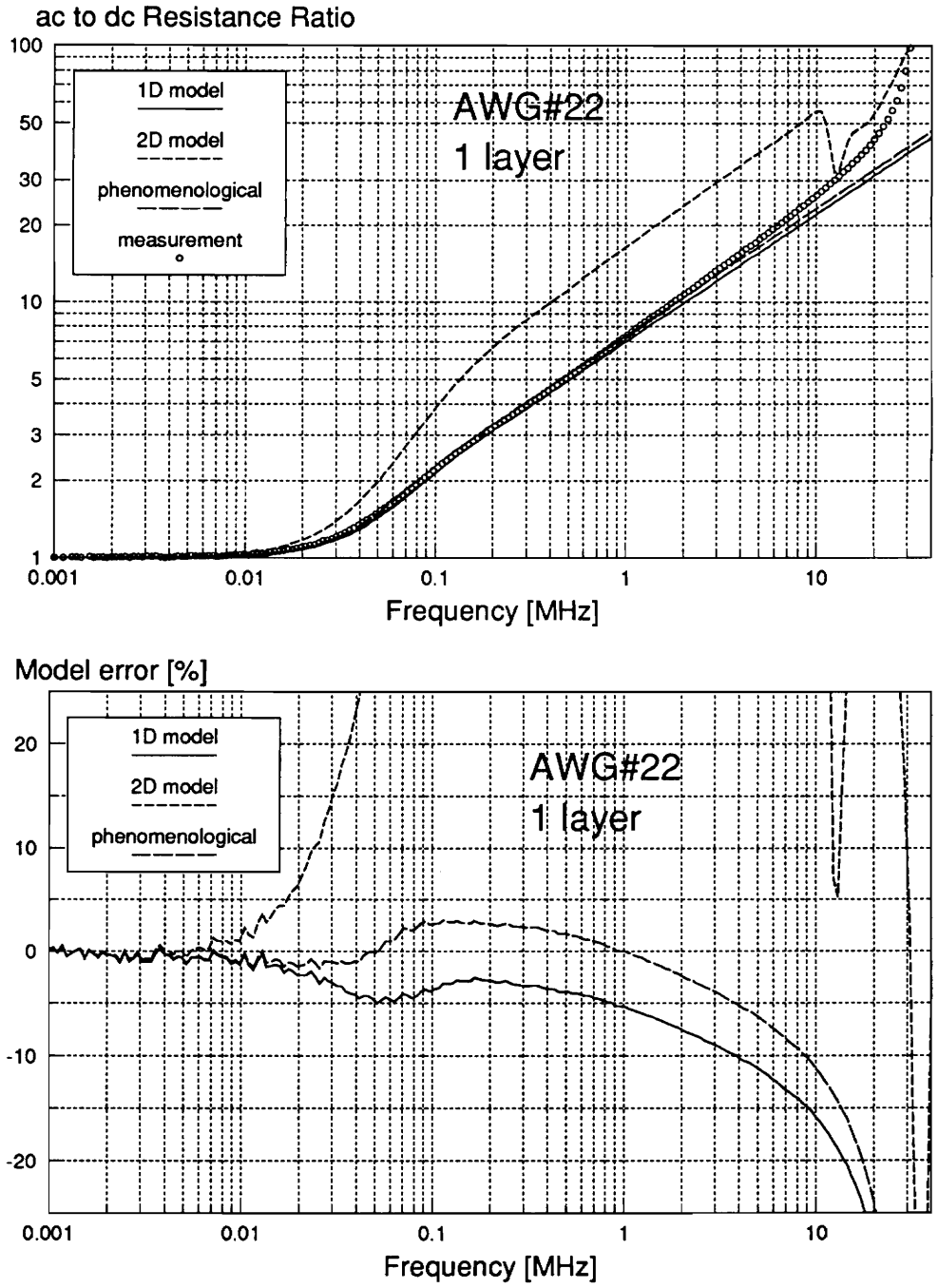

Fig. 4.11. AC to dc resistance ratio and model errors in a transformer with a single layer primary and secondary windings made of AWG #22 wire.

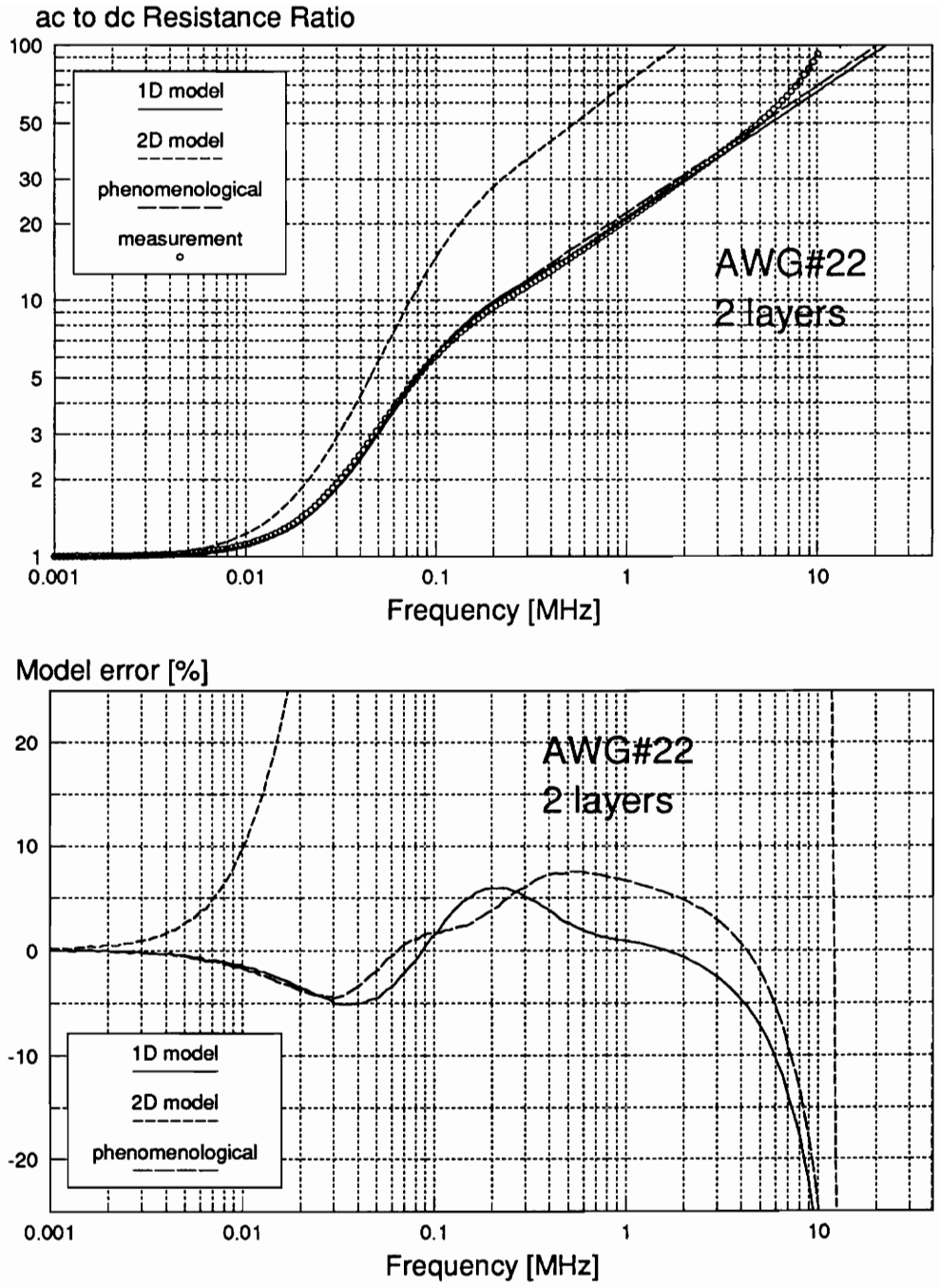

Fig. 4.12. AC to dc resistance ratio and model errors in a transformer with a double layer primary and secondary windings made of AWG #22 wire.

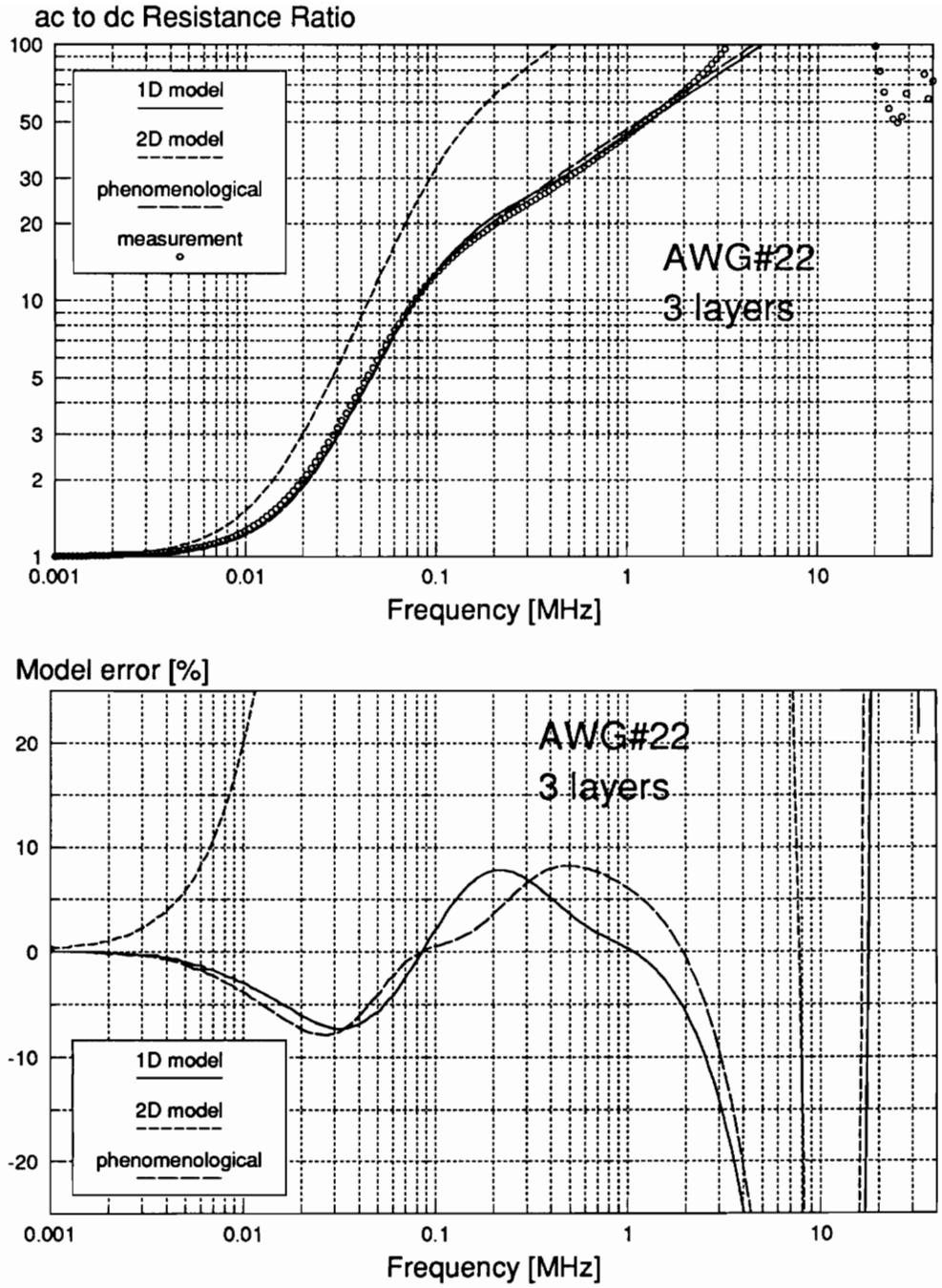

Fig. 4.13. AC to dc resistance ratio and model errors in a transformer with a triple layer primary and secondary windings made of AWG #22 wire.

At higher frequencies, when wire diameter is greater than skin depth, the field lines are forced parallel to the winding layers because they cannot penetrate the winding. Therefore, the bending of the flux lines occurs outside the winding at its ends, thus increasing the length of the flux path and lowering the amplitude of the magnetic field and losses.

The model error in this range is positive due to an overestimation of losses. At even higher frequencies, the flux path shortens asymptotically to theoretical value, since the flux lines follow conductors more closely. Then the model error drops to near zero. Finally at the highest frequencies, a resonance of the leakage inductance with the winding capacitance introduces resonant losses not predicted by a one-dimensional model. This resonance can mask some of the field distribution effects described above. The best presentation of all described errors exists in a transformer with double layer windings made of AWG #22 wire (Fig. 4.12).

One-dimensional Dowell model and phenomenological model have very similar accuracy, despite different assumptions about layer structure. The conversion from round wires to conducting sheets does not introduce any significant error. Therefore, the error originates from the one-dimensional approximation which neglects end effects in the windings. Despite that, one-dimensional models have good accuracy in wire windings and are suitable for design purposes.

The uniform field two-dimensional model, proposed by Ferreira, is not suitable for transformer winding modeling since the error substantially exceeds the errors introduced by simpler models. This is probably due to an unreasonable assumption of the uniform field in the windings at high frequencies. The calculation of the non-uniform field and eddy current losses due to such a field is probably much more complex compared to one-dimensional models. The two-dimensional analysis of losses due to the wire shape is not necessary in light of quite accurate results from one-dimensional models. Instead, the two-dimensional analysis has to be employed to find the frequency-dependent variation of magnetic field in the winding layer due to a finite breadth of the winding. The corrected value of the field could be used in one-dimensional models to improve their accuracy.

4.3.2 Litz Wire Windings

The last transformer was wound on a LP22/13 bobbin with identical primary and secondary windings, each consisting of two layers of litz wire with 175 strands of AWG #44. Each layer contained 13 turns, and the outer diameter of the coil was 17.2 mm. The losses in a litz wire windings were calculated using a modified formula, taking into account that all strands in a layer of a litz wire are subjected to the same external field:

$$F_R = F_{RS} + pF_{RP} \quad , \tag{4.15}$$

where p is the number of strands in a litz wire.

Experimental results are shown in Fig. 4.12. Similarly to the solid wire windings, there is an error due to the change of the length of the magnetic flux lines. The error is larger than in solid wire windings, probably due to lesser homogeneity of flux created by a heavy litz wire.

4.3.3 Winding Techniques

Choosing the optimum winding for a high frequency transformer is a quite difficult task due to many variables and complexity of models that determine the winding resistance. Usually the design task is to fill a given core window with the optimum winding. The problem can be illustrated with a normalized diagram shown in Fig. 4.13, created with a one-dimensional model, Eqs. (4.1)-(4.4), with a winding porosity factor $\eta = 0.67$, typical for a solid wire winding. The diagram shows the ac to dc resistance ratio as a function of a MMF winding height normalized to the skin depth. The MMF winding height is defined as the distance between a zero and a peak on the magnetomotive force (MMF) diagram. As the winding height increases, the resistance of the winding increases rapidly. The height of the winding can be increased if a multiple layer winding is used. However, the number of layers necessary to keep the resistance low grows faster then the winding height. Therefore, the higher the winding, the finer the wire

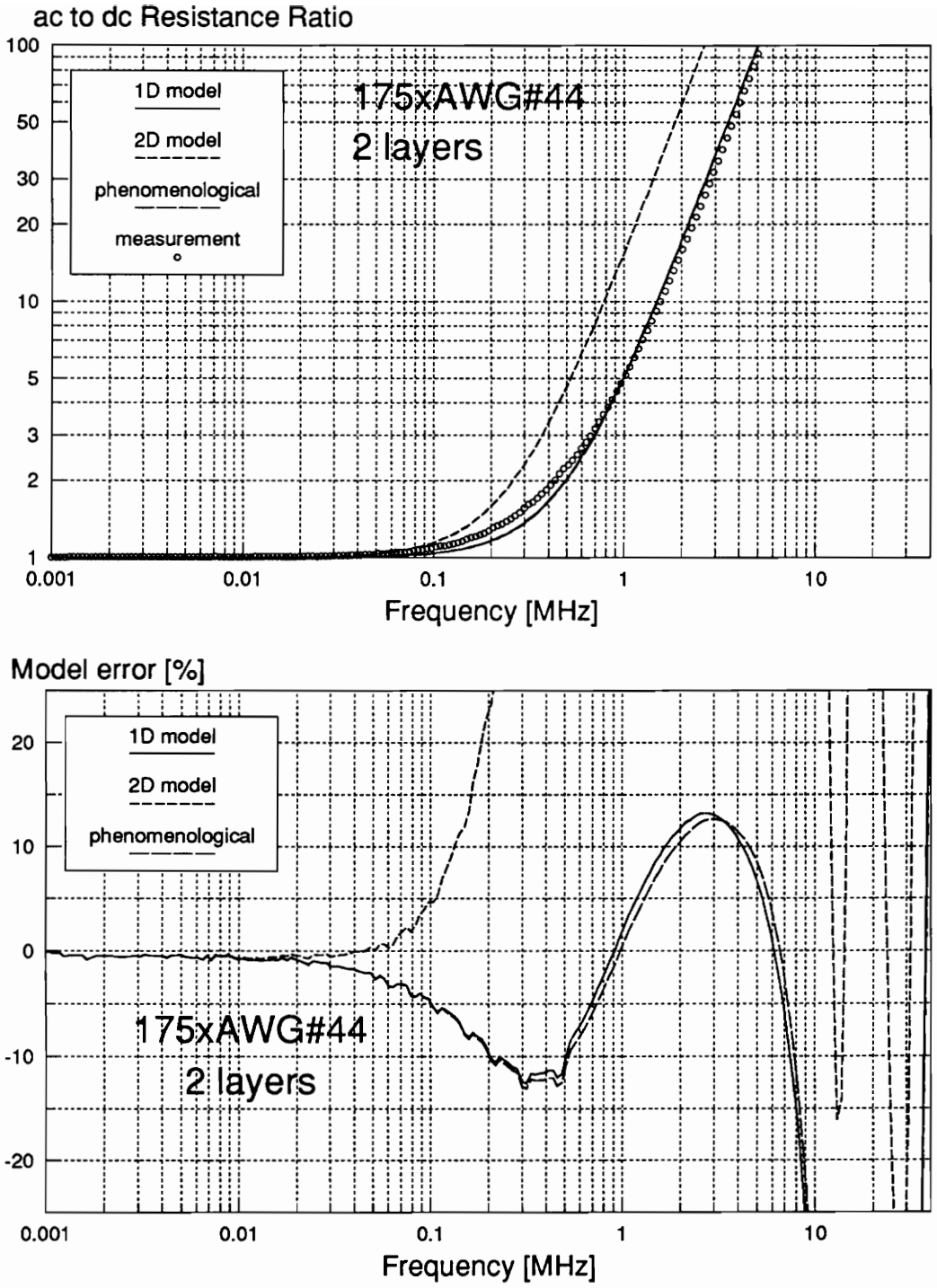

Fig. 4.14. AC to dc resistance ratio and model errors in a transformer with a double layer primary and secondary windings made of litz wire. The one-dimensional and phenomenological models coincide.

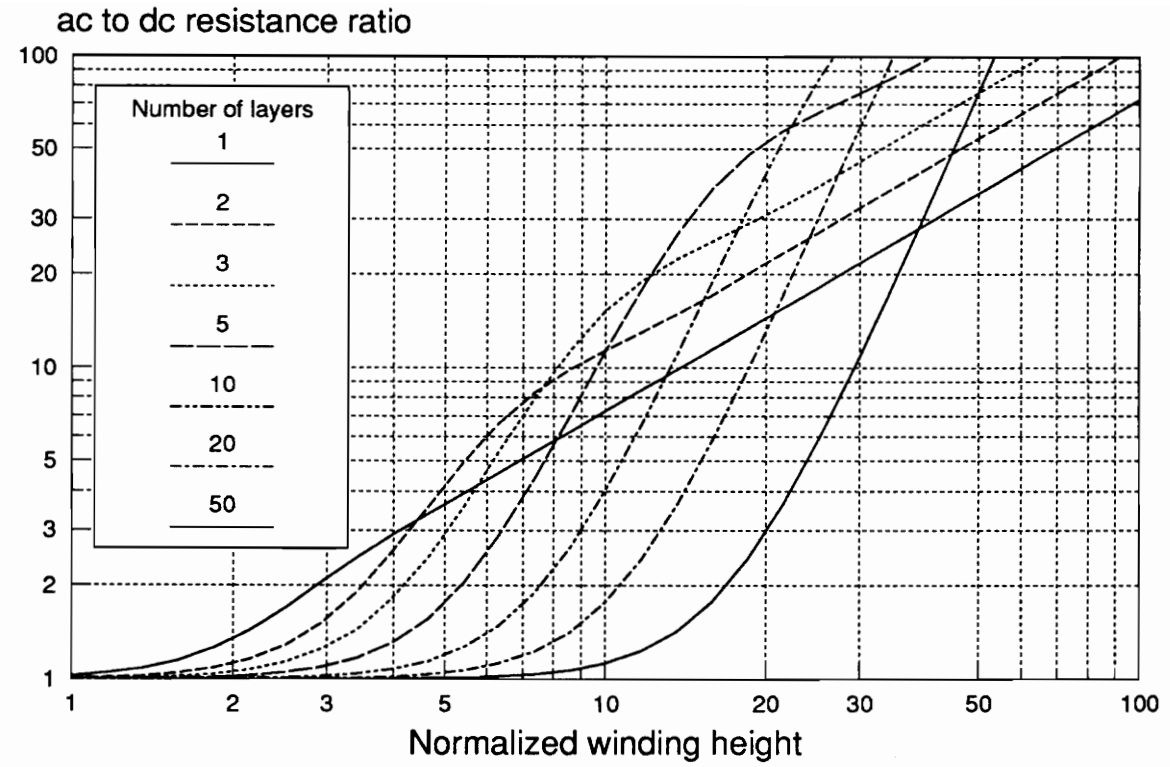

Fig. 4.15. AC to dc resistance ratio of a solid wire winding vs. MMF winding height normalized to the skin depth. Higher winding requires more layers and finer wire to keep the same winding resistance. The MMF winding height is the distance between a zero and a peak in the magnetomotive force (MMF) diagram.

that must be used. For example, instead of a single layer winding with $F_R = 1.4$ ($h_W/\delta = 2$) it is possible to use a seven times higher winding, but with fifty layers made using a conductor with seven times smaller diameter. Therefore, there is a practical limit on the height of the winding in order to keep the resistance at a reasonable value. The finer the wire is, the higher the winding can be wound. A particularly difficult problem occurs in low voltage windings when a number of turns is so small that the alternative is to use either heavy wire or a copper foil. In such case the foil is a better choice than the wire because, despite its larger cross-section area, the current flows only on its surface, and its ac resistance is much higher than the dc value. The major drawback of a foil winding is its sensitivity to a flux component perpendicular to its surface, which occurs particularly at the winding edges. Such flux generates eddy currents parallel to the large foil surface, and thus disproportionately larger loss than the main flux component parallel to the foil surface. Since the one-dimensional model can only account for losses due to the flux parallel to the winding layers, it cannot be used in most cases for foil windings.

A very important factor influencing winding losses is horizontal symmetry, particularly in windings that contain at least a single foil. This is the case even if the foil is used as an electrostatic shield. Any deviation from symmetry results in an increased flux component perpendicular to the foil surface. Such deviations from symmetry are caused by partially wound layers or windings of different breadth.

The principle method of reduction of high-frequency losses is minimization of the winding height. This can be achieved either using a long and low profile bobbin or by interleaving. Although the first method departs from the optimum core shape with minimum magnetic path length and minimum length of turn, it is much easier to manufacture due to smaller number of windings. Interleaving is more costly, but it does not have the restriction of the shape of the bobbin. In high power transformers, the height of the window is so large that the only method to reduce the winding losses is by interleaving the windings. Interleaving is not possible in inductors since they have only one winding. Therefore, high-frequency power inductors need

long, low profile bobbins.

4.4 Core Loss Calculation Using Isoloss Characteristics

The characteristics shown in Chapter 3 and their corresponding models are very useful in analysis of loss mechanisms in ferrites. However, there is also a great need to express them in a form useful for engineering purposes. Since the maximum output power in high-frequency magnetics is limited by both core loss and winding loss, it is desirable to express the core characteristics at constant power dissipation. The first such proposal was made by Stijntes [284] who introduced a performance factor, PF_{200}, which is a product of a frequency and a peak flux density that can be supported in a core at 200 mW/cm^3 power dissipation. It can be expressed in terms of normalized parallel resistance using Eq. (3.22):

$$PF_{200} \equiv \hat{B}f = \frac{\sqrt{P_m R_p}}{\sqrt{2}\pi} = \frac{\sqrt{10^5 R_p}}{\pi} \quad , \tag{4.16}$$

or in terms of the loss factor (3.23):

$$PF_{200} = \sqrt{\frac{\mu_0 P_m f}{\pi \tan\delta/\mu_i}} = \sqrt{\frac{2 \cdot 10^5 f \mu_0}{\pi \tan\delta/\mu_i}} \quad , \tag{4.17}$$

where both R_p and $\tan\delta/\mu_i$ were measured at constant core loss equal to 200 kW/m^3. The introduction of a concept of the performance factor is undoubtedly a significant progress in the representation of loss characteristics for design purposes. It enables a fair comparison between different materials at specific thermal conditions characteristic for actual applications. However, it is defined for a specific core loss of 200 mW/cm^3, while in practical convection cooled and core loss limited designs, the allowed core loss varies from 40 to 500 mW/cm^3, depending on the size of the core [285]. Therefore, for an actual design calculation, a more flexible parameter is desirable. Another desirable feature of such parameter is compatibility with an electric circuit simulation software (for example SPICE) where the core characteristics need to

be represented as circuit components. Both conditions are fulfilled by a normalized parallel resistance expressed as a function of frequency at constant core loss conditions, $R_p(f, P_m)$, referred subsequently as isoloss characteristics. This parameter is closely related to each mechanism of loss and is easily converted to a an equivalent circuit component. For ferrite with dominant permeability mechanism due to domain wall motion, the exact formula for isoloss characteristics can be derived by substituting Eq. (3.53) in Eq. (3.96). The resulting equation is of the third order, and when solved, it yields a quite complicated formula of little practical use. An alternative approach is to use the fact that at most frequencies one type of loss dominates over the other. Therefore an approximate formula derived from Eqs. (3.53) and (3.96) can be used:

$$R_p(f,P_m) \cong \frac{1}{1/R_{pr}(f) + 1/R_{ph}(f,P_m)} \quad . \tag{4.18}$$

The formula gives exact result at low frequencies, where thermal after-effect residual loss and hysteresis loss dominate, and at high frequencies where the residual loss due to domain wall damping dominates. It is only the intermediate region which is expected to have somewhat elevated inaccuracy because both mechanisms contribute losses. Some error is also expected due to assumption $\hat{B} \gg B_F$ which allows neglect of thermal after-effect losses and simplification of the model. Using Eq. (3.53), the actual formula can be written as:

$$R_p(f,P_m) = \frac{2\pi\mu_0}{\sqrt[3]{\eta_B^2/8\pi^4\mu_0^2} f^{-3/4} P_m^{1/3} + f_H/f^2 + 1/f_w[1+(f_c/f)^2]} \quad . \tag{4.19}$$

In order to investigate a suitability of such a model, three manganese-zinc power ferrites were characterized. The normalized parallel resistance was measured as a function of frequency under constant core loss excitation of 0.1, 0.2, 0.5 and 1 W/cm^3 and a constant static magnetic bias field. The results are shown in Figs. 4.14-4.35, including model errors. The experimental data did not fit well the theoretical model at lower frequencies where the hysteresis loss was dominant. Therefore, a model with modified frequency and core loss density exponents was used:

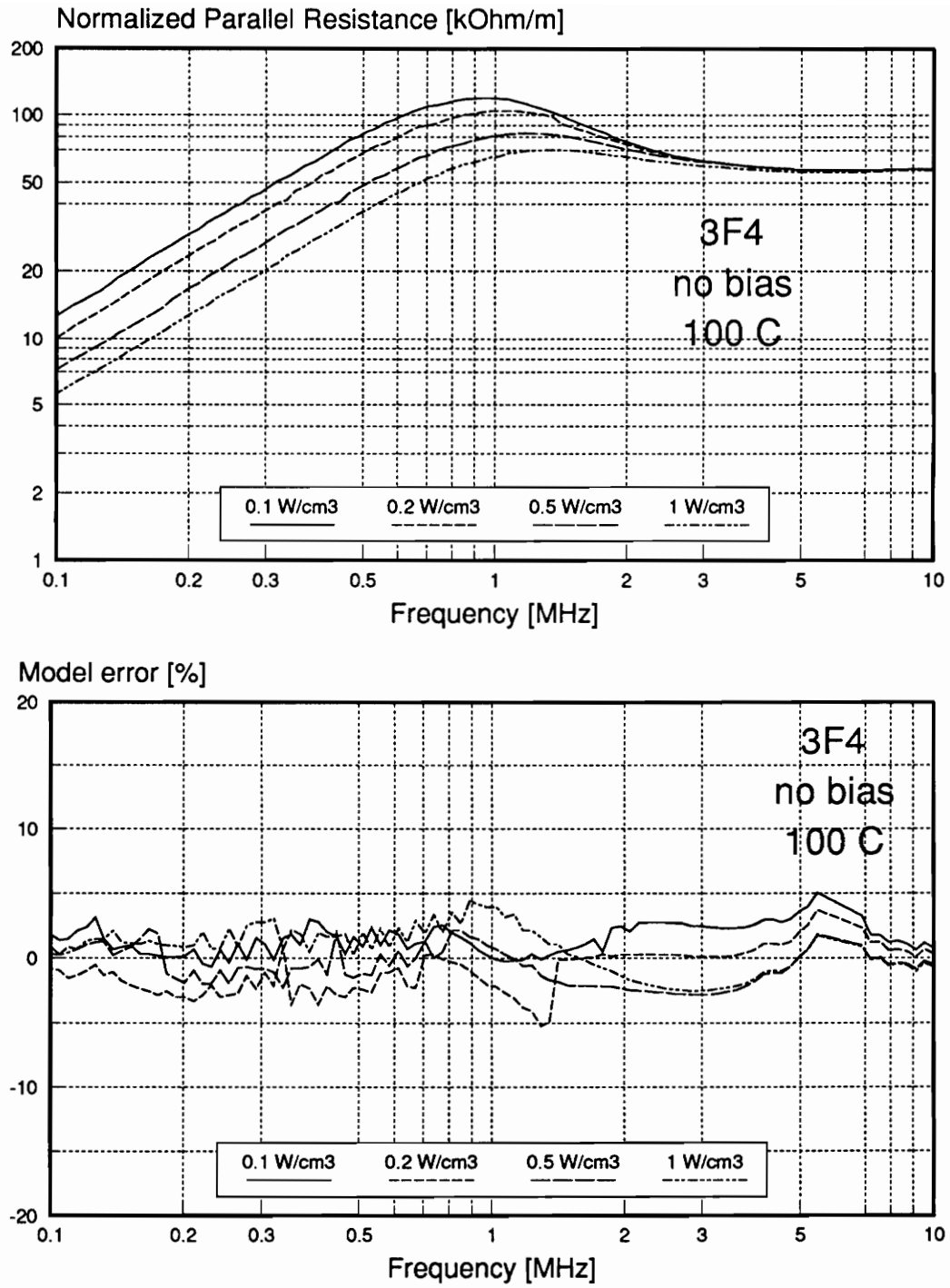

Fig. 4.16. Isoloss characteristics and model error for 3F4 ferrite without static bias and at 100 ℃ temperature.

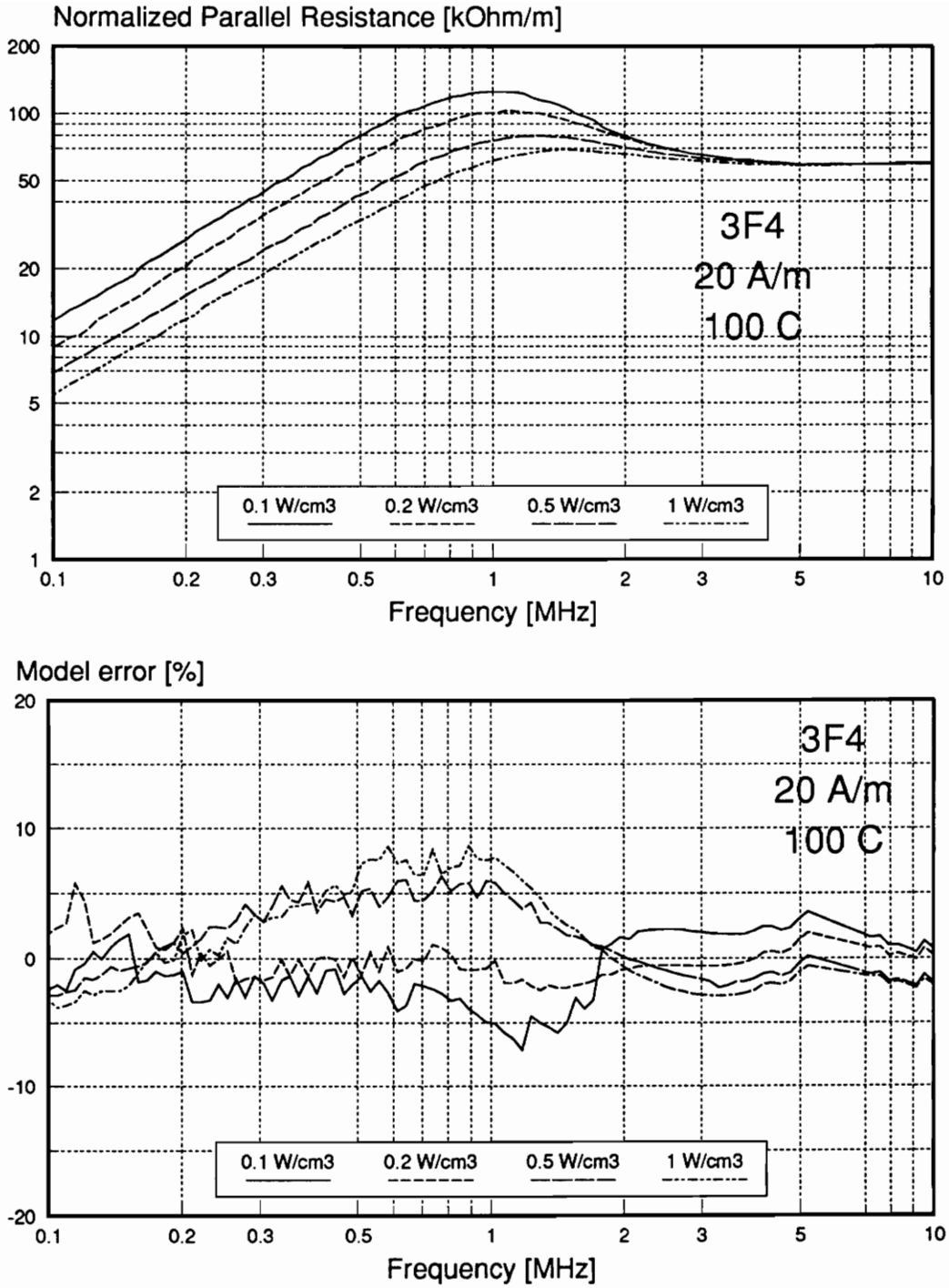

Fig. 4.17. Isoloss characteristics and model error for 3F4 ferrite at 20 A/m static bias and at 100 ℃ temperature.

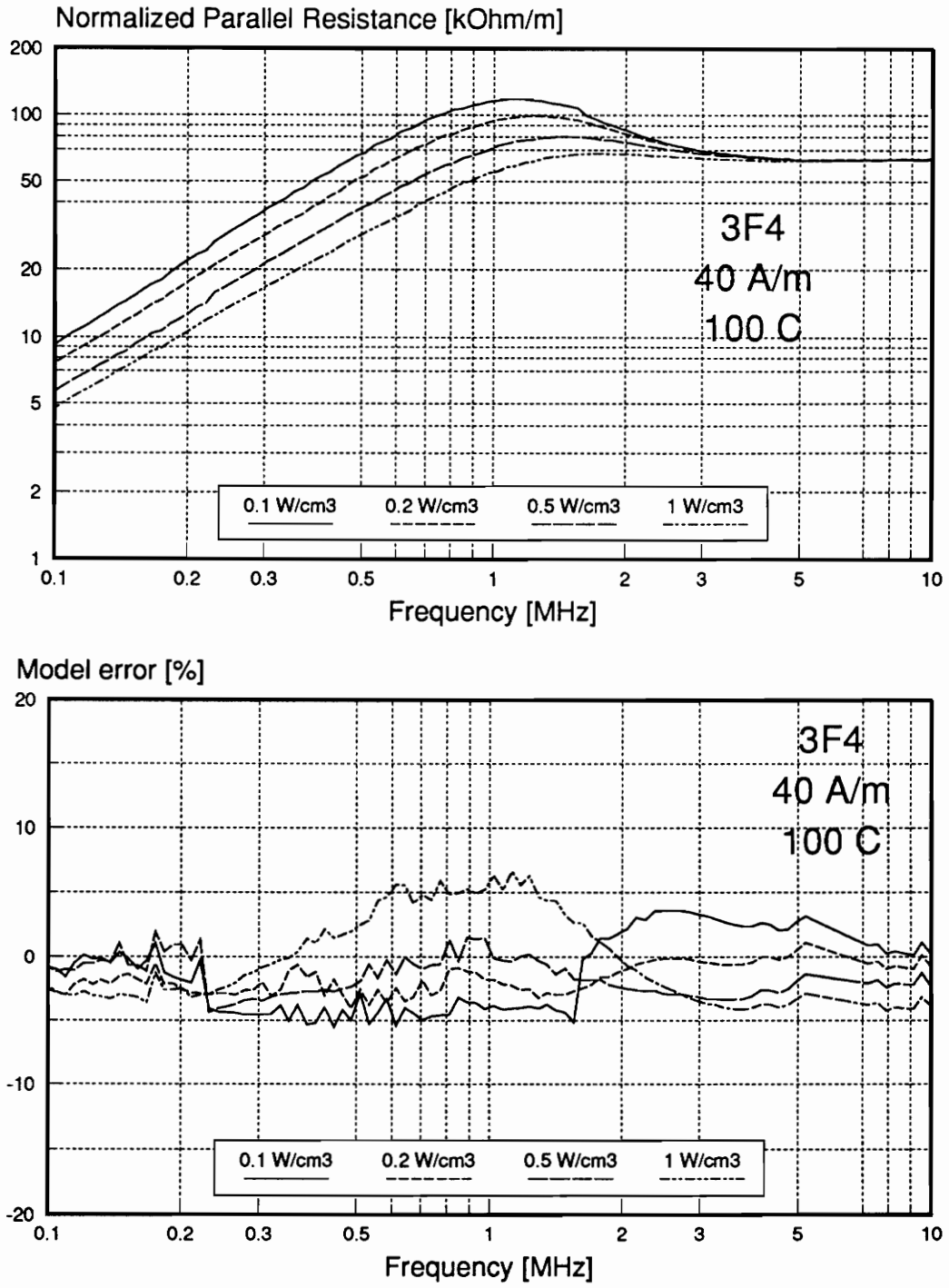

Fig. 4.18. Isoloss characteristics and model error for 3F4 ferrite at 40 A/m static bias and at 100 ℃ temperature.

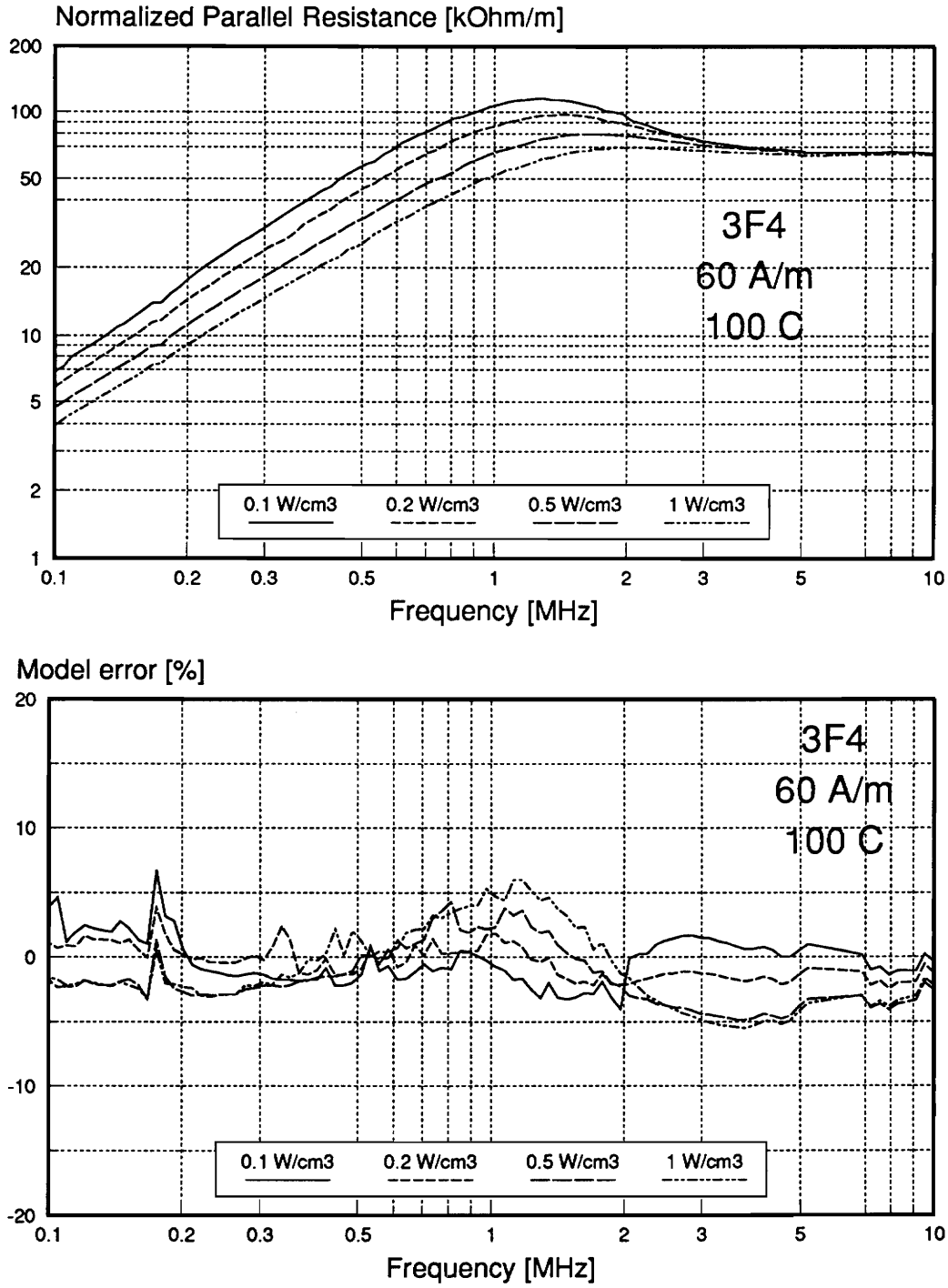

Fig. 4.19. Isoloss characteristics and model error for 3F4 ferrite at 60 A/m static bias and at 100 ℃ temperature.

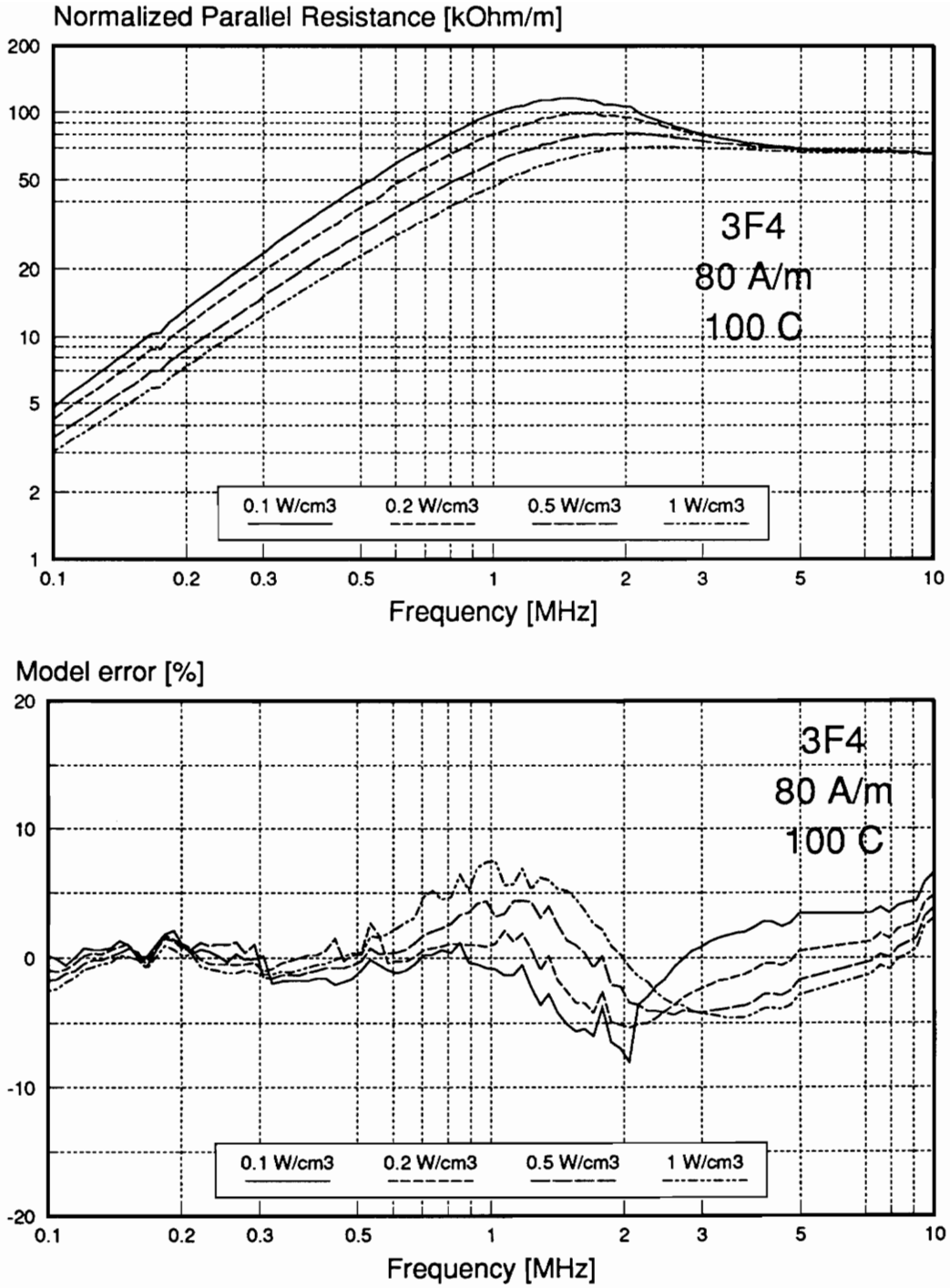

Fig. 4.20. Isoloss characteristics and model error for 3F4 ferrite at 80 A/m static bias and at 100 ℃ temperature.

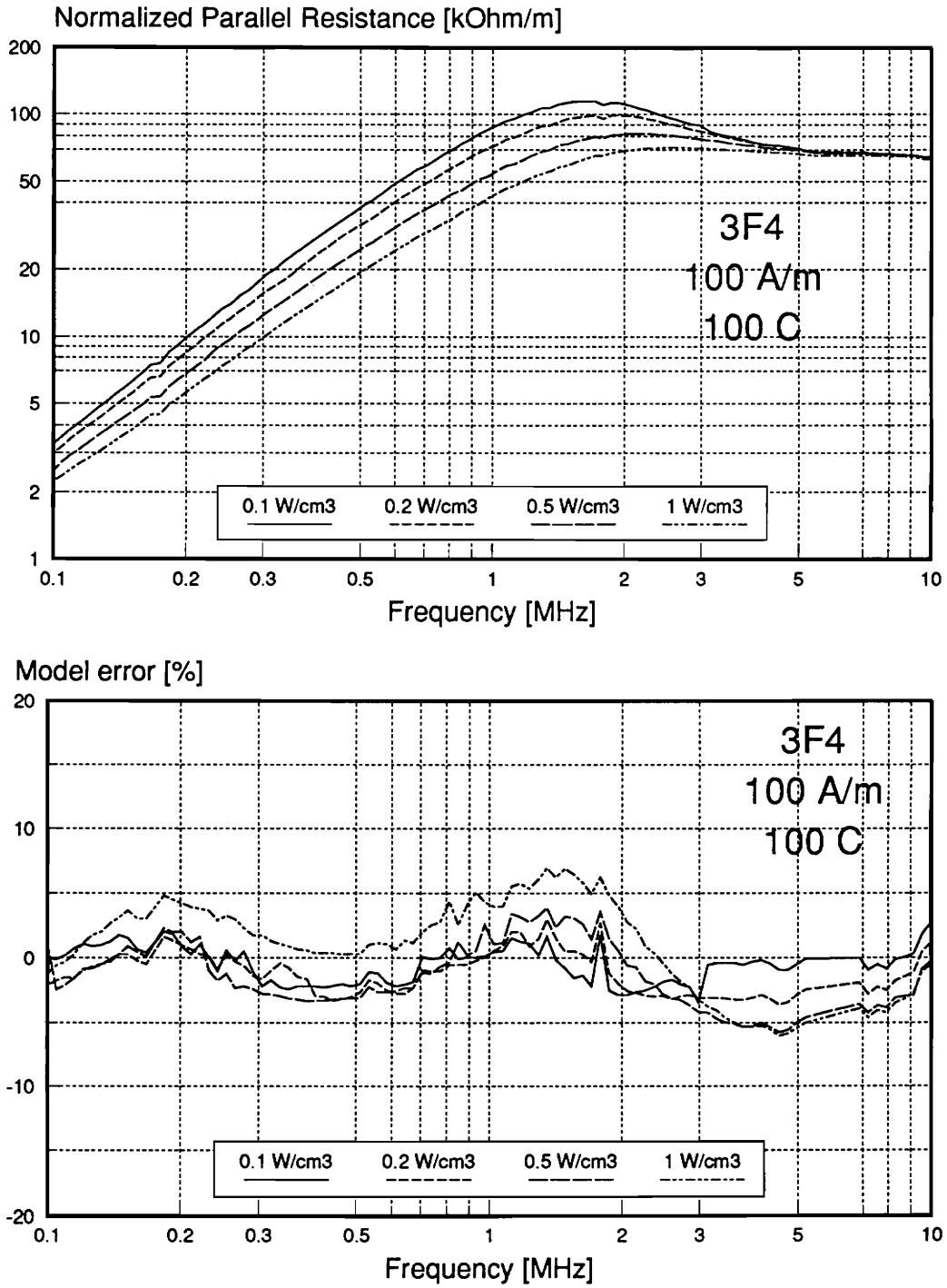

Fig. 4.21. Isoloss characteristics and model error for 3F4 ferrite at 100 A/m static bias and at 100 ℃ temperature.

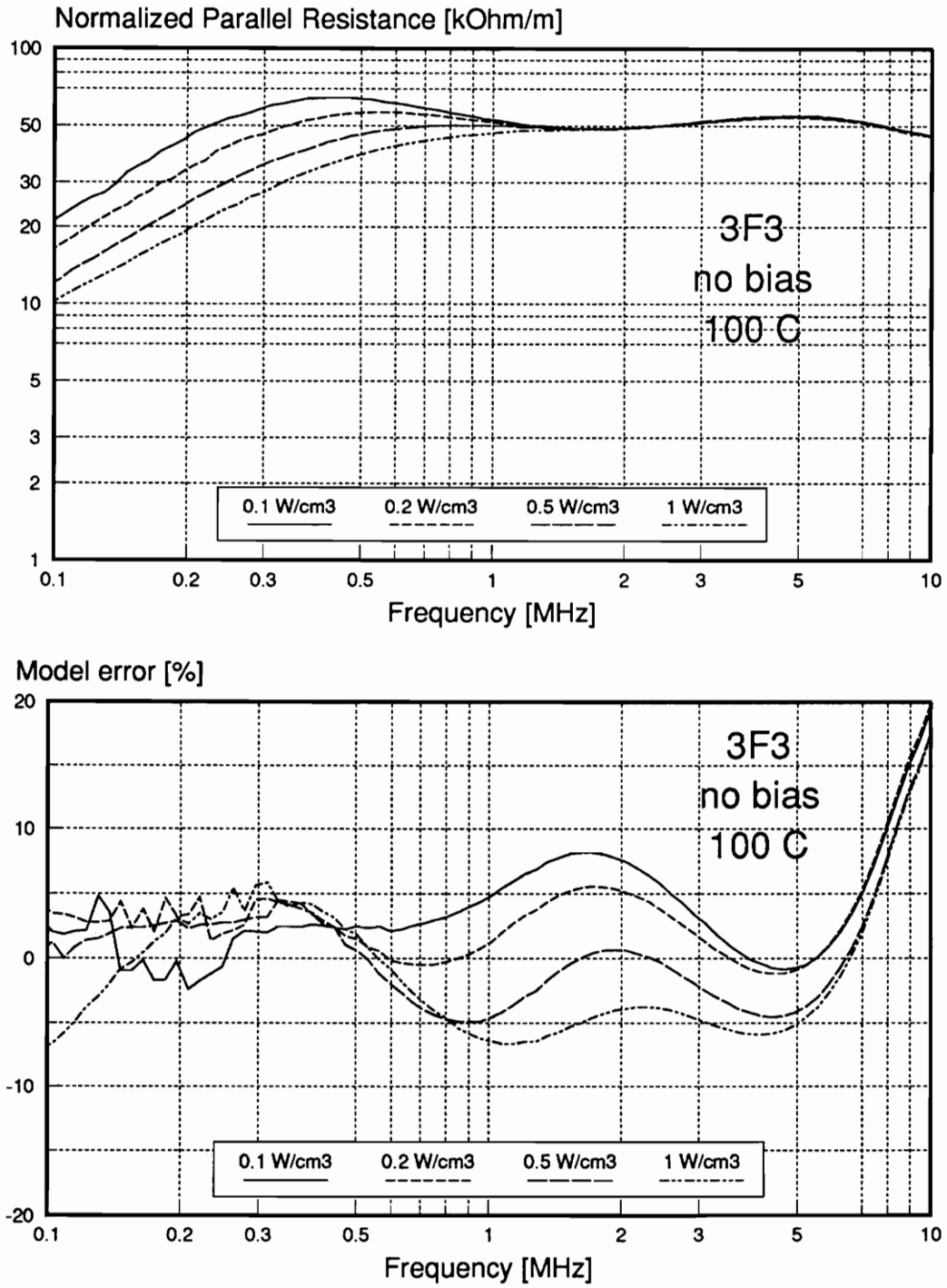

Fig. 4.22. Isoloss characteristics and model error for 3F3 ferrite without static bias and at 100 ℃ temperature.

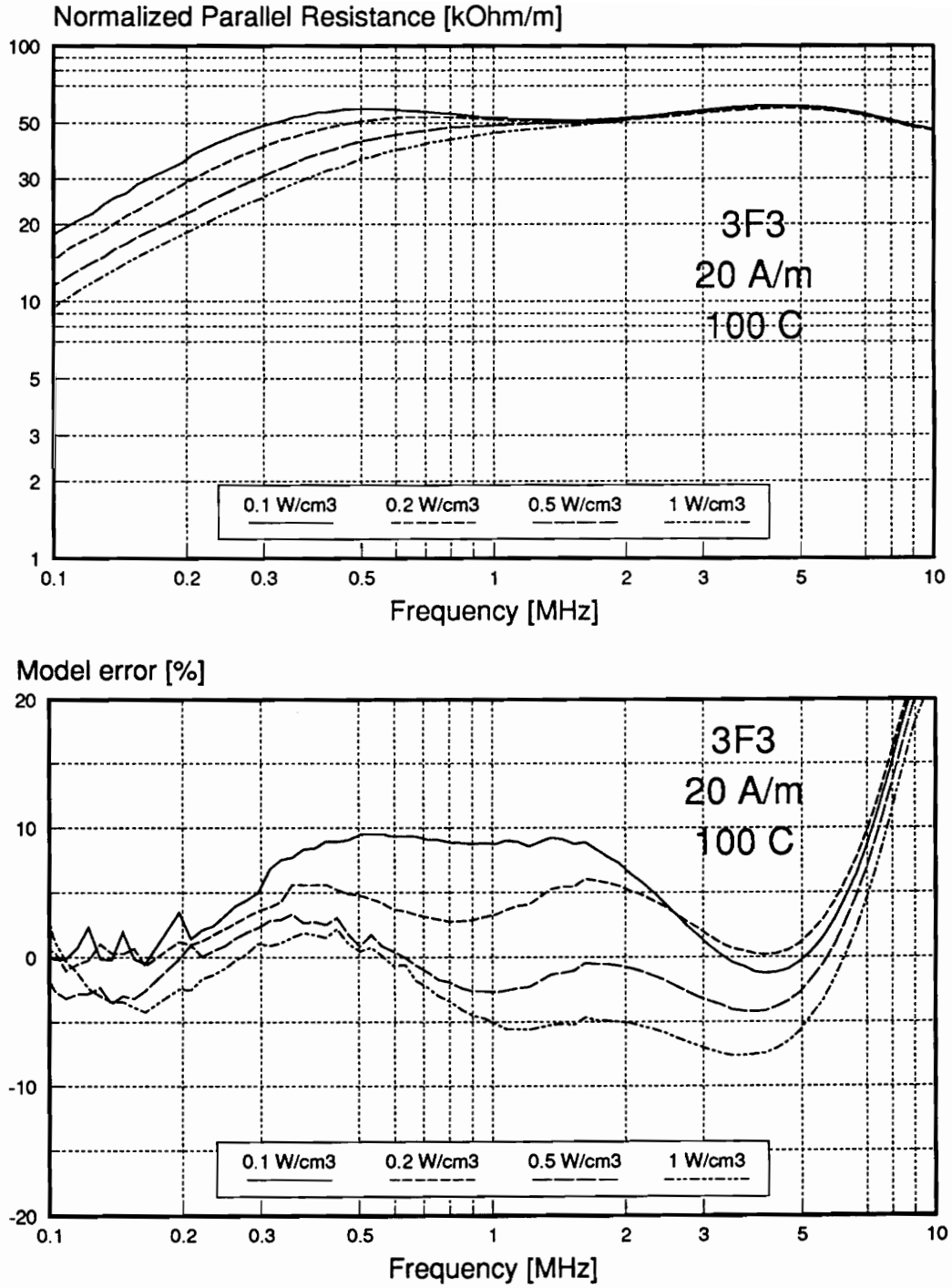

Fig. 4.23. Isoloss characteristics and model error for 3F3 ferrite at 20 A/m static bias and at 100 ℃ temperature.

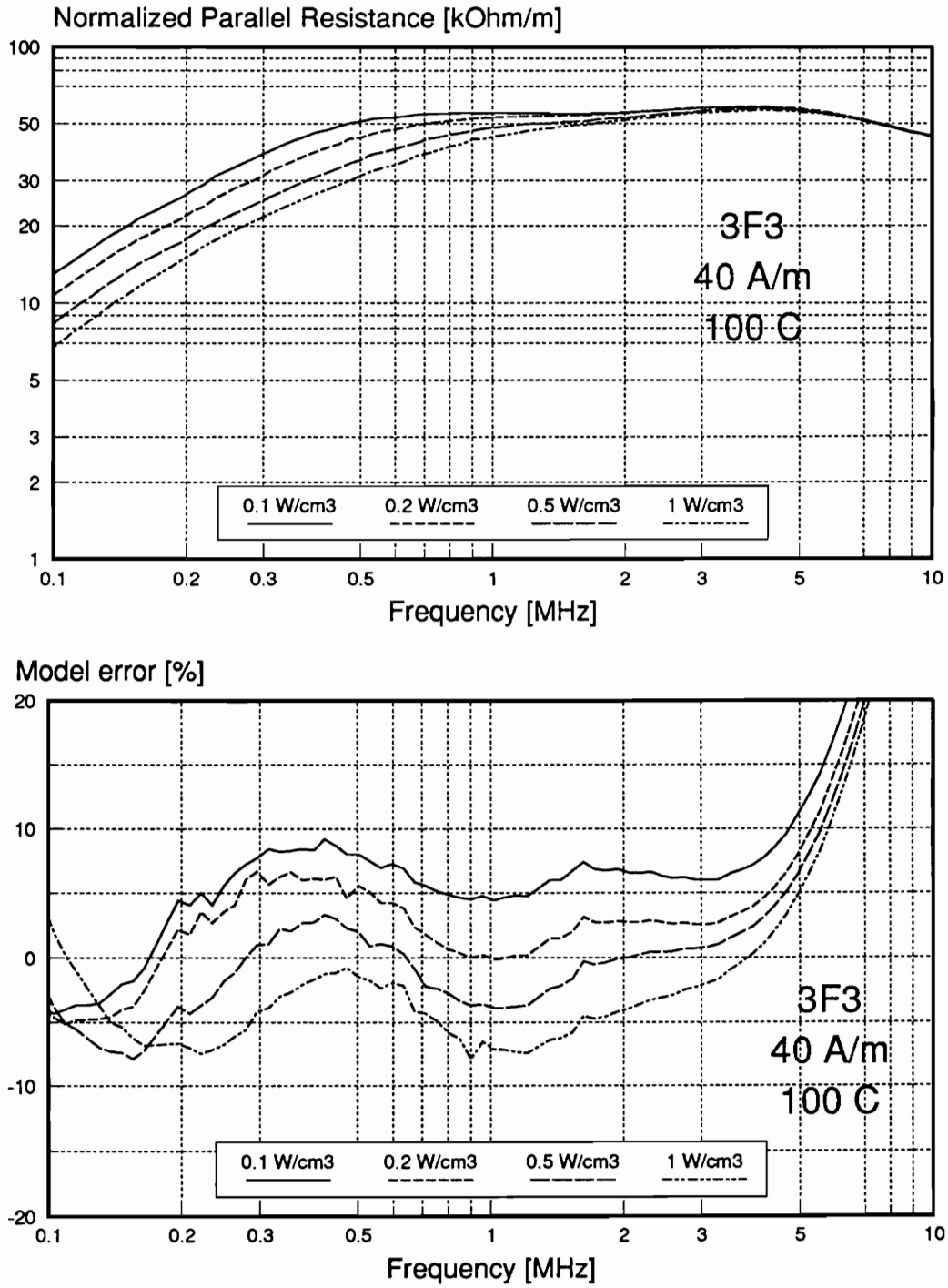

Fig. 4.24. Isoloss characteristics and model error for 3F3 ferrite at 40 A/m static bias and at 100 ℃ temperature.

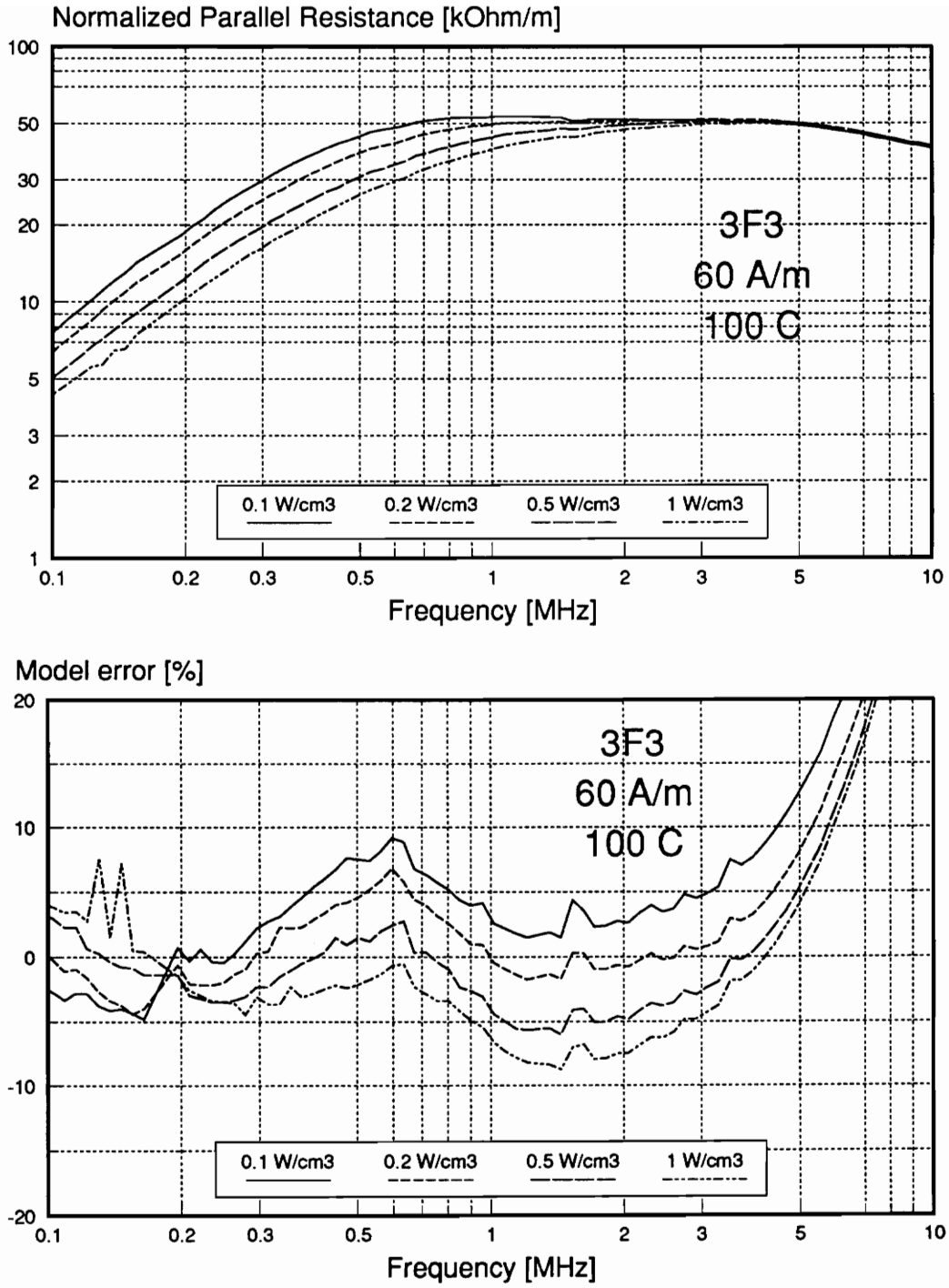

Fig. 4.25. Isoloss characteristics and model error for 3F3 ferrite at 60 A/m static bias and at 100 ℃ temperature.

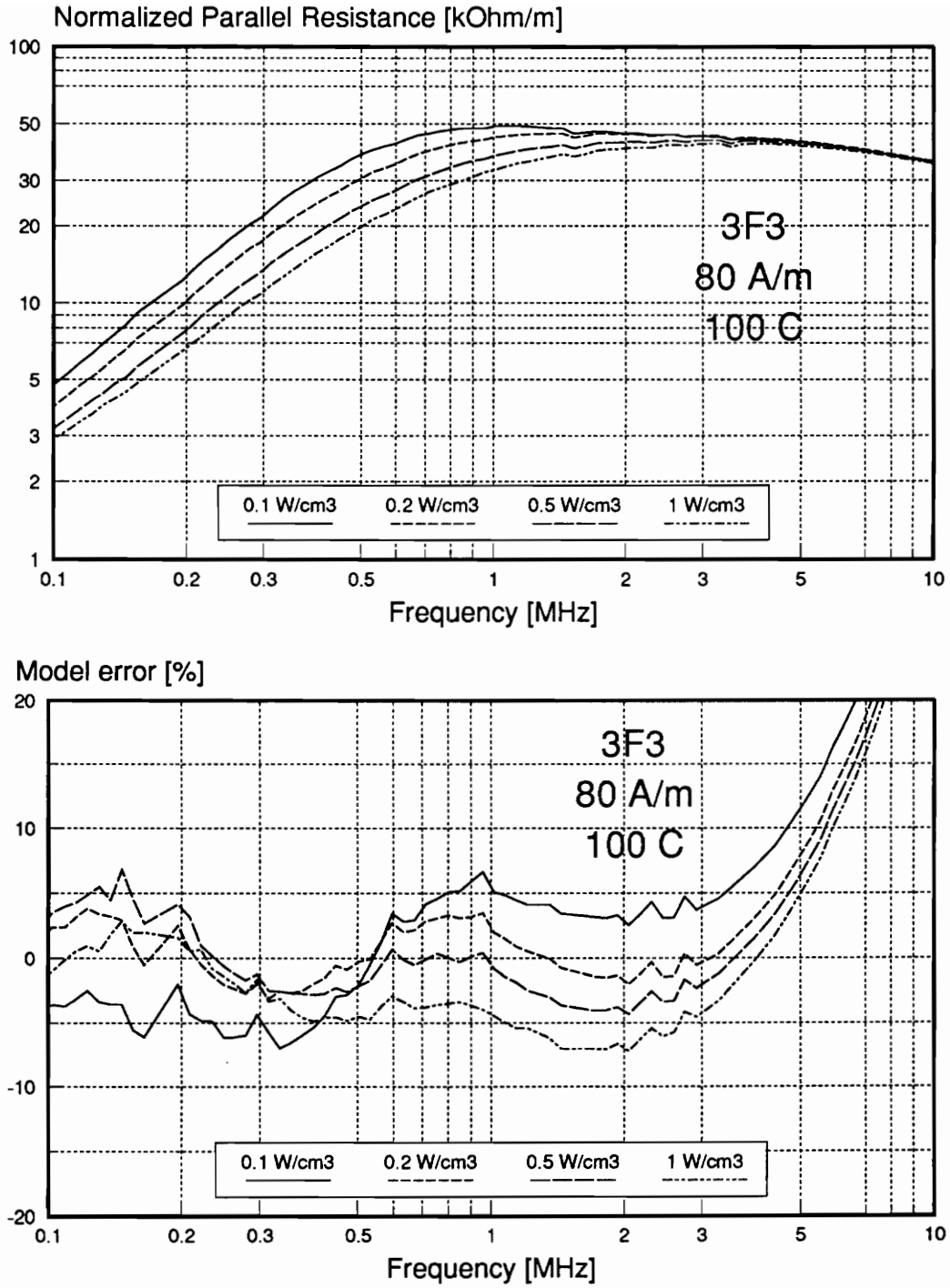

Fig. 4.26. Isoloss characteristics and model error for 3F3 ferrite at 80 A/m static bias and at 100 ℃ temperature.

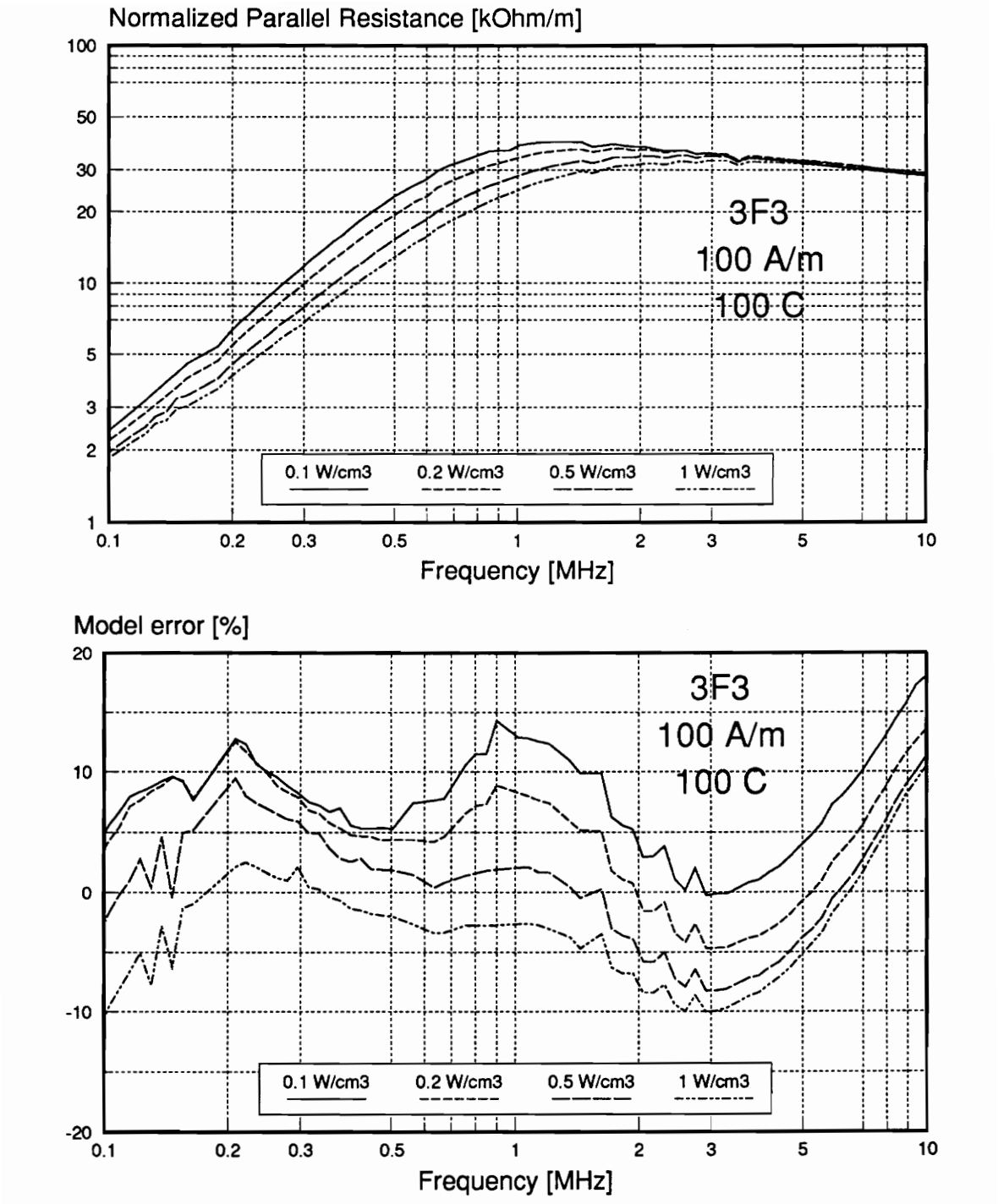

Fig. 4.27. Isoloss characteristics and model error for 3F3 ferrite at 100 A/m static bias and at 100 ℃ temperature.

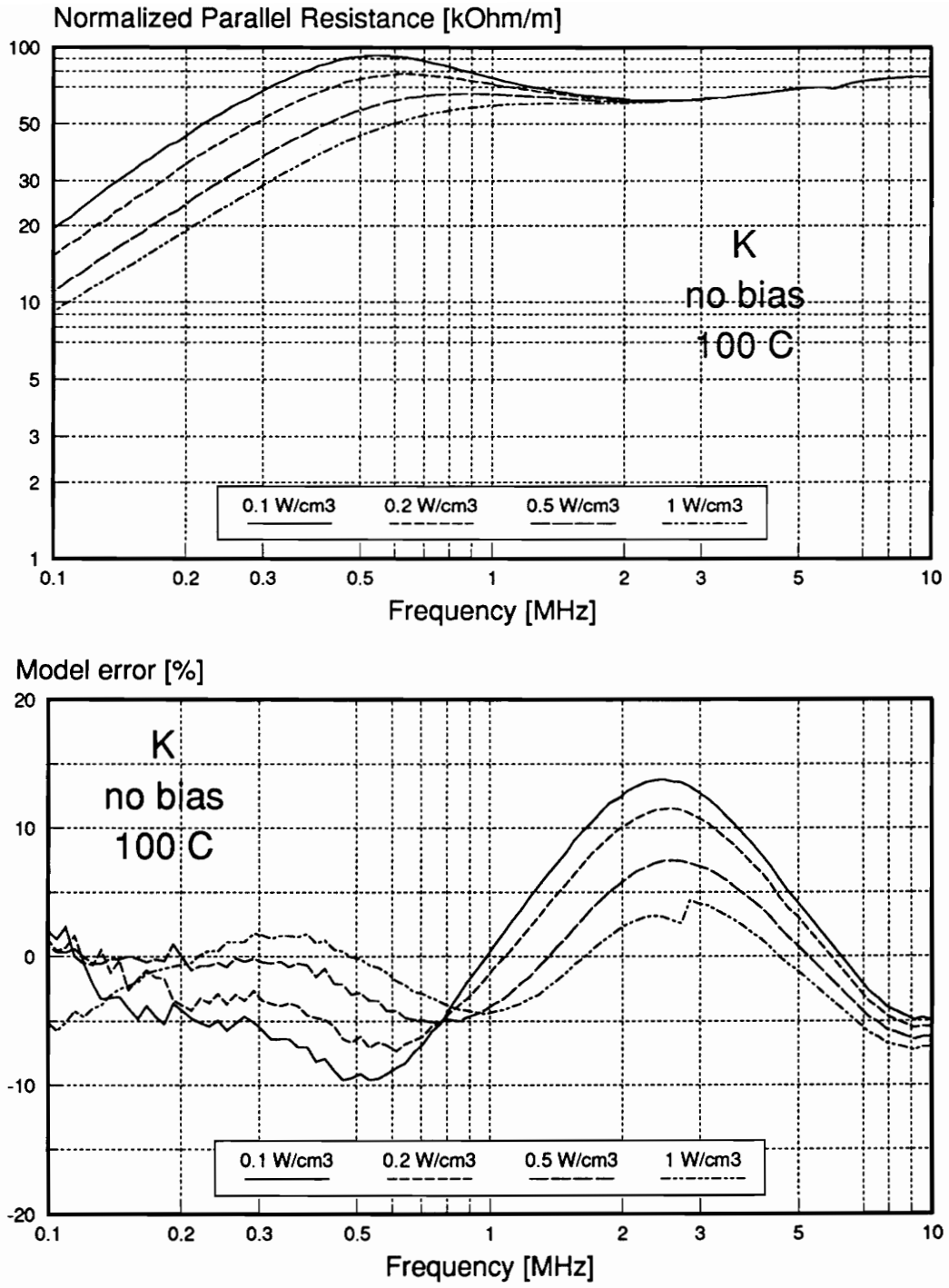

Fig. 4.28. Isoloss characteristics and model error for K ferrite without static bias and at 100 ℃ temperature.

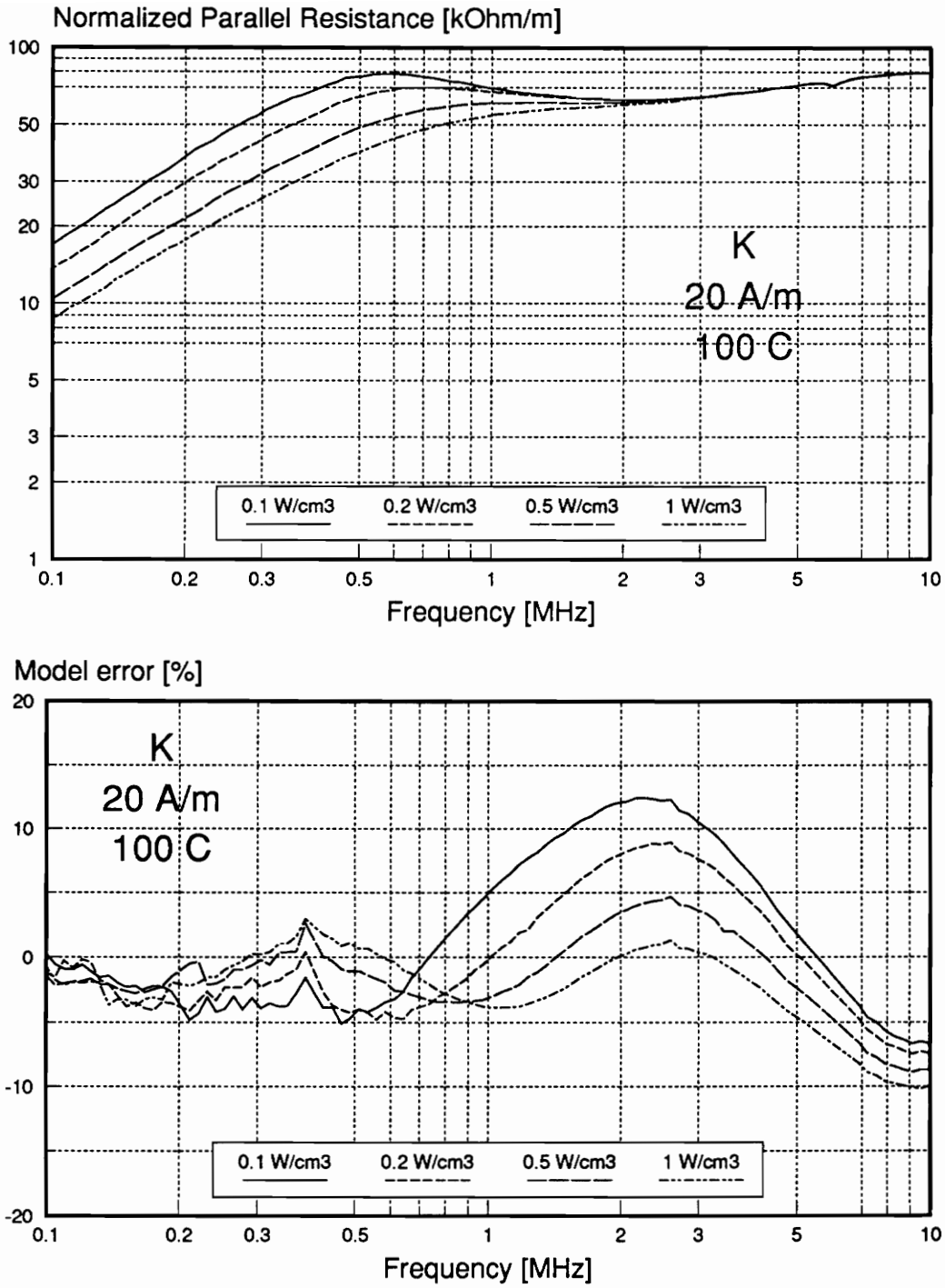

Fig. 4.29. Isoloss characteristics and model error for K ferrite at 20 A/m static bias and at 100 ℃ temperature.

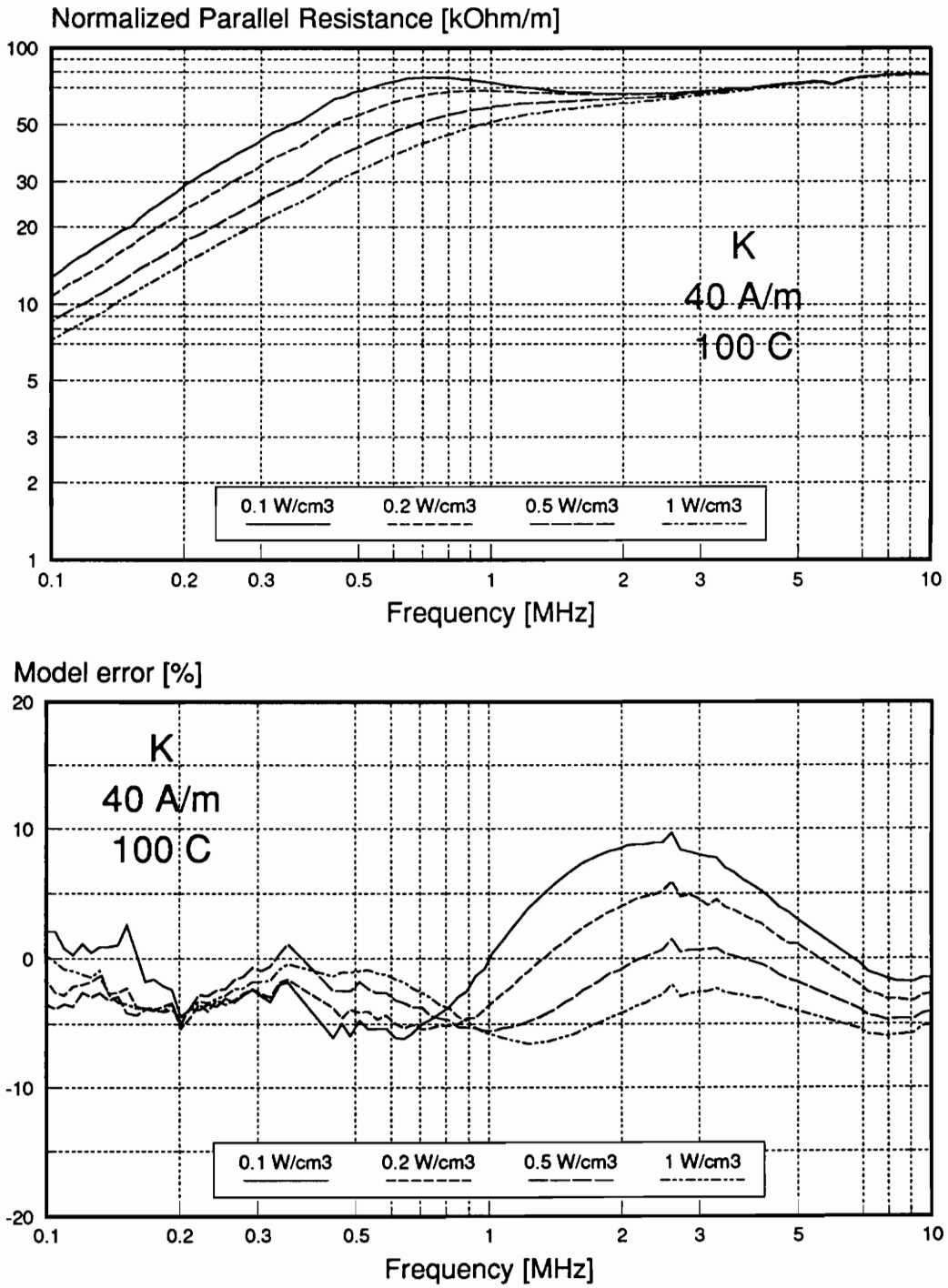

Fig. 4.30. Isoloss characteristics and model error for K ferrite at 40 A/m static bias and at 100 ℃ temperature.

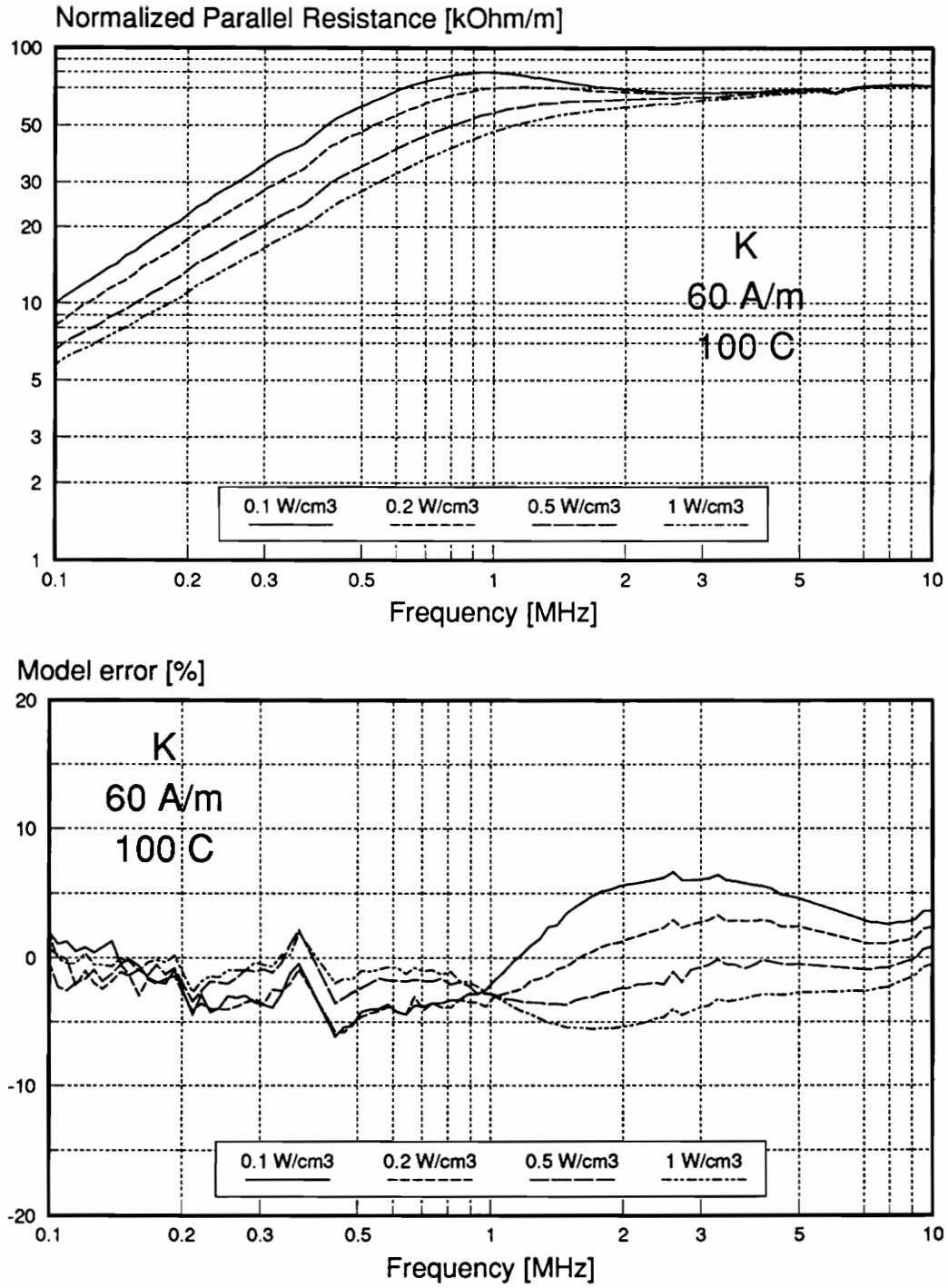

Fig. 4.31. Isoloss characteristics and model error for K ferrite at 60 A/m static bias and at 100 ℃ temperature.

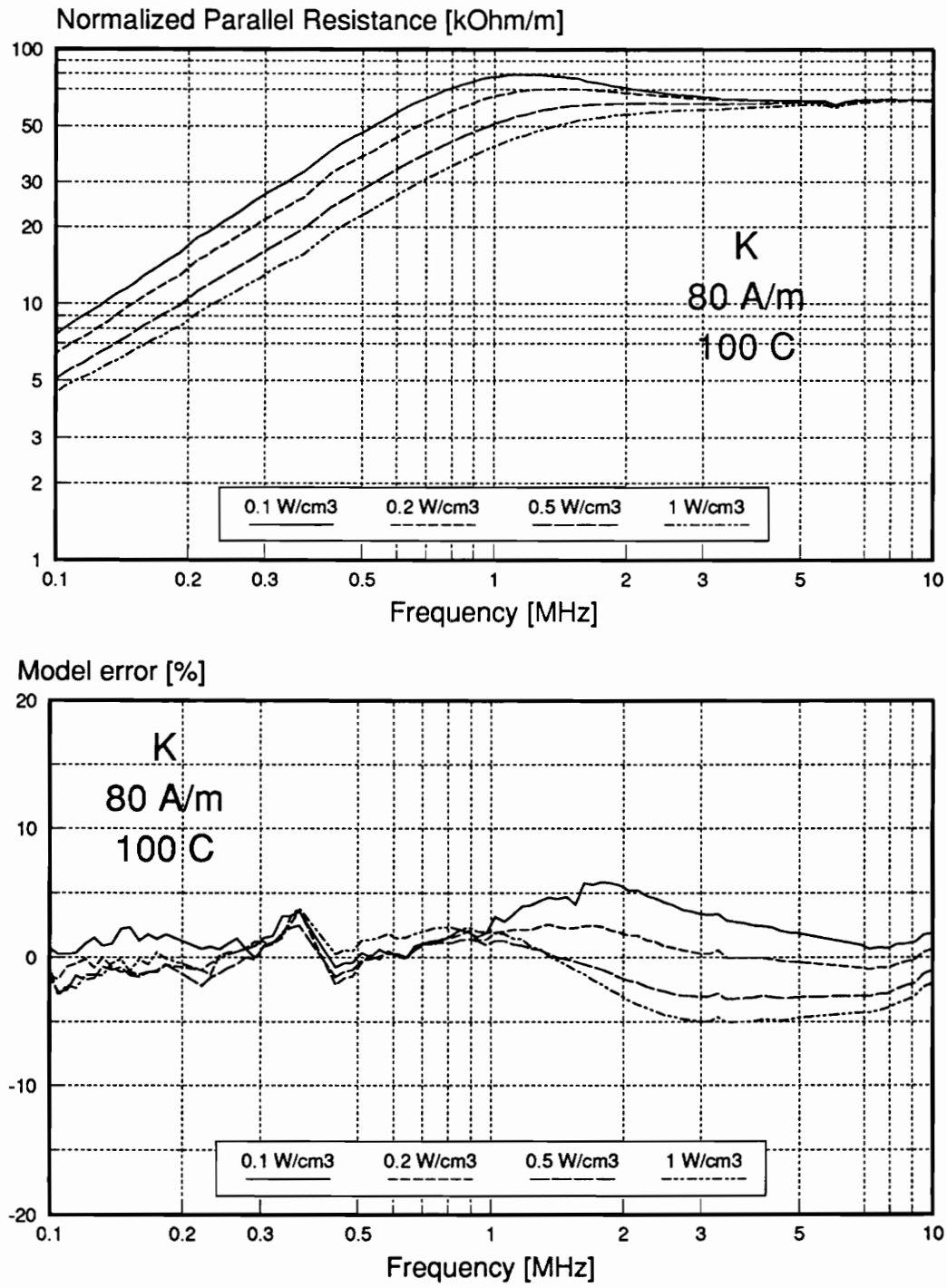

Fig. 4.32. Isoloss characteristics and model error for K ferrite at 80 A/m static bias and at 100 ℃ temperature.

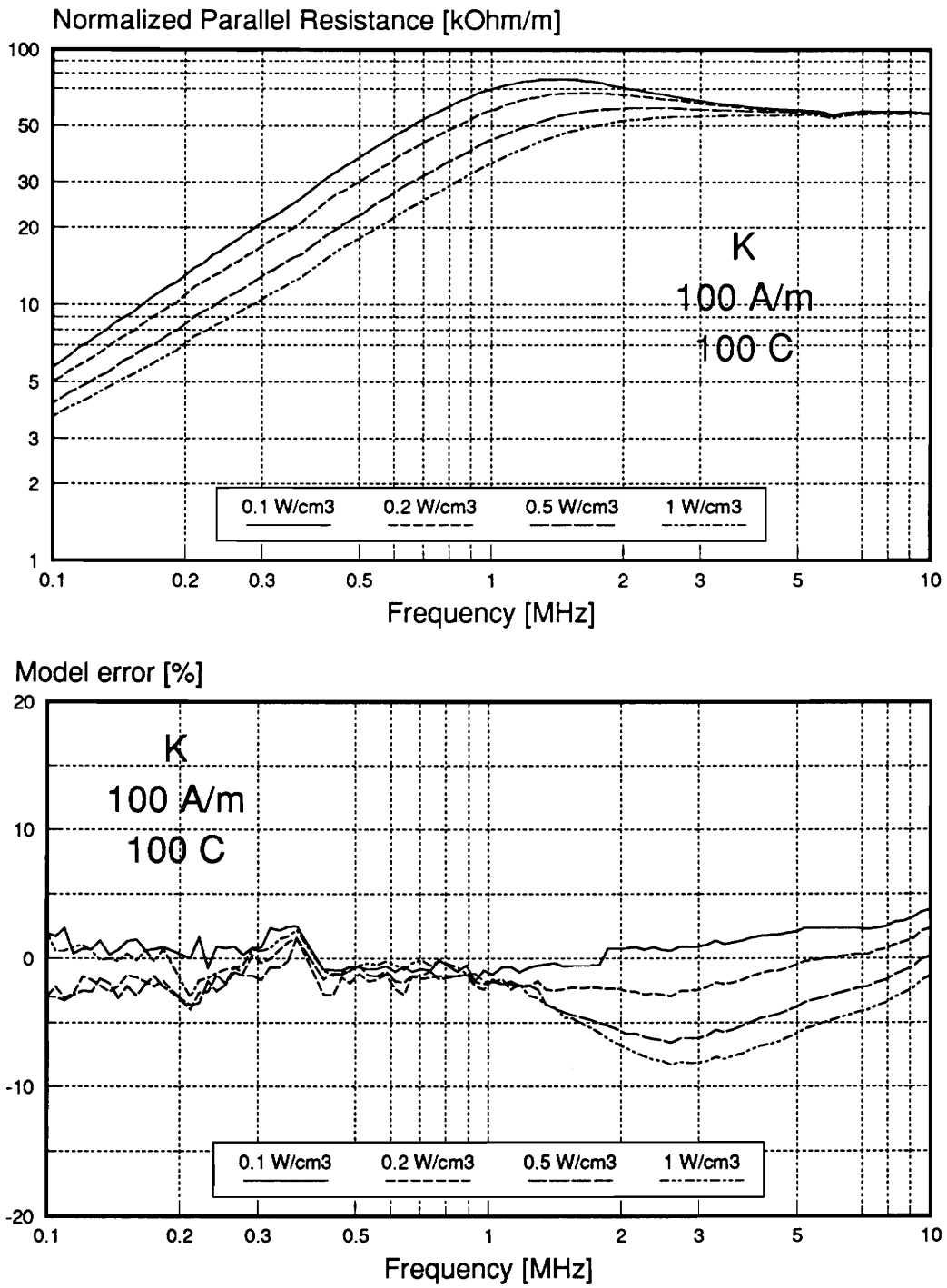

Fig. 4.33. Isoloss characteristics and model error for K ferrite at 100 A/m static bias and at 100 ℃ temperature.

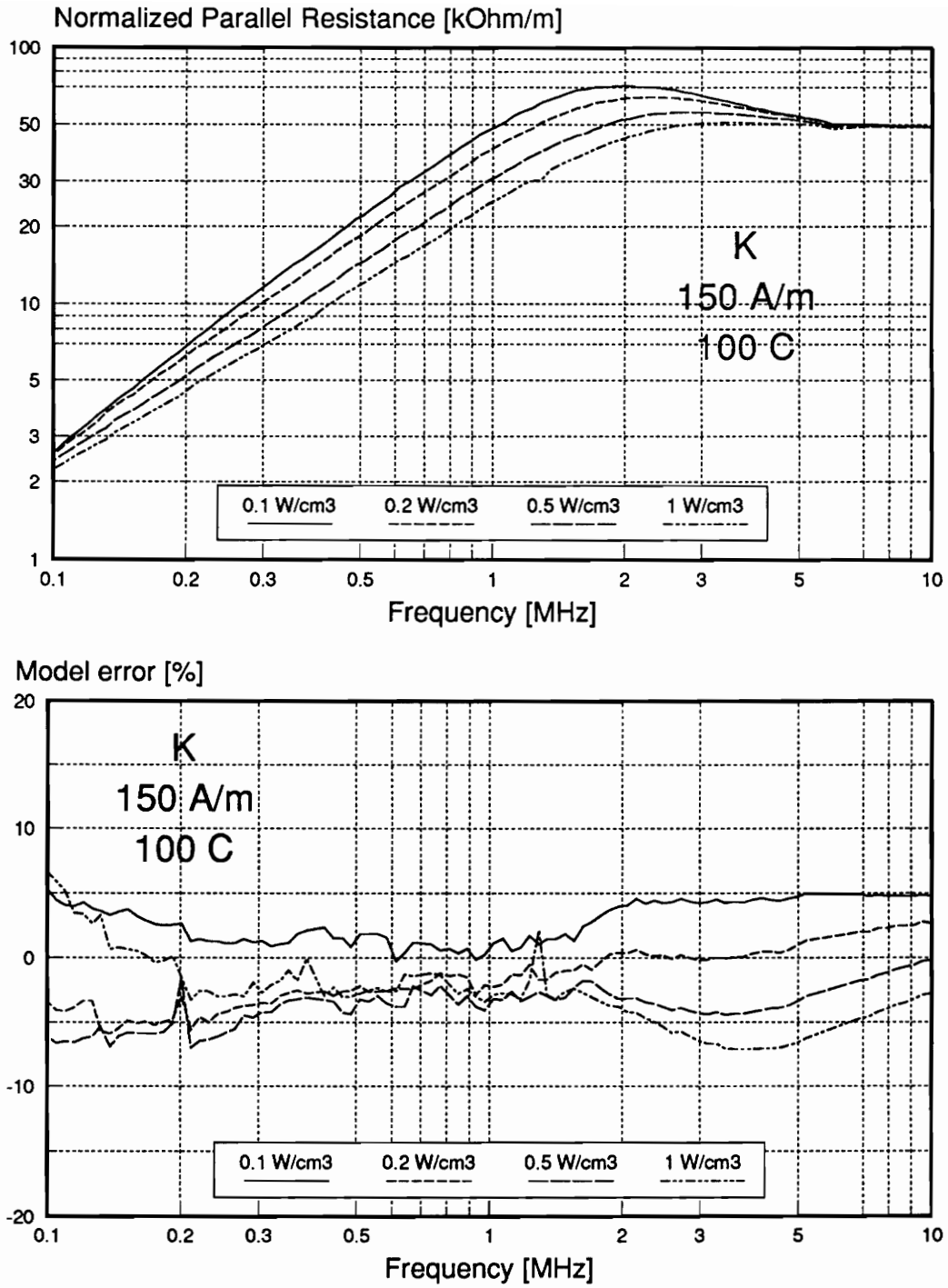

Fig. 4.34. Isoloss characteristics and model error for K ferrite at 150 A/m static bias and at 100 ℃ temperature.

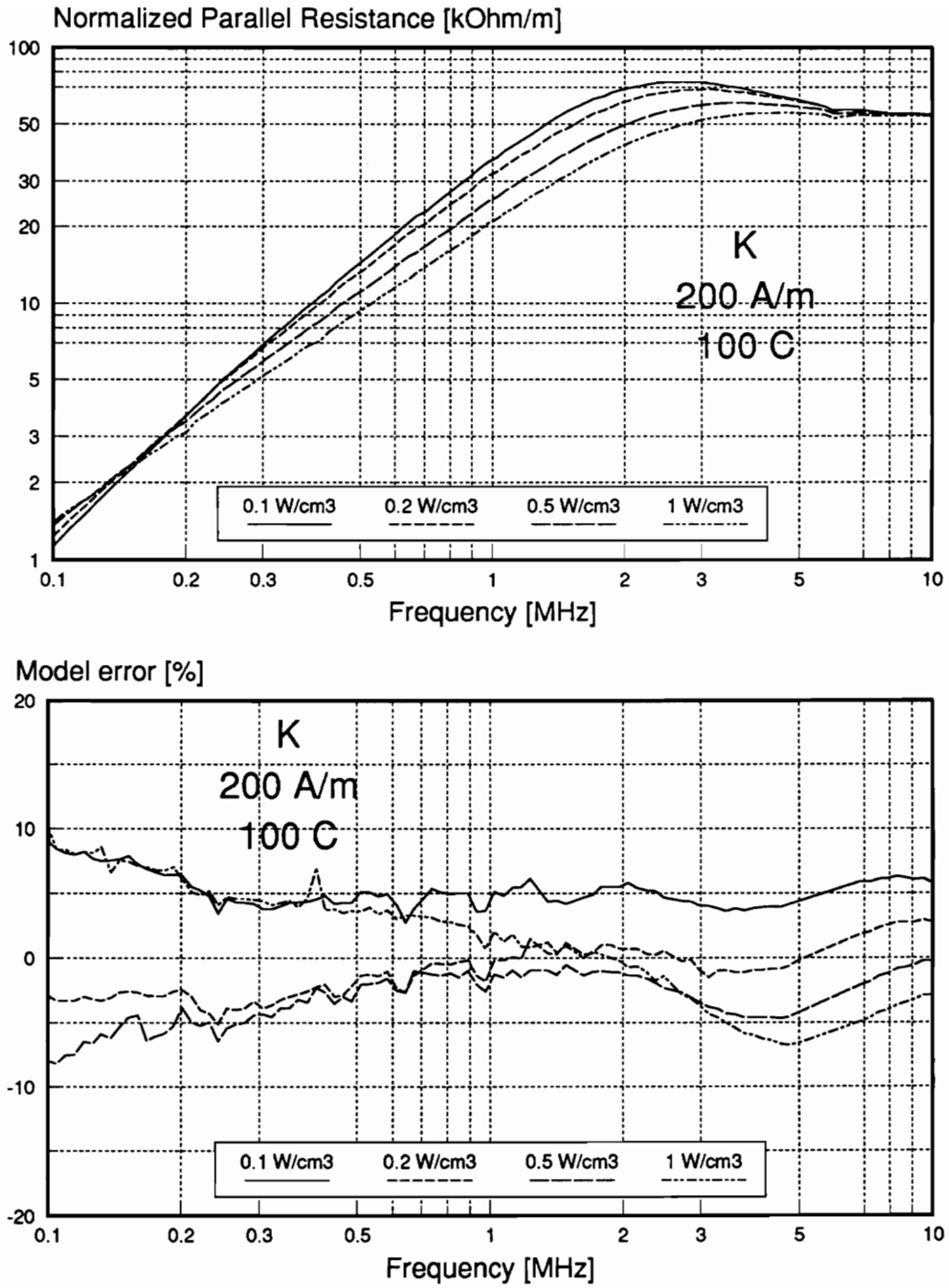

Fig. 4.35. Isoloss characteristics and model error for K ferrite at 200 A/m static bias and at 100 ℃ temperature.

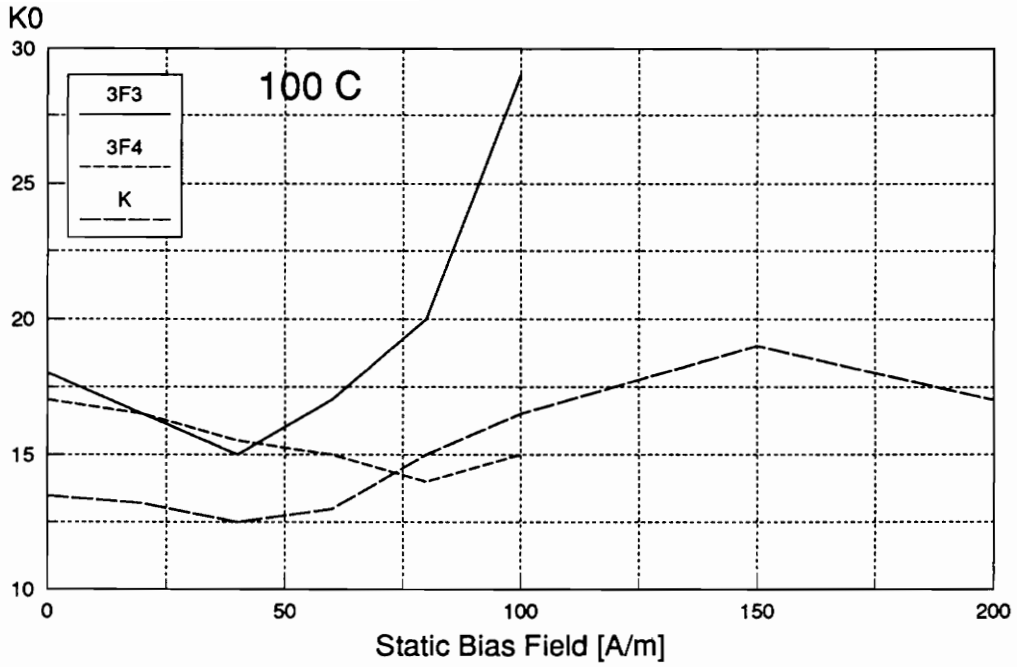

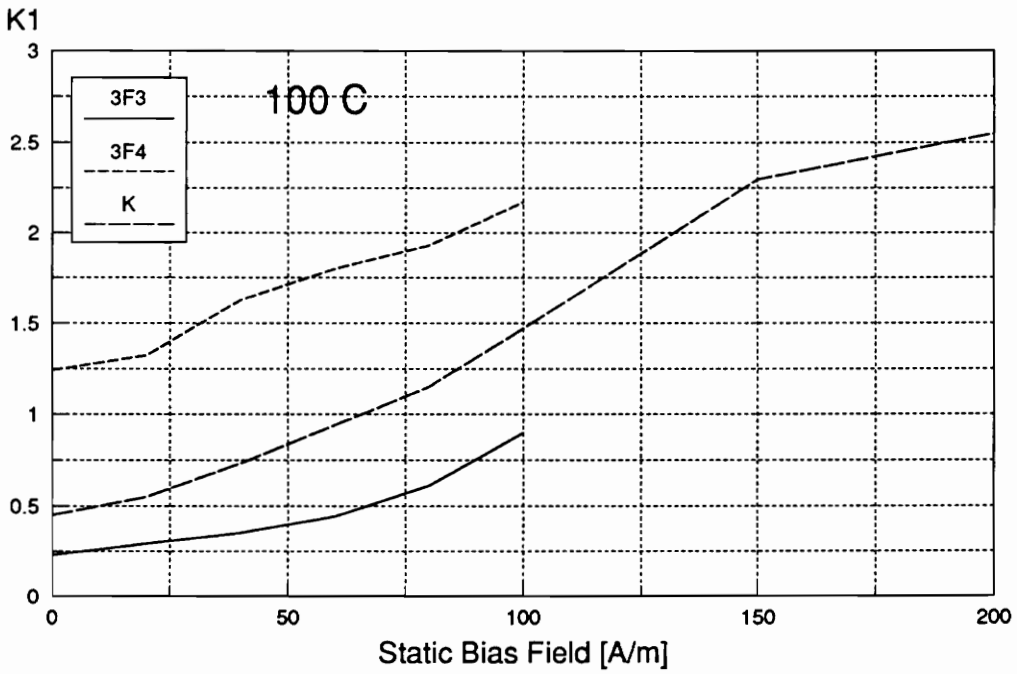

Fig. 4.36. Isoloss model parameters k_0 and k_1 as a function of static magnetic bias field for three commercial grades of MnZn ferrites.

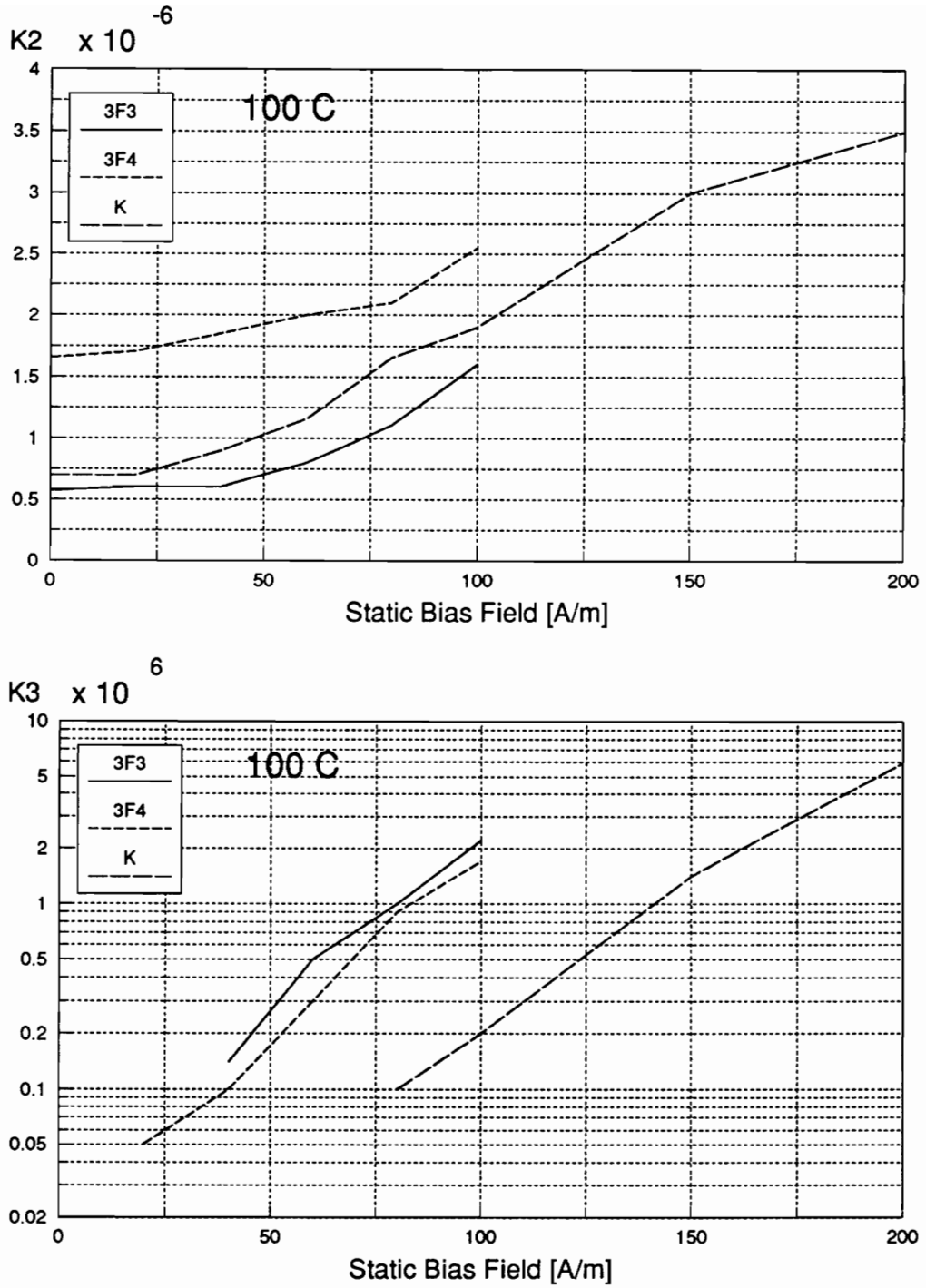

Fig. 4.37. Isoloss model parameters k_2 and k_3 as a function of static magnetic bias field for three commercial grades of MnZn ferrites.

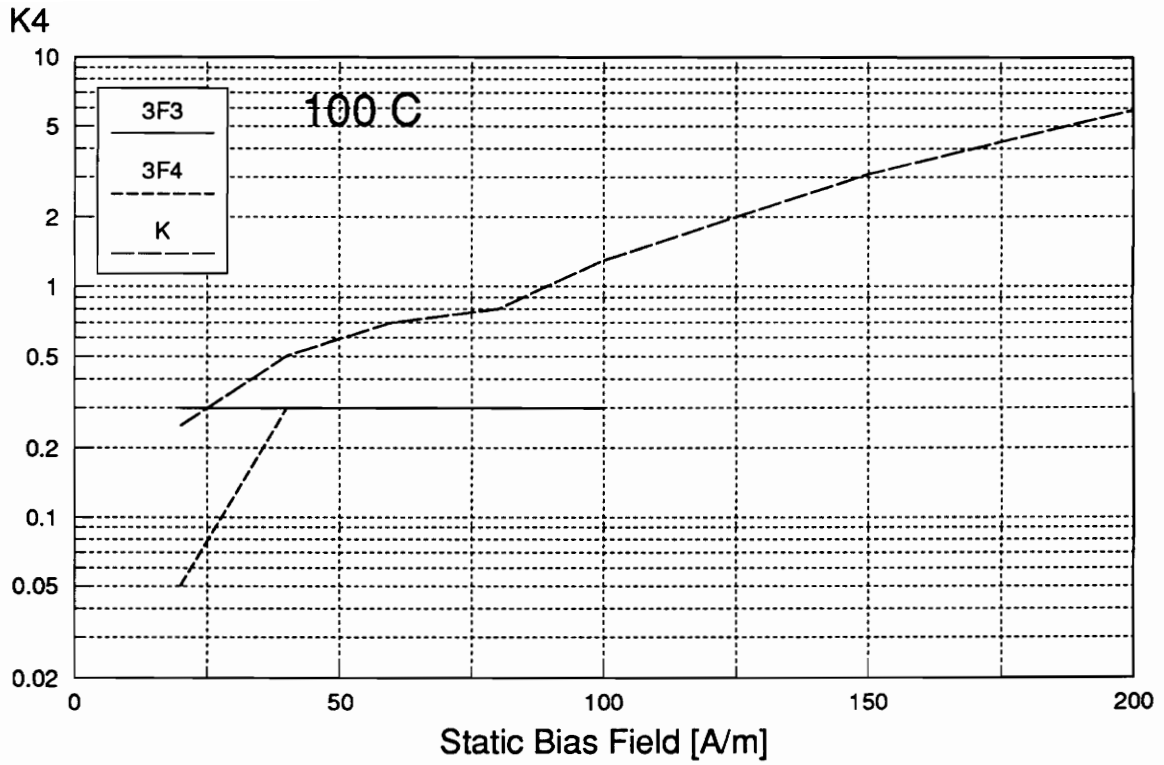

Fig. 4.38. Isoloss model parameter k_4 as a function of static magnetic bias field for three commercial grades of MnZn ferrites.

$$R_p = \frac{1}{k_0/\left[1+(k_2/f)^{k_5}\right] + k_1 f^{k_6} P_m^{0.36} + (k_3 - k_4 P_m)/f^2} \quad , \tag{4.20}$$

where k_0-k_4 are parameters dependent on static magnetic bias field and k_5 and k_6 are material constants. The exponent of the space charge effect, k_5, depends on the material and is equal to 2.5 for 3F3 and K ferrites, and 2.75 for 3F4 ferrite. The hysteresis loss in all three ferrites is proportional to $P_m^{0.36}$, which is close to the theoretical $P_m^{1/3}$, suggesting that the principle hysteresis mechanism is close to the Rayleigh approximation and is identical in these ferrites. However, the hysteresis frequency exponent, k_6, slightly depends on the material: -1.2 for 3F4, -1.15 for K, and -1.1 for 3F3, and in all cases is substantially different from the theoretical -3/4. Therefore, the frequency dependent hysteresis loss is important in these materials and varies with the material composition and microstructure. The bias dependent parameters are plotted against the bias field in Figs. 4.36, 4.37, and 4.38.

The variation of residual loss parameter, k_0, with the static bias is inconclusive. The hysteresis loss parameter, k_1, increases with bias in all materials. The materials cannot be compared based exclusively on this factor due to a material-dependent frequency exponent, k_6, in the hysteresis loss term. The additional ferromagnetic resonance residual loss due to the static bias field is modeled with parameters k_3 and k_4, where the latter is a correction due to an interaction of the ac field with a dc field. Such a correction is necessary especially at lower frequencies and very strong bias (*e.g.* K ferrite at 200 A/m), when increase in core loss is accompanied by an increase in normalized parallel resistance instead of a decrease. The k_3 parameter is exponentially dependent on the static bias field with a similar exponent for all three ferrites (like f_H in $R_p(f, B)$ model) while k_4 can assume exponential or constant function depending on the material. The accuracy of the model is particularly good for 3F4 ferrite, reaching 5% without bias and 8% with bias up to 100 A/m. For 3F3 and K ferrites, error does not exceed 15%, except for 3F3 above 5 MHz where bulk eddy current losses occur which are not taken into account in the model. The accuracy is acceptable for design purposes, and the relatively simple

analytical function makes design optimization feasible. The application of this model to the design of high-frequency power transformers and inductors is discussed in the remainder of this chapter.

4.5 Optimal Design Procedure

In this section the design procedure is established in order to minimize the volume of the power transformer or inductor. The procedure is based on the specified power handling of the device and assumes convection cooling. It is accurate only for sinusoidal voltage and current excitations. If substantial harmonics are present, the calculation of core losses and winding losses must be modified to include additional losses due to harmonics.

4.5.1 Determination of Power Rating

In inductors, the rated power is defined as the product of a rms voltage and a rms current at the terminations:

$$P_{\max} = V_{\max} I_{\max} \quad . \tag{4.21}$$

The rated power of a transformer depends on the type and efficiency of its load. In dc to dc power converters, the typical load is a rectifier. In resonant circuits, there may be an additional capacitance at the rectifier. Both the rectifier and the capacitance influence the power factor of the transformer load. The rectifier also introduces substantial conduction losses. The rated power of the transformer can be expressed as a function of the dc output power, P_{out},

$$P_{\max} = \frac{P_{out}}{\eta_{REC}\eta_{PF}} \tag{4.22}$$

where

η_{REC} - efficiency of the rectifier and the secondary circuits, and

η_{PF} - power factor of the rectifier and the secondary circuits.

4.5.2 Calculation of Magnetic Core Volume

Since the design of high-frequency transformers and inductors is thermally limited, the choice of the magnetic core essentially depends on its ability to dissipate the heat generated in the core and windings. The thermal resistance of standard magnetic cores was investigated by Mulder [286] who found the following relationship:

$$R_{th} = C_{th} V_e^{-0.54} \quad , \tag{4.23}$$

where

R_{th} - thermal resistance due to natural convection cooling,

C_{th} - constant dependent on type of insulation, and

V_e - effective magnetic volume of the core.

Therefore the maximum total power dissipation is:

$$P_{tot} = \frac{\Delta T}{C_{th}} V_e^{0.54} \quad . \tag{4.24}$$

The power rating (VA) of the thermally limited transformer or inductor is determined by the formula (B.8):

$$P_{\max} = \frac{P_{tot}}{k_W} \frac{\sqrt{k_L}}{k_L + 1} \sqrt{\frac{A_W A_e F_W R_p}{l_e l_W F_R \rho_c}} \quad , \tag{4.25}$$

where

A_W - window area,

A_e - effective core cross-section area,

l_e - effective magnetic path length,

ρ_c - conductor resistivity,

l_W - mean length of turn,

F_R - ac to dc resistance ratio of the windings,

k_L - ratio of winding loss to core loss,

k_W - number of windings rated at full power, 1 for inductors, 2 for transformers.

Since $V_e = A_e l_e$, the formula can be rearranged in the following form:

$$P_{\max} = \frac{V_e^{0.54} \Delta T \sqrt{k_L}}{C_{th} k_W (k_L + 1)} \sqrt{\frac{F_W R_p}{F_R \rho_c}} \left(\frac{A_e A_W^3}{l_e^5 l_W^3} \right)^{1/6} \sqrt[3]{V_e} \quad , \tag{4.26}$$

or

$$P_{\max} = \Delta T \frac{V_e^{0.873}}{C_{th} k_W} \frac{\sqrt{k_L}}{k_L + 1} \sqrt{\frac{F_W R_p}{F_R \rho_c}} C_2 \quad , \tag{4.27}$$

where

$$C_2 = \left(\frac{A_e A_W^3}{l_e^5 l_W^3} \right)^{1/6} \quad , \tag{4.28}$$

is a dimensionless constant which ranges from 0.07 to 0.09 for most cores. Using equation (B.3), the core loss density can be expressed as:

$$P_m = \frac{P_{tot}}{(k_L + 1) V_e} \quad . \tag{4.29}$$

Substituting the above expression in the model for normalized parallel resistance (4.20) and the result into Eq. (4.25), the formula for a power rating as a function of the magnetic effective volume is:

$$P_{\max} = \frac{C_2 V_e^{0.873} \Delta T \sqrt{k_L F_W / F_R \rho_c} / (k_L + 1) k_W C_{th}}{\sqrt{k_0 / \left[1 + (k_2 / f)^{k_5} \right] + k_1 f^{k_6} [\Delta T / (k_L + 1) C_{th}]^{0.36} V_e^{-0.166} + [k_3 - k_4 V_e^{-0.46} \Delta T / (k_L + 1) C_{th}] / f^2}} \quad . \tag{4.30}$$

Given the core material and a frequency, the volume of the core necessary to handle the required power rating is determined by rearranging Eq. (4.30) in the implicit form:

$$V_e = \left[\frac{P_{max} k_W C_{th}(k_L + 1)\sqrt{\rho_c F_R}}{C_2 \Delta T \sqrt{k_L F_W}} \right]^{1.145} \times \tag{4.31}$$

$$\times \left\{ k_0 / \left[1 + (k_2/f)^{k_5} \right] + k_1 f^{k_6} [\Delta T/(k_L + 1)C_{th}]^{0.36} V_e^{-0.166} + [k_3 - k_4 V_e^{-0.46} \Delta T/(k_L + 1)C_{th}]/f^2 \right\}^{0.572} .$$

For a reasonable seed value (*e.g.*, 10 to 1000 cm^3), about six iterations are necessary to find the effective volume of the core from the above equation. Once the volume is found, the peak flux density due to ac excitation is determined using Eqs. (B.11), (4.24), and (4.27):

$$\hat{B} = \frac{P_{max} k_W}{C_2 \pi f V_e^{1.103}} \sqrt{\frac{C_{th} F_R \rho_c (k_L + 1)}{2 \Delta T F_W k_L}} . \tag{4.32}$$

In order to prevent the thermal instability, the flux density cannot exceed a maximum value specified by the manufacturer of the magnetic material . If the calculated flux density at the frequency of choice exceeds the material specifications, a different design method must be used which assumes a fixed value of the flux density [287]. The total dissipation is found from Eq. (4.24). The number of turns of the i-th winding is determined from Eqs. (B.11), (4.24), and (4.27), the required voltage on its terminations, V_i, :

$$N_i = \frac{V_i C_2 V_e^{0.435}}{P_{max} k_W} \sqrt{\frac{C_4 \Delta T F_W k_L}{C_{th} F_R \rho_c (k_L + 1)}} . \tag{4.33}$$

The calculated number of turns refers to one or more parallel conductors necessary to fill the window area.

Defined in the Appendix B core shape constant, C_4, has the following approximate values: 6 for pot cores, 8 for RM cores, 7 to 14 for PQ cores, 11 to 18 for EE cores, 16 for ETD and EC cores, and 19 for EPC cores. For a transformer with only few turns, it is desirable to calculate the corrected core shape factor for the closest integer number of turns, N,:

$$C_4 = \left(\frac{N P_{max} k_W}{V_i C_2 V_e^{0.435}} \right)^2 \frac{C_{th} F_R \rho_c (k_L + 1)}{\Delta T F_W k_L} . \tag{4.34}$$

The core shape is determined based on the calculated C_4 value. If desirable C_4 falls outside the practical range (6 to 22), the ratio of winding loss to core loss, k_L, can differ substantially from 1. In such case k_L is determined using a core shape with the closest value of C_4. From Eq. (4.33):

$$k_L = \frac{1}{\Delta T F_W l_e V_i^2 C_2^2 C_4 V_e^{1.037} / C_{th} F_R \rho_c N^2 P_{max}^2 k_W^2 - 1} \quad . \tag{4.35}$$

The resulting k_L is substituted in Eq. (4.31). Lack of space prevents printing the final equation. The modified equation is solved also by iteration. The volume of the core can be substantially greater compared to the case $k_L = 1$.

There are two degrees of freedom in the design process: ac to dc resistance ratio, F_R, depending on the winding structure, and operating frequency, f. The ac to dc resistance ratio can be either assumed a fixed value or made frequency dependent if a conductor size is assumed. The frequency can be either fixed by circuit requirements or variable if frequency optimization is desired. The necessary value of a magnetizing inductance is obtained by gapping the core.

4.5.3 Selection of the Operating Frequency to Minimize Volume

If it is possible to choose a frequency of operation for the transformer, the expression for the effective volume needs to be evaluated for a number of frequencies, plotted, and then the minimum volume chosen. In the case of fixed ac to dc resistance ratio, the Eq. (4.31) is used or its variation with the constant number of turns and variable k_L (4.33). In the more complicated case of an inductor or a transformer using a predetermined solid wire with a diameter d, or a litz wire, the ac to dc resistance ratio can be found using one-dimensional winding models described in Section 4.2. The ac to dc resistance ratio must be expressed as a function of the effective core volume, V_e, in order to be substituted in Eq. (4.31). Therefore, the number of

layers in each winding can be calculated from geometry of the winding as follows:

$$n = \frac{h_W}{k_W s\, h_l} = \frac{h_W}{k_W s\, d\sqrt{\pi F_W p}} = \frac{C_3 \sqrt[3]{V_e}}{k_W s\, d\sqrt{\pi F_W p}} \quad , \tag{4.36}$$

where

h_W - window height,

h_l - layer height,

s - number of interleaves (or peaks in the MMF diagram),

p - number of strands in a litz wire ($p = 1$ for solid wire),

d - wire diameter,

C_3 - $h_W/\sqrt[3]{V_e}$ - window geometry constant, small for flat windows (0.2 to 0.4 in most cores).

For a simple transformer with two windings wound using the same conductor the ac to dc resistance ratio is obtained substituting Eqs. (4.1), (4.2), (4.3), and (4.34) into Eq. (4.6):

$$F_R = \frac{\xi}{2}\left[\frac{\sinh\xi + \sin\xi}{\cosh\xi - \cos\xi} + \left(\frac{4\sqrt[3]{V_e^2}C_3^2}{3k_W^2 s^2 d^2 \pi F_W p} - \frac{1}{3} \right) \frac{\sinh\xi - \sin\xi}{\cosh\xi + \cos\xi} \right] \quad , \tag{4.37}$$

where parameter ξ is described by Eq. (4.4):

$$\xi = \frac{\pi d}{2}\sqrt{\eta f \mu_0 / \rho} \quad . \tag{4.38}$$

Substituting above equations into Eq. (4.31) yields the volume of the transformer with the predetermined conductor size:

$$V_e = \left\{ \frac{P_{max} k_W C_{th}(k_L + 1)}{C_2 \Delta T \sqrt{k_L}} \sqrt{\frac{\rho_c \xi}{2F_W}\left[\frac{\sinh\xi + \sin\xi}{\cosh\xi - \cos\xi} + \left(\frac{4\sqrt[3]{V_e^2}C_3^2}{3k_W^2 s^2 d^2 \pi F_W p} - \frac{1}{3} \right) \frac{\sinh\xi - \sin\xi}{\cosh\xi + \cos\xi} \right]} \right\}^{1.145} \times \tag{4.39}$$

$$\times \left\{ k_0 / \left[1 + (k_2/f)^{k_5} \right] + k_1 f^{k_6} [\Delta T/(k_L + 1)C_{th}]^{0.36} V_e^{-0.166} + [k_3 - k_4 V_e^{-0.46} \Delta T/(k_L + 1)C_{th}]/f^2 \right\}^{0.572} .$$

If more than one wire size is used for different windings even more complex formula can be derived. In inductor windings the interleaving factor is equal to one, $s = 1$, since no interleaving is possible.

4.5.4 Design Examples

As an example, the design procedure for a transformer in a $P_{out} = 50$ W dc-to-dc resonant converter operating at the frequency of $f = 500$ kHz is presented. The operating temperature is 100°C, and the allowed temperature increase is $\Delta T = 40$°C. The magnetic core is made of 3F3 ferrite (Philips). The efficiency of the rectifier is $\eta_{REC} = 0.9$, the power factor of the rectifier is $\eta_{PF} = 0.55$. The winding is made of a litz wire 175×AWG#44 with interleaving factor, $s = 2$, copper factor, $F_W = 0.3$, and porosity factor, $\eta = 0.52$. The core factor $C_2 = 0.08$, and window shape factor $C_3 = 0.3$, which are average values for most cores. Initial guess for core shape factor is $C_4 = 14$.

1. Determine the power rating

$$P_{\max} = \frac{P_{out}}{\eta_{REC}\eta_{PF}} = \frac{50}{0.9 \cdot 0.55} \approx 100 \quad \text{VA} . \tag{4.40}$$

2. Calculate the core volume using Eq. (4.39). The iterations using seed value of 10 cm^3 are shown in Table 4.1.

3. Find ac to dc resistance ratio using Eqs. (4.37) and (4.38):

$$\xi = \frac{\pi d}{2}\sqrt{\eta f \mu_0 / \rho} = \frac{\pi 5 \cdot 10^{-5}}{2}\sqrt{0.525 \cdot 10^5 4\pi 10^{-7} / 2.22 \cdot 10^{-8}} = 0.3 \quad . \tag{4.41}$$

$$F_R = \frac{\xi}{2}\left[\frac{\sinh\xi + \sin\xi}{\cosh\xi - \cos\xi} + \left(\frac{4\sqrt[3]{V_e^2 C_3^2}}{3k_W^2 s^2 d^2 \pi F_W p} - \frac{1}{3}\right)\frac{\sinh\xi - \sin\xi}{\cosh\xi + \cos\xi}\right] = \tag{4.42}$$

$$= \frac{0.3}{2}\left[\frac{\sinh(0.3) + \sin(0.3)}{\cosh(0.3) - \cos(0.3)} + \left(\frac{4\sqrt[3]{(1.129 \cdot 10^{-6})^2 0.3^2}}{3 \cdot 2^2 2^2 (5 \cdot 10^{-5})^2 \pi 0.3 \cdot 175} - \frac{1}{3}\right)\frac{\sinh(0.3) - \sin(0.3)}{\cosh(0.3) + \cos(0.3)}\right] =$$

$$= 1.91 \quad .$$

4. Check the peak flux density using Eq. (4.32):

$$\hat{B} = \frac{P_{max} k_W}{C_2 \pi f V_e^{1.103}} \sqrt{\frac{C_{th} F_R \rho_c (k_L + 1)}{2 \Delta T F_W k_L}} = \tag{4.43}$$

$$= \frac{100 \cdot 2}{0.08\pi 5 \cdot 10^5 (1.129 \cdot 10^{-6})^{1.103}} \sqrt{\frac{0.0305 \cdot 1.91 \cdot 2.22 \cdot 10^{-8}(1+1)}{2 \cdot 40 \cdot 0.3 \cdot 1}} = 0.060 \text{ T} \quad .$$

5. Calculate the number of turns using Eq. (4.33):

$$N_i = \frac{V_i C_2 V_e^{0.435}}{P_{max} k_W} \sqrt{\frac{C_4 \Delta T F_W k_L}{C_{th} F_R \rho_c (k_L + 1)}} = \tag{4.44}$$

$$= \frac{10 \cdot 0.08 \cdot (1.129 \cdot 10^{-6})^{0.435}}{100 \cdot 2} \sqrt{\frac{14 \cdot 40 \cdot 0.3 \cdot 1}{0.0305 \cdot 1.91 \cdot 2.22 \cdot 10^{-8}(1+1)}} = 2.637 \approx 3 \quad .$$

6. This step is only necessary if N_i is less then 10 turns. The core shape factor has to be calculated again due to significant rounding error for $N_i < 10$. The required core shape factor is found using integer number of turns using Eq. (4.34):

$$C_4 = \left(\frac{N P_{max} k_W}{V_i C_2 V_e^{0.435}} \right)^2 \frac{C_{th} F_R \rho_c (k_L + 1)}{\Delta T F_W k_L} = \tag{4.45}$$

$$= \left[\frac{3 \cdot 100 \cdot 2}{10 \cdot 0.08 \cdot (1.129 \cdot 10^{-6})^{0.435}} \right]^2 \frac{0.0305 \cdot 1.91 \cdot 2.22 \cdot 10^{-8}(1+1)}{40 \cdot 0.3 \cdot 1} = 18.13 \quad .$$

The core volume must be equal or greater than the calculated value. The core shape factor can be slightly larger or smaller from the calculated one.

A suitable core is EE 20/20/5 with effective magnetic volume $V_e = 1.34$ cm^3, and core shape factor $C_4 = 15.2$.

In order to minimize the volume of the transformer with respect to frequency, similar calculations are conducted from 10 kHz to 10 MHz. The minimum volume of the transformer and required core shape constant are shown in Fig. 4.39. If the number of turns is small, the optimum frequency, f, and the core shape constant, C_4, have to be determined with the aid of the plot for discrete number of turns. The discrete number of turns restricts the choice of C_4 at

particular frequency. Therefore, the minimum volume can be achieved at 400 kHz only using two turns on the pot core (P18/11 with $V_e = 1.12$ cm^3) or three turns on the EE core (EE 20/20/5 with $V_e = 1.34$ cm^3). Use of other shapes will not lead to minimum volume.

The study of an effect of the winding structure on the size of the transformer is conducted on two transformers with power rating of 100 VA and 1 kVA. Four winding configurations are compared for each transformer: AWG#24 solid wire windings without interleaving (s=1) and interleaved (s=2), and 175×AWG#44 litz wire without interleaving (s=1) and interleaved (s=2). The minimum effective volumes of 100 VA and 1 kVA transformer cores are shown in Fig. 4.46. At very low frequencies, a solid wire yields lower volume due to a better copper factor than the litz wire. At higher frequencies the litz wire is a better choice because of its low proximity losses, despite its lower copper factor. However, in the megahertz frequency range (above 2 MHz in the example cases), when the diameter of the strand is comparable with the skin depth the litz wire windings have much higher losses due to the proximity effect in a large number of strands than do similar solid wire windings. Therefore, it is very important to choose the conductor type according to operating frequency. When the same type of winding is used a transformer rated at a higher power has higher volume and lower the optimum frequency of operation compared to the lower rated transformer. Interleaved windings have lower conduction losses.

Table 4.1. Calculation of the effective core volume of the transformer.

Iteration	V_e [cm^3]
0	10
1	1.745
2	1.203
3	1.139
4	1.130
5	1.129
6	1.129

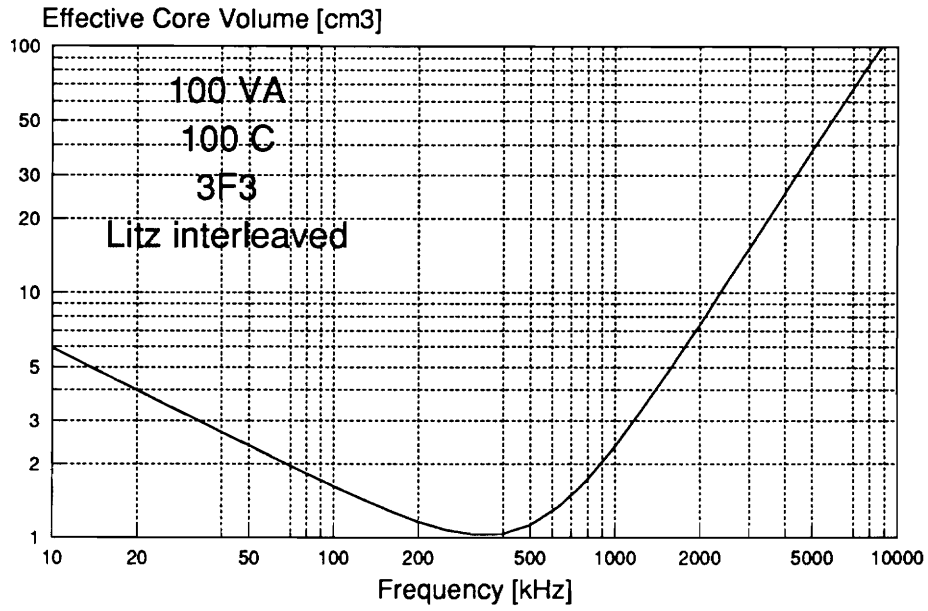

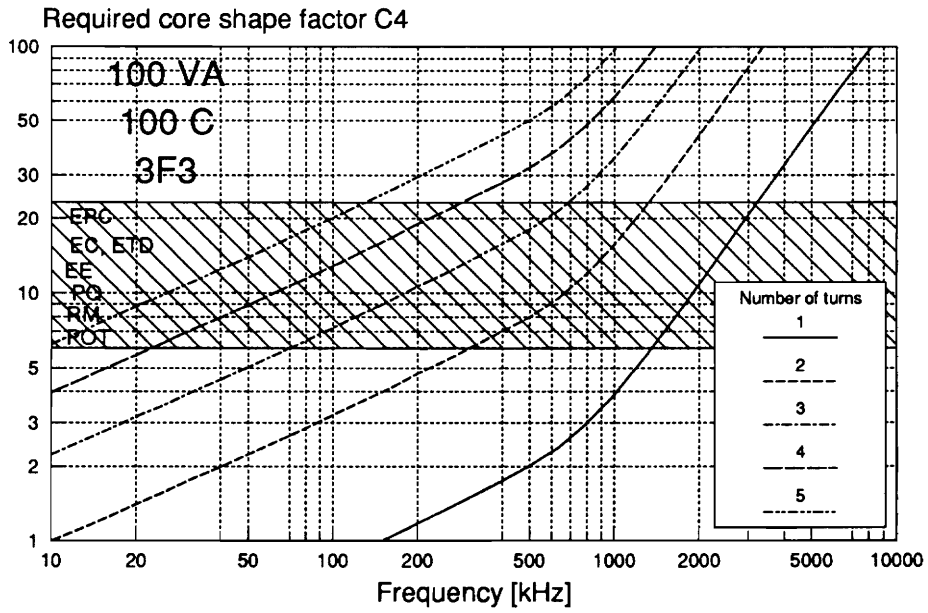

Fig. 4.39. Selection of the optimum operating frequency. If the number of turns is small, the optimum frequency, f, and the core shape constant, C_4, have to be determined with the aid of the plot for discrete number of turns. The discrete number of turns restricts the choice of C_4 at particular frequency. Therefore, the minimum volume can be achieved at 400 kHz only using two turns on the pot core or three turns on the EE core. Use of other shapes will not lead to minimum volume since k_L is not equal to 1.

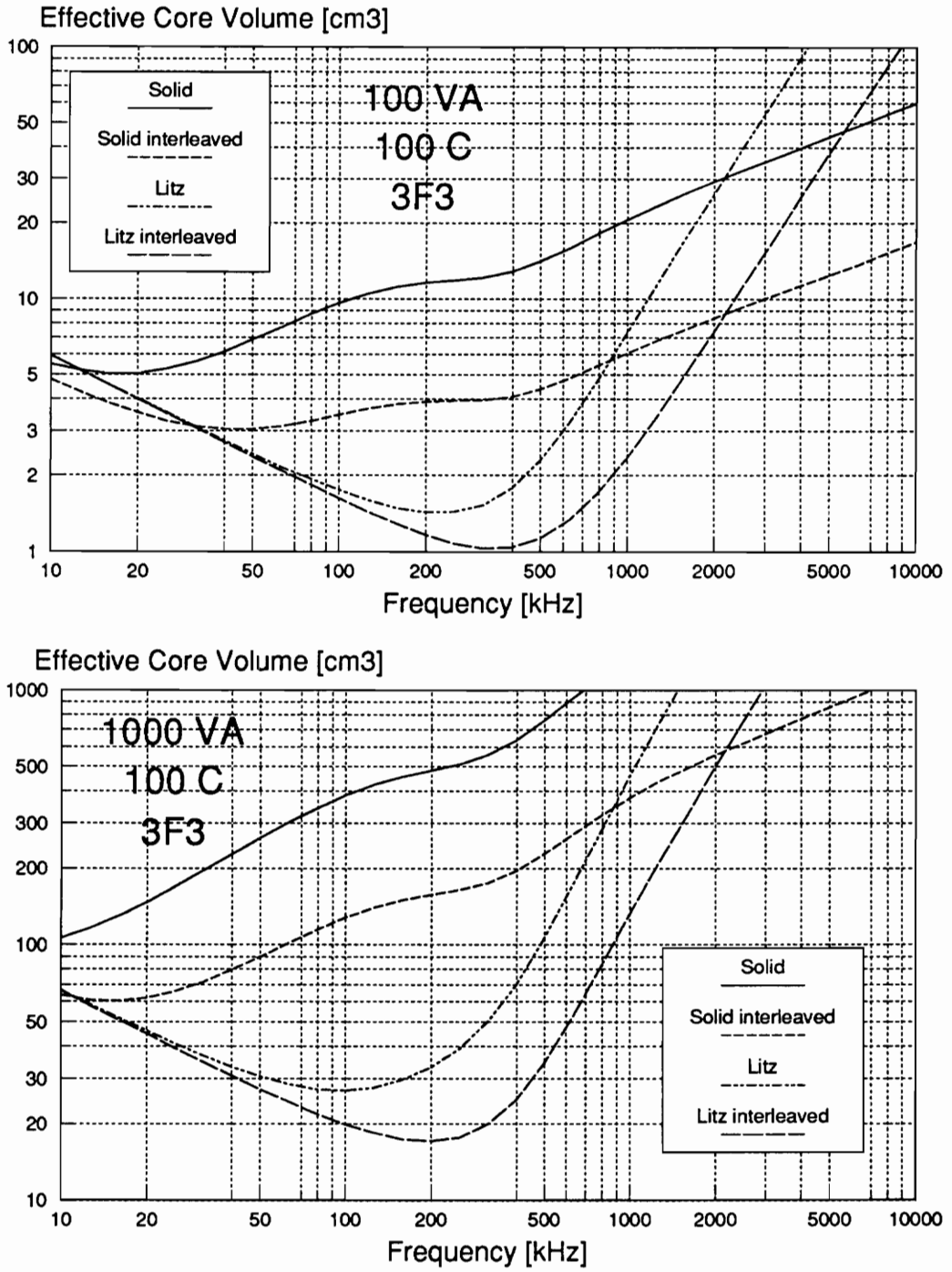

Fig. 4.40. Volume of the optimum power transformer as a function of a frequency for different winding configurations in a 100 VA and 1 kVA transformers.

Conclusions and Future Work

This work presents an analysis, modeling, and design of ferrite power transformers and inductors for high-frequency power applications.

A new method of characterization of power magnetic materials is established. The method enables convenient calibration and accurate measurements of permeability and losses with constant flux density or constant power dissipation in the core with dc or dynamic bias. Accurate measurements are possible from 50 kHz to 100 MHz at large signal excitations. This fast measurement technique makes practical high-resolution frequency scanning to identify magnetoelastic resonances in magnetic cores.

After an overview of magnetic losses, the electric field in a ferrite grain is analyzed. The formation of the space charge and the distribution of the electric field is studied. The effect of the grain boundary on the frequency dependence of the domain wall damping is calculated. The influence of the orientations of domain walls on the electric field is discussed. The effect of multiple domain walls inside the single ferrite grain on the space charge and the distribution of the electric field is studied.

A new theory of residual losses is proposed to account for high-frequency losses related to the electric field inside ferrite grains. The theory deals with magnetoelectric interactions between spins and polarons in magnetic semiconductors. The additional loss is due to higher energy barrier and lower hopping frequency when polarons form clusters under the influence of the electric field. The theory explains influence of doping with paramagnetic ions on residual losses.

The magnetic losses in three major soft ferrites (MnZn, NiZn, and MnMg) were investigated. Extensive measurements were performed in wide frequency and flux density range, at different temperatures, and under static and dynamic magnetic bias field. The influence of the core material, core shape, and magnetic bias on magnetoelastic resonances was studied. In most cases multiple resonances occur. The frequencies of these resonances are very difficult to predict except for toroidal cores. In MnZn ferrites the resonances appear only when static bias field is applied. The measurement of permeability and losses under time-varying bias revealed that ionic diffusion after-effect has much greater influence on the core loss than on the permeability. The after-effect loss increases with the increase of the rate of change of the bias field.

Two new models of losses in ferrites are proposed. First model expresses losses in terms of flux density and frequency. It is very suitable for the analysis of losses. The second model describes the normalized parallel resistance as a function of frequency and core loss density. Therefore, it is specifically suited for design purposes. To obtain agreement with experimental data, the frequency exponent in the hysteresis loss term was substantially modified. This indicates that the hysteresis loss in ferrites depends strongly on frequency. The accuracy of the model ranges from 5 to 15 percent depending on the material and dc bias. Both models include a parametric dependence on the static bias field.

The experimental verification and analysis of errors of one- and two-dimensional models of winding losses was performed in solid and litz wire windings. The method of separation of winding loss into skin effect and proximity effect is presented, and the phenomenological model is developed. It is shown that conversion of round wires to conducting sheets (due to Dowell) does not introduce additional error to one-dimensional model. The one-dimensional models are reasonably accurate compared to experiment. The model errors are related to the end effects in the windings. The two-dimensional uniform field model is not usable due to a substantial disagreement with the measurements.

The method for design of a thermally limited power transformer and inductor is proposed, including the optimization of the operating frequency. Given the power handling capability, core material, frequency of operation, and temperature difference to ambient, the procedure allows calculation of the minimum volume of the transformer or inductor. If the frequency is not fixed, further optimization is performed with respect to frequency. A modified procedure is given for transformers with low voltage windings which have small number of turns. The procedure suggests particular core shapes in order to minimize the volume of the transformer or inductor.

Future research regarding the above topics should address

- a detailed quantum theory of residual losses including magnetoelectric effect,
- a theory of frequency-dependent hysteresis loss in ferrites,
- more elaborate modeling of losses in ferrite materials with a functional dependence on the static flux density due to magnetic bias,
- an improvement of the one-dimensional model to include edge effects,
- an analysis of losses in foil windings, including the contribution of the perpendicular flux component,
- an analysis of magnetic field and winding losses, both for wire and foil, in inductors with gapped cores, and
- an improved procedure for the design of a thermally limited transformer and inductor with a functionally dependent bias to enable an optimization of transformers in single-ended power converters.

Appendix A

Analysis of Multilayer Windings

Round conductors of a diameter d can be converted into square conductors of the same cross-sectional area. The size of the square wires is $h_{CU} = d\sqrt{\pi}/2$. Let the ratio of the magnetic fields on the outside and the inside of the winding (consisting of n identical layers of thickness h_{CU} each, shown in Fig. A.1) be:

$$\theta = \alpha + j\beta = \frac{H_z(0)}{H_z(n\, h_{CU})} \quad . \tag{A.1}$$

Assuming equal current in all layers of the winding, the magnetic field on top of m-the layer is:

$$H_z(m\, h_{CU}) = H_z(0) + [H_z(n\, h_{CU}) - H_z(0)]\frac{m}{n} \tag{A.2}$$

$$= H_z(n\, h_{CU})\left[\theta + (1-\theta)\frac{m}{n}\right] \quad .$$

The ratio of the magnetic fields for m-the layer is:

$$\phi = \frac{H_z[(m-1)h_{CU}]}{H_z(m\, h_{CU})} = \frac{n\theta + (1-\theta)(m-1)}{n\theta + (1-\theta)m} \quad . \tag{A.3}$$

The time-averaged energy loss density, $< Q_J >$, in a single infinite current sheet was derived in [288] and [289]:

$$< Q_J > = \frac{|H_z(h_{CU})|^2}{\eta\sigma_{CU}\delta}[(1+\alpha^2+\beta^2)F_1(\xi) - 4\alpha F_2(\xi)] \quad , \tag{A.4}$$

where

$$F_1(\xi) = \frac{\sinh 2\xi + \sin 2\xi}{\cosh 2\xi - \cos 2\xi} \quad , \tag{A.5}$$

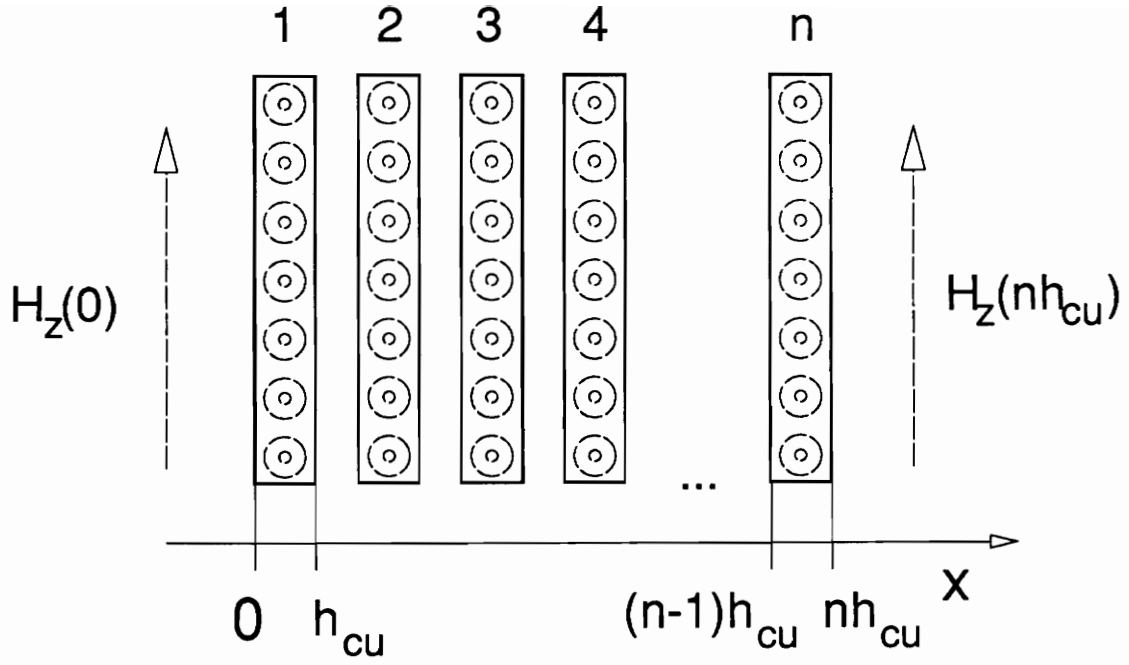

Fig. A.1. Magnetic field in a multilayer winding.

$$F_2(\xi) = \frac{\sinh\xi\cos\xi + \cosh\xi\sin\xi}{\cosh 2\xi - \cos 2\xi} \quad , \quad \text{and} \tag{4.6}$$

$$\xi = \frac{\sqrt{\pi\eta}\,d}{2\delta} \quad . \tag{4.7}$$

Substituting Eqs. (A.2) and (A.3) into (A.4), the power dissipation per square meter in *m*-the layer is:

$$< Q_J >_m = \frac{|H_Z(n\,h_{CU})|^2}{\eta\sigma_{CU}\delta}\left|\theta + (1-\theta)\frac{m}{n}\right|^2 [(1+|\phi|^2)F_1(\xi) - 4\Re(\phi)F_2(\xi)] \quad . \tag{A.8}$$

Substituting Eqs. (A.1) and (A.3) into (A.4) and expanding, we obtain:

$$\begin{aligned} < Q_J >_m = \frac{|H_Z(n\,h_{CU})|^2}{\eta\sigma_{CU}\delta} \cdot \frac{1}{n^2}\{ & 2m^2(\alpha^2 - 2\alpha + \beta^2 + 1)[F_1(\xi) - 2F_2(\xi)] \\ & - 2m[2n(\alpha^2 - \alpha + \beta^2) + \alpha^2 - 2\alpha + \beta^2 + 1][F_1(\xi) - 2F_2(\xi)] \\ & + F_1(\xi)[2n^2(\alpha^2 + \beta^2) + 2n(\alpha^2 - \alpha + \beta^2) + \alpha^2 - 2\alpha + \beta^2 + 1] \\ & - 4F_2(\xi)n[n(\alpha^2 + \beta^2) + \alpha^2 - \alpha + \beta^2]\} \quad . \end{aligned} \tag{A.9}$$

Thus, after summing for n layers in the winding and division by dc loss, the ac to dc resistance for the multilayer winding is:

$$F_R = \frac{\sum_{m=1}^{n} < Q_J(\xi) >_m}{n < Q_J(\xi \to 0) >_n} = \frac{\xi}{3}\left\{2n^2\frac{\alpha^2 + \alpha + \beta^2 + 1}{\alpha^2 - 2\alpha + \beta^2 + 1}[F_1(\xi) - 2F_2(\xi)] + [F_1(\xi) + 4F_2(\xi)]\right\} \quad . \tag{A.10}$$

The skin effect factor can be found for a symmetrical magnetic field when $\alpha = -1$, $\beta = 0$, and $n = 1$:

$$F_{RS} = \frac{\xi}{2}[F_1(\xi) + 2F_2(\xi)] \quad . \tag{A.11}$$

Assuming orthogonality of skin and proximity effects, the ac to dc resistance can be expressed as the sum of skin and proximity effects [290] as:

$$F_R = F_{RS} + F_{RP} \quad . \tag{A.12}$$

Therefore, the proximity effect of the winding with *n* layers is:

$$F_{RP} = F_R - F_{RS} = \frac{\xi}{6}\left(4n^2 \frac{\alpha^2+\alpha+\beta^2+1}{\alpha^2-2\alpha+\beta^2+1} - 1\right)[F_1(\xi) - 2F_2(\xi)] \quad . \tag{A.13}$$

Using properties of trigonometric and hyperbolic functions:

$$F_1(\xi) \pm 2F_2(\xi) = \frac{\sinh 2\xi + \sin 2\xi \pm 2\cos\xi \sinh\xi \pm 2\sin\xi \cosh\xi}{\cosh 2\xi - \cos 2\xi} \tag{A.14}$$

$$= \frac{2(\sinh\xi \pm \sin\xi)(\cosh\xi \pm \cos\xi)}{2\cosh^2\xi - 1 - (2\cos^2\xi - 1)}$$

$$= \frac{(\sinh\xi \pm \sin\xi)(\cosh\xi \pm \cos\xi)}{(\cosh\xi - \cos\xi)(\cosh\xi + \cos\xi)} = \frac{\sinh\xi \pm \sin\xi}{\cosh\xi \mp \cos\xi} \quad .$$

The skin factor can be expressed as:

$$F_{RS} = \frac{\xi}{2}\frac{\sinh\xi + \sin\xi}{\cosh\xi - \cos\xi} \quad , \tag{A.15}$$

and the proximity factor of a winding with n layers as:

$$F_{RP} = \frac{\xi}{6}\left(4n^2 \frac{\alpha^2+\alpha+\beta^2+1}{\alpha^2-2\alpha+\beta^2+1} - 1\right)\frac{\sinh\xi - \sin\xi}{\cosh\xi + \cos\xi} \quad . \tag{A.16}$$

In the particular case of an inductor or a two-winding transformer, with each winding consisting of n identical layers, the magnetomotive force diagram yields $\alpha = \beta = 0$, and the proximity factor is

$$F_{RPI} = \frac{\xi}{6}(4n^2 - 1)\frac{\sinh\xi - \sin\xi}{\cosh\xi + \cos\xi} \quad . \tag{A.17}$$

Only the proximity effect is the function of the number of layers and the external magnetic field (A.16). The lowest proximity effect occurs in the first outside layer of the winding without external field ($\alpha = \beta = 0$, $n = 1$). The Eq. (A.17) yields:

$$F_{RP0} = \frac{\xi}{2}\frac{\sinh\xi - \sin\xi}{\cosh\xi + \cos\xi} \quad . \tag{A.18}$$

Substituting the above equation into (A.16) and (A.12), the ac to dc resistance of the winding can be expressed without detailed knowledge of a particular layer structure as:

$$F_R = F_{RS} + \frac{1}{3}\left(4n^2 \frac{\alpha^2+\alpha+\beta^2+1}{\alpha^2-2\alpha+\beta^2+1} - 1\right) F_{RP0} \quad . \tag{A.19}$$

Appendix B

Power Rating of the Thermally Limited Power Transformer or Inductor

The total power loss in the transformer is a sum of the core loss and winding loss:

$$P_{tot} = P_C + P_W \quad . \tag{B.1}$$

The ratio of winding loss to core loss is:

$$k_L = \frac{P_W}{P_C} \quad . \tag{B.2}$$

Therefore, it is possible to express core and winding loss as follows:

$$P_C = \frac{P_{tot}}{k_L + 1} \quad , \quad \text{and} \tag{B.3}$$

$$P_W = \frac{k_L}{k_L + 1} P_{tot} \quad . \tag{B.4}$$

Using Ohm's law the winding loss can be expressed as:

$$P_W = I_1^2 R_W = \frac{k_W^2 I_1^2 \rho_c F_R N_1^2 l_W}{A_W F_W} \quad , \tag{B.5}$$

where

R_W - total winding resistance,

A_W - window area,

ρ_c - conductor resistivity,

l_W - mean length of turn,

F_R - ac to dc resistance ratio of the windings,

N_1 - number of turns in the primary winding,

I_1 - primary current, and

k_W - number of windings rated at full power, 1 for inductors, 2 for transformers.

From Eq. (3.15) and the Ohm's law the core loss can be expressed as :

$$P_C = \frac{V_1^2}{r_p} = \frac{V_1^2 l_e}{R_p N_1^2 A_e} \quad , \tag{B.6}$$

where

V_1 - primary voltage,

r_p - parallel resistance due to magnetic core losses,

R_p - normalized parallel resistance due to magnetic losses.

The power rating of the magnetic device is

$$P_{max} = V_1 I_1 \quad , \quad \text{and} \tag{B.7}$$

the V_1, and I_1 can be eliminated by substituting Eqs. (B.5) and (B.6) into (B.7). Using Eqs. (B.3) and (B.4) P_C and P_W are eliminated, and the formula for a total output power is:

$$P_{max} = \frac{P_{tot}}{k_W} \frac{\sqrt{k_L}}{k_L + 1} \sqrt{\frac{A_W A_e F_W R_p}{l_e l_W F_R \rho_c}} \quad . \tag{B.8}$$

Rearranging (B.6), the required number of turns to obtain a desired rms value of the voltage on the winding is:

$$N_1 = V_1 \sqrt{\frac{l_e}{P_C R_p A_e}} = V_1 \sqrt{\frac{l_e (k_L + 1)}{P_{tot} R_p A_e}} \quad . \tag{B.9}$$

If the dimensionless core shape constant is defined as

$$C_4 = \frac{l_e}{A_e} \sqrt[3]{V_e} \quad ,$$

the Eq. (B.9) can be written as

$$N_1 = V_1 \sqrt{\frac{C_4 (k_L + 1)}{P_{tot} R_p \sqrt[3]{V_e}}} \quad . \tag{B.10}$$

When the design is limited by an integer number of turns the ratio of winding loss to core loss can be expressed from (B.9) as:

$$k_L = \frac{N_1^2 P_{tot} R_p A_e}{V_1^2 l_e} - 1 \quad . \tag{B.11}$$

To avoid saturation of the core, the flux density cannot exceed a maximum value specified by the manufacturer. The peak operating flux density can be determined by substituting (B.3) and (B.6) into Faraday's law

$$\hat{B} = \frac{1}{\pi f} \sqrt{\frac{P_{tot} R_p}{2(k_L + 1) A_e l_e}} \quad , \tag{B.12}$$

and has to be compared with the maximum allowed for the specific magnetic material.

REFERENCES

[1] W. C. Bowman, J. F. Balicki, F. T. Dickens, R. M. Honeycutt, W. A. Nitz, W. Strauss, W. B. Suiter, and N. G. Zeisse, "A resonant dc-to-dc converter operating at 22 Megahertz," *IEEE Applied Power Electronics Conference Proceedings*, 3-11 (1988).

[2] C. P. Henze, H. C. Martin, D. W. Parsley, "Zero-Voltage Switching in High Frequency Power Converters Using Pulse Width Modulation," *IEEE Applied Power Electronics Conference Proceedings*, 33-40 (1988).

[3] L. F. Casey, M. F. Schlecht, "A High-Frequency, Low-Volume, Point-of-Load Power Supply for Distributed Power System," *IEEE Trans. Power Electronics* **3** [1], 72-82 (1988).

[4] A. Estrov, "Power Transformer Design for 1 Mhz Resonant Converter," *First High Frequency Power Conversion Conference Proceedings*, 36-54 (1986).

[5] A. F. Goldberg, J. G. Kassakian and M. F. Schlecht, "Issues Related to 1-10 MHz Transformer Design," *IEEE Transactions on Power Electronics* **4** [1], 113-23 (1989).

[6] B. Carsten, "High Frequency Conductor Losses in Switchmode Magnetics," *High Frequency Power Conversion Conference Proceedings*, 155-176 (1986).

[7] F. C. Lee, W. A. Tabisz, M. M. Jovanovic, "Recent Developments in High-Frequency Quasi-Resonant and Multi-Resonant Technologies," *Proceedings of the European Conference on Power Electronics and Applications*, 401-10 (1989).

[8] K. H. Liu, F. C. Lee, "Resonant Switch - A Unified Approach to Improve Performance of Switching Converters," *IEEE International Telecommunication Energy Conference Proceedings*, 334-41 (1984).

[9] K. Liu, F. C. Lee, "Zero-Voltage Switching Technique in dc/dc Converters," *IEEE Power Electronics Specialists Conference Record*, 58-70 (1986).

[10] W. A. Tabisz, F. C. Lee, "Zero-Voltage-Switching Multi-Resonant Technique - A Novel Approach to Improve Performance of High-Frequency Quasi-Resonant Converters," *IEEE Power Electronics Specialists Conference Record*, 9-17 (1988).

[11] Rayleigh, "Notes on Electricity and Magnetism III. On the Behaviour of Iron and Steel Under the Operation of Feeble Magnetic Forces," *Phil. Mag.* **23**, 225 (1887).

[12] Weiss, *Éclairage Électrique* **8**, 436 (1896).

[13] M. Wien, "Ueber die Magnetisirung durch Wechselstrom," *Ann. Phys. Chem.* **66** [13], 859-953 (1898).

[14] G. A. Kelsall, "Permeameter for Alternating Current Measurements at Small Magnetizing Forces," *J. Opt. Soc. Am. Rev. Sci. Instr.* **8** [2], 329-38 (1924).

[15] H. J. Lindenhovius and J. C. van der Breggen, "The Measurement of Permeability and Magnetic Losses of Non-Conducting Ferromagnetic Material at High Frequencies," *Philips Res. Rep.* **3** [1], 37-45 (1948).

[16] P. H. Haas, "A Radio-Frequency Permeameter," *J. Res. NBS* **51** [5], 221-8 (1953).

[17] A. L. Rasmussen, A. W. Enfield, and A. Hess, "Advances in the Design and Application of the Radiofrequency Permeameter," *J. Res. NBS* **56** [5], 261-8 (1956).

[18] C. A. Hoer and A. L. Rasmussen, "Equations for the Radiofrequency Magnetic Permeameter," *J. Res. NBS* **67C** [1], 69-76 (1963).

[19] C. A. Hoer and R. D. Harrington, "Parallel Reversible Permeability Measurement Techniques From 50 kc/s to 3 Gc/s," *J. Res. NBS* **67C** [3], 259-65 (1963).

[20] A. L. Rasmussen and R. C. Powell, "A Low-Impedance Maxwell Bridge for Measuring Toroidal Magnetic Materials from 1 kc to 100 kc," *Proc. IRE* **50** [12], 2505-6 (1962).

[21] Christensen, "Radio Frequency B-H Tracer and Power Measurement of Ferrites," *AIEE Conf. Magn. Magn. Mat.* **T-78**, 361-4 (1955).

[22] Bady, "Measurement of Losses of Magnetic Materials at High Inductions at Frequencies up to 100 Megacycles," *J. Appl. Phys.* **29** [3], 393-4 (1958).

[23] P. P. Lombardini, R. F. Schwartz, and R. J. Doviak, "Measurement of the Properties of Various Ferrites Used in Magnetically Tuned Resonant Circuits in the 2.5-45 Mc/sec Region," *J. Appl. Phys.* **29** [3], 395-6 (1958).

[24] V. Cagan and M. Guyot, "Fast and Convenient Technique for Broadband Measurements of the Complex Initial Permeability of Ferrimagnets," *IEEE Trans. Magn.* **MAG-20** [5], 1732-4 (1984).

[25] R. B. Goldfarb and H. E. Bussey, "Method for Measuring Complex Permeability at Radio Frequencies," *Rev. Sci. Instrum.* **58** [4], 624-7 (1987).

[26] A. Fessant, J. Gieraltowski, J. Loaëc, and H. Le Gall, "Strip-Line Method for Measuring the Complex Permeability of Magnetic Materials," *J. Magn. Magn. Mat.* **83**, 557-8 (1990).

[27] W. E. Babcock, "A Simplified Method of Determining High Frequency Characteristics of Magnetic Core Materials," *Proc. Powercon* **10**, F3-1-17 (1983).

[28] T. Katane, T. Yamaguchi, T. Ito, T. Sato, and Y. Sakaki, "A High Frequency Iron Loss Measuring System," *IEEE Trans. Magn.* **MAG-20** [5], 1729-31 (1984).

[29] V. J. Thottuvelil, T. G. Wilson, and H. A. Owen, Jr., "High-Frequency Measurement Techniques for Magnetic Cores," *IEEE Power Electronics Specialists Conference Record* **85CH2117-0**, 412-25 (1985).

[30] T. G. Wilson, V. J. Thottuvelil, and H. A. Owen, Jr., "Magnetics Problems in Power Electronics," *Adv. Ceram.* **16**, 433-46 (1985).

[31] T. Mochizuki, I. Sasaki, and K. Murakawa, "A High Frequency Core Loss Automatic Measuring System," *IEEE Trans. Magn.* **MAG-22** [5], 668-70 (1986).

[32] T. Sato and Y. Sakaki, "100kHz-10MHz Iron Loss Measuring System," *IEEE Trans. Magn.* **MAG-23** [5], 2593-5 (1987).

[33] A. F. Goldberg, "High Field Properties of Nickel-Zinc Ferrites at 1-10 MHz," *IEEE Applied Power Electronics Conference*, New Orleans, LA, February 1-5, 1988.

[34] Jordan, "Die ferromagnetischen Konstanten für schwache Wechselfelder," *Elek. Nach. Tech.* **1**, 7-29 (1924).

[35] E. C. Snelling, *"Soft Ferrites,"* 2nd Ed., Butterworth & Co., London, 66 (1988).

[36] J. K. Watson and S. Amoni, "Using Parallel Complex Permeability for Ferrite Characterization," *IEEE Trans. Magn.* **25** [5], 4224-6 (1989).

[37] C. Kittel and J. K. Galt, "Ferromagnetic Domain Theory," *Sol. St. Phys.* **3**, 437-564 (1956).

[38] F. Brown and C. L. Gravel, "Domain Rotation in Nickel Ferrite," *Phys. Rev.* **97** [1], 55-9 (1955).

[39] D. C. Jiles and D. L. Atherton, "Theory of Ferromagnetic Hysteresis," *J. Appl. Phys.* **55** [6], 2115-20 (1984).

[40] K. Sixtus and L. Tonks, "Propagation of Large Barkhausen Discontinuities," *Phys. Rev.* **37**, 930-58 (1931).

[41] R. H. Pry and C. P. Bean, "Calculation of the Energy Loss in Magnetic Sheet Materials Using a Domain Model," *J. Appl. Phys.* **29** [3], 532-3 (1958).

[42] Y. Saito, S. Hayano, and Y. Sakaki, "A Parameter Representing Eddy Current Loss of Soft Magnetic Materials and its Consecutive Equation," *J. Appl. Phys* **64** [10], 5684-6 (1988).

[43] Y. Sakaki and T. Sato, "Large Signal Eddy Current Losses Beyond 100 kHz," *IEEE Trans. Magn.* **MAG-20** [5], 1487-9 (1984).

[44] T. Shimazu and M. Shiozaki, "Effect of Grain Size and Frequency on Eddy Current Loss in Si-Fe Sheets," *IEEE Trans. Magn.* **26** [5], 1972-4 (1990).

[45] C. Kittel, "Note on the Inertia and Damping Constant of Ferromagnetic Domain Boundaries," *Phys. Rev.* **80** [5], 918 (1950).

[46] A. A. Thiele, "Excitation Spectrum of Magnetic Domain Walls," *Phys. Rev. B* **7** [1], 391-7 (1973).

[47] J. F. Janak, "Dynamics of Diffusion-Damped Domain Wall Motion," *J. Appl. Phys.* **34** [4], 1119-20 (1963).

[48] A. A. Thiele, "Applications of the Gyrocoupling Vector and Dissipation Dyadic in the Dynamics of Magnetic Domains," *J. Appl. Phys.* **45** [1], 377-393 (1974).

[49] F. H. de Leeuw, R. van den Doel, and U. Enz, "Dynamic Properties of Magnetic Domain Walls and Magnetic Bubbles," *Rep. Prog. Phys.* **43** [6], 689-783 (1980).

[50] T. Merceron, M. Guyot, and V. Cagan, "Domain-Wall Damping and Diffusion in Pure Polycrystalline YIG," *Phys. Let.* **95A** [7], 388-90 (1983).

[51] Merceron, M. Guyot, A. Messekher, and V. Cagan, "Do the Diffusants Contribute to the Wall Damping in Polycrystalline Garnets," *Adv. Ceram.* **15**, 481-5 (1985).

[52] M. Guyot, T. Merceron, V. Cagan, and A. Messekher, "Mobility and/or Damping of the Domain Wall. Comparison between Experimental and Theoretical Values in Ferrimagnets," *Phys. Stat. Sol. A* **106**, 595-612 (1988).

[53] H. Harper and R. W. Teale, "Damping of Magnetic Domain-Wall Motion in Pure and Ytterbium-Doped Yttrium Iron Garnet," *J. Phys. C (Solid St. Phys.)* **2**, 1926-33 (1969).

[54] J. L. Snoek, "Gyromagnetic Resonance in Ferrites," *Nature* **160**, 90 (1947).

[55] G. T. Rado, "Magnetic Spectra of Ferrites, "*Rev. Mod. Phys.* **25** [1], 81-9 (1953).

[56] D. Park, "Magnetic Rotation in a Polycrystalline Ferrite," *Phys. Rev.* **97** [1], 60-6 (1955).

[57] E. G. Visser, J. J. Roelofsma, and G. J. M. Aaftink, "Domain Wall Loss and Rotational Loss in High Frequency Power Ferrites," *Proc. ICF-5*, 605-609 (1989).

[58] G. W. Pierce, "Magnetostriction Oscillators," *Proc. IRE* **17** [1], 42-88 (1929).

[59] S. Butterworth and F. D. Smith, "The Equivalent Circuit of the Magnetostriction Oscillator," *Proc. Phys. Soc.* **43**, 166-85 (1931).

[60] W. F. Brown, Jr., "Irreversible Magnetic Effects of Stress," *Phys. Rev.* **75** [1], 147-54 (1949).

[61] C. M. van der Burgt and H. S. J. Pijls, "Dynamical Physical Parameters of the Magnetostrictive Excitation of Extensional and Torsional Vibrations," *Philips Res. Rep.* **8**, 91-132 (1953).

[62] E. Callen and H. B. Callen, "Magnetostriction, Forced Magnetostriction, and Anomalous Thermal Expansion in Ferromagnets," *Phys. Rev.* **139** [2A], A455-71 (1965).

[63] D. C. Jiles and D. Atherton, "Theory of the Magnetisation Process in Ferromagnets and its Application to the Magnetomechanical Effect," *J. Phys. D: Appl. Phys.* **17**, 1265-81 (1984).

[64] M. J. Sablik, H. Kwun, G. L. Burkhardt, and D. C. Jiles, "Model for the Effect of Tensile and Compressive Stress on Ferromagnetic Hysteresis," *J. Appl. Phys.* **61** [8], 3799-801 (1987).

[65] K. C. Pitman, "The Influence of Stress on Ferromagnetic Hysteresis," *IEEE Trans. Magn.* **26** [5], 1978-80 (1990).

[66] Butterworth and F. D. Smith, *Proc. Phys. Soc.* **43**, 166 (1931).

[67] C. M. van der Burgt and H. S. J. Pijls, "Dynamical Physical Parameters of the Magnetostrictive Excitation of Extensional and Torsional Vibrations," *Philips Res. Rep.* **8**, 91-132 (1953).

[68] E. L. Boyd, "Magnetoelastic Resonances in Ferrite Memory Cores," *Journal of Applied Physics*, Vol. 38, No. 5, pp. 2367-2375, April 1967.

[69] Modzelewski, H. T. Savage, L. T. Kabacoff, and A. E. Clark, *IEEE Transactions on Magnetics* **17**, 2837 (1981).

[70] V. J. Thottuvelil, T. G. Wilson, and H. A. Owen, Jr., "High-Frequency Characteristics of Amorphous Metallic-Alloy Tape-Wound Cores," *IEEE Power Electronics Specialists Conference Record*, Albuquerque, New Mexico, June 1983, 83CH1877-0, pp. 168-1331.

[71] B. Hathaway and M. L. Spano, "Measurement of High Magnetomechanical Coupling Factors by Resonance Techniques," *J. Appl. Phys.* **55** [6], 1765-1767 (1984).

[72] V. J. Thottuvelil, T. G. Wilson, and H. A. Owen, Jr., "Unusual High-Frequency Behavior of Some Amorphous Metallic-Alloy Tape-Wound Magnetic Cores," *IEEE Transactions on Magnetics*, Vol. 20, No. 4, July 1984, pp. 570-578.

[73] V. J. Thottuvelil, T. G. Wilson, and H. A. Owen, Jr., "High-Frequency Core-Loss Characteristics of Biased $Fe_{79}B_{16}Si_5$ Amorphous Metallic-Alloy Tape-Wound Cores," *IEEE Transactions on Magnetics*, **20** [5], 1329-1331 (1984).

[74] V. R. V. Ramanan, C. H. Smith, and L. Barbieri, "Magnetomechanical Resonant Losses in Metallic Glasses," *Journal of Applied Physics*, **57** [1], 3493-3495 (1985).

[75] Néel, "Directional Order and Diffusion Aftereffect," *J. Appl. Phys.* **30** [4, Suppl.], 3S-8S (1959).

[76] H. L. Garbarino, "Some Properties of the Optimum Power Transformer Design," *AIEE Trans. pt. III-A: Power Appar. Syst.* **73**, 675-83 (1954).

[77] R. E. Turkington, "Effect of Operating Frequency on the Weight and Other Characteristics of Missile Alternators and Transformers," *Trans. AIEE* **77** pt. 2, 289 (1958).

[78] J. W. Kallander, "Designing Minimum Weight Magnetic Cores," *Electr. Manuf.* **61** [2], 118-23 (1958).

[79] Jakielski and Tillinger, "Computer Design of Small Power Transformers and Inductors," *IEEE Winter General Conference*, Paper CP63-466 (1963).

[80] D. S. Shull, "Rapid Design of Electronic Power Transformers Using a Computer Time-Sharing System," *IEEE Trans. Magn.* **MAG-5**, 934-8 (1969).

[81] P. E. Reeves, "Computer-Aided Design of Power Converter Transformers," *Proc. Workshop on Applied Magnetics*, Washington, D.C. (May 1972).

[82] M. D. Palmer, "Small Transformer Design by Computer," *Technical Report* **73155**, Royal Aircraft Establishment, Farnborough, England (Feb. 1974).

[83] P. H. Odessey, "Transformer Design by Computer," *IEEE Trans. Mfg. Tech.* **MFT-3**, 1-17 (1974).

[84] F. F. Judd and D. R. Kressler, "Design Optimization of Small Low-Frequency Power Transformers," *IEEE Trans. Magn.* **MAG-13** [4], 1058-69 (1977).

[85] E. C. Snelling, *Soft Ferrites*, 2nd Ed., Butterworth & Co., London, 1988, 291-6.

[86] J. P. Vandelac, and P. Ziogas, "A novel approach for minimizing high frequency transformer copper losses," *IEEE Power Electronics Specialists Conference Record,* 355-367 (1987).

[87] N. R. Coonrod, "Transformer Computer Design Aid for Higher Frequency Switching Power Supplies," *IEEE Trans. Power Electronics* **PE-1** [4], 248-56 (1986).

[88] P. L. Dowell, "Effect of Eddy Currents in Transformer Windings," *Proc. IEE* **113** [8], 1387-94 (1966).

[89] B. Carsten, "High Frequency Conductor Losses in Switchmode Magnetics," *High Frequency Power Conversion Conf.*, 155-76 (1986).

[90] M. P. Perry, "Multiple Layer Series Connected Winding Design for Minimum Losses," *IEEE Trans. Power App. Syst.* **PAS-98** [1], 116-23 (1979).

[91] J. P. Vandelac and P. Ziogas, "A Novel Approach for Minimizing High Frequency Transformer Copper Losses," *IEEE PESC Record* **87CH2459-6**, 355-67 (1987).

[92] P. S. Venkatraman, "Winding Eddy Current Losses in Transformer Windings Due to Rectangular Wave Currents," *Proc. Powercon* **11** [A-1], 1-11 (1984).

[93] A. M. Urling, V. A. Niemela, G. R. Skutt, and T. G. Wilson, "Characterizing High-Frequency Effects in Transformer Windings — A Guide to Several Significant Articles," *IEEE Power Electronics Specialists Conference Record* **CH2719-3**, 373-85 (1989).

[94] Van A. Niemela, G. R. Skutt, A. M. Urling, Y. Chang, T. G. Wilson, H. A. Owen, Jr., R. C. Wong, "Calculating the short-circuit impedances of a multiwinding transformer from its geometry," *IEEE Power Electronics Specialists Conference Record* **CH2721-9**, 607-617 (1989).

[95] *Hewlett-Packard Co.*, "Test and Measurement Catalog," 1991.

[96] P. M. Gradzki and F. C. Lee, "Power Tests of Ferrite Materials in 1 to 20 MHz Range," *VPEC Power Electronics Seminar*, Blacksburg, VA, September 1989, pp. 175-180.

[97] M. Gradzki and F. C. Lee, "High-Frequency Core Loss Characterization Based on Impedance Measurement," *High Frequency Power Conference*, 1991, Toronto, Canada.

[98] A. F. Goldberg, "High Field Properties of Nickel-Zinc Ferrites at 1-10 MHz," *Applied Power Electronics Conference*, New Orleans, LA, February 1-5, 1988.

[99] J. Tamsky, "A Cathode-Ray B-H Tracer," *Elect. Eng.* **66**, 678-80 (1947).

[100] B. Christensen, "Radio Frequency B-H Tracer and Power Measurement of Ferrites," *AIEE Conf. Magn. Magn. Mat.* **T-78**, 361-4 (1955).

[101] T. Katane, T. Yamaguchi, T. Ito, T. Sato, and Y. Sakaki, "A High Frequency Iron Loss Measuring System," *IEEE Trans. Magn.* **MAG-20** [5], 1729-31 (1984).

[102] T. Mochizuki, I. Sasaki, and K. Murakawa, "A High Frequency Core Loss Automatic Measuring System," *IEEE Trans. Magn.* **MAG-22** [5], 668-70 (1986).

[103] T. Sato and Y. Sakaki, "100kHz-10MHz Iron Loss Measuring System," *IEEE Trans. Magn.* **MAG-23** [5], 2593-5 (1987).

[104] A. F. Goldberg, "High Field Properties of Nickel-Zinc Ferrites at 1-10 MHz," *Applied Power Electronics Conference*, (1988).

[105] H. W. Lord, "Dynamic Hysteresis Loop Measuring Equipment," *AIEE Trans. Part 1: Comm. Electron.* **71**, 269-72 (1952).

[106] M. Honda, "*The Impedance Measurement Handbook. A Guide to Measurement Technology and Techniques*," Yokogawa-Hewlett-Packard, 1989.

[107] M. Wien, "Ueber die Magnetisirung durch Wechselstrom," *Ann. Phys. Chem.* **66** [13], 859-953 (1898).

[108] R. C. Pal, "Harmonic Correction Theory for Measuring Iron-loss by Bridge-method," *J. Technol.* **5**, 127-44 (1960).

[109] I. Bady, "Measurement of Losses of Magnetic Materials at High Inductions at Frequencies up to 100 Megacycles," *J. Appl. Phys.* **29** [3], 393-4 (1958).

[110] B. Carsten, "Fast, Accurate Measurement of Core Loss at High Frequencies," *Power Conversion and Intelligent Motion* **12** [8], 14-24 (1986).

[111] J. K. Bowman, R. F. Cascio, M. P. Sayani, and T. G. Wilson, "A Calorimetric Method for Measurement of Total Loss in a Power Transformer," *PESC91 Record* **91CH3008-0**, 634-40 (1991).

[112] E. C. Snelling, "Soft Ferrites," *Butterworth, London, 1988,* pp. 28-30.

[113] P. Weiss, "L'Hypothése du champ moléculaire et la propriété ferromagnétique," *J. Phys. (Paris)* **6**, 661 (1907).

[114] L. Landau and E. Lifshitz, "On the Theory of the Dispersion of Magnetic Permeability in Ferromagnetic Bodies," *Phys. Z. Sowjet.* **8**, 153-169 (1935).

[115] K. Ejiri, "Grain Shapes in Two-Dimensional Sections of Sintered Bodies," *J. Cryst. Growth*, **19** [1], 77-8 (1973).

[116] J. G. Oudemans, "Continuous Hot Pressing," *Philips Tech. Rev.* **29** [2], 45-53 (1968).

[117] L. A. Brissentte, E. A. Grossi, J. A. Tillar, K. Chevren, and R. M. Spriggs, "Hot Pressed Ferrites; Magnetic-Mechanical-Microstructural Interactions," *Sci. Sintering* **7** [2], 155-60 (1975).

[118] C. Büthker, T. Berben, "Hot Isostatic pressing of Mn-Zn Ferrites for magnetic Recording Heads," *J. Phys. (Paris) Colloque* **38** [C1, suppl. 4], C1 —341-3 (1977).

[119] H. Löbl, P. Neusser, M. Zenger, J. Frey, "A New Ferrite Material for Video Recording Heads," *J. Phys. (Paris) Colloque* **38** [C1, suppl. 4], C1 —345-8 (1977).

[120] M. I. Mendelson, "Average Grain Size in Ceramics," *J. Am. Ceram. Soc.* **52** [8], 443-6 (1969).

[121] G. H. Jonker and A. L. Stuijts, "Controlling the Properties of Electroceramic Materials through their Microstructure," *Philips Tech. Rev.* **32** [3/4], 79-95 (1971).

[122] H. J. Vink, "Sintering," *Philips Tech. Rev.* **35** [7/8], 188-95 (1975).

[123] K. Ishino and Y. Narumiya, "Development of Magnetic Ferrites: Control and Application of Losses," *Ceram. Bull.* **66** [10], 1469-74 (1987).

[124] A. Nakata, H. Chihara, and A. Sasaki, "Microscopic Study of Grain-Boundary Region in Polycrystalline Ferrites," *J. Appl. Phys.* **57** [1], 4177-9 (1985).

[125] P. F. Bongers, F. J. A. den Broeder, J. P. M. Damen, P. E. C. Franken, and W. T. Stacy, "Defects, Grain Boundary Segregation, and Secondary Phases of Ferrites in Relation to the Magnetic Properties," *Ferrites: Proc. Int. Conf. (Japan)*, 265-71 (1980).

[126] G. C. Jain, B. K. Das, and S. Kumari, "On the Origin of Core Losses in a Manganese Zinc Ferrite with Appreciable Silica Content," *J. Appl. Phys.* **49** [5], 2894-7 (1978).

[127] C. Kittel, "Theory of the Structure of Ferromagnetic Domains in Films and Small Particles," *Phys. Rev.* **70**, 965-971 (1946).

[128] C. Kittel, "Physical Theory of Ferromagnetic Domains," *Rev. Mod. Phys.* **21** [4], 541-83 (1949).

[129] L. Néel, "Propriétés d'un ferromagnétique cubique en grains fins," *Compt. Rend.* **224**, 1488-90 (1947).

[130] G. Rankis, *Dynamics of Magnetization in Polycrystalline Ferrites*, Zinatne, Riga, 25-32, 1981 (in Russian).

[131] J. B. Goodenough, "A Theory of Domain Creation and Coercive Force in Polycrystalline Ferromagnets," *Phys. Rev.* **95** [4], 917-32 (1954).

[132] A. G. Tobin and D. I. Paul, "Stability of Ferromagnetic Domain Structures at Grain Boundaries," *J. Appl. Phys.* **40** [9], 3611-4 (1969).

[133] I-N. Lin, R. K. Mishra, and G. Thomas, "Interaction of Magnetic Domain Walls with Microstructural Features in Spinel Ferrites," *IEEE Trans. Magn.* **MAG-20** [1], 134-9 (1984).

[134] J. Smit and H. P. J. Wijn, *Ferrites*, John Wiley & Sons, New York, 72-73 (1959).

[135] G. Rankis, "The Model of Initial Magnetic Permeability of Polycrystalline Ferrites," *Latv. PSR Zinat. Akad. Vest. Fiz. Teh. Zinat. Ser.* [2], 27-34 (1984). In Russian.

[136] I-N. Lin, R. K. Mishra, and G. Thomas, "Interaction of Magnetic Domain Walls with Microstructural Features in Spinel Ferrites," *IEEE Trans. Magn.* **MAG-20** [1], 134-9 (1984).

[137] R. Becker, "Zur Theorie der Magnetisierungcurve," *Z. Phys.* **62**, 253-9 (1930).

[138] M. Kersten, "Die Wölbung del Blochwand als Elementarvorgang reversibler Magnetisierungsänderungen (Anfangspermeabilität und ΔE-Effekt)," *Z. Angew. Phys.* **8** [7], 313-22 (1956).

[139] M. Kersten, "Zur Deutung des Temperaturganges der Anfangspermeabilität (Mn_2Sb, Kobalt, Eisen, Nickel)," *Z. Angew. Phys.* **8** [8], 382-6 (1956).

[140] A. Globus, "Influence des dimensions des parois sur la perméabilité initiale," *C. R. Acad. Sci.* **255** [15], 1709-11 (1962).

[141] H. Kaplan, "The Determination of the Energy of a Ferromagnetic Domain Boundary," *Phys. Rev.* **81** [5], 885 (1951).

[142] J. Smit and H. P. J. Wijn, *Ferrites*, John Wiley & Sons, New York, 72-73 (1959).

[143] B. Hoekstra, E. M. Gyorgy, P. K. Gallagher, D. W. Johnson, Jr., G. Zydzik, and L. G. van Uitert, "Initial Permeability and Intrinsic Magnetic Properties of Polycrystalline Mn-Zn Ferrites," *J. Appl. Phys.* **49** [9], 4902-7 (1978).

[144] D. Stoppels, "Relationship Between Magnetocrystalline Anisotropy, Including Second-Order Contribution, and Initial Magnetic Permeability for Monocrystalline MnZn Ferrous Ferrite," *J. Appl. Phys.* **51** [5], 2789-94 (1980).

[145] G. Rankis, "Comparison of the Theory of Initial Magnetic Permeability with the Experiment," *Latv. PSR Zinat. Akad. Vest. Fiz. Teh. Zinat. Ser.* [2], 35-42 (1984). In Russian.

[146] V. P. Miroshkin, "Models for the Initial Susceptibility of Polycrystalline Ferrites," *Sov. Phys. Tech. Phys.* **28** [3], 329-31 (1983).

[147] V. P. Miroshkin, Y. I. Panova, E. A. Popova, and L. N. Gar'kin, "Application of the Model of Bending Domain Walls to the Analysis of the Temperature Dependence of the Susceptibility and Magnetic Spectra of Polycrystalline Ferrites," *Sov. Phys. Tech. Phys.* **32** [11], 1329-31 (1987).

[148] H. Jordan, "Die ferromagnetischen Konstanten für schwache Wechselfelder," *Elek. Nach. Tech.* **1**, 7-29 (1924).

[149] V. E. Legg, "Magnetic Measurements at Low Flux Densities Using the Alternating Current Bridge," *Bell. Syst. Tech. J.* **15**, 39-62 (1936).

[150] R. Becker and W. Döring, *Ferromagnetism*, Springer-Verlag, Berlin, 1939.

[151] J. Smit and H. P. J. Wijn, *Ferrites*, John Wiley & Sons, New York, 135 (1959).

[152] H. J. Williams, W. Shockley, and C. Kittel, "Studies of the Propagation Velocity of a Ferromagnetic Domain Boundary," *Phys. Rev.* **80**, 1090-4 (1950).

[153] R. H. Pry and C. P. Bean, "Calculation of the Energy Loss in Magnetic Sheet Materials Using a Domain Model," *J. Appl. Phys.* **29** [3], 532-3 (1958).

[154] R. M. Bozorth, *Ferromagnetism*, D. van Nostrand Co., New York, 769-810 (1951).

[155] E. P. T. Tyndall, "The Barkhausen Effect," *Phys. Rev.* **24** [4], 439-51 (1924).

[156] K. Sixtus and L. Tonks, "Propagation of Large Barkhausen Discontinuities," *Phys. Rev.* **37**, 930-58 (1931).

[157] R. S. Tebble, I, C. Skidmore, and W. D. Corner, "The Barkhausen Effect," *Proc. Phys. Soc.* **63** pt. 7 [367A], 739-60 (1950).

[158] G. Bertotti, "Space-Time Correlation Properties of the Magnetization Process and Eddy Current Losses: Applications, " *J. Appl. Phys.* **55** [12], 4339-55 (1984).

[159] F. Bloch, "Zur Theorie des Austauschproblems und der Remanenzerscheinung der Ferromagnetika," *Z. Phys.* **74**, 295-335 (1932).

[160] E. Kondorsky, "On the Nature of the Coercive Force and Irreversible Changes in Magnetization," *Phys. Z. Sow.* **11**, 590-620 (1937).

[161] M. Kersten, *Probleme der Technischen Magnetisierungcurve, Zur Deutung der Koerzitivkraft*, edited by R. Becker, Springer Verlag, Berlin; reprinted J. W. Edwards, Ann Arbor, 42-72 (1938).

[162] M. Kersten, *Grundlagen einer Theorie der ferromagnetischen Hysterese und der Koerzitivkraft*. J. W. Edwards, Ann Arbor, Michigan, (1943).

[163] L. Néel, "Effet des cavités et des inclusions sur le champ coercitif," *Cah. Phys.* **25**, 21-44 (1944).

[164] L. Néel, "Bases d'une nouvelle théorie générale du champ coercitif," *Ann. Univ. Grénoble Sect. Sci. Math. Phys.* **22**, 299-343 (1946).

[165] C. Kittel and J. K. Galt, "Ferromagnetic Domain Theory," *Sol. St. Phys.* **3**, 437-564 (1956).

[166] F. Brown and C. L. Gravel, "Domain Rotation in Nickel Ferrite," *Phys. Rev.* **97** [1], 55-9 (1955).

[167] D. C. Jiles and D. L. Atherton, "Theory of Ferromagnetic Hysteresis," *J. Appl. Phys.* **55** [6], 2115-20 (1984).

[168] J. Smit and H. P. J. Wijn, *Ferrites*, John Wiley & Sons, New York, 75 (1959).

[169] D. I. Paul, "The Coercive Force and the Theory of Ferromagnetic Domain Wall Pinning," *AIP Conf. Proc.* **29**, 545-50 (1975).

[170] D. I. Paul, "General Theory of the Coercive Force Due to Domain Wall Pinning," *J. Appl. Phys.* **53** [3], 1649-54 (1982).

[171] Lord Rayleigh, "Notes on Electricity and Magnetism III. On the Behaviour of Iron and Steel Under the Operation of Feeble Magnetic Forces," *Phil. Mag.* **23**, 225 (1887).

[172] E. C. Snelling and A. D. Giles, *Ferrites for Inductors and Transformers*, John Wiley and Sons, New York, 52 (1983).

[173] A. D. Giles and F. F. Westendorp, "Some Loss Relationships in Mn-Zn Ferro Ferrites and Their Response to Magnetic Disturbance," *IEEE Trans. Magn.* **MAG-18** [4], 944-50 (1982).

[174] L. Néel, "Some Theoretical Aspects of Rock Magnetism," *Adv. Phys. (Phil. Mag. Suppl.)* **4**, 191-244 (1955).

[175] D. Park, "Magnetic Rotation in a Polycrystalline Ferrite," *Phys. Rev.* **97** [1], 60-6 (1955).

[176] J. L. Snoek, "Gyromagnetic Resonance in Ferrites," *Nature* **160**, 90 (1947).

[177] C. Kittel, "Ferromagnetic Resonance," *J. Phys. Radium* **12**, 291-302 (1951).

[178] W. F. Brown, Jr., "Irreversible Magnetic Effects of Stress," *Phys. Rev.* **75** [1], 147-54 (1949).

[179] J. Smit and H. P. J. Wijn, *Ferrites*, John Wiley & Sons, New York, 287-9 (1959).

[180] G. W. Pierce, "Magnetostriction Oscillators," *Proc. IRE* **17** [1], 42-88 (1929).

[181] C. M. van der Burgt and H. S. J. Pijls, "Dynamical Physical Parameters of the Magnetostrictive Excitation of Extensional and Torsional Vibrations," *Philips Res. Rep.* **8**, 91-132 (1953).

[182] C. M. van der Burgt, "Performance of Ceramic Ferrite Resonators as Transducers and Filter Elements," *J. Acoust. Soc. Am.* **28** [6], 1020-32 (1956).

[183] C. M. van der Burgt, "Ferrites for Magnetic and Piezomagnetic Filter Elements with Temperature-Independent Permeability and Elasticity," *Proc. IEE* **104B** [Suppl. 7], Paper No. 2287R, 550-7 (1957).

[184] C. M. van der Burgt, "Motional Positive Feedback Systems for Ultrasonic Power Generators," *IEEE Trans. Ultrason. Eng.*, 2-19 (1963).

[185] E. Callen and H. B. Callen, "Magnetostriction, Forced Magnetostriction, and Anomalous Thermal Expansion in Ferromagnets," *Phys. Rev.* **139** [2A], A455-71 (1965).

[186] E. Callen, "Magnetostriction," *J. Appl. Phys.* **39** [2], 519-27 (1968).

[187] E. L. Boyd, "Magnetoelastic Resonances in Ferrite Memory Cores," *J. Appl. Phys.* **38** [5], 2367-75 (1967).

[188] A. Akhieser, "Theory of the Relaxation Processes in Ferromagnetics at Low Temperatures," *J. Phys. U.S.S.R* **10**, 217-30 (1946).

[189] W. Döring, "Über die Trägheit der Wände zwischen Weisschen Bezirken," *Z. Naturforsch.* **3a**, 373-9 (1948).

[190] G. T. Rado, "Magnetic Spectra of Ferrites, "*Rev. Mod. Phys.* **25** [1], 81-9 (1953).

[191] F. B. Hagedorn and E. M. Gyorgy, "Domain Wall Mobility in Single-Crystal Yttrium Iron Garnet," *J. Appl. Phys.* **32** [3, Suppl.], 282S-3S (1961).

[192] G. T. Rado, R. W. Wright, and W. H. Emerson, "Ferromagnetism at Very High Frequencies. III. Two Mechanisms of Dispersion in a Ferrite," *Phys. Rev.* **80** [2], 273-80 (1950).

[193] E. G. Visser, J. J. Roelofsma, and G. J. M. Aaftink, "Domain Wall Loss and Rotational Loss in High Frequency Power Ferrites," *Proc. ICF-5*, 605-609 (1989).

[194] J. L. Snoek, "Non-Metallic Magnetic Materials for High Frequencies," *Philips Tech. Rev.* **8** [12], 353-84 (1946).

[195] H. P. J. Wijn and H. van der Heide, "A Richter Type After-Effect in Ferrites Containing Ferrous and Ferric Ions," *Rev. Mod. Phys.* **25** [1], 98 (1953).

[196] J. Smit and H. P. J. Wijn, *Ferrites*, John Wiley & Sons, New York, 289-97 (1959).

[197] V. G. Bar'yakhtar, "Phenomenological Description of Relaxation Processes in Magnetic Materials," *Sov. Phys. JETP* **60** [4], 863-7 (1984).

[198] V. G. Bar'yakhtar, "The Phenomenological Theory of Relaxation Process in Magnetics," *Proc. 4th Int. Conf. Phys. Magn. Mat.* (Poland), 21-41 (1988).

[199] T. G. W. Stijntjes, J. Klerk, and A. Broese van Groenou, "Permeability and Conductivity of Ti-Substituted MnZn Ferrites," *Philips Res. Rep.* **25**, 95-107 (1970).

[200] A. Broese van Groenou, P. F. Bongers, and A. L. Stuyts, "Magnetism, Microstructure and Crystal Chemistry of Spinel Ferrites," *Mater. Sci. Eng.* **3**, 353-4 (1968/69).

[201] V. P. Miroshkin, Y. I. Panova, and T. V. Stakhieva, "Electrical Conductivity of Manganese-Zinc Ferrospinels," *Phys. Stat. Sol. (A)* **66**, 503-7 (1981).

[202] I. I. Zyatkov, V. P. Miroshkin, and Y. I. Panova, "High-Frequency Conductivity of Manganese-Zinc Ferrites," *Phys. Stat. Sol. (A)* **83**, 645-50 (1984).

[203] I. I. Zyatkov, V. P. Miroshkin, and Y. I. Panova, "Investigation of the Mechanism of Electrical Conduction in Manganese Zinc Ferrites," *Sov. Phys. Solid State* **30** [5], 748-50 (1988).

[204] S. Chikazumi, *Physics of Magnetism*, John Wiley and Sons, New York, 344 (1964).

[205] E. J. W. Verwey and P. W. Haaijman, "Electronic Conductivity and Transition Point of Magnetite (Fe_3O_4)," *Physica* **8**, 979-87 (1941).

[206] E. J. W. Verwey, P. W. Haaijman, F. C. Romeyn, and G. W. van Oosterhout, "Controlled Valency Semiconductors," *Philips Res. Rep.* **5**, 173-87 (1950).

[207] A. M. van Diepen and F. K. Lotgering, "Electron Exchange Between Fe^{2+} and Fe^{3+} on Octahedral Sites in Spinels," *Physica* **86-88**, 961-2 (1977).

[208] V. N. Berzhanskii, I. I. Evstafev, and V. I. Ivanov, "Charge Carrier Transfer in Ferrite Spinels Affected by Magnetic Ordering," *Phys. Stat. Sol. (B)* **158**, 643-52 (1990).

[209] A. Broese van Groenou, P. F. Bongers, and A. L. Stuyts, "Magnetism, Microstructure and Crystal Chemistry of Spinel Ferrites," *Mater. Sci. Eng.* **3**, 348-51 (1968/69).

[210] L. Néel, "Directional Order and Diffusion Aftereffect," *J. Appl. Phys.* **30** [4, Suppl.], 3S-8S (1959).

[211] C. Kittel and J. K. Galt, "Ferromagnetic Domain Theory," *Sol. St. Phys.* **3**, 437-564 (1956).

[212] P. F. Bongers, F. J. A. den Broeder, J. P. M. Damen, P. E. C. Franken, and W. T. Stacy, "Defects, Grain Boundary Segregation, and Secondary Phases of Ferrites in Relation to the Magnetic Properties," *Ferrites: Proc. Int. Conf. (Japan)*, 265-71 (1980).

[213] A. Nakata, H. Chihara, and A. Sasaki, "Microscopic Study of Grain-Boundary Region in Polycrystalline Ferrites," *J. Appl. Phys.* **57** [1], 4177-9 (1985).

[214] A. M. Donets, V. N. Fedosov, and L. S. Ochneva, "Energy Dissipation in High-Frequency Remagnetization of Ferrites," *Sov. Phys. J.* **28** [6], 442-5 (1985).

[215] Y. Saito, S. Hayano, and Y. Sakaki, "A Parameter Representing Eddy Current Loss of Soft Magnetic Materials and its Consecutive Equation," *J. Appl. Phys.* **64** [10], 5684-6 (1988).

[216] T. Sano, A. Morita, and A. Matsukawa, "Power Ferrite Has Less than 400 mW/cm ^{3} Core Loss at 1 MHz," *Power Conv. Intel. Mot.* **14** [7], 19-25 (1988).

[217] Y. Naito, "On the Permeability Dispersion of a Spinel Ferrite," *Electron. Comm. Jap.* **56-C** [2], 118-23 (1973).

[218] Y. Naito, "Formulation of Frequency Dispersion of Ferrite Permeability," *Electron. Comm. Jap.* **59-C** [5], 100-23 (1976).

[219] V. P. Miroshkin, Y. I. Panova, and V. V. Pasynkov, "Determination of Certain Parameters of Mn-Zn Ferrites from the Radio-Frequency Susceptibility," *Sov. Phys. Tech. Phys.* **23** [11], 1371-3 (1978).

[220] G. P. Kramar and Y. I. Panova, "Resonance and Relaxation of Domain Walls in Polycrystalline Ferrites," *Phys. Stat. Sol. (A)* **77**, 483-9 (1983).

[221] G. P. Kramar and Y. I. Panova, "The Permeability Dispersion in Ferrites at Different Levels of Direct Current Magnetic Biasing," *Phys. Stat. Sol. (A)* **86**, 283-7 (1984).

[222] C. G. Koops, "On the Dispersion of Resistivity and Dielectric Constant of Some Semiconductors at Audiofrequencies," *Phys. Rev.* **83** [1], 121-4 (1951).

[223] V. P. Miroshkin, Y. I. Panova, and V. V. Passynkov, "Dielectric Relaxation in Polycrystalline Ferrites," *Phys. Stat. Sol. (A)* **66**, 779-82 (1981).

[224] S. Yamada, E. Otsuki, and T. Otsuka, "AC Resistivity of Mn-Zn Ferrites," *Proc. Intelec'91* **CH2970-2/91**, 703-8 (1991).

[225] A. D. Giles and F. F. Westendorp, "Some Loss Relationships in Mn-Zn Ferro Ferrites and Their Response to Magnetic Disturbance," *IEEE Trans. Magn.* **MAG-18** [4], 944-50 (1982).

[226] T. G. W. Stijntjes and J. J. Roelofsma, "Low-Loss Power Ferrites for Frequencies up to 500 kHz," *Adv. Ceram.* **16**, 493-500 (1985).

[227] T. Sato and Y. Sakaki, "Mechanism Generating Power Losses in MHz Band in Polycrystalline Mn-Zn Ferrite Cores Used for Switching Power Supplies," *Electron. Comm. Jpn. Part 2*, **72** [6], 42-50 (1989).

[228] V. V. Dyakin and B. M. Letfulov, "Localized Spin-Polaron States in Ferromagnets," *Theor. Mat. Phys.* **73** [3], 1337-43 (1987).

[229] L. D. Landau and E. M. Lifshitz, *Electrodynamics of Continuous Media*, Addison-Wesley Publishing Co., Reading, MA, (1960).

[230] I. E. Dzyaloshinskii, "On the Magneto-Electrical Effect in Antiferromagnets," *Sov. Phys. JETP* **10**, 628-9 (1960).

[231] D. N. Astrov, "The Magnetoelectric Effect in Antiferromagnets," *Sov. Phys. JETP* **11**, 708-9 (1960).

[232] D. N. Astrov, "Magnetoelectric Effect in Chromium Oxide," *Sov. Phys. JETP* **13** [4], 729-33 (1961).

[233] G. T. Rado, "Present Status of the Theory of Magnetoelectric Effects," *Int. J. Magn.* **6**, 121-33 (1974).

[234] V. I. Salyganov, Yu. M. Yakovlev, and Yu. R. Shil'nikov, "Magnetoelectric Resonance in Magnetic Semiconductors," *JETP Lett.* **18**, 215-6 (1973).

[235] P. Kuivalainen, J. Sinkkonen, and T. Stubb, "Contribution to the Theory of Magnetoelectric Effect in Magnetic Semiconductors," *Phys. Scr.* **21**, 115-21 (1980).

[236] V. P. Gnedkov, V. P. Seminozhenko, V. L. Sobolev, and D. F. Fil', "Magnon Drag of Conduction Electrons in Magnetic Semiconductors in the Field of a Strong Electromagnetic Wave," *Sov. Phys. Solid State* **32** [11], 1858-60.

[237] G. T. Rado and J. M. Ferrari, "Electric Field Dependence of the Magnetic Anisotropy Energy in Magnetite (Fe_3O_4)," *Phys. Rev. B* **12** [11], 5166-74 (1975).

[238] G. T. Rado and J. M. Ferrari, "Linear and Bilinear Magnetoelectric Effects in Magnetically Biased Magnetite (Fe_3O_4)," *Phys. Rev. B* **15** [1], 290-7 (1977).

[239] G. Aubert, "A Novel Approach of the Magnetoelectric Effects in Ferrimagnets," *J. Appl. Phys.* **53** [11], 8125-8 (1982).

[240] G. Aubert, "A Novel Approach of the Magnetoelectric Effects in Ferrimagnets," *J. Magn. Magn. Mat.* **31-34**, 767-8 (1983).

[241] E. V. Babkin and N. G. Cherkunova, "Influence of an Electric Field on the Magnetic Anisotropy of Magnetite," *Sov. Phys. Solid State* **26** [6], 1098-1101 (1984).

[242] V. N. Berzhanskii, I. I. Evstaf'ev, and T. N. Metlyayev, "Giant Anisotropy of the magnetoconductivity of Ferrites," *Sov. Tech. Phys. Lett.* **14** [5], 407-8 (1988).

[243] E. G. Rozin, I. S. Zheludev, and M. N. Shipko, "Influence of an Electric Field on the Hyperfine Structure of the Nuclear Gamma Resonance Spectra of Ferrite $Mn_{0.8}Zn_{0.2}Fe_2O_4$," *Sov. Phys. Solid State* **29** [1], 124-5 (1987).

[244] E. Z. Kastnelson and A. G. Karoza, "On the Irreversibility of the Processes during Photomagnetization of Ferrites," *Phys. Stat. Sol. A* **106**, 277-82 (1988).

[245] E. Z. Kastnelson and A. G. Karoza, "On the Irreversibility of the Processes during Photomagnetization of Ferrites," *Phys. Stat. Sol. A* **106**, 277-82 (1988).

[246] A. Largeteau, J. Ravez, and I. S. Jacobs, "Ceramic Ferrites with Grain Boundary Barrier Layers: Role of Grain Composition on Dielectric Properties," *Mater. Sci. Eng.* **B6**, 33-6 (1990).

[247] A. Largeteau, J. M. Reau, and J. Ravez, "Dispersions diélectrique et d'impédance et énergies d'activation de céramiques à couches d'arrêt de type spinelle non stoechiométrique," *Phys. Stat. Sol. A* **121**, 627-34 (1990).

[248] A. Largeteau, J. Ravez, and J. L. Miane, "Space Charge Relaxation in Ferrite Ceramics with Grain Boundary Barrier Layers," *J. Non-Cryst. Solids* **131-133**, 1224-6 (1991).

[249] A. Largeteau, J. L. Miane, J. Ravez, "Modelisation d'une relaxation diélectrique de type charges d'espace dans les ferrites NiZn à couches d'arrêt," *Phys. Stat. Sol. A* **125**, 697-705 (1991).

[250] T. G. W. Stijntjes, J. Klerk, and A. Broese van Groenou, "Permeability and Conductivity of Ti-Substituted MnZn Ferrites," *Philips Res. Rep.* **25**, 95-107 (1970).

[251] M. H. Berger, J. Y. Laval, F. Kools, and J. Roelofsma, "Relations Between Grain Boundary Structure and Hysteresis Losses in Mn-Zn Ferrites for Power Applications," *Proc. ICF-5*, 619-24 (1989).

[252] Philips Components, "3F4 ferrite for MHz power conversion," *Philips Technical Publication* **MA001**, 1-7 (1991).

[253] S. Chikazumi, *Physics of Magnetism*, John Wiley & Sons, New York, (1964).

[254] V. P. Miroshkin, Y. I. Panova, and T. V. Stakhieva, "Electrical Conductivity of Manganese-Zinc Ferrospinels," *Phys. Stat. Sol. (A)* **66**, 503-7 (1981).

[255] J. Smit and H. P. J. Wijn, *Ferrites*, John Wiley & Sons, New York, 343 (1959).

[256] V. P. Miroshkin, Y. I. Panova, and T. V. Stakhieva, "Electrical Conductivity of Manganese-Zinc Ferrospinels," *Phys. Stat. Sol. (A)* **66**, 503-7 (1981).

[257] I. I. Zyatkov, V. P. Miroshkin, and Y. I. Panova, "High-Frequency Conductivity of Manganese-Zinc Ferrites," *Phys. Stat. Sol. (A)* **83**, 645-50 (1984).

[258] V. P. Miroshkin, "The Polycrystalline Ferrites Donor Centers Concentration According to the dc Conductivity Measurements," *Act. Phys. Pol.* **A76** [1], 53-6 (1989).

[259] V. P. Miroshkin, V. V. Passynkov, and K. Perzynska, "The Influence of Mn Ions on the Dielectric Properties of Mn-Zn Ferrites," *Act. Phys. Pol.* **A77** [5], 715-21 (1990).

[260] J. E. Knowles, "Some Observations of Bitter Patterns on Polycrystalline Square Loop Ferrites, and a Theoretical Explanation of the Loop Shape and Pulse Characteristics of the Material," *Proc. Phys. Soc.* **75** [6], 885-97 (1960).

[261] J. E. Knowles, "A Further Explanation of the Shape of the Hysteresis Loop of Square Loop Ferrites," *Proc. Phys. Soc.* **77** [2], 225-9 (1961).

[262] J. E. Knowles, "The Irreversible Change of Magnetization produced in Square Loop Ferrite by Pulsed Magnetic Fields," *Proc. Phys. Soc.* **77** [3], 576-86 (1961).

[263] J. E. Knowles, "The Estimation of Domain Wall Velocity in a Square Loop Ferrite and some Observations on the Reversal Process," *Proc. Phys. Soc.* **78** [2], 233-8 (1961).

[264] J. E. Knowles, "The Magnetization Reversal Process in Square-Loop Ferrites," *Philips Tech. Rev.* **24** [8], 242-51 (1962/3).

[265] J. E. Knowles and K. Tweedale, "The Origin of Delta Noise in Square-Loop Ferrites," *IEEE Trans. Magn.* **MAG-2** [3], 593-7 (1966).

[266] J. E. Knowles, "The Simulation of Domain Wall Motion in Square Loop Ferrites, and Other Aspects of Wall Behaviour," *Brit. J. Appl. Phys.* **1**, 821-30 (1968).

[267] V. J. Thottuvelil, T. G. Wilson, I. Miyazaki, and H. A. Owen, Jr., "High-Frequency Characteristics of Amorphous Metallic-Alloy Tape-Wound Cores," *IEEE Power Electronics Specialists Conference*, 168-80 (1983).

[268] V. J. Thottuvelil, T. G. Wilson, and H. A. Owen, Jr., "Unusual High-Frequency Behavior of Some Amorphous Metallic-Alloy Tape-Wound Magnetic Cores," *IEEE Trans. Magn.* **MAG-20** [4], 570-8 (1984).

[269] V. J. Thottuvelil, T. G. Wilson, and H. A. Owen, Jr., "High-Frequency Core-Loss Characteristics of Biased $Fe_{79}Be_{16}Si_5$ Amorphous Metallic-Alloy Tape-Wound Cores," *IEEE Trans. Magn.* **MAG-20** [5], 1329-31 (1984).

[270] V. R. V. Ramanan, C. H. Smith, and L. Barbieri, "Magnetomechanical Resonant Losses in Metallic Glasses," *J. Appl. Phys.* **57** [1], 3493-5 (1985).

[271] Chih-Wen Chen, *"Magnetism and Metallurgy of Soft Magnetic Materials,"* Dover Publications, Inc., New York, 75-82 (1986).

[272] K. Ohta and N. Kobayashi, "Magnetostriction Constants of Mn-Zn-Fe Ferrites," *Japn. J. Appl. Phys.* **3** [10], 576-80 (1964).

[273] K. Ohta and T. Yamadaya, "Induced Magnetic Anisotropy and Disaccommodation of Manganese-Zinc Ferrites," *J. Phys. Soc. Japn.* **17** [Suppl. B-I], 291-5 (1962).

[274] J. Kotschy and G. Roespel, "Disaccommodation of Permeability of Ferrite Cores after Partial Shocks," *Siemens Rev.* **37**, 263-6 (1970).

[275] L. P. M. Bracke, "High -Frequency Ferrite Power Transformer and Choke Design, Part 2: Switched-Mode Power Supply Magnetic Considerations and Core Selection," *Philips Technical Publication* **206**, 1-7 (1986).

[276] S. A. Mulder, "On the Design of Low Profile High Frequency Transformers," *Proc. High Frequency Power Conversion Conf.*, 141-59 (1990).

[277] E. Bennet and S. C. Larson, "Effective Resistance of Alternating Currents of Multi-layer Windings," *Trans. AIEE* **59**, 1010-7 (1940).

[278] P. L. Dowell, "Effect of Eddy Currents in Transformer Windings," *Proc. IEE* **113** [8], 1387-94 (1966).

[279] J. A. Ferreira, "Appropriate Modelling of Conductive Losses in the Design of Magnetic Components," *IEEE Power Electronics Specialists Conference Record* **CH2873-8**, 780-5 (1990).

[280] C. Manneback, "An integral equation for skin effect in parallel conductors," *J. Math. Phys. MIT* **1**, 123-46 (1922).

[281] S. Butterworth, "Eddy Current Losses in Cylindrical Conductors with Special Applications to the Alternating Current Resistance of Short Coils," *Phil. Trans. R. Soc.* **A222**, 57 (1922).

[282] S. Butterworth, "Effective Resistance of Inductance Coils at Radio Frequency," *Exp. Wireless* **3**, 203 (1926).

[283] J. A. Ferreira, "Appropriate Modelling of Conductive Losses in the Design of Magnetic Components," *IEEE Power Electronics Specialists Conference Record* **CH2873-8**, 780-5 (1990).

[284] T. G. W. Stijntjes, "Power Ferrites; Performance and Microstructure," *Proc. ICF-5*, 587-94 (1989).

[285] S. A. Mulder, "On the Design of Low Profile High Frequency Transformers," *Proc. High Frequency Power Conversion Conf.*, 141-59 (1988).

[286] S. A. Mulder, "On the Design of Low Profile High Frequency Transformers," *Proc. High Frequency Power Conversion Conf.*, 141-59 (1990).

[287] E. C. Snelling, *Soft Ferrites*, 2nd Ed., Butterworth & Co., London, 1988, 291-6.

[288] J. P. Vandelac and P. Ziogas, "A Novel Approach for Minimizing High Frequency Transformer Copper Losses," *IEEE PESC Record* **87CH2459-6**, 355-67 (1987).

[289] V. A. Niemela, G. R. Scutt, A. M. Urling, Y. Chang, T. G. Wilson, H. A. Owen, Jr., R. C. Wong, "Calculating the short-circuit impedances of a multiwinding transformer from its geometry," *IEEE Power Electronics Specialists Conference Record* **CH2721-9**, 607-617 (1989).

[290] J. A. Ferreira, "Appropriate Modelling of Conductive Losses in the Design of Magnetic Components," *IEEE Power Electronics Specialists Conference Record* **CH2873-8**, 780-5 (1990).

Vita

The author was born in Warsaw, Poland. He received his M.S. degree in Electronic Engineering from Warsaw Technical University in 1984. From 1984 to 1985 he was with Institute of Radioelectronics of Warsaw Technical University, developing software and designing microwave interdigital band-pass filters for mobile radio communication.

In 1985 he received his postgraduate training in Gfeller AG, Bern, Switzerland, designing EMI measurement fixture and EMI filters for telecommunication lines.

Since 1986 he has been with Virginia Polytechnic Institute and State University, Blacksburg, Virginia, working towards his doctoral degree. His research interests include analysis, modeling, and design of high-frequency power magnetic devices, thick-film circuits, and power converters.

The author is a member of IEEE Power Electronics Society.